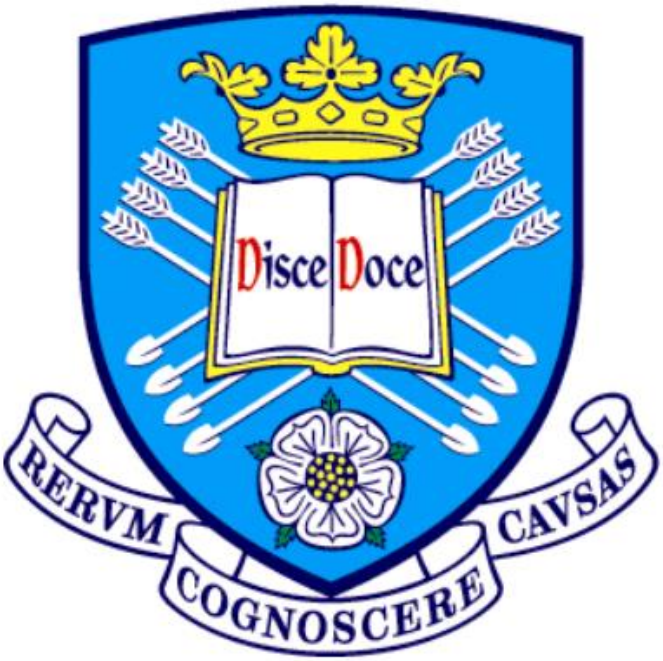

Novel Stator Wound Field Synchronous Machines with Permanent Magnets on Slot Openings

Miss Mei Zheng

A thesis submitted for the degree of Doctor of Philosophy (PhD)

Department of Electronic and Electrical Engineering

University of Sheffield

United Kingdom

22 March 2018

Abstract

The hybrid-excited stator slot opening PM machines (HSSPMMs) can be modified from variable flux machines (VFMs) by adding PMs on the stator slot openings. The PMs in HSSPMMs can be utilized to reduce the stator magnetic saturation caused by DC field excitation in VFMs, and hence to enhance the torque density.

According to the operation principle, the PM flux of the HSSPMMs is shunted in the stator and can be pushed to the rotor via the air-gap by the flux produced from DC field excitation. Hence, the open-circuit characteristics of the HSSPMMs, such as cogging torque and back-EMF, are negligible. However, the electromagnetic performance can be affected by different DC field excitations. The performance of the HSSPMMs will be increased with the increasing field current but limited when the field current is over-excited due to stator magnetic saturation caused by DC field excitation.

In this thesis, novel HSSPMMs are developed by adding PMs in the stator slot openings of the slots for DC windings of DC-excited switched flux machines (SFMs). The PM volume of the novel HSSPMMs is fixed and similar to that of the conventional HSSPMMs for fair comparison. The operation principle and electromagnetic performance of novel HSSPMMs with different rotor poles are investigated. It shows that compared with DC-excited SFMs, the novel HSSPMMs exhibit improved electromagnetic performance and maintain good flux regulation capability. The finite element predicted open-circuit characteristics, e.g. back-EMF and cogging torque, and on-load static torque of the novel HSSPMMs are experimentally validated.

Furthermore, based on the conventional HSSPMMs, the HSSPMMs with ‘U-shaped’ segmental stator can be developed by alternatively removing half of the stator back-irons and PMs. The modular stator HSSPMMs with different rotor pole numbers are optimised and their electromagnetic performance investigated. The modular stator HSSPMMs can also operate as modular stator slot opening PM machines (SSPMMs) without the DC excitation and their corresponding electromagnetic performance is also investigated.

Acknowledgements

First of all, I would like to express my gratitude to my supervisor, Prof. Z. Q. Zhu, for his encouragement, valuable suggestion, and technical discussions to conduct this research. He also spent much time reading the draft of each chapter and offering advice to help me to complete this thesis writing.

I would also like to thank my colleagues for their technical discussions and advice. Mr. Shun Cai, Mr. Huayang Li, and Mr. Yue Liu gave me helpful assistance during prototype testing. The technical staff of the Electrical Machines and Drives Research Group in the Department of Electronic and Electrical Engineering, University of Sheffield, U.K. and the engineers at Wolong Holding Group in China, are also thanked for their support and assistance with building prototypes.

Finally, I thank my parents for their love, support and encouragement.

Nomenclature

B_r	Remanence of flux density	T
B_r	Radial component of air gap flux density	T
B_α	Circumferential component of air gap flux density	T
f	Frequency	
F, UMF	Unbalanced magnetic force	N
F_{rx}, F_{ry}	XY-axis components of radial magnetic force	N
F_{tx}, F_{ty}	XY-axis components of tangential magnetic force	N
F_x, F_y	XY-axis magnetic forces	N
G	Air-gap length	mm
GCD	Greatest common divider	
H_{BI}	Back-iron height	mm
H_{PM}	Permanent magnet height	mm
H_{Rtooth}, H_{rt}	Rotor tooth height	mm
I_a	Armature current (rms)	A
I_a, I_b, I_c	Maximum currents for phases A, B and C	A
i_d, i_q	dq-axis inductances	
I_f, I_{DC}	DC field current	A
I_{rated}	Rated armature current	A
J_{ratio}	Ratio of field to armature slot current density	
k_1, k_2	Integers	
k_d	Distribution factor	
k_p	Packing factor	
k_p	Pitch factor	
k_w	Winding factor	

LCM	Least common multiple	
l_{end_a}	Total armature end-winding length	mm
l_{end_f}	Total field end-winding length	mm
l_{stack}	Stack length	mm
MMF	Magneto-motive force	
N_a	Number of turns per armature coil	
N_f	Number of turns per field coil	
N_{ph}	Number of phases	
N_r	Number of rotor poles	
N_s	Number of stator poles	
P_{Cu}	Copper loss	W
q	Number of coils per phase	
r	Air-gap radius	mm
R_a	Total armature winding resistance	Ω
R_f	Total field winding resistance	Ω
R_{Rshaft}	Shaft radius	mm
R_{SI}	Stator inner radius	mm
R_{SO}	Stator outer radius	mm
S_a	Total area for armature coils	mm^2
S_{DC}	Total area for field coils	mm^2
t	Time	s
T_{ave}, T, T_e	Average electromagnetic torque	Nm
T_{max}	Maximum electromagnetic torque	Nm
T_{min}	Minimum electromagnetic torque	Nm
$T_{p\text{-}p}$	Peak-to-peak electromagnetic torque	Nm

T_{ripple}	Torque ripple	%
V_{PM}	PM volume	mm^3
W	Magnetic co-energy change	
w_{st}	Stator tooth width	mm
α_e	Electrical degree between two adjacent coil back-EMFs	
α_m	Mechanical degree between adjacent coils	
θ_{rt}	Rotor pole arc	Mech. Deg.
θ_{st}	Stator pole arc	Mech. Deg.
μ_0	Permeability of free space	
μ_r	Permeability of magnet material	
ρ_{Cu}	Electrical resistivity of copper	
σ	Angular phase angle between adjacent EMF phasors	Elec. Deg.
τ_p	Stator coil pitch	
τ_r	Rotor pole pitch	
ψ_d, ψ_q	dq-axis flux linkages	
ψ_{DC}	DC flux-linkage	
ψ_{phase}	Phase flux-linkage	
ψ_{PM}	PM flux linkage	
2D	2 dimensional	
A1	Armature coil pitch of one slot pitch	
A2	Armature coil pitch of two slot pitches	
A3	Armature coil pitch of three slot pitches	
BDFDSM	Brushless double-fed doubly-salient machine	
BFPMM	Bias flux permanent magnet machine	

DL-	Double layer-	
DSPMM	Double salient permanent magnet machine	
F1	Field coil pitch of one slot pitch	
F2	Field coil pitch of two slot pitches	
F3	Field coil pitch of three slot pitches	
FEA	Finite element analysis	
FRM	Flux reversal machine	
HSFPMM	Hybrid-excited switched flux permanent magnet machine	
HSSPMM	Hybrid-excited stator slot opening permanent magnet machine	
MS-	Modular stator-	
NSWFSM	Non-overlapping stator wound field synchronous machine	
PM	Permanent magnet	
PS-	Partitioned stator-	
SFM	Switched flux machine	
SFPMM	Switched flux permanent magnet machine	
SL-	Single layer-	
SPM	Surface mounted permanent magnet machine	
SRM	Switched reluctance machine	
SSPMM	Stator slot opening permanent magnet machine	
SWFSM	Stator wound field synchronous machine	
VFM	Variable flux machine	
VFRM	Variable flux reluctance machine	
WFSFM	Wound field switched flux machine	
WFSM	Wound field synchronous machine	

Publications

Conference papers:

[1] M. Zheng, X. Liu and Z. Q. Zhu, "Comparison of variable flux reluctance, switched flux and fractional slot PM 12-stator slots machines having 10- and 14-rotor poles," *17th International Conf. on Electrical Machines and Systems (ICEMS)*, 2014, pp. 2882-2887.

[2] M. Zheng, Z. Z. Wu and Z. Q. Zhu, "Partitioned stator flux reversal machines having Halbach array PMs," *IEEE International Magnetics Conf. (INTERMAG)*, 2015.

[3] H. Hua, Z. Q. Zhu, M. Zheng, Z. Z. Wu, D. Wu and X. Ge, "Performance comparison of partitioned stator machines with NdFeB and ferrite magnets," *IEEE International Electric Machines & Drives Conf. (IEMDC)*, 2015, pp. 461-467.

Journal papers published:

[1] M. Zheng, Z. Z. Wu and Z. Q. Zhu, "Partitioned stator flux reversal machines having Halbach array PMs," *COMPEL: The International Journal for Computation and Mathematics in Electrical and Electronic Engineering*, vol. 35, no. 2, pp.396-406, 2016.

[2] H. Hua, Z. Q. Zhu, C. Wang, M. Zheng, Z. Z. Wu, D. Wu and X. Ge, "Partitioned stator machines with NdFeB and ferrite magnets," *IEEE Trans. on Ind. Appl.*, vol. 53, no. 3, pp. 1870-1882, 2017.

Journal papers submitted:

[1] M. Zheng, Z. Q. Zhu, S. Cai, H.Y. Li, and Y. Liu, "A new topology of stator hybrid-excited doubly salient machine with permanent magnets located on slot openings," submitted to *IEEE Trans. on Magnetics*.

[2] M. Zheng, Z. Q. Zhu, S. Cai, H.Y. Li, and Y. Liu, "Influence of stator and rotor pole number combinations on the electromagnetic performance of stator slot-opening PM hybrid-excited machine," submitted to *IEEE Trans. on Energy Conversion*.

[3] M. Zheng, and Z. Q. Zhu, "Modular stator hybrid-excited machine with magnets allocated in stator slot-opening," to be submitted to *IEEE Trans. on Magnetics*.

[4] M. Zheng, Z. Q. Zhu, S. Cai, H. Y. Li, and Y. Liu, “Influence of magnetic saturation and rotor eccentricity on back-EMF of novel hybrid-excited stator slot opening permanent magnet machine,” submitted to *Intermag 2018*.

Contents

Chapter 1 General Introduction

1.1. Introduction

Synchronous machines can be grouped into permanent magnet-excited machines, electrical-excited machines [1], reluctance machines, and hybrid-excited machines with both PM- and DC-excitation.

Due to high torque density and high efficiency, permanent magnet (PM) machines are widely used [2], and the conventional PM-excited machines locate the PMs in the rotor (rotor-PM). The stator-PM machines are developed to solve the issues caused by the PMs such as reducing rotor mechanical strength [3] and causing heat dissipation difficulty. According to the PM position, the stator-PM machines can be classified as the PMs located in the stator back-irons, on the surface of the stator tooth, in the slot openings, and inserted in stator tooth. However, the stator-PM machines will cause the reduction of slot area to increase the copper loss. It is worth mentioning that most of the stator-PM machines have the structure topology of doubly saliency.

The electrical-excited machines have no PMs, low cost, simple structure and good flux regulation capability. Thus, this type of machines will not be affected by the fluctuations in the market prices of rare-earth magnet material. The machines can be classified into the conventional switched reluctance machines and the wound field synchronous machines. Some of the stator wound field synchronous machines can be modified from the stator-PM machines by replacing PMs to DC coils which include brushless double-fed doubly-salient machines, DC-excited switched flux machines and DC-excited variable flux machine. Due to no magnet in this type of machines, the torque density of the machine is reduced significantly. Wound field synchronous machines (WFSMs) have good flux weakening performance due to the utilization of DC-excitation. However, because of the field windings, the total copper losses of the WFSMs are increased.

Hybrid-excited machines utilize both PM- and DC-excited sources and offer advantages of both PM-excited and DC-excited machines. The stator hybrid excitation machines with doubly salient structure include hybrid-excited doubly salient machine, hybrid-excited switched flux machine, and hybrid-excited stator slot opening PM machine. Because of the PM and DC field excitations, the machines have higher torque density than the electrical excitation machines

and the synergies of two excitation sources also provide flux regulation capability which can improve the efficiency and speed regulation.

The novel hybrid-excited stator slot opening PM machines (HSSPMMs) are developed from some topologies of DC-excited switched flux machines (SFMs) in this thesis. Besides, HSSPMMs and stator slot opening PM machines (SSPMMs) with modular stator are developed from the conventional HSSPMMs and SSPMMs, respectively.

The idea of inserting PMs between adjacent stator poles is given in [4, 5]. The single phase doubly salient self-excited reluctance generator has ferrite magnets located between stator poles, and since the ferrite magnets can offer residual magnetism, the machine material can be chosen as the low-loss iron core material. In that case, the generator has simple and robust structure and the efficiency will be high as well. The generator also has the ability to build up electromotive force in armature winding with the assistance of the magnetization of the PMs since the residual magnetism can be offered by PMs which will not easily disappeared in the stator iron core. The generator can be used in small scale steam, wind and water turbines since the structure and can offer high resistance at high temperature.

It is worth mentioning that the novel HSSPMMs and the modular stator machines have similar operation principle as the conventional SSPMMs and HSSPMMs. Thus, the switched flux PM machines, the DC-excited switched flux machines, the DC-excited variable flux machines, the hybrid-excited switched flux machines, the hybrid-excited stator slot opening PM machines, and the stator slot opening PM machines will be highlighted and reviewed in this chapter.

1.2. Stator PM and switched flux PM machines

As mentioned earlier, the PM-excited machines can be divided into rotor-PM brushless machines and stator-PM brushless machines. The rotor-PM brushless machines in this category include the PM on the rotor surface and the PM buried in the rotor [6, 7]. The PMs on rotor surface machines contain surface mounted PM machines (SPMs) and surface inset PM machines. The conventional SPMs usually have limited flux-weakening capability due to large equivalent air-gap and low winding inductance. However, SPMs employing concentrated windings and alternate teeth wound may have phases electrically and magnetically isolated, and large effective self-inductance but negligible mutual inductances can limit the short-circuit fault current, and hence, the machines can have a high fault-tolerance capability [8, 9] and a relatively high flux-weakening capability. In particular, for a fractional slot SPM machine, the

machine has (1) lower end-winding and copper loss for the concentrated windings; (2) inherently low cogging torque since the cogging torque is mainly caused by the interaction between the stator slots and the rotor PMs while the number of slots per pole is fractional [10], (3) high efficiency and power density, and (4) good flux weakening capability due to large effective self-inductance and negligible mutual inductance between phases [11-16]. The SPMs can also have Halbach array PMs [17-20]. The machines have the advantages of high torque, low iron loss, low cogging torque and torque ripple, and sinusoidal back-EMF due to sinusoidal self-shielding magnetization. The surface inset PM machine [21, 22] has the magnet pole-arc less than a full pole pitch and reluctance torque since the q-axis inductance is larger than the d-axis inductance, both are beneficial to reduction of the cost of the machine. The PMs buried in rotor machine can be separated into two different rotor structures by the PM magnetization direction: (1) interior radially magnetized PM machine and (2) interior circumferentially magnetized PM machine. This type of machines has the extended speed for maximum torque and constant power [23]. When the interior radially magnetized PM machine has "V-shaped" magnets, the PM torque is increased due to flux focusing. The interior PM machine has better flux-weakening performance when compared with the SPM due to higher d-axis inductance and lower PM flux-linkage [24]. Besides, multi-layered magnets with the material of ferrite or rare-earth can be utilised in the radially magnetized PM machine [25] to obtain an enhanced reluctance torque and a wide flux-wakening capability. The interior circumferentially magnetized PM machine [26] can employ the ferrite magnet to improve the air-gap flux density and maintain high back-EMF by utilising the flux focusing. The stator winding and rotor PM topologies of rotor-PM machines described above are shown in Fig. 1.1.

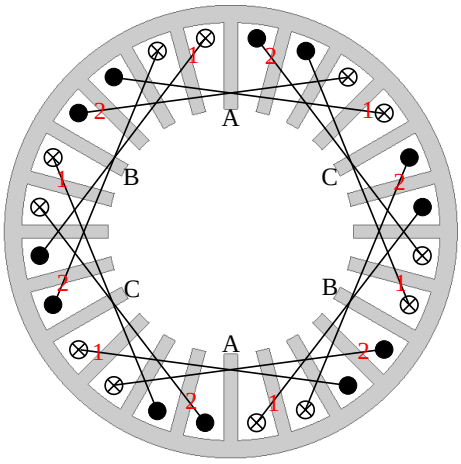

(a) Distributed overlapping

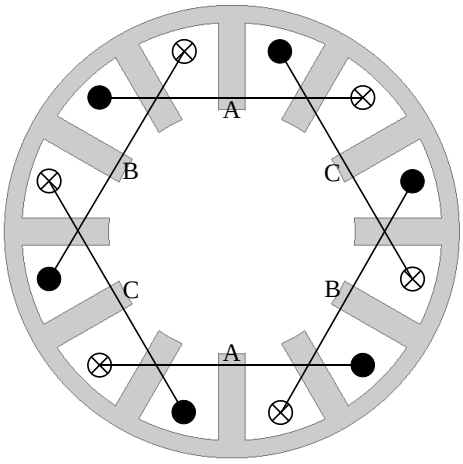

(b) Concentrated overlapping

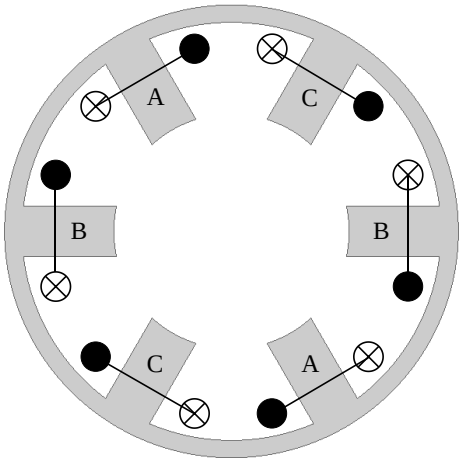

(c) Double layer non-overlapping

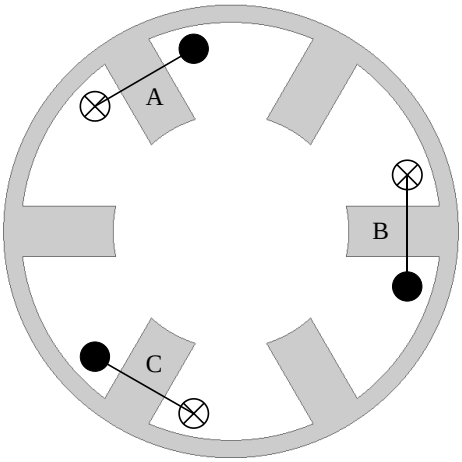

(d) Single layer non-overlapping

(I) Stator winding topologies

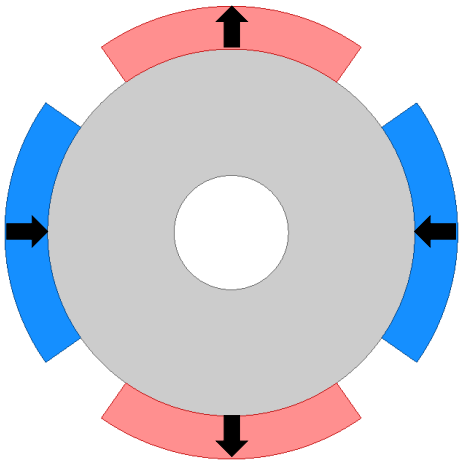

(a) Surface mounted PMs

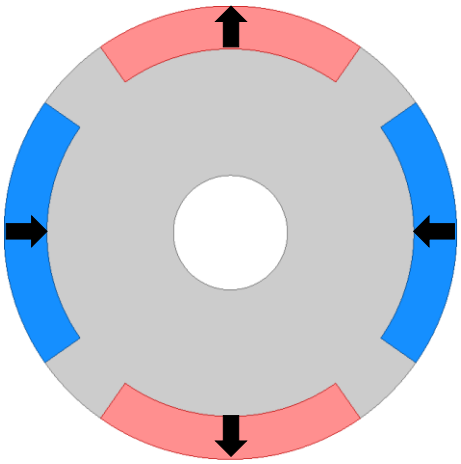

(b) Surface inset PMs

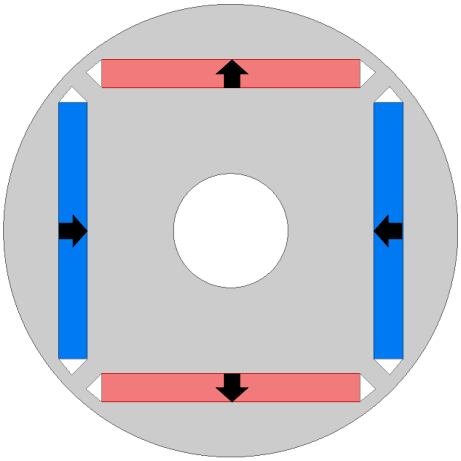

(c) Interior radially magnetized PMs

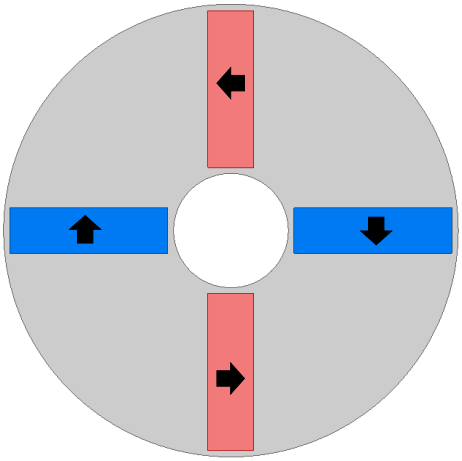

(d) Interior circumferentially magnetized PMs

(II) Rotor PM topologies

Fig. 1.1 Schematic diagrams of conventional rotor-PM machines (4 poles).

However, the rotor-PM machines for high speed operation have containment issue for PMs. The high centrifugal force on the rotor at high rotational speed will limit mechanical strength [3]. In addition, due to space MMF harmonics which are not synchronous with the rotor speed, rotor-PM machines, especially with a fractional-slot stator, will produce significant eddy current loss and heat in the PMs, which cannot be easily dissipated through the air-gap [27]. To ease the heat dissipation, the stator-PM machines can be employed.

The stator-PM machines can be modified from a switched reluctance machine (SRM) which is shown in Fig. 1.2. The SRM has the advantages of robustness, low cost, simple and convenient manufacture and maintenance, and good fault tolerance capability [28, 29]. The SRMs have the structure of doubly salient with only concentrated armature windings wound on simple teeth. The machine can be controlled by exciting with unipolar currents, and the torque can be produced by the variation of inductance with the rotor position (reluctance torque) with appropriate phase current excitations.

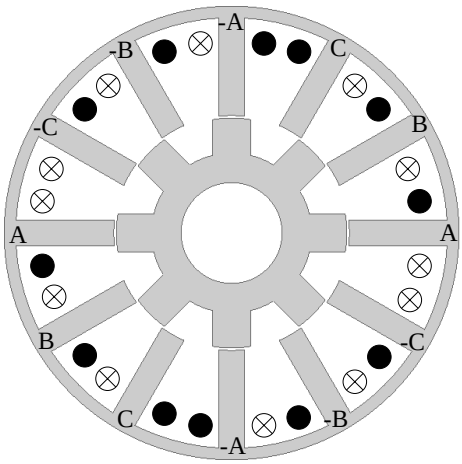

Fig. 1.2 Conventional 12 stator pole – 8 rotor pole switched reluctance machine [30].

The stator-PM doubly salient machines have three different structures, i.e. yoke PM machines shown in Fig. 1.3(a), slot opening PM machines shown in Fig. 1.3(b), and tooth surface PM and tooth inserted PM machines shown in Figs. 1.3(c) and (d). Generally, most of the stator PM machines can be developed based on the SRM. Thus, the stator-PM machines have the advantages of simple and robust rotor structure.

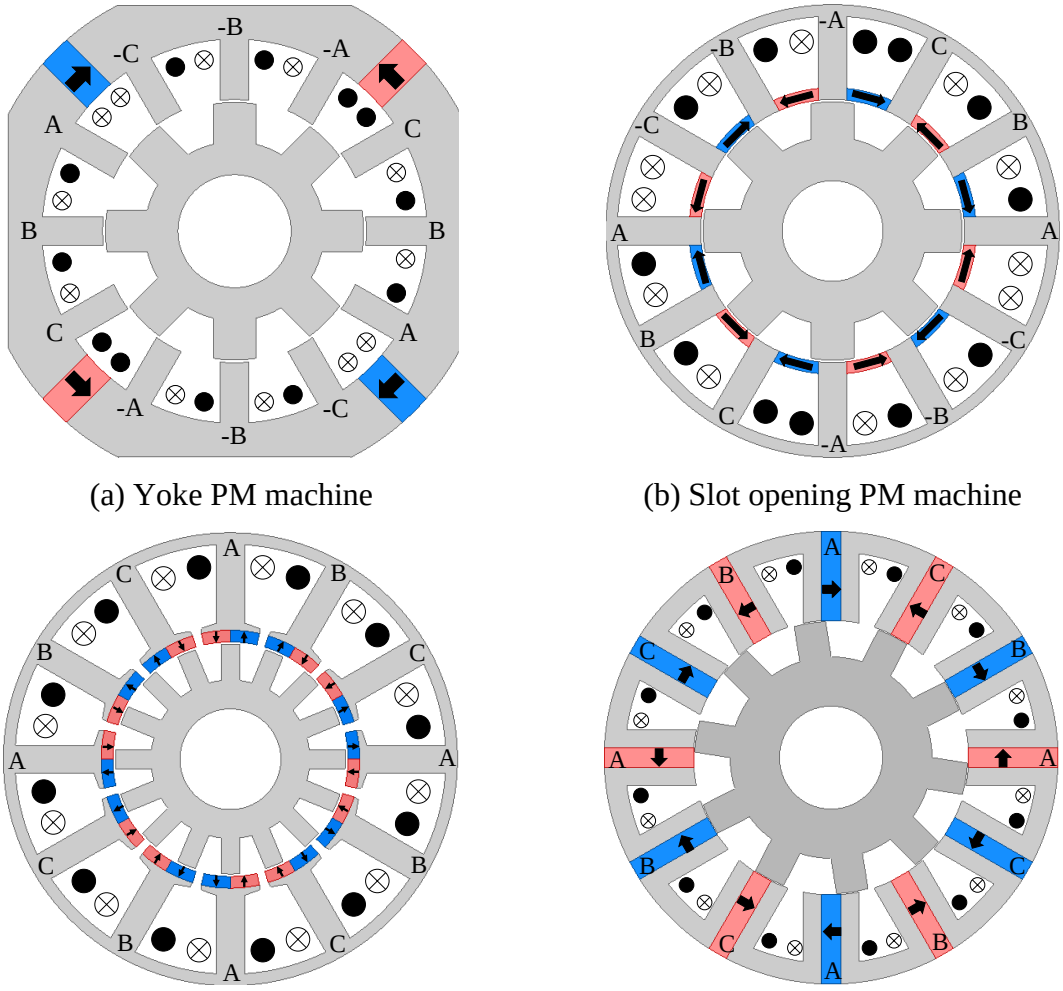

(a) Yoke PM machine

(b) Slot opening PM machine

(c) Tooth surface PM machine

(d) Tooth insert PM machine

Fig. 1.3 Schematic diagrams of stator-PM machines.

The double salient PM machine (DSPMM) is a yoke PM machine which has been developed from the SRM by plugging PMs in the stator back-iron [31] as shown in Fig. 1.4(a). Due to employing PMs, the machine can provide a PM torque component due to the PM induced back-EMFs in armature windings. From [32], it is found that the flux-linkage of the DSPMM is unipolar which makes the machine have relatively low torque density when compared with switched flux PM machine. Nevertheless, the DSPMM has the synergies of both SRM and brushless PM machine. It has a robust rotor and better torque and power density than SRM. Apart from the DSPMM, the bias flux PM machine (BFPMM) has PMs located on every stator back-irons which is shown in Fig. 1.4(b). Both DSPMM and BFPMM have negligible reluctance torque due to very similar dq-axis inductances and the stator and rotor pole combinations of the machines will be more flexible when compared with SRM. The BFPMM has better torque performance than the DSPMM due to the larger usage of PMs and hence is

more expensive [33]. The flux focusing technique can be employed in both machines to enhance the electromagnetic torque [34].

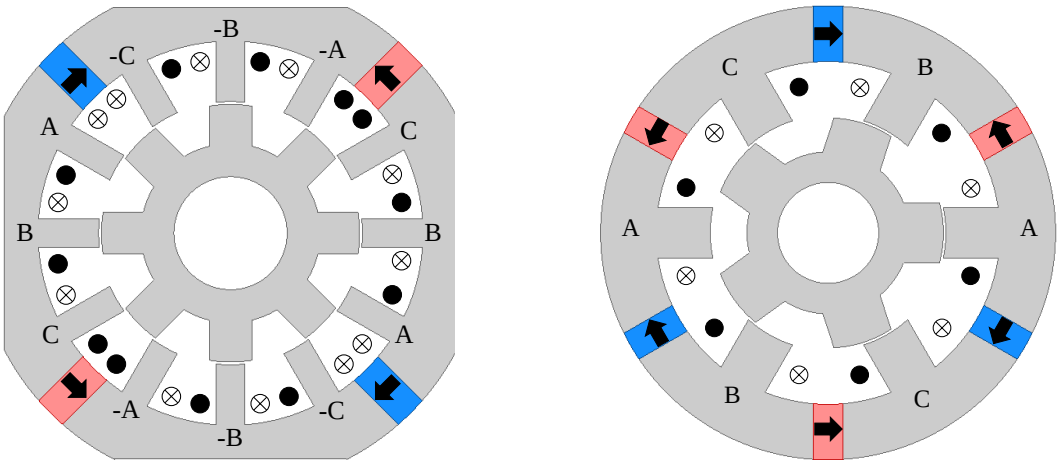

(a) DSPMM (b) BFPMM

Fig. 1.4 Yoke PM machines.

The slot opening PM machines can be developed from SRM by adding PMs in the slot openings and will be introduced in detail later.

The flux reversal machine (FRM) which is shown in Fig.1.3(c) is one type of the tooth PM machines. This machine can be modified from the SRM by adding a pair of PMs with opposite polarities on the surface of each stator tooth [35]. Due to the structure and PM magnetization direction, the FRM has bipolar flux-linkage and back-EMF since the flux-linkage of each coil reversed polarity with rotor rotation. The FRM has the nature of low inductance variation with rotor position and current and inherent fault-tolerance capability due to natural isolation between phases. However, the PMs tend to be partially demagnetized and may cause high eddy current loss by the PM location [2]. In addition, the effective air-gap length between the stator and rotor poles is affected by the PM thickness which can have significant effect on the electromagnetic performance of the FRM.

Another type of the stator-PM machine is the switched flux PM machines (SFPMMs), which were firstly described as a single phase PM alternator in [36]. The SFPMMs have stator embedded permanent magnets which are sandwiched circumferentially and alternatively between ‘U-shape’ laminated segments. Non-overlapping coils are wound on each stator tooth. The machine has a pair of alternate magnetic poles for each coil, and thus, the PM flux linkage is bipolar. The SFPM machines and the rotor-PM machines have been compared in [37] and [38]. The SFPMMs exhibit nearly sinusoidal back-EMF, higher torque and power density and

efficiency due to flux focusing effect. However, the machine stator is more saturated with increasing copper loss when compared with rotor-PM machines.

The conventional three phase SFPM machines with 12-slot/10-rotor poles having all- and alternate pole wound are shown in Fig 1.5(a) and (b) [39]. The winding connections for different stator and rotor pole combinations are discussed in [40]. Alternate pole wound machine can provide fault-tolerance since the phase coils are isolated and the mutual couplings between phases are reduced. The reduction of mutual couplings depends on stator and rotor pole combination [39, 41 and 42]. Since the SFPMMs have PMs inserted in each stator tooth, large volume of PMs is employed. Due to high price of rare earth PM materials, ferrite material can be used. Another way to reduce the cost of PMs is to reduce the PM volume. In that case, the conventional SFPMMs with alternate poles wound can remove the PMs in the teeth without coil windings and make the remaining teeth as simple stator teeth [43], and the E-core SFPMM is developed which is shown in Fig. 1.5(c). Furthermore, the middle teeth for the E-core SFPMMs can be completely removed and consequently the C-core SFPMMs [44] are developed as shown in Fig. 1.5(d). Due to the half of the stator teeth, the C-core SFPMMs have larger stator slot area. The rotor pole numbers for the C-core and E-core SFPMMs are similar to those of the conventional SFPMMs and the stator and rotor pole combinations for both type of machines are described in [43, 44]. In addition, the multi-tooth structure can be applied to the SFPMMs [45], and the multi-tooth SFPMMs have half of the PM volume with high stator and rotor pole numbers when compared with the conventional SFPMMs as shown in Fig. 1.5(e). The stator and rotor pole combinations are investigated in [46]. For the C-core, E-core and multi-tooth SFPMMs, the usage of PM volume is halved, but the torque density is improved compared with the conventional SFPMMs. Due to the alternate poles wound, the three types of machines have good fault tolerance performance [47]. For the flux-weakening performance, the conventional and multi-tooth SFPMMs have higher base speed due to the low flux-linkage and high number of poles, respectively; and the multi-tooth SFPMMs have infinite speed range for constant power since the machine has large inductance and small flux linkage [48].

The sandwiched SFPMMs shown in Fig. 1.5(f) are developed with a pair of PMs with opposite polarities inserted in one stator tooth. The sandwiched SFPMMS have halved the stator pole number but similar PM numbers when compared with the conventional SFPMMs. Due to the halved stator teeth, the machine has lower copper loss than the conventional machine. The torque density of the machine is also higher than that of the conventional machine. However, the sandwiched PM machine has higher frequencies in the irons than the conventional PM

machine, which leads to a higher iron loss, and further, the placement of PMs will cause more serious saturation [49]. A sandwiched SFPMM with V-shaped PMs in one pole is utilized to enhance the torque density and PM usage efficiency but reduce the PM volume by utilising the flux-focusing [50]. Some other structures of the SFPMMs include the machines with modular rotor shown in Fig. 1.5(g), outer rotor shown in Fig. 1.5(h), and modular stator shown in Fig. 1.5(i). The modular PM machines have significantly reduced iron loss since the stator back-irons are not fully utilized for flux path during one electrical period [51]. The outer stator machine can be employed for in-wheel machines to enhance the torque performance, power density and flux-weakening capability due to the better utilization of the machine inner space than the inner rotor machine [52].

Since both the PMs and windings located in a single stator will lead to reduced slot area and increased copper loss, a partitioned stator (PS) SFPMM which separates the PMs and windings is developed in [53-56]. [53] gives the topology of conventional PS-SFPMMs, which is shown in Fig. 1.5(j), with all poles wound and the stator and rotor pole combinations. The torque and power densities of the PS-SFPMM are increased due to the increased copper and PM volume. The E-core and C-core PS-SFPMMs are investigated in [54, 55]. The flux-weakening capability of the PS-SFPMM can be mechanically adjusted by the inner stator rather than adjusting the d-axis current. From [54], it is found that when the position of the stator teeth and PM poles is unaligned, the phase flux-linkage is the lowest; while the position is aligned, the phase flux-linkage is the highest. Moreover, when the relative position between two stators is moved from alignment to un-alignment, the base speed is increased while the constant torque is reduced.

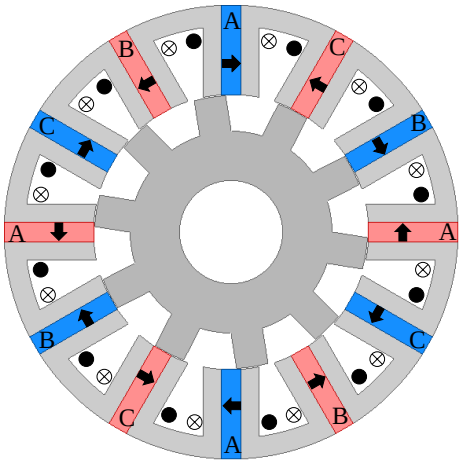

(a) Double layer (all pole wound)

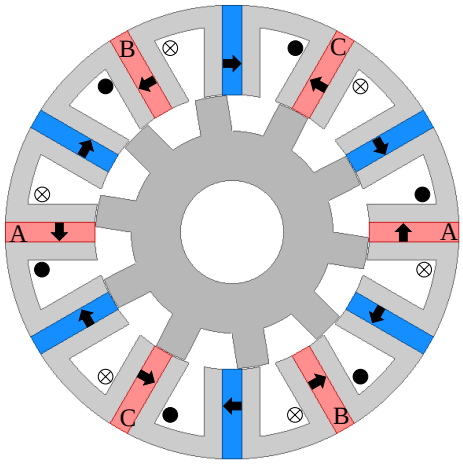

(b) Single layer (alternate pole wound)

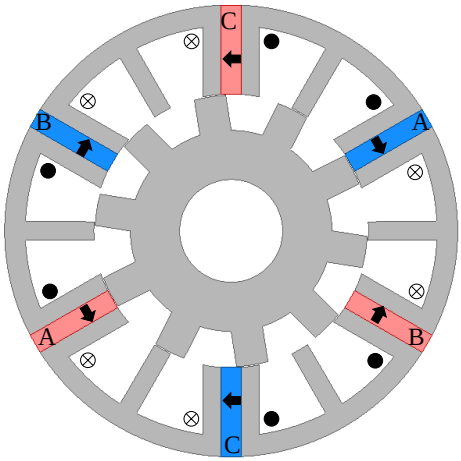

(c) E-core

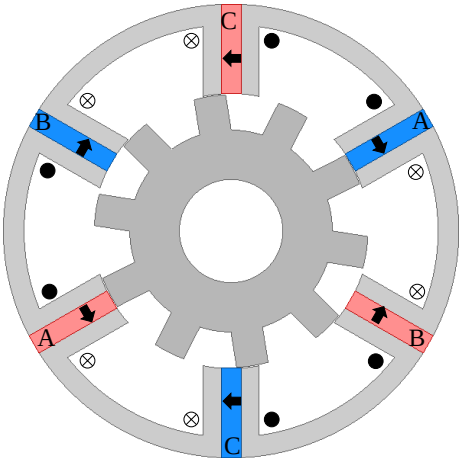

(d) C-core

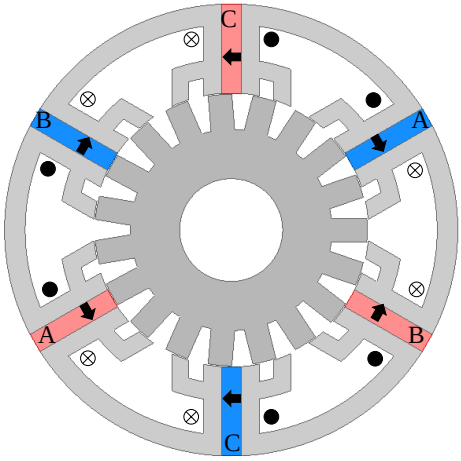

(e) Multi-tooth

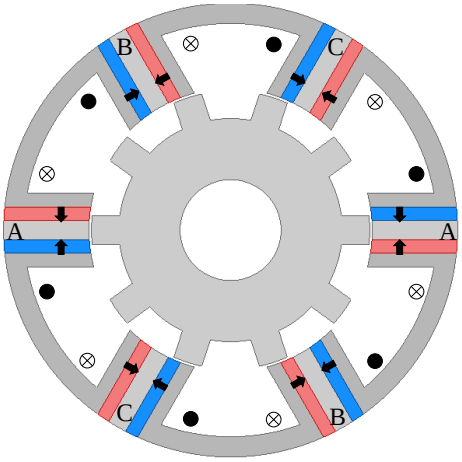

(f) Sandwiched PMs

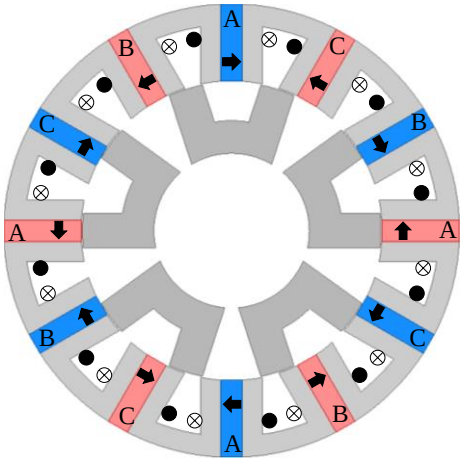

(g) Modular rotor

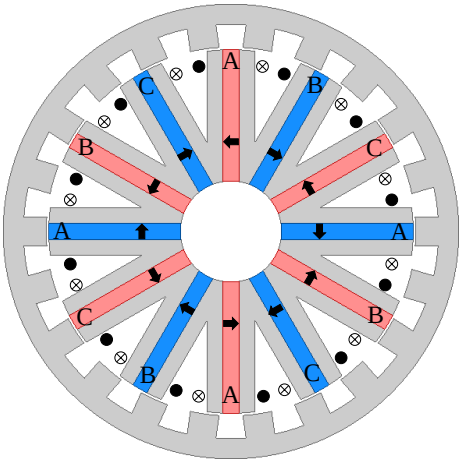

(h) Outer rotor

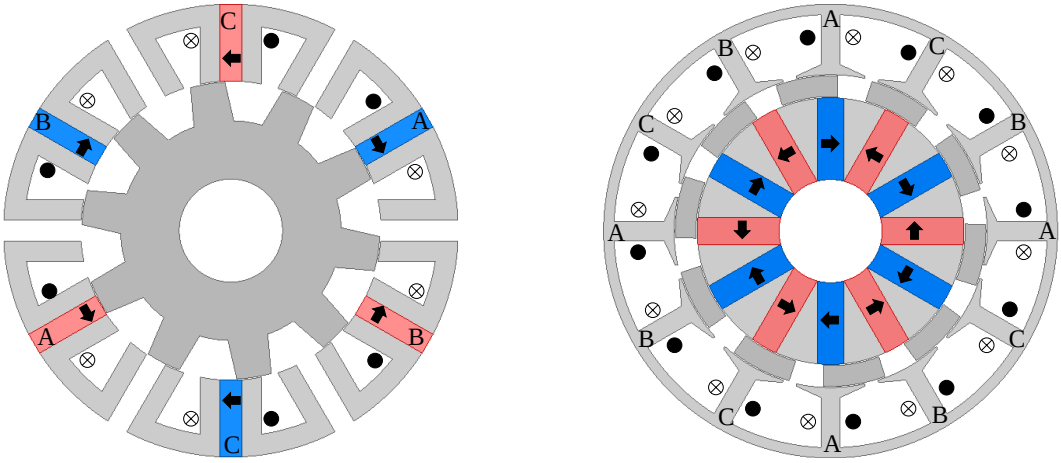

(i) Modular stator (j) Partitioned stator

Fig. 1.5 Switched flux PM machines.

1.3. Stator wound field synchronous machines

Since the PM-excited machines have the issue of high price of rare-earth magnet and uncontrollable PM flux, in the wound field synchronous machines (WFSMs) the PMs are replaced by DC coils. The WFSMs have the field windings on the rotor which are presented in [57-60]. The rotor wound field synchronous machines can be modified from an IPM synchronous machine (e.g. Toyota Prius 2010). This type of machines has the advantages of no magnets, controllable field and simple structure. The machine has a wide speed range at constant power. However, the machine has additional rotor losses and reduced efficiency. Meanwhile, thermal design should be considered. Further, in order to supply the rotor field excitation, the brushes and slip-rings are usually required.

The WFSMs with DC-excitation on stator are also possible. For instant, the brushless double-fed doubly-salient machines (BDFDSMs) can be directly converted from the DSPMMs. The machine structure is investigated in [61, 62], and the stator and rotor combination is similar to the SRM. The BDFDSMs, as well as the DSPMMs, can offer better efficiency with good flux-weakening capability when compared with the SRMs due to the DC-excitation, respectively. Moreover, because of the DC-excitation in BDFDSM, the inductance of the machine depends on rotor position and the torque is produced by the interaction between the armature reaction flux and field current flux [63].

The DC-excited switched flux machines (SFMs) and variable flux reluctance machines (VFRMs) will be described as follows.

1.3.1. DC-excited SFMs

The DC-excited SFMs have the advantages of simple and robust rotor structure and low cost due to no PM usage. The machine has been investigated in [64-74]. The most direct method for converting PM-excited to DC-excited SFMs is shown in Fig. 1.6(a) which replaces the PMs by field windings. Since the operation principle of the DC-excited SFM is similar to the conventional SFPMM, the U-shaped stator segments in conventional SFPMM need to be connected with laminated cores for field windings in DC-excited SFM [65]. However, the flux produced by the outer field windings will be leaked out of the stator outer surface. Thus, another type of DC-excited SRM can be designed [64] and investigated [66, 67 and 69], which is shown in Fig. 1.6(b). For this machine, the areas for PMs become stator slots and the field windings can be arranged in the slots with a coil span of 2 slot pitches (F2) and the DC excitation based on the PM magnetization direction. The armature coils span 2 slot pitches (A2) as well since the PM located area becomes field winding slot. The alternate field coils wound and alternate armature coils wound are shown in Fig. 1.6(c) and Fig. 1.6(d) [69], respectively. The alternate field coils wound machine has similar electromagnetic performance as all field coils wound machine and has less copper loss [67]. From [69], it shows the stator and rotor pole combinations of the alternate armature coils wound DC-excited SFMs, and the average torque, power, efficiency, and maximum speed for each machine. When compared with the PM machine, the DC-excited SFM can achieve better flux regulation capability but significantly reduced torque density. An outer rotor topology of the F2A2 DC-excited SFM in which the coil pitches of both the field and armature windings are 2 is presented in [75].

The topologies of non-overlapping stator wound field synchronous machines (NSWFSMs) are investigated in [68, 72] with different field coil polarities and different stator slot and rotor pole number combinations. The NSWFSMs have alternate teeth wound for both armature and field windings (F1A1) and the two types of coils are wound separately on the stator teeth and the machines have different or same field coil polarities as shown in Figs. 1.6(e) and 1.6(f), respectively. The NSWFSMs have good flux regulation capability, but the torque ripple is high due to alternate wound windings. The machine can employ segmented rotor as shown in Fig. 1.6(g). Because of the rotor structure, the torque ripple for the machine is increased with significantly decreased electromagnetic torque, and the rotor is not robust [70, 71]. From [72], it is found that the NSWFSMs with different field coil polarities have quit low electromagnetic torque when compared with NSWFSMs with same field coil polarities due to the restriction of

the field coil polarities. The machine with segmented rotor can utilize the restriction of the field polarities, but the machine topology of wide stator tooth tips and large rotor segments can cause the reducing of the stator slot area, and the increasing of leakage between rotor segments due to saturation. Thus, the segmented rotor machine has less average torque than the NSWFSM with same field coil polarities.

Based on the DC-excited SFM topologies presented above, a machine with field and armature windings having different coil pitches of 1 and 3 slot pitches (F1A3), respectively, is shown in Fig. 1.6(h). The F1A3 DC-excited SFM has better torque density than the F1A1 NSWFSM and the F2A2 SFMs at low current density, due to large stator slot number leading to increased flux leakage of the WFSM. However, when the current density is high, the stator of the F1A3 SFM is easily saturated [76]. It is worth mentioning that when the stator and rotor pole numbers of the F1A3 and F2A2 machines are doubled, the electromagnetic torque is almost reduced by half, since the electromagnetic torque is directly proportional to the ratio of rotor pole number to the square of stator slots number [77]. To ease the optimization, the stator slots in F2A2 and F1A3 DC-excited SFM are assumed to be same. Since the slots for armature and field windings are separated, the slots can be unequal and the machine with unequal slots has higher torque density than the machine having equal slots [74]. From [73], it shows that the F1A3 DC-excited SFM can be modified from a sandwiched PMs SFPMM, and two more DC excited SFM topologies can be modified from the E-core machine with different armature coil wound methods, which have field coil pitch of 3 slot pitches (F3) and armature coil pitches of 2 (A2) and 1 (A1) slot pitches as shown in Fig. 1.6(i), and (j), respectively.

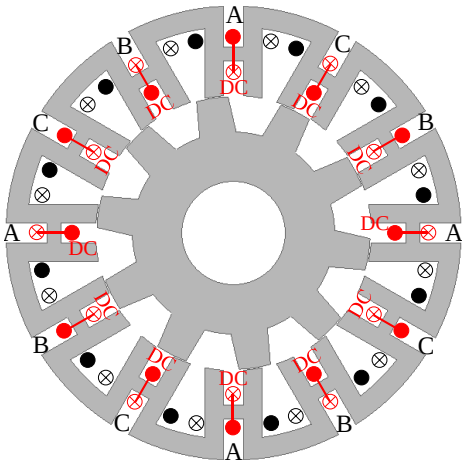

(a) DC-excited SFM

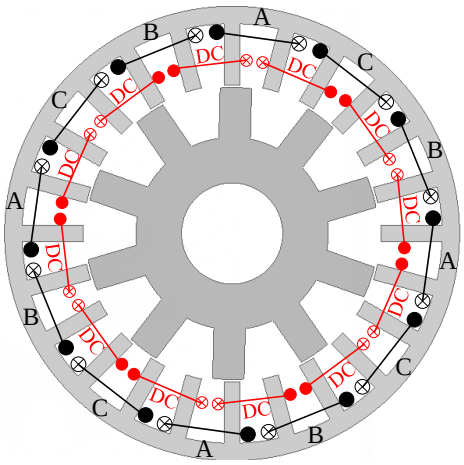

(b) F2A2 SFM

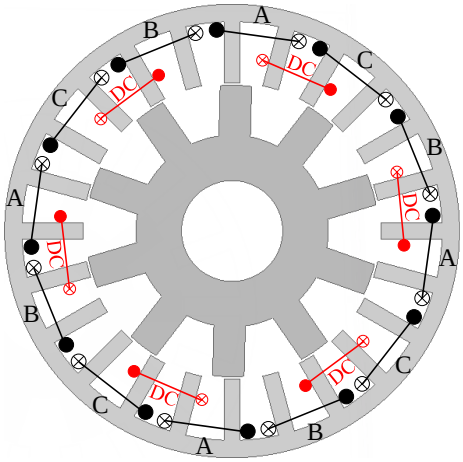

(c) F2A2 SFM, field alternate teeth wound

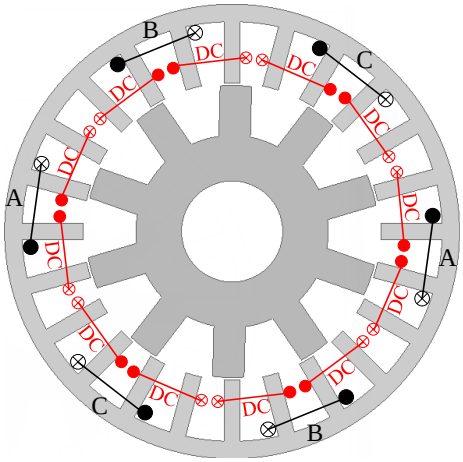

(d) F2A2 SFM, armature alternate teeth wound

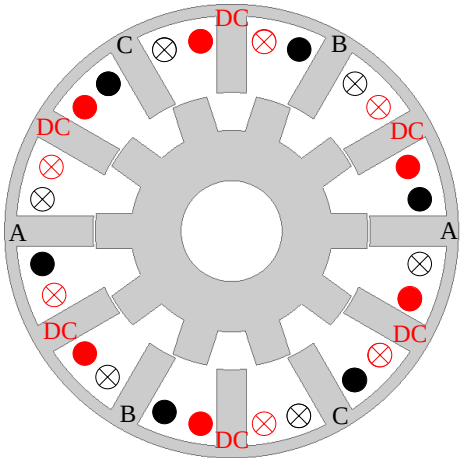

(e) NSWFSM, different field coils polarities

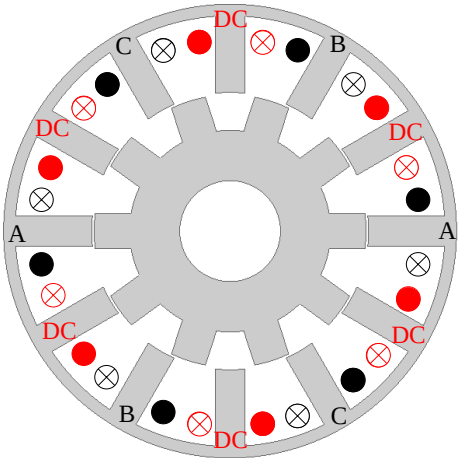

(f) NSWFSM, same field coils polarities

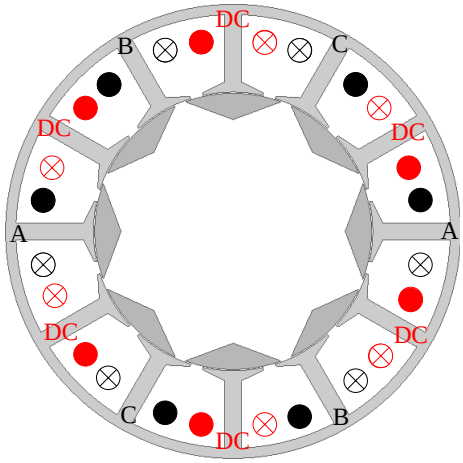

(g) NSWFSM with segmented rotor

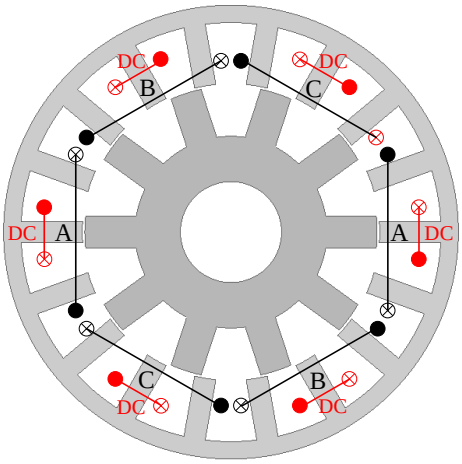

(h) F1A3 SFM

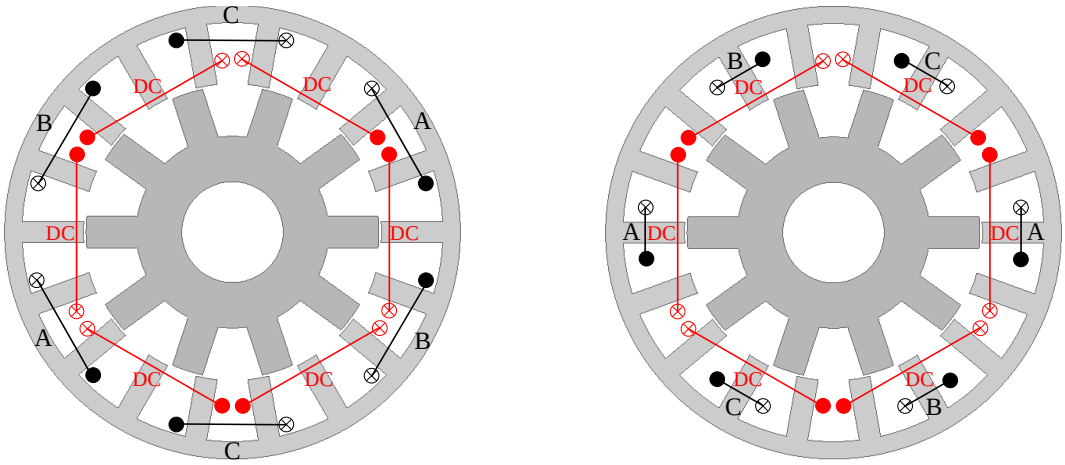

(i) F3A2 SFM (j) F3A1 SFM

Fig. 1.6 DC-excited stator switched flux machines.

1.3.2. DC-excited variable flux reluctance machines

The variable flux reluctance machines (VFRMs) have the structure of all poles wound armature and field coils, and an example of 12/10 stator/slot pole VFRM is shown in Fig. 1.7. The operation principle of the VFRMs is quite similar to the DC-excited SFMs, and the machine has simple structure with robust rotor and low cost as well. The VFRMs can be developed from a stator DC current excited Vernier reluctance machine. The non-overlapping concentrated winding for VFRMs can resolve the issue of bulky end-winding and low packing factor caused by distributed windings in the Vernier reluctance machines. From [78, 79], the VFRMs with multipoles have been introduced and investigated. The stator and rotor poles and operation principle of the multipole VFRMs are given and explained mathematically. It proves that the field flux can be independently controlled by DC excitation. The VFRMs with 6 stator poles or 12 stator poles with different rotor poles are investigated in [80, 81]. The high unbalance magnetic force in 6 stator VFRMs can be reduced by doubling the stator and rotor pole numbers. According to [77], the electromagnetic torque of the VFRM is combined with the reluctance torque, cogging torque and synchronous torque. Since the cogging torque is negligible and synchronous torque is the dominate part for average torque, the torque for the VFRM is mainly determined by the mutual inductance between field and armature windings, and the machine tends to the synchronous machine. The high torque ripple for VFRMs with even rotor pole number is caused by large reluctance torque ripple which is relative to the high variation of self-inductance of armature windings. The partitioned stator VFRM is investigated in [82], and

the torque density for the machine is increased and higher than the VFRM due to the utilization of machine inner space and larger field and armature slot areas.

It is worth mentioning that according to the identically located DC coils, the flux-linkage and back-EMF for VFRMs are symmetrical, the VFRMs have better torque performance than the BDFDSMs. The better usage of DC-link voltage can be achieved since the symmetrical flux-linkage and back-EMF are beneficial to the speed range control [83, 84]. From [84], it is found that the DC excited current will only adjust the torque value but not the base speed in torque speed characteristics, while the increased armature winding resistance may lead to a reduction of base speed and output power.

Generally, the stator wound field synchronous machines (SWFSMs) have wider speed range than the PM excited machines due to the DC field winding which makes the flux adjustable. When compared with SRM, the air-gap flux can be independently controlled by DC excitation. Also, apart from controlling by the asymmetric bridge inverter, the SWFSMs can be controlled by the three phase inverter, and the noise and vibration issues in SRM are reduced.

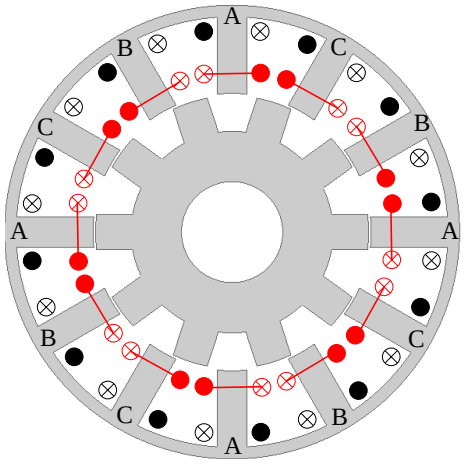

Fig. 1.7 Variable flux reluctance machine. (red: field windings; black: armature windings)

1.4. Stator hybrid-excited machines with PMs on stator slot openings

Since there is no PM excitation in the WFSMs and the machine stator is easily magnetically saturated by DC excitation, the torque density for the WFSMs is significantly lower than that of the PM excited machines. The hybrid excited machines are investigated due to their low cost and relatively higher torque density than WFSMs. The stator hybrid excited machines include the hybrid excited switched reluctance machine, hybrid excited doubly salient machines, hybrid excited switched flux PM machines (HSFPMMs), and hybrid excited stator slot opening PM machines (HSSPMMs).

In this section, the stator slot opening PM machines with no DC coils (SSPMMs) will be introduced to illustrate the operation principle of the hybrid-excited stator slot opening PM machines, and some HSFMs need to be introduced since their working principle might be similar to that of the slot opening PM machines.

1.4.1. Stator slot opening PM machines

The stator slot opening PM machines (SSPMMs) are employed to enhance the torque and power densities of the SRMs. The SSPMM is investigated in [85] and the topology of the machine is shown in Fig. 1.8(a). Since the SSPMMs is modified from SRMs, the machine is excited with unipolar currents by employing an asymmetric half-bridge converter. Due to the PM bias, the working area of the SSPMM is wider than that of the SRM. Meanwhile, the torque of the SSPMM is improved since it is proportional to the working area. From [86, 87], the SSPMMs are designed to have modular stator segments. The SSPMMs have located circumferentially magnetized PMs with opposite magnetization directions between the adjacent stator poles; and for the modular stator SSPMMs, the PMs are employed in the stator segments and have same magnetization direction. According to the operation principle of the modular SSPMMs, the flux produced by PM will be shunted in the stator without current excitation, and the flux will be pushed to the rotor via air-gap by the flux produced by the armature current. Thus, without armature excitation, the cogging torque of the machines should be negligible as well as the variation of back-EMF and flux-linkage with rotor position. The modular stator SSPMMs have different winding methods compared with the conventional SSPMMs, and have coils in the same phase wound on one stator segment with more rotor pole numbers available to choose. The modular stator SSPMMs are shown in Fig. 1.8(b) and (c).

A novel SSPMM has been designed and investigated in [88, 89]. The novel machine can have conventional three phase windings, and the stator and rotor pole combinations are more feasible than those in the SRM and the conventional SSPMM. The operation principle is the same as the machines presented above. The coils in novel SSPMMs can be wound for either double layer or single layer, which are shown in Fig. 1.8(d) and (e), respectively. The machines have non-zero open-circuit characteristics which are reduced with the reducing PM remanent. That is because the stator magnetic saturation caused by the PMs is reduced which decreases the flux-leakage from stator to rotor. Since the PMs are located on the stator slot opening area and the directions of the fluxes produced by the PM and the current excitation are opposite, the fringing flux may cause the PM demagnetization at the corners close to air-gap. PM shaping

by cutting corners is applied to eliminate the risk of local irreversible demagnetization [88]. The demagnetization can also be reduced by locating the PMs higher above the stator slot openings or placing the PMs above the stator tooth tips [90]. The single layer SSPMMs have better fault tolerance performance due to the reduced coupling between phases caused by the higher self-inductance and lower mutual-inductance [89]. Furthermore, a SSPMM with Halbach array PMs is presented in [91].

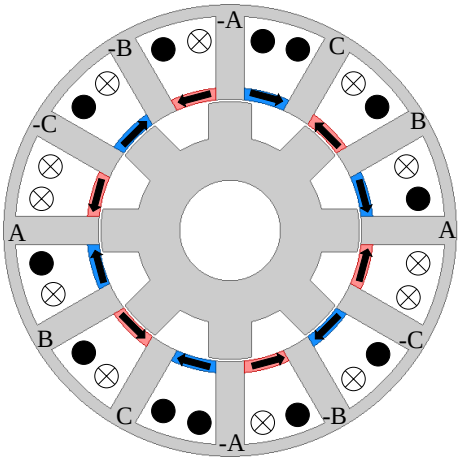

(a) Stator slot opening PM SRM

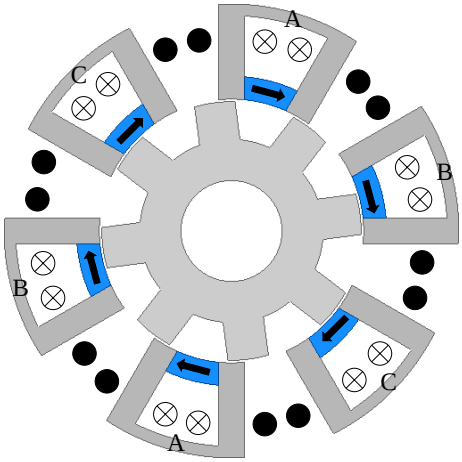

(b) Modular stator slot opening PM SRM I

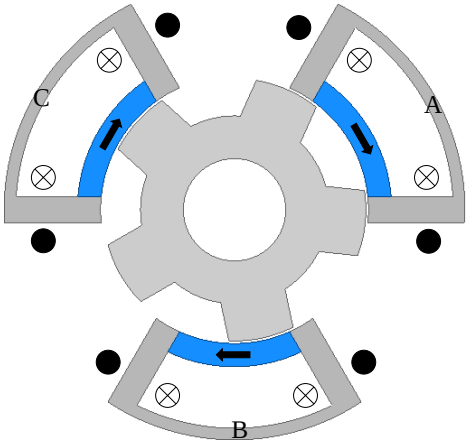

(c) Modular stator slot opening PM SRM II

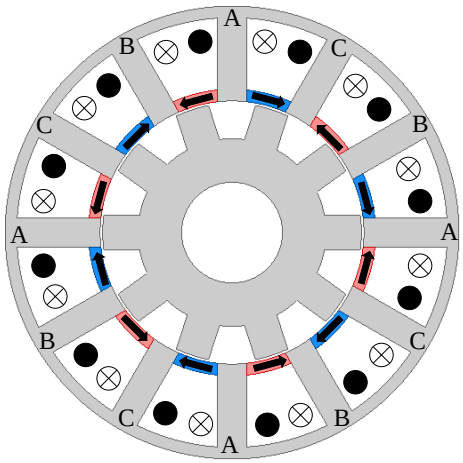

(d) Double layer SSPMM

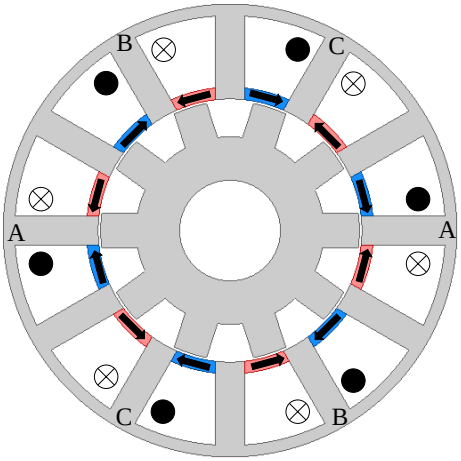

(e) Single layer SSPMM

Fig. 1.8 Stator slot opening PM machines.

1.4.2. Hybrid-excited stator slot opening PM machines

Generally, the hybrid-excited stator slot opening PM machines (HSSPMMs) have similar operation principle as the SSPMMs, and the machines can be modified from the VFRMs by adding circumferentially magnetized PMs between the adjacent stator poles. The HSSPMMs are designed and investigated in [92, 93]. Comparing the HSSPMMs with the VFRMs, it is found that the PMs are used to reduce the stator magnetic saturation caused by current excitation and the back-irons of the HSSPMMs can be designed to be thin with higher saturation when PMs are removed [92]. The open-circuit characteristics without current excitation are almost negligible since the flux produced by PMs are mainly shunted in stator. By adding increasing DC field excitation currents, the magnitudes of the phase back-EMFs will be increased significantly and then reduced since the DC current will be over-excited, leading to the stator magnetic saturation by DC current. Similar to the SSPMMs, the PMs have the risk of demagnetization at the corners closed to air-gap due to the fringing flux. Due to the utilization of DC field current, the risk of demagnetization happened both on open-circuit and on-load. In addition, the risk will be increased with the increasing DC field current [92]. The stator and rotor pole combinations of the double-layer and single-layer HSSPMMs are presented in [93] which are shown in Fig. 1.9(a) and (b), respectively. It is worth mentioning that when VFMs, SSPMMs and HSSPMMs have similar iron core topologies, the HSSPMMs have the highest electromagnetic torque while the VFRMs have the lowest. The VFRMs and HSSPMMs have good flux regulation capability due to the DC field excitation, which lead to larger base speed and wider constant power region than the SSPMMs. Due to the more serious

saturation, the losses in SSPMMs are larger than those in HSSPMMs. The HSSPMMs have the highest efficiency both for low and high torque and speed [94].

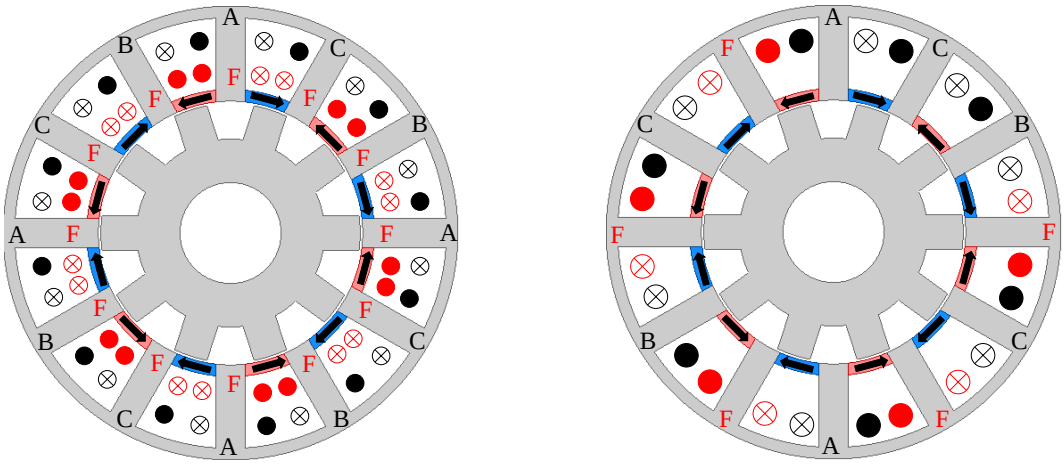

(a) Double Layer (b) Single layer

Fig. 1.9 Hybrid-excited stator slot opening PM machines.

1.4.3. Hybrid-excited switched flux machines

The most convenient way to produce a hybrid-excited switched flux PM machine (HSFPMM) is to add field coils in the stator slots. In [43], the E-core HSFPMM is developed by winding DC coils on the middle tooth of the E-core SFPMM. In [95], the DC coils are wound on the stator teeth of a conventional SFPMMs. Thus, the machines have the advantages of simple manufacturing, reduced PM volume and good flux regulation capability.

In [96, 97], the HSFPMMs having the PMs in conventional SFPMMs reduced to save the space for the DC windings are investigated and shown in Fig. 1.10(a). The DC current excitation can be used to strengthen and weaken the air-gap flux density, but the effectiveness of the DC excitation is limited by the PMs, especially when the remanence of PM is high. In [98], several HSFPMMs with different DC coil positions are presented and the machines with part of the PMs replaced by DC coils have higher torque density and better torque performance. Among them, when the DC coils located at the outer stator, the HSFPMM has the highest average torque and high peak back-EMF with good effectiveness of DC excitation. When iron-bridges employed in the stator, which is shown in Fig. 1.10(b), the effectiveness of DC excitation is enhanced but the torque density will be slightly reduced [99]. The DC field coils can be placed in the stator back-irons [100, 101], which is presented in Fig. 1.10(c). The structure of the machine is similar to the HSFPMMs with outer iron flux-bridge as shown in [99]. Since the HSFPMMs with DC coils located in stator back-irons, the PM flux is shunted in the stator at

open-circuit and can be pushed to rotor by the flux produced by current excitation, which is similar to the working principle of the HSSPMMs. However, the flux produced by large DC excitation may cause the stator teeth saturated and make the flux produced by armature excitation and PM produce negative torque. Thus, in [102], the slots areas of field and armature winding are reduced to have wider stator teeth. Furthermore, another structure by adjusting the field and armature winding slots, the slot area and the PM shape as well, can also achieve wider stator teeth [103].

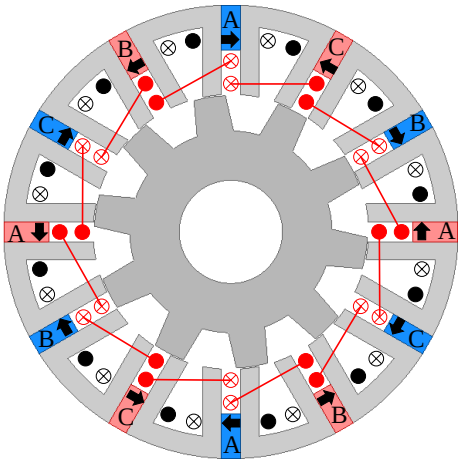

(a) DC coils in PM slots

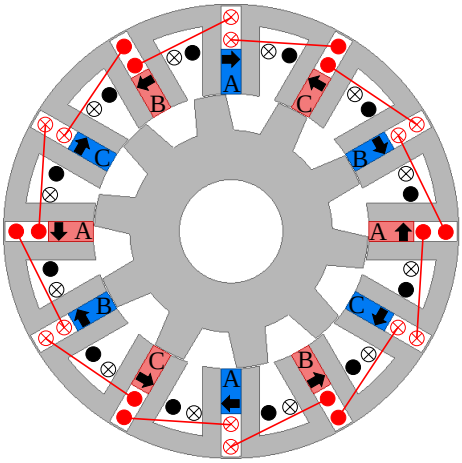

(b) DC coils in PM slots with outer iron flux bridges

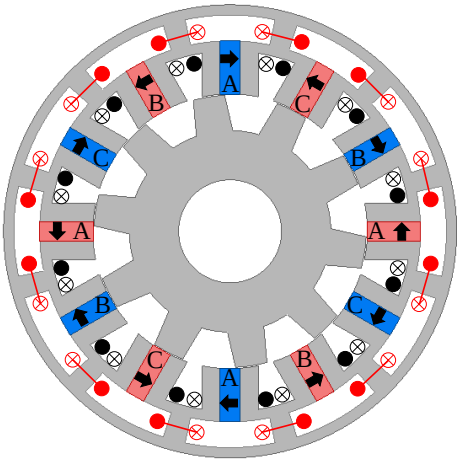

(c) DC coils in stator back-irons

Fig. 1.10 DC-excited switched flux PM machines.

1.5. Research scope and contributions

1.5.1. Research scope

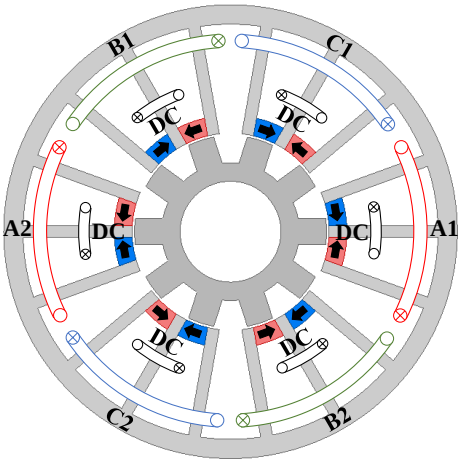

(a) F1A3 HSSPMM

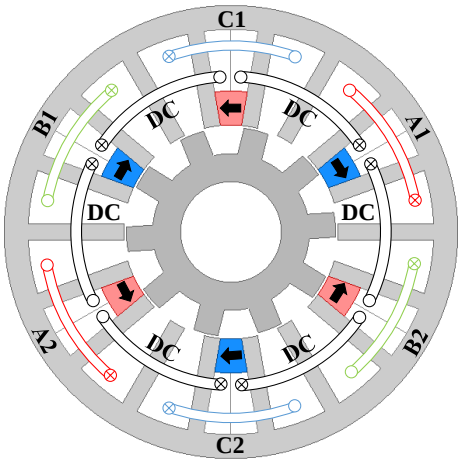

(b) F3A2 HSSPMM

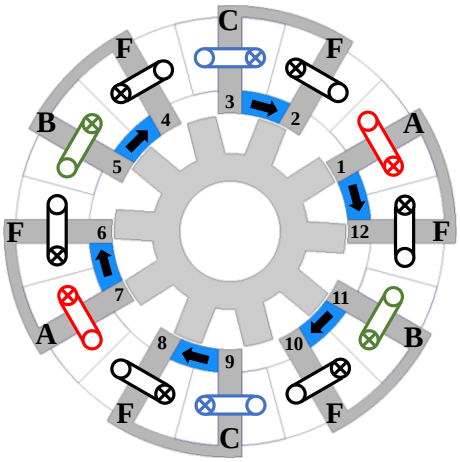

(c) Modular stator HSSPM

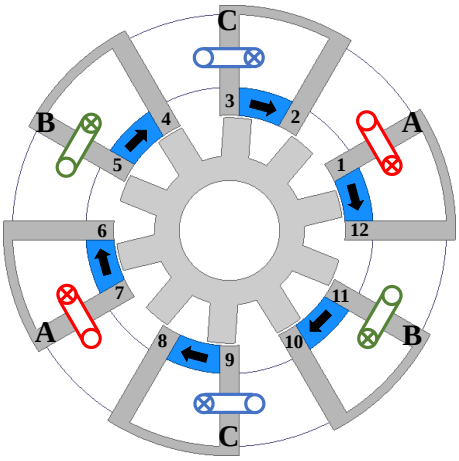

(d) Modular stator SSPM

Fig. 1.11 Novel hybrid-excited stator slot opening permanent magnet machine (HSSPMM) and modular stator PM-excited stator slot opening permanent magnet machine (SSPMM).

The research in this thesis is focused on novel stator hybrid-excited machines with PMs located on the slot opening area. The F1A3 and F3A2 hybrid-excited stator slot PM machines (HSSPMM), which are shown in Figs. 1.11(a) and (b), respectively, are developed by inserting the PMs into the slots openings of the DC field windings of the hybrid-excitation switched flux machines (HSFM) as shown in Figs. 1.5(h) and (i), respectively. The machines are investigated by finite element analyses and the operation principle is experimentally validated. The modular stator topologies for HSSPMMs and SSPMMs, which are shown in Figs. 1.11(c) and (d) respectively, are designed and investigated, together with the conventional HSSPMMs and SSPMMs. The F3A2 HSSPM and MS-HSSPM machines will have good fault tolerance

capability since the machines have magnetically and mechanically isolation, respectively. Since all the machines have shunted flux in the stator at open-circuit condition, the machines will have low cogging torque, and especially negligible back-EMF which can make the machines suitable for high speed machine.

- **Chapter 1**

This introduction chapter reviews the state of the art on stator PM machines and hybrid-excited stator PM machines.

- **Chapter 2**

A novel stator hybrid-excited stator slot permanent magnet machine (HSSPM) with field windings span one stator slot pitch (F1) and armature windings span three stator slot pitches (A3) is designed and investigated. Since the novel HSSPMM employs the same magnet volume as the conventional HSSPMM for the F1A3 HSSPMM which has located the magnet and the DC coil in one slot, the conventional HSSPMM is used as a baseline to compare the open-circuit and on-load performances with the F1A3 HSSPMM. The operation principles of the two machines are investigated and the losses are compared as well. The influence of DC excitation of the machines is given to illustrate that the DC excitation can enhance the machine performance till the saturation point. Finally, the influence of different rotor pole numbers of the F1A3 HSSPMM is analysed.

- **Chapter 3**

The HSSPM with field windings span three stator slot pitch (F3) and armature windings span two stator slot pitches (A2) is designed. The operating principle of the F3A2 HSSPMMs is analysed. The different stator and rotor pole combinations are investigated and the coil positions of the machines are presented. The open-circuit and on-load performance of the F3A2 HSSPMMs are compared, including the unbalanced magnetic force. In addition, the influence of DC-excitation of the machines is analysed and presented.

- **Chapter 4**

The conventional single layer HSSPM and single layer wound field synchronous machines are modified to the hybrid-excited stator slot opening PM machines with segmented stator. The modular stator HSSPMM has alternatively removed half back-irons and PMs compared with the conventional HSSPMM with one armature coil and one field coil wound on each stator segment. The modular stator HSSPMM is optimized under two sets of restriction parameters, and the optimized machines are investigated and compared in terms of electromagnetic

performance and losses. Furthermore, the modular machines with different stator and rotor pole combinations are investigated with and without field coils.

- **Chapter 5**

The operating principle and performance of the F1A3 and F3A2 HSSPMMs are experimentally validated. Due to the structure defects and the manufacturing errors, the F1A3 HSSPMM exhibits the back-EMF without current excitation and the mechanical rotor eccentricity. The flux-leakage and approximate rotor eccentric position of the F1A3 HSSPMM is simulated and analysed by 2D finite element method.

- **Chapter 6**

The conclusions are drawn and the potential future work highlighted.

1.5.2. Research contributions

The contributions of the thesis can be summarized as follows:

- Design and analysis of the new F1A3 HSSPMMs. The electromagnetic performance on open-circuit and on-load for the F1A3 HSSPMM is compared with the conventional HSSPMM. The structure defects will produce high flux-leakage in the machine, which are analysed and experimentally validated for the first time. The electromagnetic performance of F1A3 HSSPMMs having 6-7/8/10/11/13 stator/rotor poles are investigated as well.
- Design and analysis of the new F3A2 HSSPMMs. The electromagnetic performance of the machines having 6-7/8/10/11/13/14 stator/rotor poles are investigated and experimentally validated.
- The F1A3 and F3A2 HSSPMMs have field and armature windings separated in different stator slots. The stator slots can be assumed to be identical for convenience in the machine optimization. However, in this case, it is found that the ratio of field to armature current density is an important parameter for optimization.
- Design and analysis of the new modular-stator HSSPMMs. The electromagnetic performance of the machine with equal/unequal stator tooth width and stator back-iron are compared to show that when the two parameters are unequal, the machines have higher electromagnetic torque with larger PM volume. The electromagnetic performance for the modular stator HSSPMMs and modular stator SSPMMs having 6 stator segments and 10/11/13/14 rotor poles are investigated.

Chapter 2 Stator Hybrid-excited Doubly Salient Machine with Permanent Magnets Located on Slot Openings

2.1. Introduction

Permanent magnet machines have high torque density and efficiency and are widely used and investigated [2], especially recently for the stator-PM machines. The switched flux PM (SFPM) machine is one type of stator-PM machines. It has simple and robust rotor [104-106]. The torque performance of the SFPM machine depends on the usage of PM. However, the price of rare-earth PM is high. Thus, the NdFeB magnets may be replaced by low cost ferrite magnets or field windings.

The wound field switched flux (WFSF) machines and variable flux machines (VFM) are modified from the SFPM machines which exhibit most of the advantages of SFPM machines. Besides, the flux-weakening can be better than the PM machine due to DC field excitation. Some WFSF machine topologies and VFM machine topologies are shown in [64, 72, 107, and 108] and [83, 109], respectively. Although the WFSF machine has the advantage of simple and easy manufacturing structure, easy cooling, and flux regulation capability due to DC excitation, the limitations exist, such as high copper loss due to the DC winding and over-lapped end winding, and the significantly reduced torque with severe magnetic saturation caused by DC field excitation without PM excitation.

Thus, to enhance the torque density, PM can be remained but with additional DC excitation in the SFPM machines, or added in a VFM in the stator as hybrid excitation [92, 95, 96, 99, 101, 102, and 110]. The permanent magnets in the SFPM machines can be partly replaced by DC windings in different position [95, 96 and 99]. However, the effectiveness of the DC excitation is still limited by the high PM reluctance path. Adding iron flux-bridge will enhance the effectiveness by sacrificing some torque density [99]. In addition, DC windings inserted in the stator yoke above PM [95, 101 and 102] with additional iron bridge is another method. This can be modified to the machine topology as shown in [110], which has a similar working principle as the machine with PM inserted in stator slot [85]. The stator slot PM machine has the advantage of good flux regulation capability for the flux path produced by two excitation sources which are paralleled. However, it still has the risk of demagnetization on the corner of magnet [92].

This chapter presents a new topology of stator hybrid excitation machine with the PMs inserted in the slot opening area of DC winding slot, as shown in Fig. 2.1. This machine is based on a F1A3 WFSF machine which has a coil span of one slot pitch for field windings (F1) while a coil over three slot pitches for the armature windings (A3) [72]. As the PM and the field winding are in the same stator slot, it is difficult to set the optimization objective. Thus, a F1A1 HSSPM machine which is shown in Fig. 2.2 has been used as a baseline.

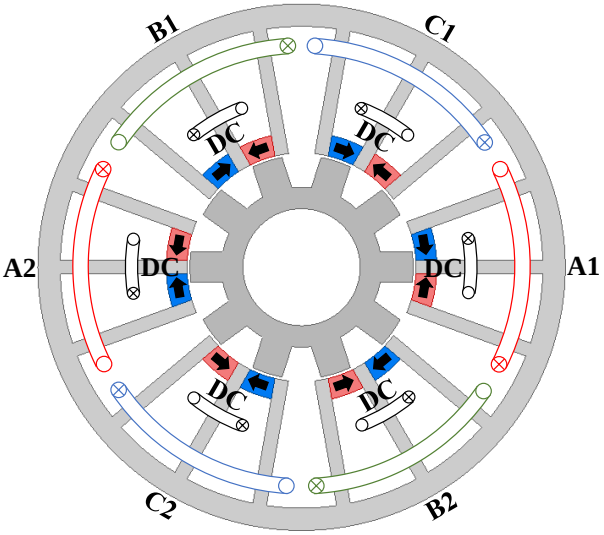

Fig. 2.1 Stator slot opening PM hybrid-excited (HSSPM) machine with F1A3 coil windings.

The F1A1 HSSPM machine is fed by three phase sinusoidal currents and is developed from a 12-stator/10-rotor pole VFM by inserting PMs between stator poles [92]. Compared with a VFM, the F1A1 HSSPM machine has improved torque density and efficiency. According to the operation principle of the HSSPM machine, the machine has almost no electromagnet force (EMF) without DC excitation since the flux generated by magnet is shunted in stator, and the PM and DC-excited fluxes have opposite directions. The machine has both PM and DC fluxes passing through the air-gap and modulated by the salient pole rotor to induce the EMFs in coils. The DC excitation can adjust the total flux [92]. Since the F1A1 HSSPM machine has the armature winding in one slot together with the field winding and the slot opening PM, the PM usage can be limited in the optimization.

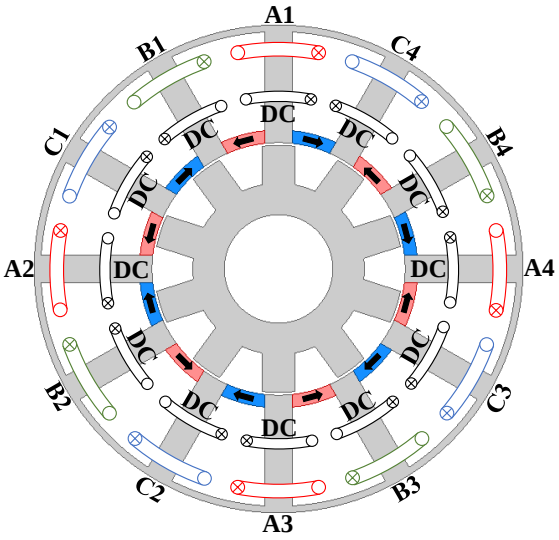

Fig. 2.2 Stator slot opening PM hybrid-excited (HSSPM) machine with F1A1 coil windings.

The research in this chapter can be summarized as follows:

- The basic working principle of the F1A3 HSSPM machine and the F1A1 HSSPM.
- Machine optimization.
- Electromagnetic performance comparison of the F1A3 and F1A1 HSSPM machines, which include open-circuit flux-linkage, back-EMF, cogging torque, on-load torque performance and losses.
- The influence of DC current excitation.
- The influence of different rotor poles.

2.2. Machine structure and operation principle

The basic operation principle of the machine can be explained by Fig. 2.3. The short circuit for PM path is possible on both conditions with and without DC current for both machines. Without field coil excitation, most of PM flux is short circuited via the stator teeth and yoke, and only a little PM flux links the rotor via air-gap for F1A3 HSSPM machine, Fig. 2.3 (a), that might because the PMs are not located in all of the slot opening in this machine and the flux-leakage results due to magnetic saturation. Thus, the flux linkage of this machine is low which leads to the low EMF induced in the coil. That is the difference from the F1A1 HSSPM machine which has only shot-circuit PM flux in the same situation. In Fig. 2.3 (b), both field coil current and PM are present and the flux from both sources can pass to the rotor via air-gap and contribute to the induced EMF in the coil for F1A3 HSSPM machine. Although there are two sources in F1A3 HSSPM machine, when the field current is low, the machine will be

mainly dominated by PM source with the total flux path similar to the PM flux path. With the increasing of field coil current, the field strengthening control may take main action gradually. When the field excitation current is large enough, the magnetic flux generated by the field excitation coil does not pass though the PMs and can make the PM flux path change to the path indicated by the red line in Fig. 2.3 (b). Meanwhile, the short circuit for PM flux is significantly reduced. Thus, the field strengthening control has the capability to produce high torque due to the increase in back-EMF. For F1A1 HSSPM machine, the flux generated by field current has significant influence on the PM flux path, which leads the PM flux passes through the air-gap. Both F1A3 and F1A1 HSSPM machines have similar main basic operation principle, however, slight difference exits at no current excitation situation due to different PM location method.

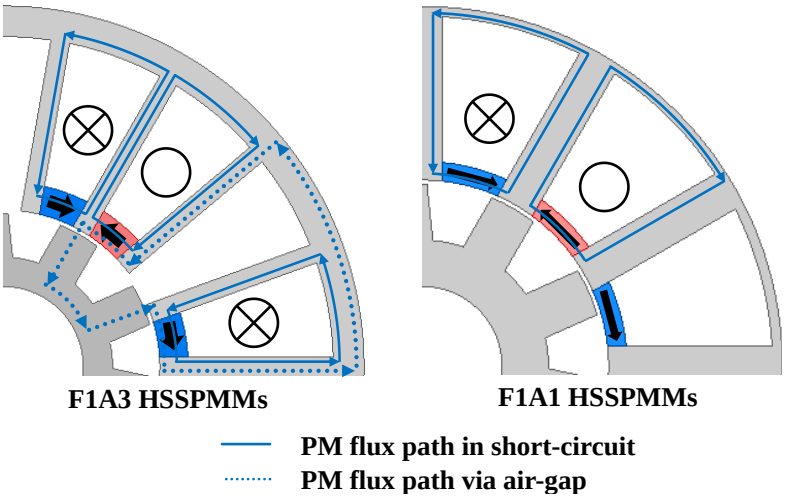

(a) I_{dc} = 0A

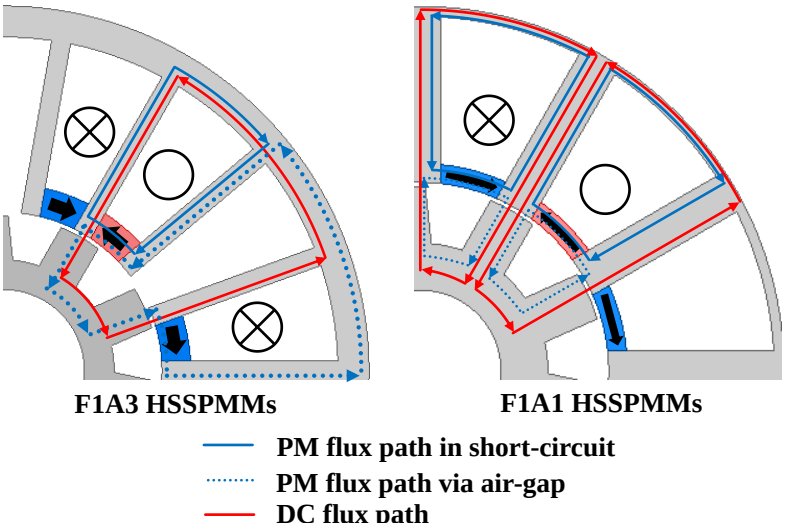

(b) I_{dc} =rated current

Fig. 2.3 DC and flux paths in quarter machine models at open-circuit for F1A3 and F1A1 HSSPMMs.

2.3. Design optimization

Since the F1A3 HSSPM machine having PMs in the stator slot opening of the DC winding slot, it is difficult to set the aim of optimization with PM volume free since it will result in either no PM for low cost or no DC coil for maximum torque. Thus, as a stator hybrid excitation machine with slot opening PM, the F1A1 HSSPM machine [92] is implemented to have the PM usage of the new F1A3 HSSPM machine fixed. Beside, to ensure a fair comparison with the F1A1 HSSPM machine, the optimization restrictions are summarised as follows:

1) The machines have the same stator outer radius, air-gap length and stack length.
2) The total copper losses of the machines are the same.
3) The machines are optimized with end-winding considered.
4) The material properties for PM and iron are the same.
5) The machines have the same total number of turns for either field or armature winding.

The genetic algorithm (GA) is used to implement the global optimization for the maximum average torque, using the commercial Maxwell finite element software.

The F1A3 HSSPM machine is developed from the F1A3 (18-slot/10-pole) WFSF machine [72]. Hence, the DC winding is concentrated and the armature winding is overlapped and covers three stator teeth and two DC field slots. The machine has six pairs of PMs with opposite magnetization directions for one pair. The cross section of this machine is shown in Fig. 2.2.

The restrictions for optimization are listed in Table 2.1. To obtain the global optimization of this machine, the parameters such as stator inner radius R_{SI}, stator tooth angle θ_{st}, stator yoke angle H_{BI}, rotor tooth angle θ_{rt}, and rotor tooth height H_{Rtooth} are considered and to be optimized. The geometric parameters for the HSSPM machine are shown in Fig. 2.4 (a).

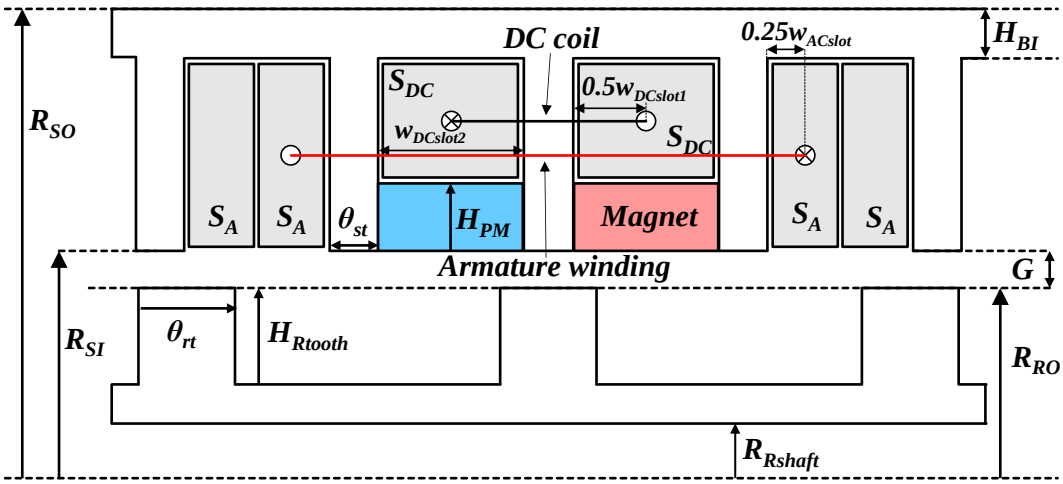

(a) Illustration of the stator and rotor geometric parameters.

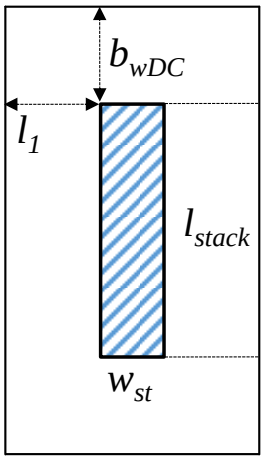

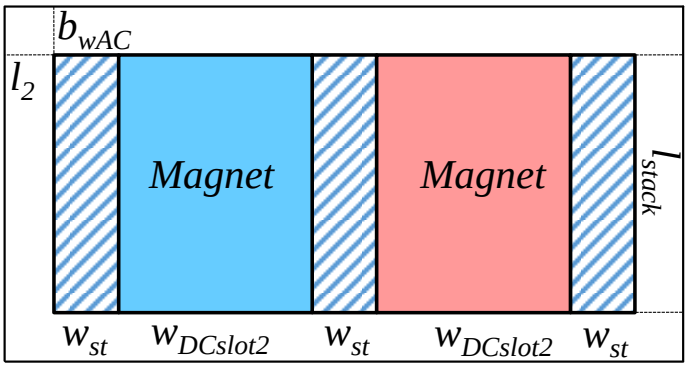

(b) Cross-section for one field coil. (c) Cross-section for one armature coil.

Fig. 2.4 Design parameters and coil winding configuration for F1A3 HSSPM machine.

Table 2.1 Restrictions for optimization

Parameters	**Unit**	**F1A3 HSSPM machine**
Stator outer radius (R_{SO})	mm	45
Stack length (l_{stack})	mm	25
Air-gap length (G)	mm	0.5
Shaft radius (R_{Rshaft})	mm	10
Copper loss (P_{Cu})	W	60
PM volume (V_{PM})	mm^2	5403.8
Packing factor (k_p)		0.59
PM N38SH at 20 °C (Br/μ_r)		1.2T/1.05
Turns/coil (armature) (N_a)		92
Turns/coil (field) (N_f)		92
Total number of turns (armature)		552
Total number of turns for (field)		552
Rated speed	rpm	400

The copper loss P_{Cu} of the F1A3 HSSPM machine can be expressed as

$$P_{Cu} = I_a^2 R_a + I_f^2 R_f \tag{2.1}$$

where I_a and I_f are the rms armature current and the field current, R_a and R_f are the total armature and field winding resistances. The end-winding has considered in the optimization. Thus, the total armature winding resistance is given in (2.2) and the total field winding resistance is given in (2.3).

$$R_a = \frac{N_a^2 \rho_{Cu}(12 l_{stack} + l_{end\_a})}{S_A k_p} \tag{2.2}$$

$$R_f = \frac{N_f^2 \rho_{Cu}(12 l_{stack} + l_{end\_f})}{S_{DC} k_p} \tag{2.3}$$

where N_a and N_f are the numbers of turns per armature coil and field coil, respectively. ρ_{Cu} is the electrical resistivity of copper, S_a and S_{DC} are the areas for armature and field coils separately, l_{end_a} and l_{end_f} are the total armature and field end-winding lengths, respectively. The configurations for armature and field coils are shown in Fig. 2.4 (b) and (c), respectively.

To simplify the calculation, it is assumed $b_{wDC} = l_1 = 0.5w_{DCslot1}$, and $b_{wAC} = l_2 = 0.25w_{ACslot}$. For the end-windings are mainly comprised by arc, the field coil end-winding length can be given in (2.4), and the armature coil end-winding length can be expressed in (2.5).

$$l_{end\_f} = 2\left(\frac{6}{9}\left((S_{SO} - H_{BI}) + (S_{SI} + H_{PM})\right)\pi - 6w_{st}\right) \tag{2.4}$$

$$l_{end\_a} = 2((S_{SO} + H_{BI}) - S_{SI})\pi \tag{2.5}$$

where H_{PM} is the PM height and w_{st} is the stator tooth width.

The optimization is implemented at a rotor speed of 400 rpm. Since the areas of armature and field coils are different the armature and field currents are also different. Hence, during optimization, the ratio of field to armature slot current density is considered. The optimization parameters are shown in Table 2.2. The optimization of F1A1 HSSPM machine is based on [92].

Table 2.2 Optimized parameters for HSSPM machines

Parameters	**Unit**	**F1A3**	**F1A1**
Back-iron height (H_{BI})	mm	3.83	1.22
Stator pole arc (θ_{st})	Mech. Deg.	6.91	12.43
Stator tooth width (w_{st})	mm	2.35	5.05
Rotor pole arc (θ_{rt})	Mech. Deg.	15.84	15.10
Rotor tooth height (H_{Rtooth})	mm	5.45	7.10
Stator inner radius (R_{SI})	mm	19.54	23.30
PM thickness (H_{PM})	mm	3.54	2.32
PM volume (V_{PM})	mm^3	5403.8	
Split ratio		0.423	0.507
Ratio of field to armature slot current density (J_{ratio})		0.567	1
Total AC slot area (S_a)	mm^3	1069.4	1428.4
Total DC slot area (S_f)	mm^3	1922.8	1428.4

2.4. Open-circuit electromagnetic performance analysis

In this section, the open-circuit performance of F1A3 and F1A1 HSSPM machines are compared. The armature excitation current and the field excitation current are calculated at total copper loss of 60W with the optimized ratio of field to armature slot current density. The flux line distribution on open circuit is shown in Fig. 2.5. When the current excitation is 0A in the F1A1 HSSPMM, the flux is mainly shunted in the stator and the stator is much saturated than the machine with field current. In contrast, the flux in the F1A3 HSSPMM is only increased slightly.

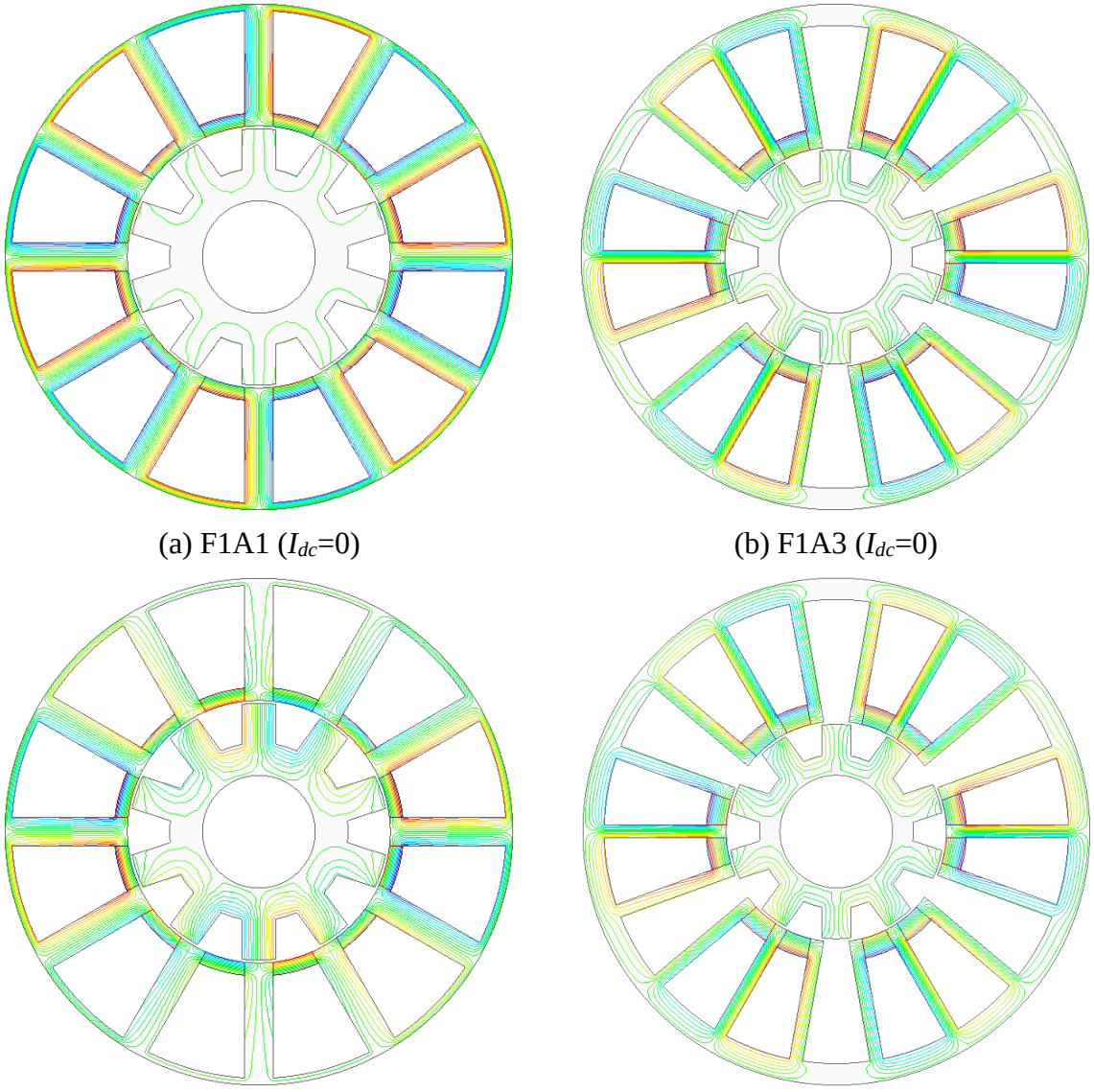

(a) F1A1 (I_{dc}=0) (b) F1A3 (I_{dc}=0)

(c) F1A1 (I_{dc}=rated DC excitation=5.080A) (d) F1A1 (I_{dc}= rated DC excitation=4.717A)

Fig. 2.5 Open-circuit flux distribution for F1A1 and F1A3 HSSPM machines

2.4.1. Flux linkage

The flux-linkage waveforms for F1A1- and F1A3-HSSPMMs with and without DC excitation current and the harmonics for phase A are shown in Fig. 2.6. It shows that when the field excitation current is zero, the flux linkage for the F1A1 HSSPM machine is quite small since the flux mainly shunts in the stator as shown in Fig. 2.5 (a). The significant increasing amplitude for F1A1 HSSPM machine with DC current demonstrates that the influence of field excitation coil source is vital in this machine. For the F1A3 HSSPM machine, when the machine with DC current, the amplitude of the waveform is slightly higher than that without DC current since the DC excitation current is low and the machine is mainly controlled by PM and the influence of field excitation coil is not observed at low DC excitation current. The stator and rotor with linear materials is employed for the F1A3 and F1A1 HSSPM machines and the flux linkage waveforms with no current excitation are shown in Fig. 2.6 (c). The flux linkage waveforms of the HSSPM machines with linear material stator and rotor are negligible. This means the two HSSPM machines exhibit some flux-leakage at different degree due to the machine stator magnetic saturation which can be observed in Fig. 2.7. The F1A3 HSSPM machine is easier to be magnetically saturated due to the machine structure, and the large flux-linkage is produced by large flux-leakage.

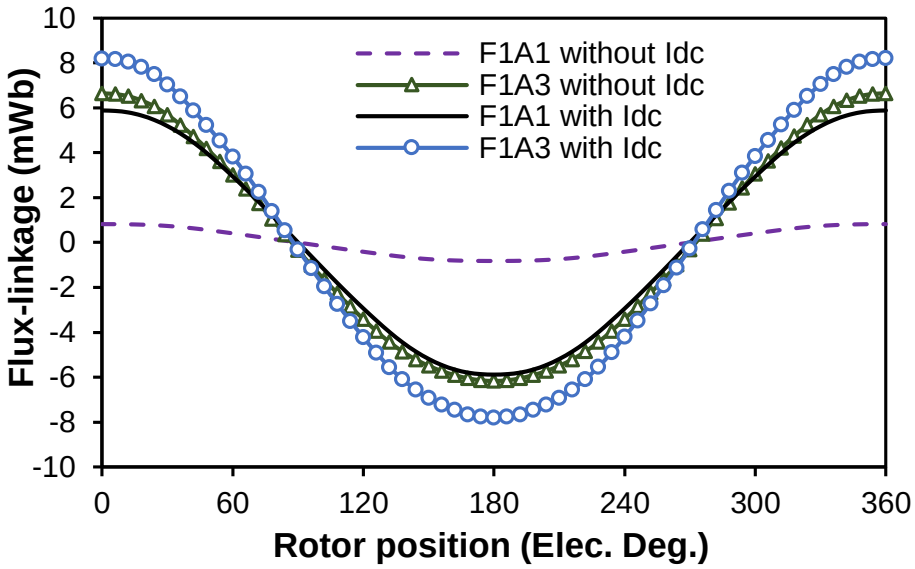

(a) Phase 'A' flux-linkage waveforms (I_{dc}=rated current)

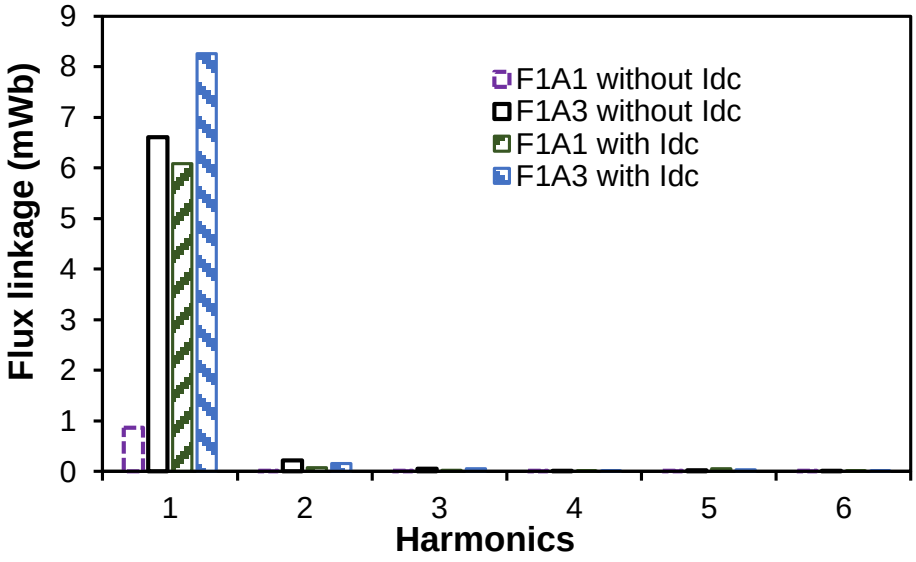

(b) Harmonics, Phase 'A'

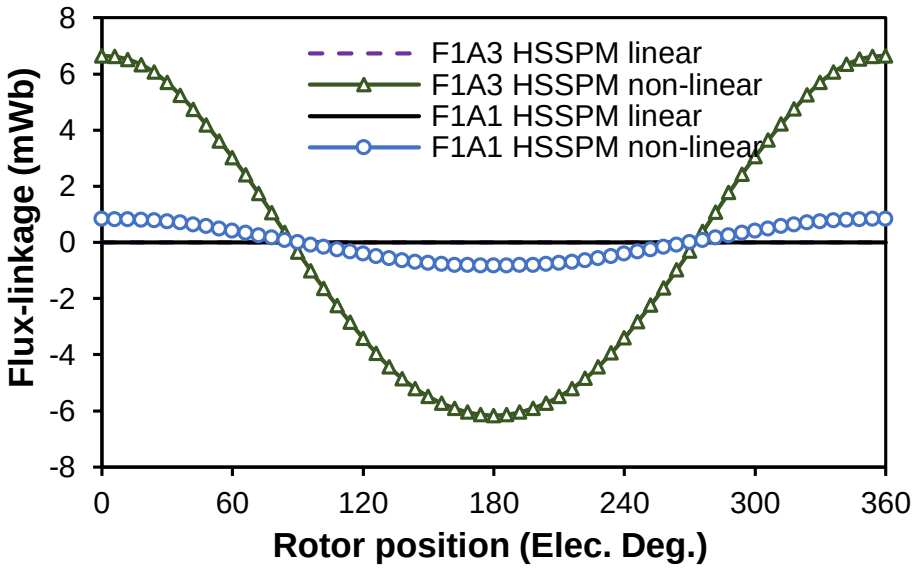

(c) Phase 'A' flux-linkage waveforms of non-linear and linear material stator and rotor (I_{dc}=0)

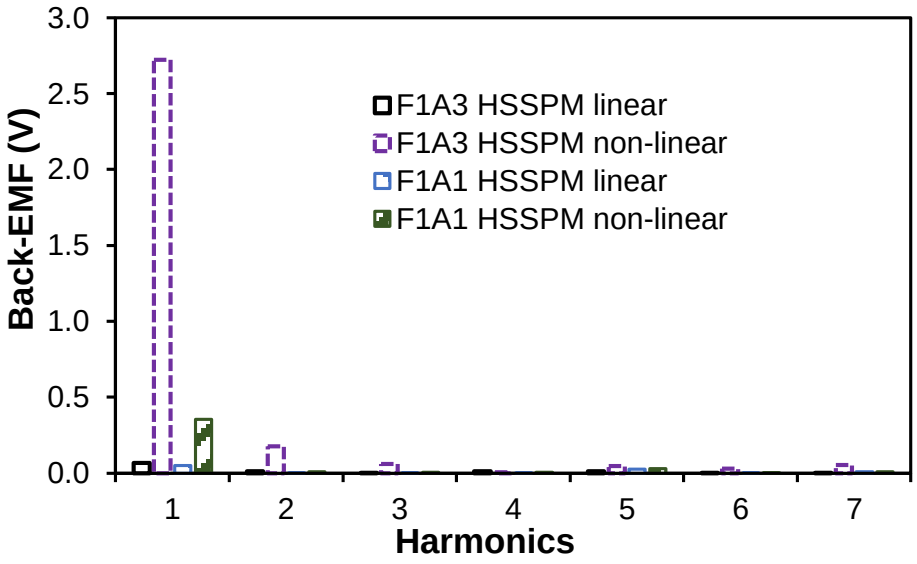

(d) Harmonics, Phase 'A'

Fig. 2.6 Open-circuit phase flux-linkage waveforms of F1A1- and F1A3-HSSPM machines (rotating speed = 400 rpm).

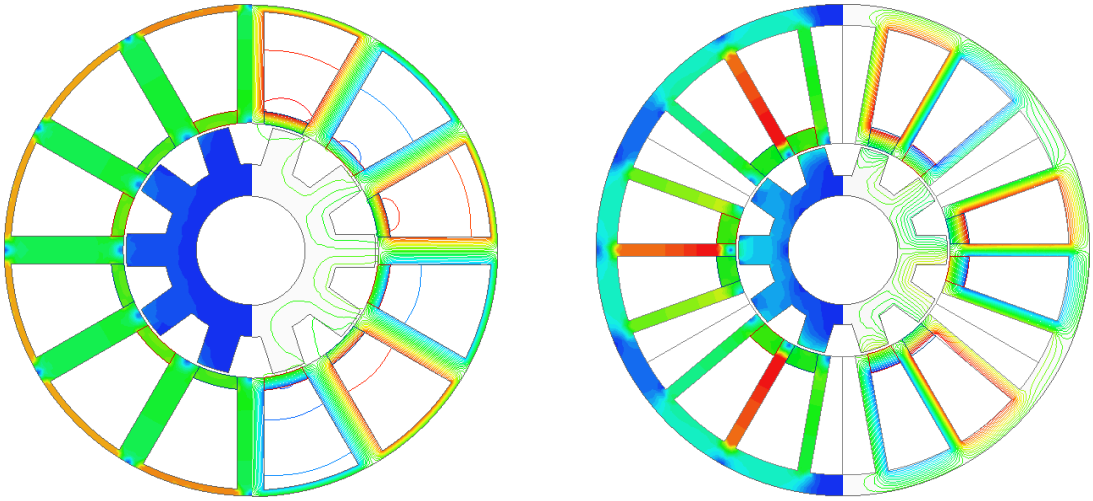

Non-linear stator and rotor materials

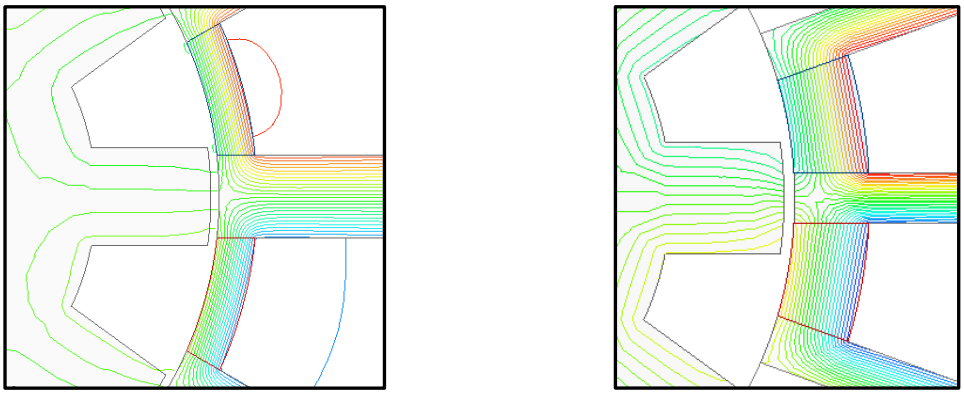

Zoom in

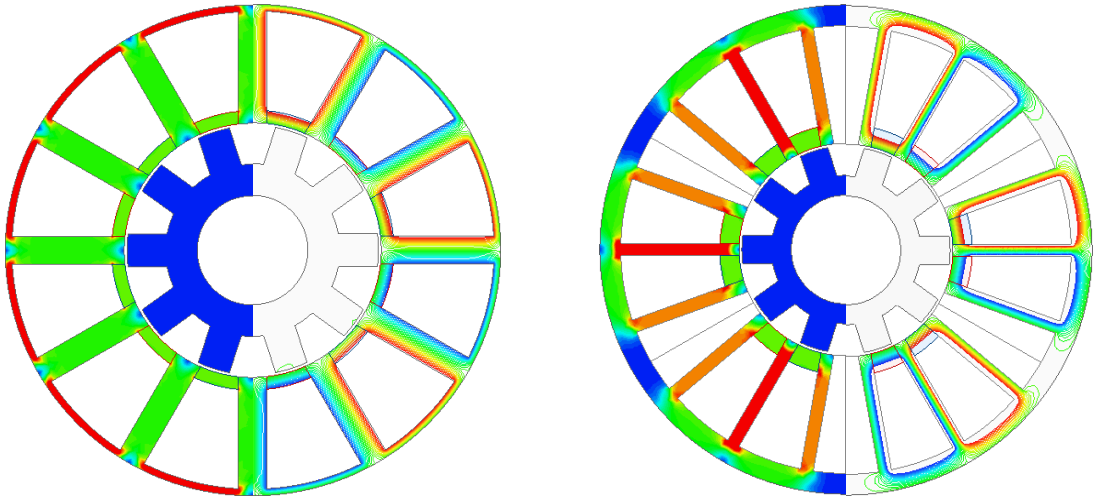

Linear stator and rotor materials (relative permiability = 4000)

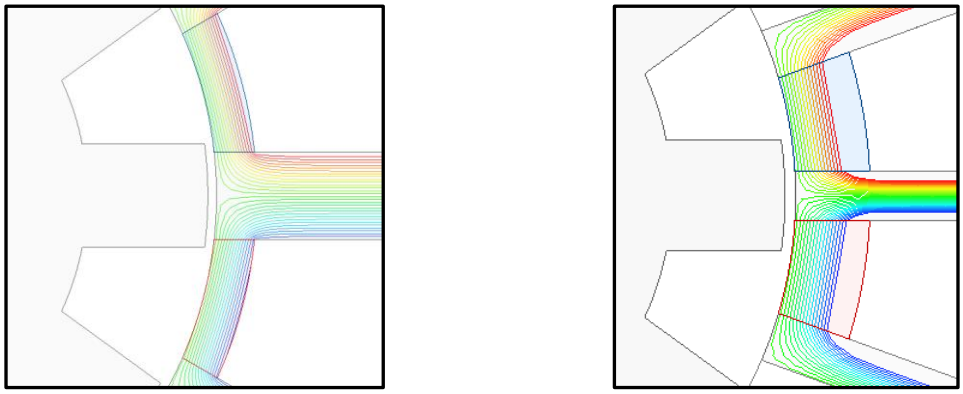

Zoom in

(a) F1A1 HSSPM machine (b) F1A3 HSSPM machine

Fig. 2.7 The flux density distributions of F1A1 and F1A3 HSSPM machines at 180° rotor position (electrical degree).

2.4.2. Phase back-EMF

When I_{dc} = 0A, the phase back-EMF is small for the F1A1 HSSPM machine as shown in Fig. 2.8. The amplitude of back-EMF for the F1A3 HSSPM machine with DC current is slightly higher than that without DC current, which is similar to the flux linkage waveforms. The back-EMF waveforms for F1A1 HSSPM machine are sinusoidal, thus the higher order harmonics are negligible as shown in Fig. 2.8 (b). The waveforms of the F1A3 HSSPM machine are less sinusoidal, that may account consequently for large torque ripple in both cogging torque and electromagnetic torque.

Besides, as the flux-linkage waveforms shown in Fig. 2.6, the back-EMF waveforms at no current excitation are caused by flux-leakage since the back-EMF waveforms for the machine stator and rotor having linear material are negligible, Fig. 2.8 (c).

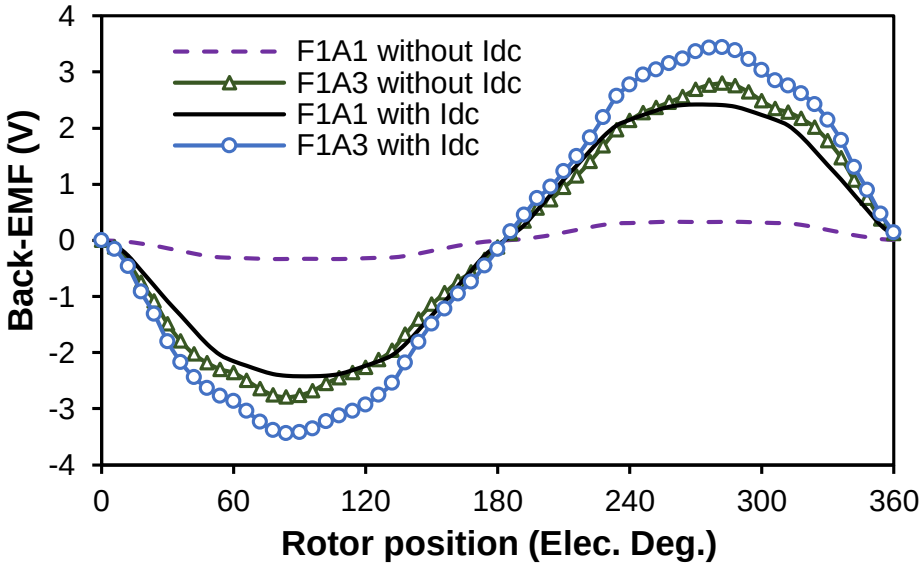

(a) Phase 'A' back-EMF waveforms (I_{dc}=rated current)

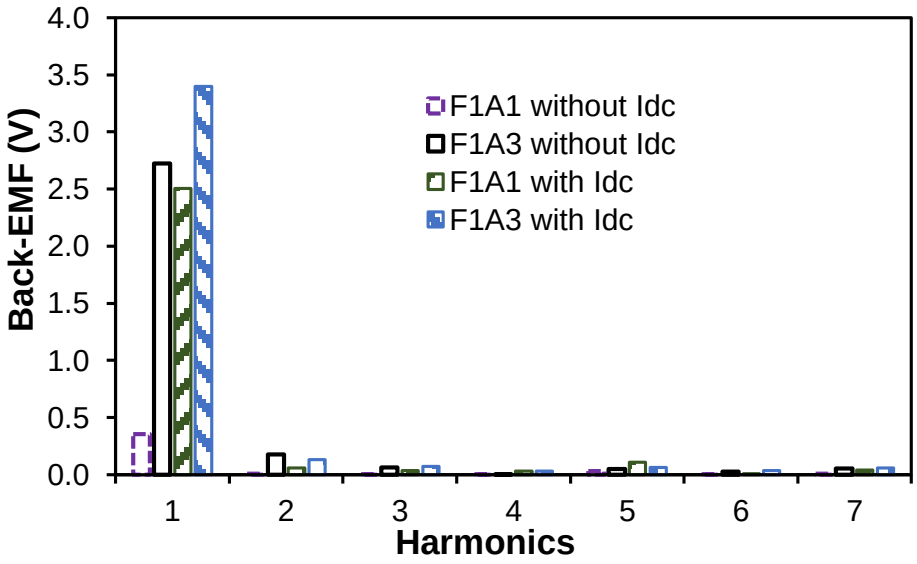

(b) Harmonics, Phase 'A'

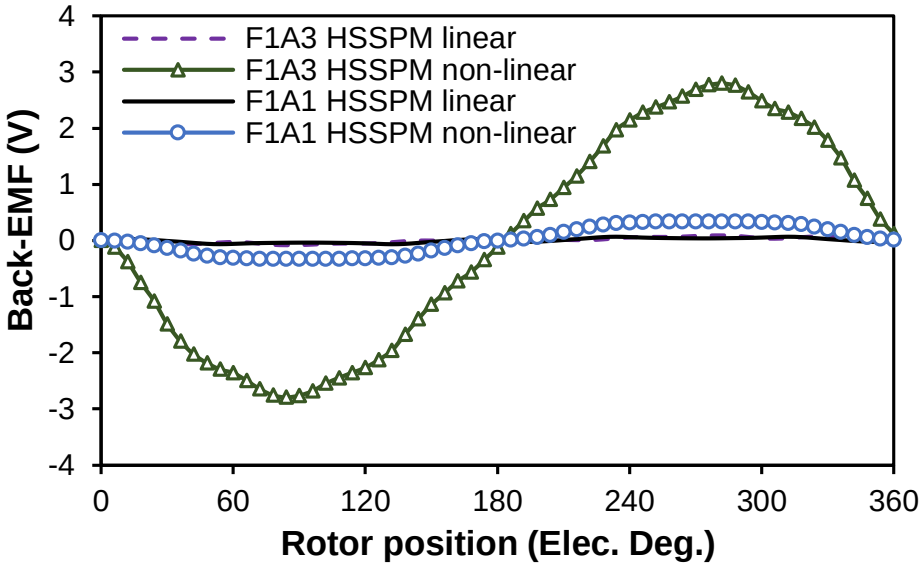

(c) Phase 'A' back-EMF waveforms of non-linear and linear material stator and rotor (I_{dc}=0)

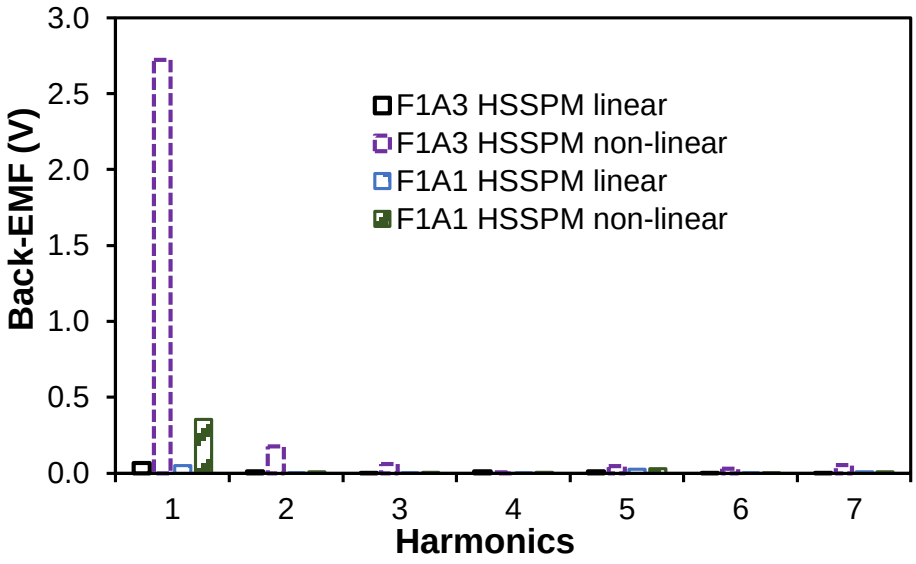

(d) Harmonics, Phase 'A'

Fig. 2.8 Open-circuit phase back-EMF waveforms of F1A1- and F1A3-HSSPM machines (rotating speed = 400 rpm).

2.4.3. Cogging torque

As shown in Fig. 2.9 (a), the amplitudes of cogging torque for both machines are increased with the addition of DC current. For the F1A3 machine, the ripple for the cogging torque is quite high. In Fig. 2.9 (b), it can be seen that the 3rd order harmonic can be observed in the F1A3 HSSPMM, while the 6th harmonic dominates in the F1A1 HSSPMM. The cogging torque

for the F1A1 HSSPMM is negligible at no DC current due to the flux shunted in the stator. It is worth mentioning that the cogging torque for the F1A1 HSSPMM remains small.

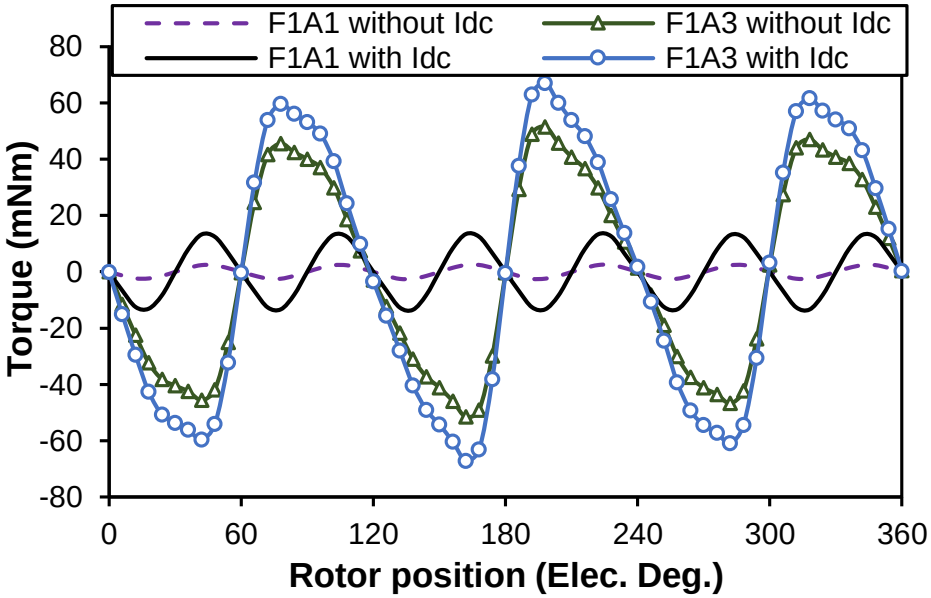

(a) Cogging torque waveforms

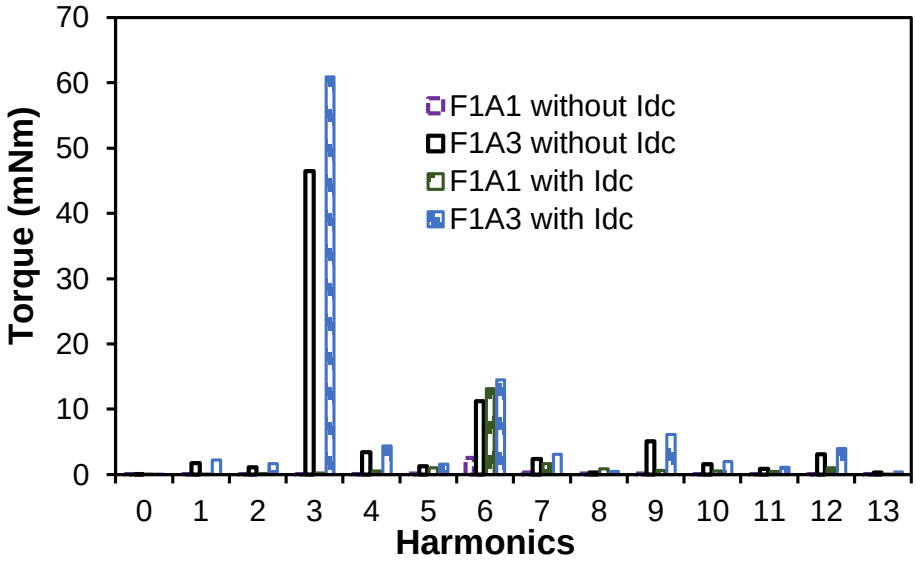

(b) Harmonics

Fig. 2.9 Cogging torque waveforms for F1A1 and F1A3 HSSPM machines.

2.5. Influence of field excitation current

From [92], it shows that the HSSPM machines will increase the electromagnetic torque and the amplitude of phase back-EMF with the raising DC current. However, the machine can be over-excited when the DC excitation current is large enough due to magnetic saturation. Fig. 2.10

shows the variation of fundamental harmonic of phase back-EMF waveforms with DC excitation current for the F1A1 and F1A3 HSSPM machines. When the machines have excited negative DC field current, the variation of the first harmonic of the back-EMF for both machines are slightly. That is because the direction of flux produced by DC coils and PMs are the same which make the machine stator severe magnetically saturated. Since the HSSPMMs located the PMs in the slot opening, part of the flux will be passed through the air-gap when the stators are magnetically saturated which produces flux leakage. The leaked flux can be connected between stator and rotor by main flux loop because of the specific structure, in that case, the leaked flux will be varies with the variation of rotor position which can produce back-EMF. For the F1A1 HSSPMM, the leaked flux can be caused by DC field current; while for the F1A3 HSSPMM, because of the negative DC field current, the leaked PM flux will not follow the main flux path, and thus, the fundamental magnitude of back-EMF is reduced when compared with those at no DC field current and positive DC field current excitation. The F1A1 HSSPM machine has significantly increased back-EMF magnitude with increasing DC current because the machine is sensitive to the field coil excitation. From Fig. 2.10 (b), the influence of field excitation source for F1A3 HSSPM machine is dull with low DC current excitation. The F1A1 HSSPMM becomes over-excited at 8-12A, while that of the F1A3 HSSPMMs at 12-18A. When DC current in the F1A1 HSSPM machine achieves 10A, and 15A for the F1A3 HSSPM machine, the machines can achieve the highest average electromagnetic torque since the fundamental harmonics of the phase back-EMF at these DC currents are the highest, all the fluxes linking the stator and rotor via air-gap, as shown in in Fig. 2.11. In addition, it shows that the F1A1 HSSPM machine is easily to be magnetically saturated at stator yoke, while the F1A3 HSSPM machine is saturated at stator teeth. The peak DC excitation current for the F1A3 HSSPM machine is larger than the F1A1 HSSPM machine since the F1A1 HSSPM machine is easier to be saturated with the increasing DC excitation current.

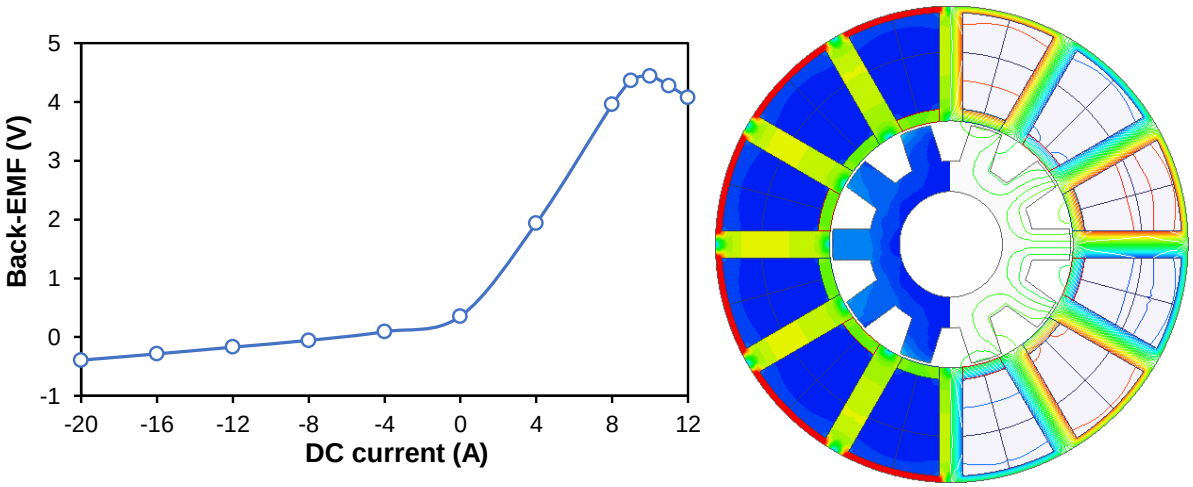

(a) F1A1 HSSPM machine

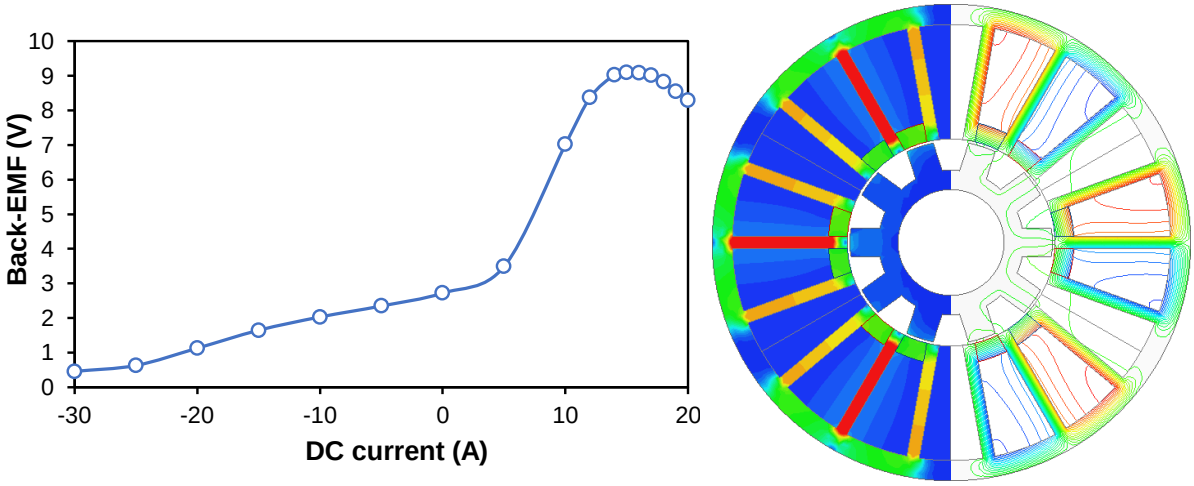

(b) F1A3 HSSPM machine

(I) fundamental magnitude back-EMF (II) I_{dc} = -20A

Fig. 2.10 Open-circuit phase 'A' back-EMF fundamental harmonic against DC excitation current for HSSPM machines.

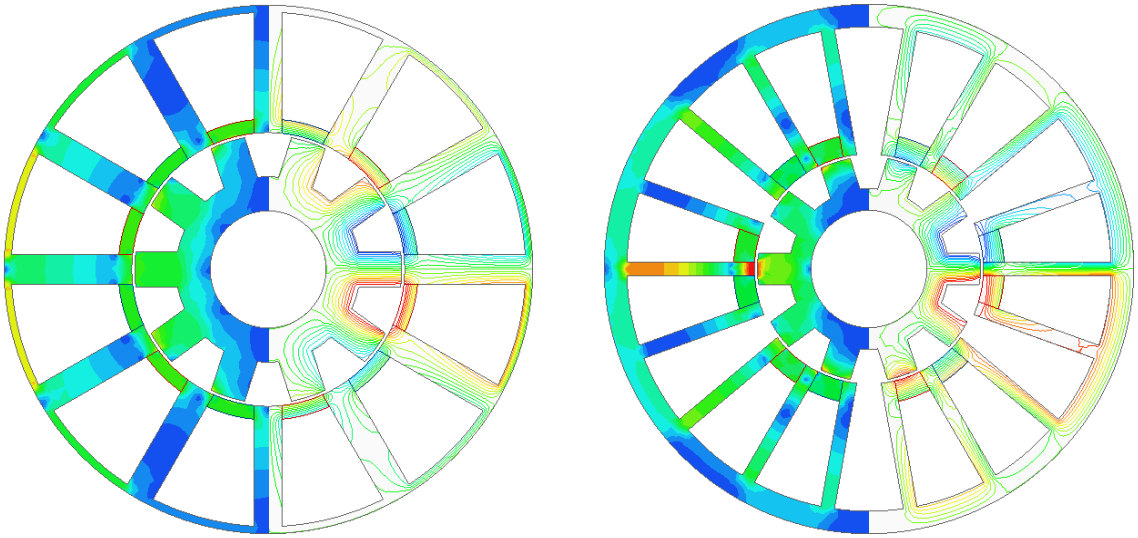

(a) F1A1 HSSPM machine (b) F1A3 HSSPM machine

Fig. 2.11 Flux density and flux line distributions of the HSSPM machines at 180° rotor position at electrical degree.

For Fig. 2.10 (b), the variation of back-EMF magnitude against DC current of the F1A3 HSSPM machine shows that when the DC current is between 0A to 5A, the magnitude of back-EMF increases slightly since the flux produced by DC current is used to reduce the magnetic saturation in the F1A3 HSSPM machine. With the DC current increased to 15A, the DC excitation is used to push the flux produced by PMs to the rotor part. This will increase the magnitude of back-EMF significantly when compared with that when the DC current is less than 5A. When the DC current is larger than 15 A, the magnitude of the back-EMF is reduced. This is due to the fact that the machine is magnetically saturated by the flux produced by DC current excitation. The flux density and flux line distribution of the F1A3 HSSPM machines are shown in Fig. 2.12 which proves the variation of back-EMF magnitude against DC current.

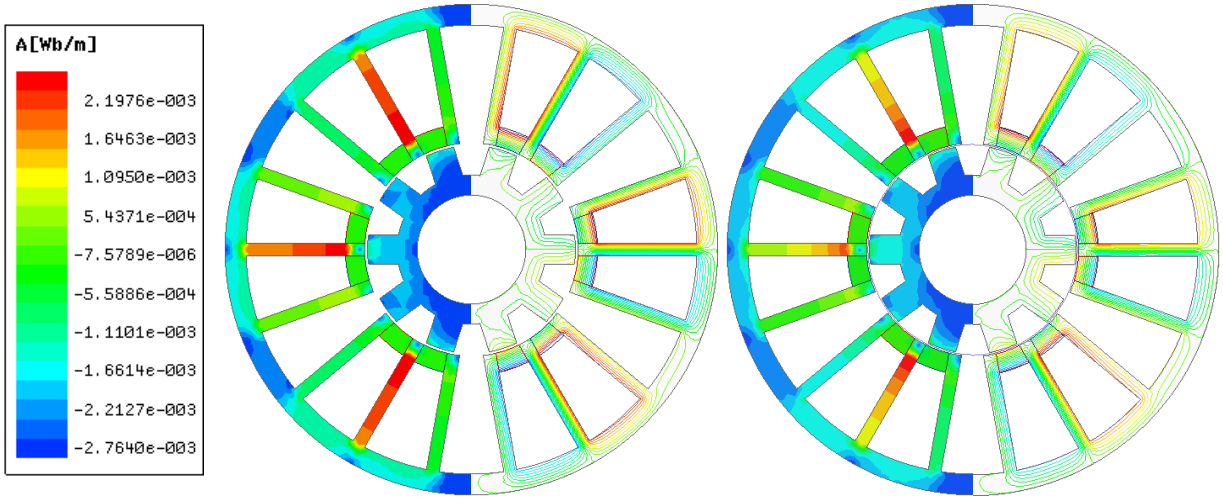

(a) I_{dc} = 0 (b) I_{dc} = 5A (rated current)

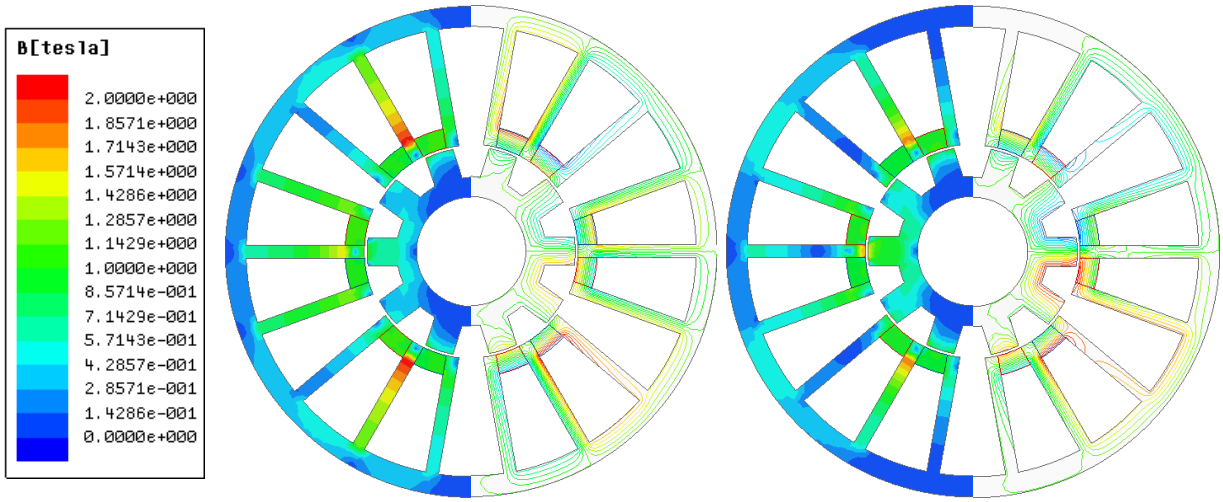

(c) I_{dc} = 7A (d) I_{dc} = 10A

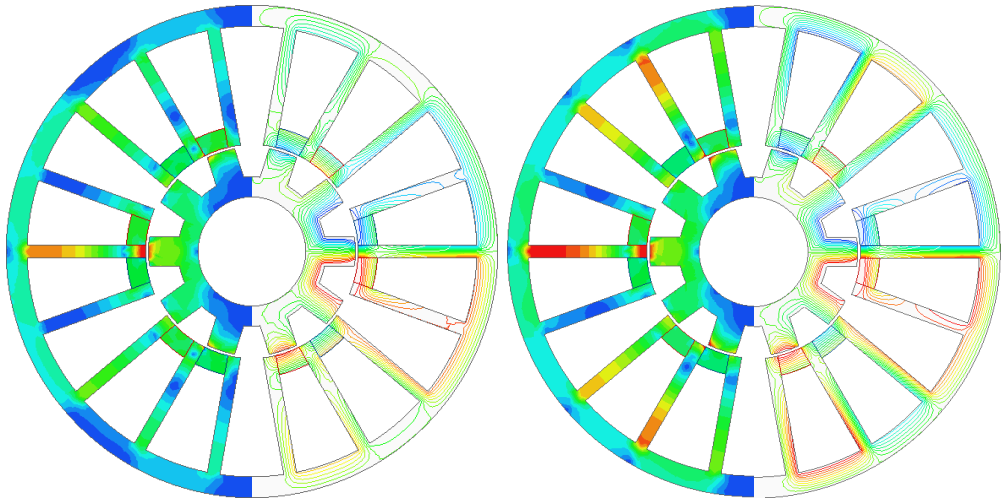

(i) I_{dc} = 15A (f) I_{dc} = 20A

Fig. 2.12 Flux density and flux line distributions of F1A3 HSSPM machine with different DC current excitation at 180° rotor position (in electrical degree).

2.6. Electromagnetic performance analysis

2.6.1. Electromagnetic torque

The electromagnetic torques of the F1A1 and F1A3 HSSPMMs are compared for the same copper loss, Fig. 2.13. The average electromagnetic torque for the F1A3 HSSPM machine can be increased by up to 50% than the F1A1 HSSPMM. However, the F1A3 HSSPMM has high torque ripple which is up to 28%. That is caused by non-sinusoidal back-EMF waveform and higher cogging torque. Besides, the electromagnetic torque for the F1A3 HSSPM machine is always higher than the F1A1 HSSPM machine at either low or high copper loss, Fig. 2.14. The F1A1 HSSPM machine has a limited average torque because of the magnetic saturation in the stator due to the thin stator yoke. Optimising the current angles for the machines can ensure the maximum average torque, which is shown in Fig. 2.15. Both machines can achieve the maximum average electromagnetic torque when the current angle is almost 0 when total copper loss of the machines are 60W, and thus, the machines have small/negligible reluctance torque. As the machines have raising the total copper loss to 120W, the maximum average torque will be achieved when the current angle is around 10 electrical degree, which is because the machines are severe magnetically saturated.

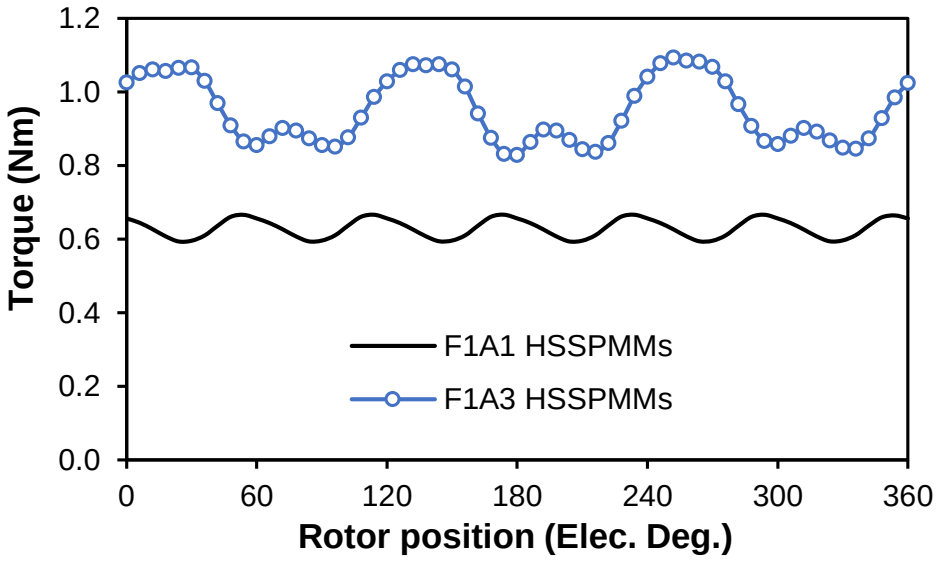

Fig. 2.13 Electromagnetic torque waveforms for F1A1- and F1A3-HSSPM machines (total copper loss = 60W).

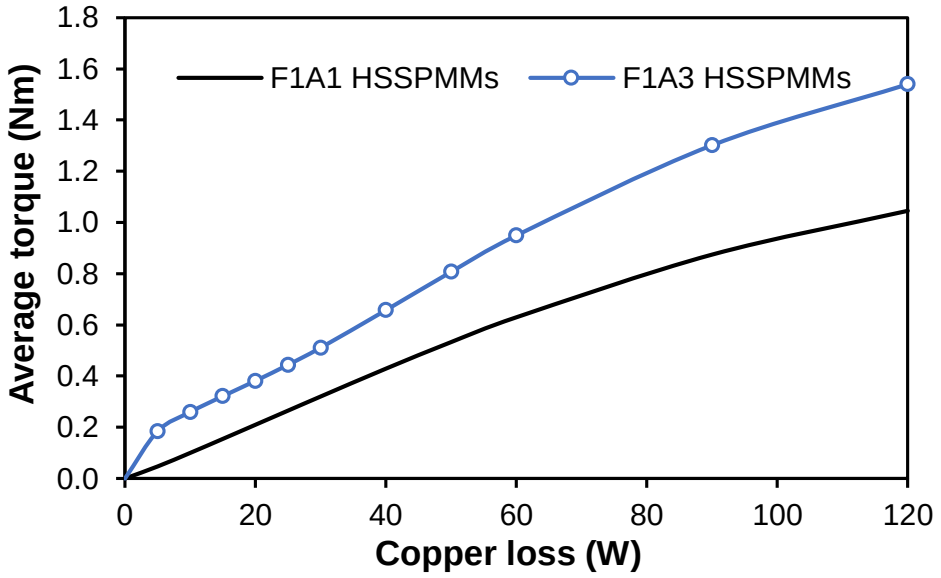

Fig. 2.14 Variation of average torque against variable copper loss for F1A1- and F1A3-HSSPM machines.

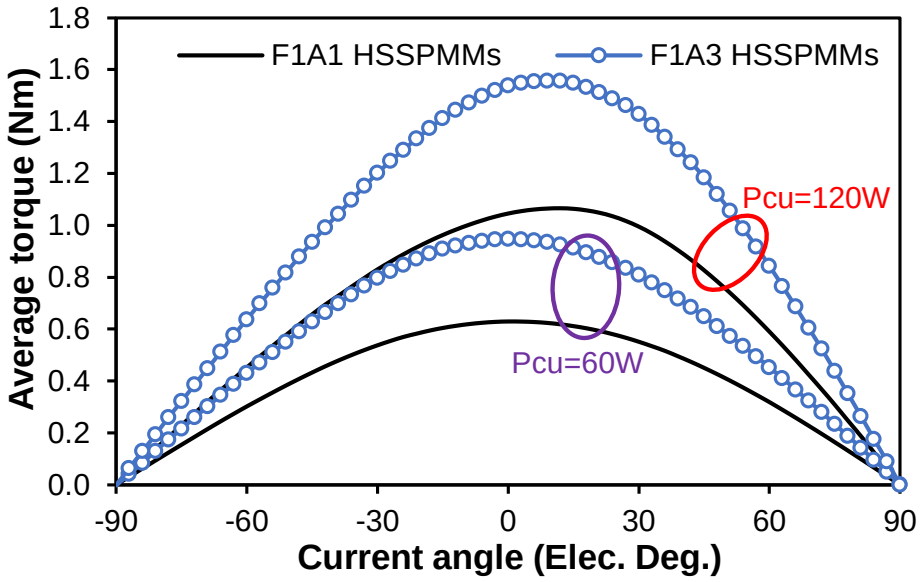

Fig. 2.15 Electromagnetic torque against current angle for F1A1- and F1A3-HSSPM machines (total P_{Cu} = 60W and 120W).

2.6.2. Iron loss and PM eddy current loss

The variations of iron loss and PM eddy current loss with rotor speed are shown in Fig. 11. The losses are calculated at total machine copper loss of 60W. In Fig. 2.16(a), it shows that for both machines, the iron loss in stator is much higher than that in rotor especially with increasing rotor speed. Meanwhile, the iron loss in stator for F1A3 HSSPM machine is higher than that for F1A1 HSSPM machine especially when the machine rotor speed is larger than 500rpm. While the iron loss in rotor of the machine has observable difference when the rotor speed is larger than 2000rpm since the back iron in the F1A3 machine is thicker.

Fig. 2.16(b) shows the average PM eddy current loss which is relatively low for the F1A1 HSSPMM even at high rotor speed. However, the PM eddy current loss for the F1A3 HSSPMM is much higher especially at high rotor speed.

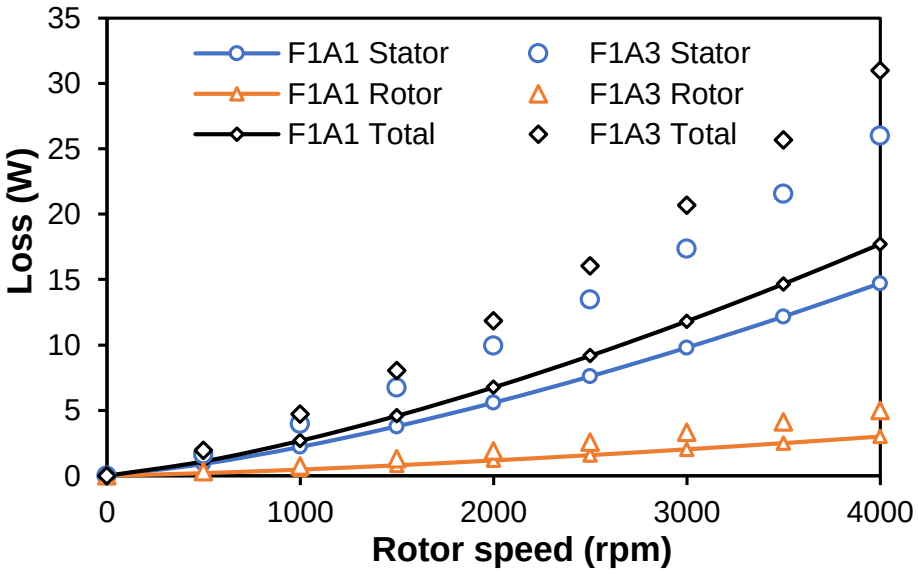

(a) Iron loss at total copper loss of 60W

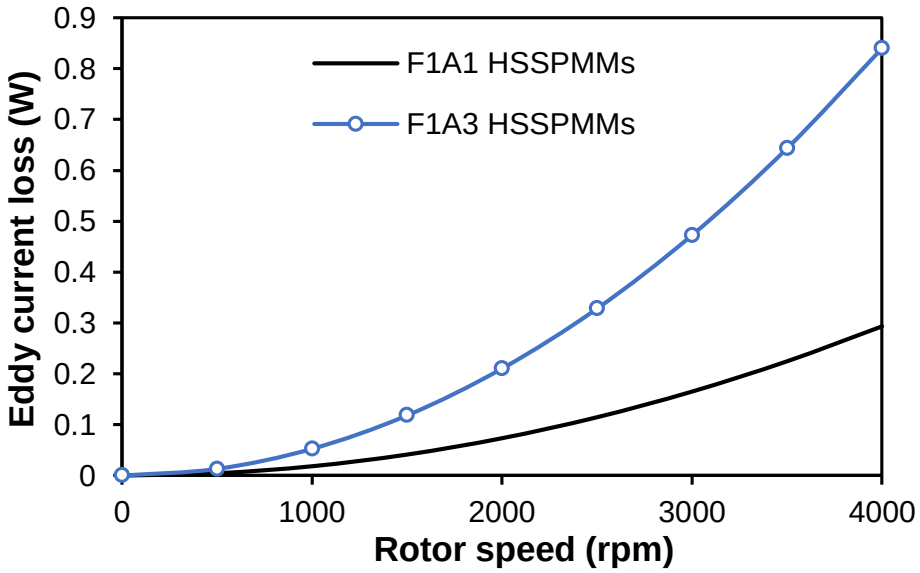

(b) PM eddy current loss

Fig. 2.16 Average iron loss and PM eddy current loss for F1A1 and F1A3 HSSPMMs at total copper loss of 60W.

To study the loss characteristic against copper loss for both machines, the F1A3 HSSPMM has much higher iron loss and PM eddy current loss especially at high copper loss, Fig. 2.17. Both machines are with fast increasing iron loss when the copper loss is lower than 100W, Fig. 2.17(a). The PM eddy current loss for the F1A1 HSSPMM remains low with the increasing copper loss, Fig. 2.17(b).

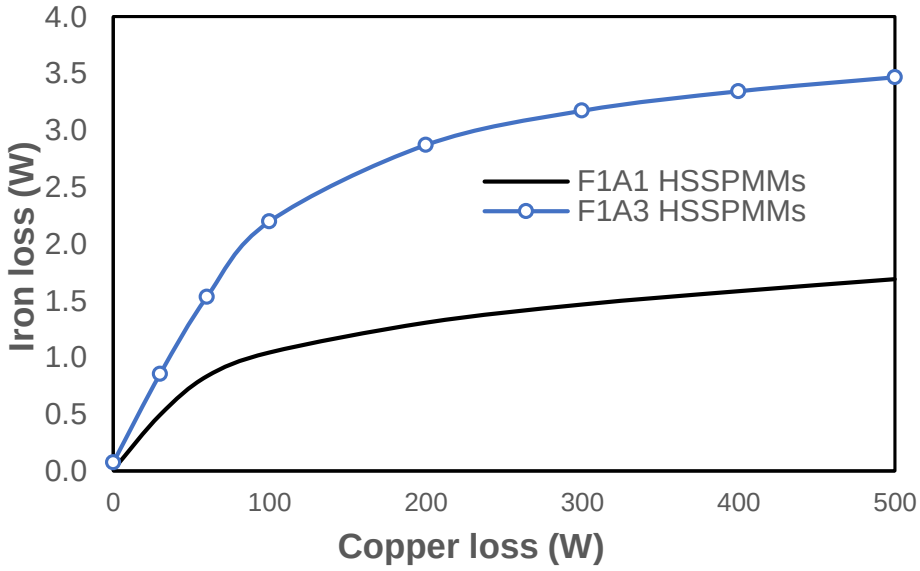

(a) Iron loss

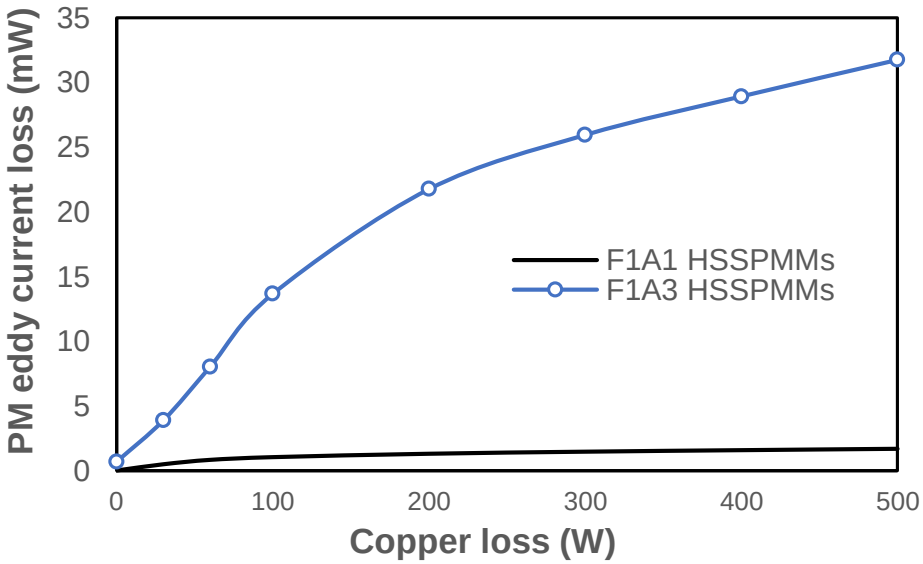

(b) PM eddy current loss

Fig. 2.17 Iron loss and PM eddy current loss for F1A1 and F1A3 HSSPMMs against copper loss @ rotor speed of 4000rpm.

2.7. Influence of rotor pole numbers

The previous sections introduced and investigated the 10 rotor pole F1A3 HSSPMM, and different numbers of rotor poles can also be introduced in this type of machine. The method to locate the PMs in F1A3 HSSPMM is similar to the sandwiched switched flux PM machine [49] which is shown in Fig. 2.18. Since the machine has the C-core switched flux PM machine structure but with two paralleled PMs have opposite magnetic polarities in one stator tooth and the stator tooth has been separated into three iron parts, the winding factor of the machine is difficult to define which is similar to the F1A3 HSSPMM. In this section, the F1A3 HSSPMMs with 7-, 8-, 10-, 11-, and 13-rotor poles will be investigated based on $N_s = k_1 N_{ph}$, $N_r = 2N_s \pm k_2$, and k_1, k_2 = 1, 2, etc., where N_s, N_r, N_{ph} are the number of stator poles, the number of rotor poles and the number of phases, respectively.

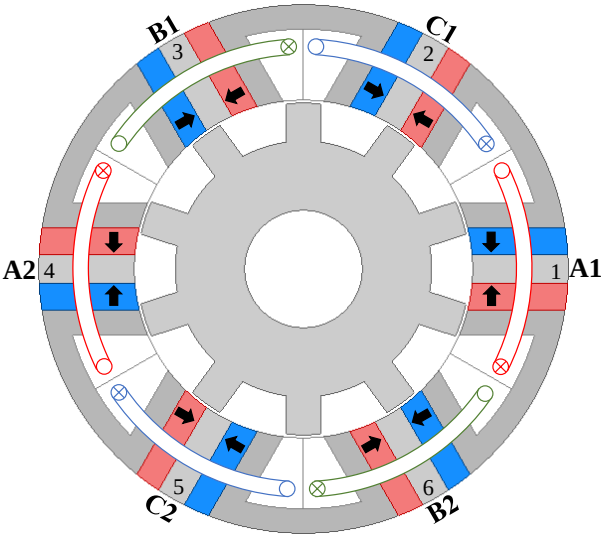

Fig. 2.18 The cross section of sandwiched switched flux PM machine.

The F1A3 HSSPMMs with different rotor poles are globally optimized to achieve the maximum torque. To make a fair comparison, the machines are optimized with a few conditions as (1) fixed copper loss (60W), (2) fixed stator outer diameter and stack length, (3) fixed air-gap length, (4) fixed turns per phase and turns for field windings, and (5) same stator, rotor and PM material properties. Besides, the ratio of field to armature slot current density and the fixed PM volume which mentioned in section 2.3 have to be considered during the optimization. The restriction parameters and the optimized parameters for F1A3 HSSPMMs are shown in Table 2.3 and Table 2.4, respectively.

Table 2.3 Restriction parameters for optimization

Parameters	**Unit**	**6-7/8/10/11/13**
Stator outer radius (R_{SO})	mm	45
Stack length (l_{stack})	mm	25
Air-gap length (G)	mm	0.5
Shaft radius (R_{Rshaft})	mm	10
Copper loss (P_{Cu})	W	60
PM volume (V_{PM})	mm^2	5403.8
Packing factor (k_p)		0.59
PM N38SH at 20 °C (Br/μ_r)		1.2T/1.05
Turns/coil (armature) (N_a)		92
Turns/coil (field) (N_f)		92
Total number of turns of armature winding		552
Total number of turns of field winding		552
Rated speed	rpm	400

Table 2.4 F1A3 HSSPMMs design parameters

Parameters	**Unit**	**7 pole**	**8 pole**	**10 pole**	**11 pole**	**13 pole**
Back-iron thickness (H_{BI})	mm	5.726	4.030	3.830	5.893	5.890
Stator pole arc (θ_{st})	Mech. Deg.	8.48	8.46	6.91	9.07	7.95
Stator tooth width (w_{st})	mm	2.78	2.76	2.35	3.01	3.12
Rotor pole arc (θ_{rt})	Mech. Deg.	17.09	18.87	15.84	11.16	10.47
Rotor tooth thickness (H_{Rtooth})	mm	4.00	4.50	5.45	3.61	4.78
Split ratio		0.406	0.404	0.423	0.412	0.489
PM thickness (H_{PM})	mm	4.02	4.03	3.54	4.13	3.38
Stator inner radius (R_{SI})	mm	18.76	18.69	19.54	19.05	22.53
Ratio of field to armature slot current density (J_{ratio})		0.480	0.498	0.567	0.534	0.864
Total armature slot area (S_a)	mm^3	1593.4	1830.3	1922.8	1501.3	1302.8
Total field slot area (S_f)	mm^3	904.7	1023.2	1069.4	858.7	759.4

2.7.1. Open-circuit phase flux-linkage and back-EMF

Fig. 2.19 and Fig. 2.30 shows the phase flux-linkage and phase back-EMF waveforms for the F1A3 HSSPMMs with different rotor poles. According to the machine operation principle, when the machines have no current excitation, the machines should have no flux-linkage and back-EMF. However, only the machine which has 13-rotor pole has small flux-linkage and back-EMF at no current excitation conditions. That is because the flux-leakage due to the stator magnetic saturation caused by PMs as mentioned in section 2.4. The flux distribution for the machines with no current excitation is shown in Fig. 2.31. It shows that the stator teeth between the adjacent PMs are saturated, and from the flux line distribution, it shows that the 13-rotor pole machine has less flux leakage.

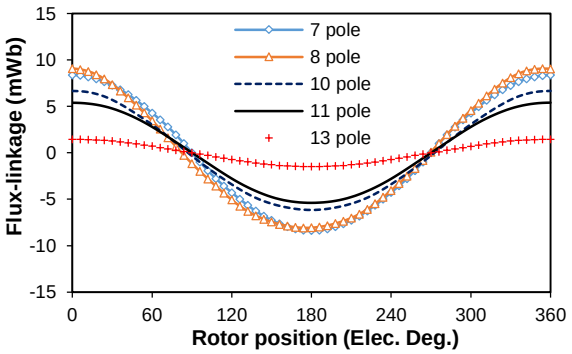

(a) I_{dc} = 0A

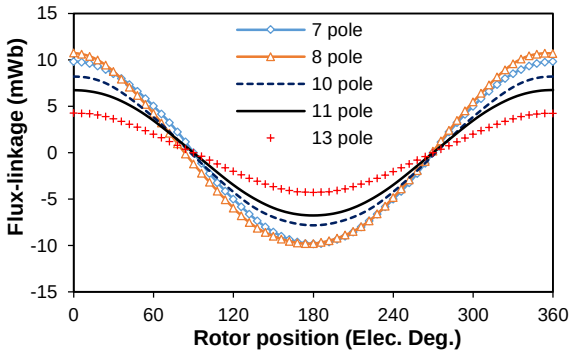

(b) I_{dc} = rated DC current

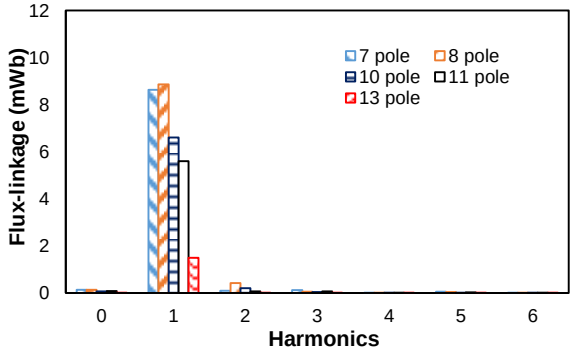

(c) Harmonics, I_{dc} = 0A

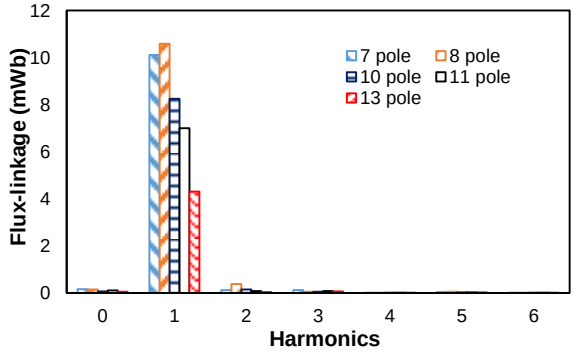

(d) Harmonics, I_{dc} = rated DC current

Fig. 2.19 Phase flux-linkage waveforms for F1A3 HSSPMMs

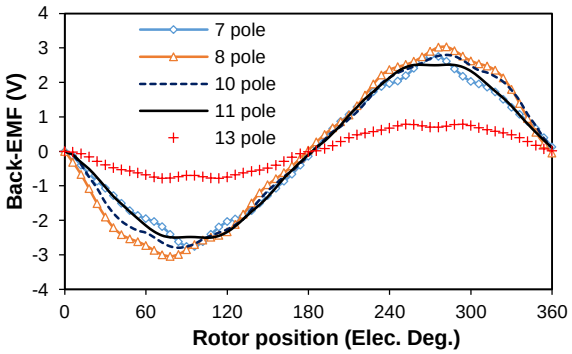

(a) I_{dc} = 0A

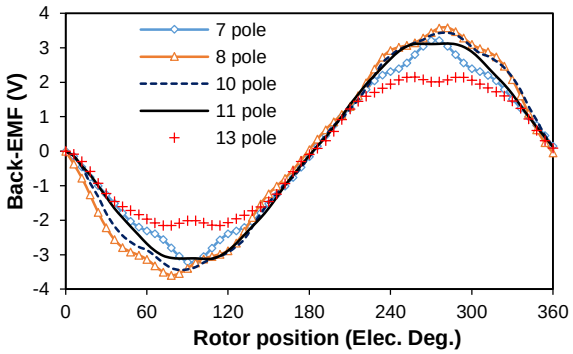

(b) I_{dc} = rated DC current

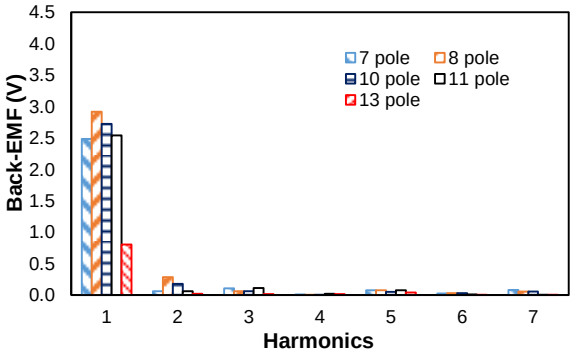

(c) Harmonics, I_{dc} = 0A

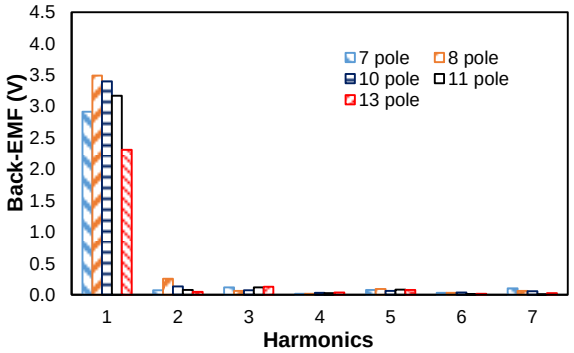

(d) Harmonics, I_{dc} = rated DC current

Fig. 2.20 Phase back-EMF waveforms for F1A3 HSSPMMs

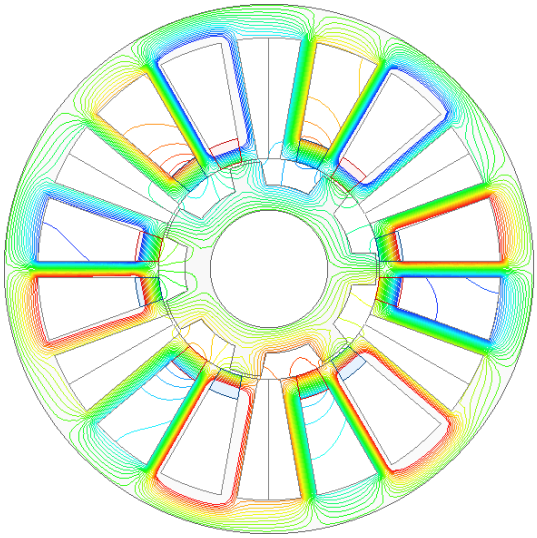

(a) Flux line distribution

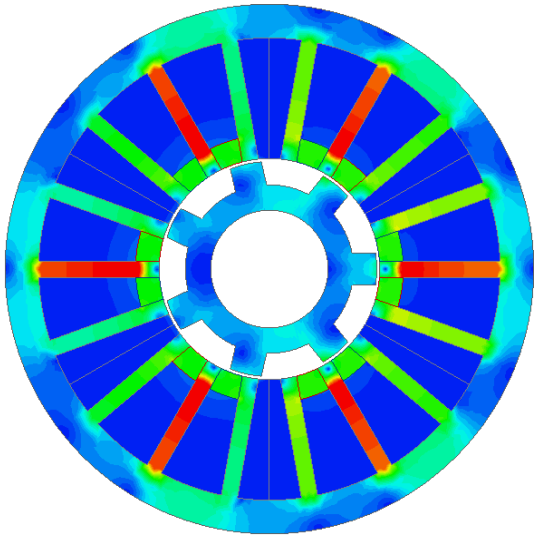

(b) Flux density distribution

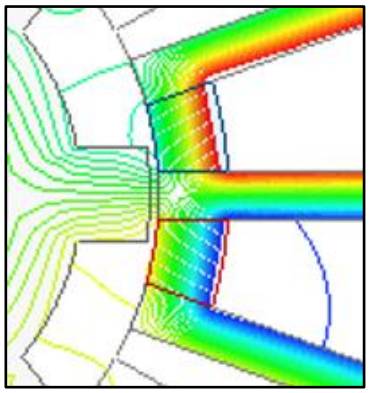

(c) Zoom in

(I) 7 rotor pole

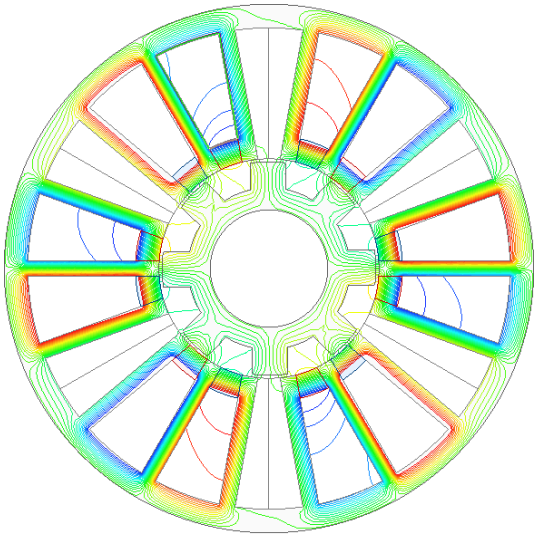

(a) Flux line distribution

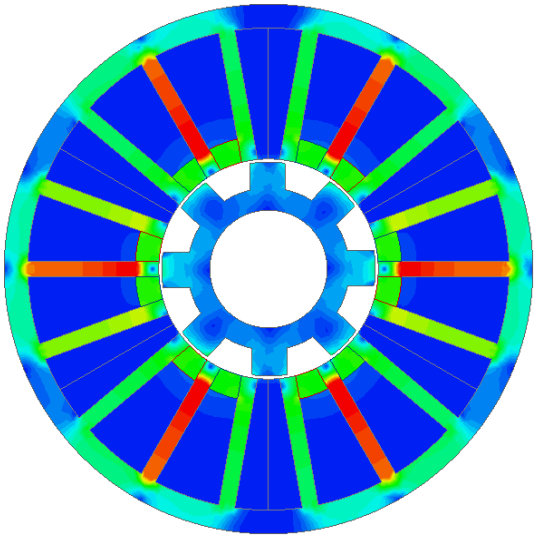

(b) Flux density distribution

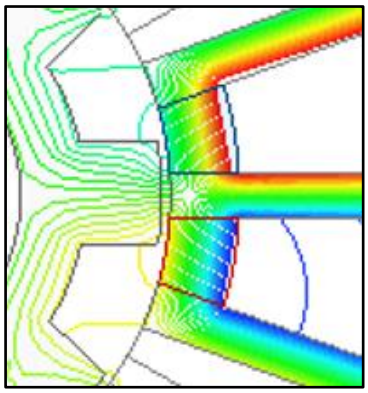

(c) Zoom in

(II) 8 rotor pole

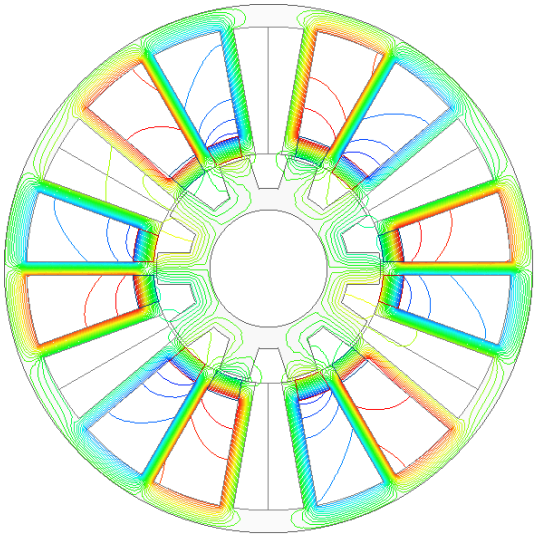

(a) Flux line distribution

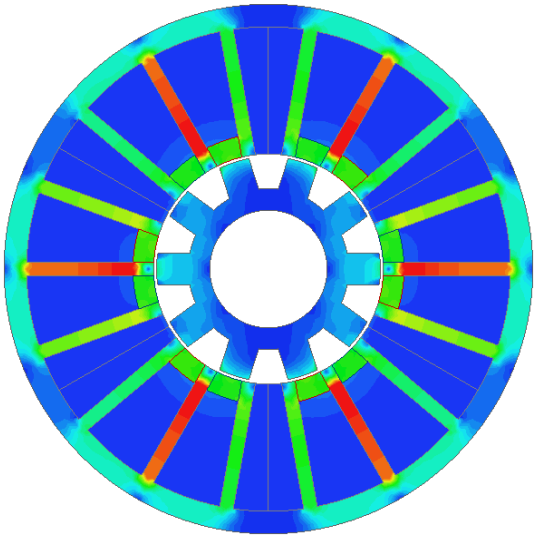

(b) Flux density distribution

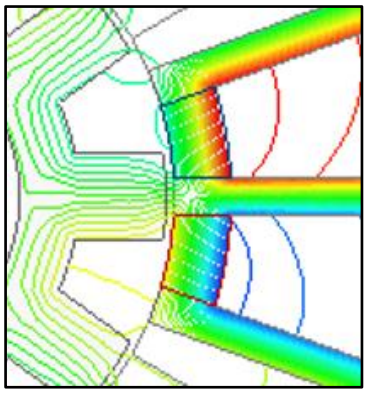

(c) Zoom in

(III) 10 rotor pole

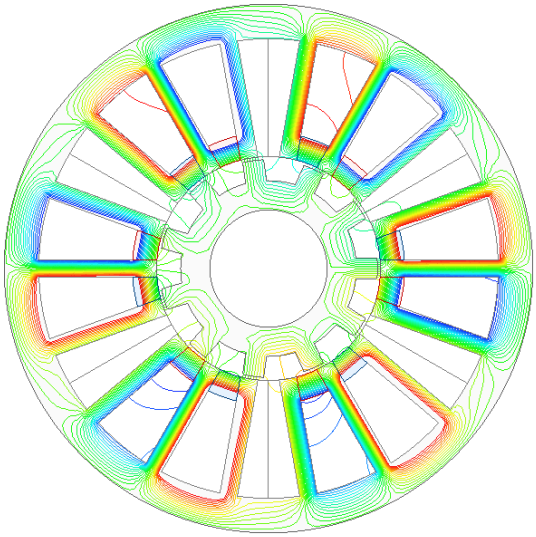

(a) Flux line distribution

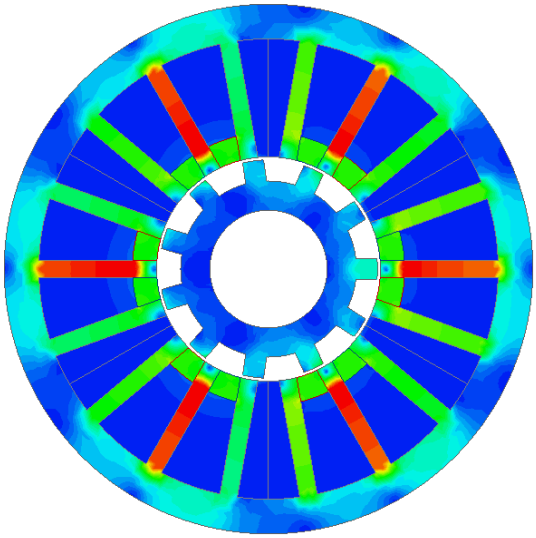

(b) Flux density distribution

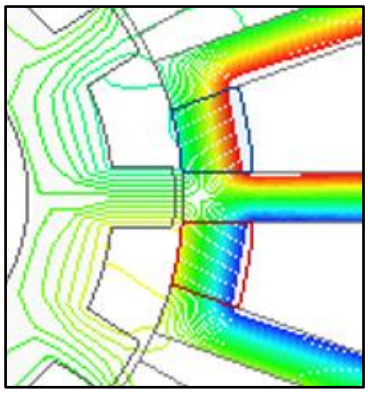

(c) Zoom in

(IV) 11 rotor pole

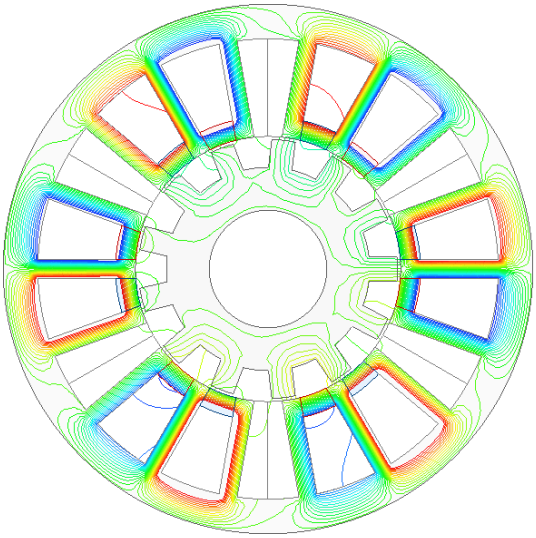

(a) Flux line distribution

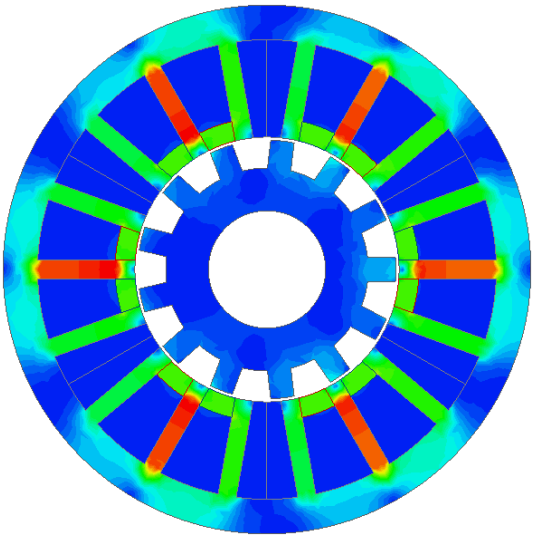

(b) Flux density distribution

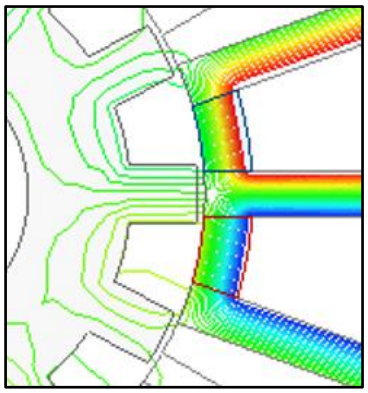

(c) Zoom in

(V) 13 rotor pole

Fig. 2.21 Flux line and density distributions for F1A3 HSSPMMs with no DC current excitation.

2.7.2. Cogging torque

Fig. 2.22 shows the cogging torque of the machines. Due to the large flux-leakage in the machines, the machines have cogging torque even when there is no current excitation. It shows that when the machines have even rotor poles, they have large cogging torque while for the odd rotor poles, the cogging torques remain small. Since the odd rotor pole machines have the 6 periods of cogging toque, the machines have dominant 6^{th} order harmonic and have no 3^{rd} and 9^{th} harmonics. While the 3 periods of cogging torque make the even rotor pole machines have dominant 3^{rd} harmonic.

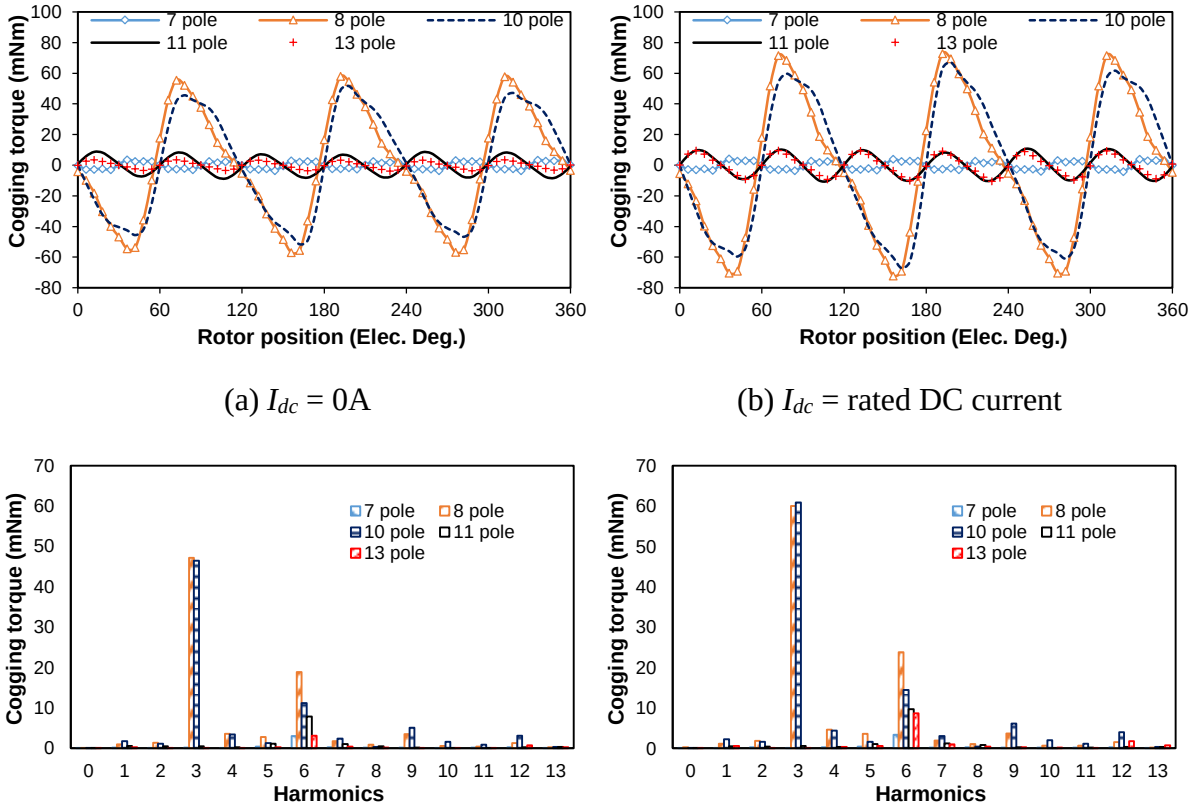

(a) I_{dc} = 0A

(b) I_{dc} = rated DC current

(c) Harmonics, I_{dc} = 0A

(d) Harmonics, I_{dc} = rated DC current

Fig. 2.22 Cogging torque waveforms for F1A3 HSSPMMs.

2.7.3. Influence of field excitation current

From Fig. 2.19, Fig. 2.20 and Fig. 2.22, it shows that when the machines are excited with a rated DC current, the phase flux-linkage, back-EMF and cogging torque have slightly increased, and the reason has been mentioned in section 2.5. This is because the DC current is firstly applied to reduce the stator magnetic saturation, and the rated DC currents for the machines are all in this range. Since the 13-rotor pole machine has small flux-leakage, the influence of

excited rated DC current is significant. The influence of the DC current is shown in Fig. 2.23. From Fig. 2.23, it shows that for 7/8/10/11 rotor pole machines, when the current is less than 5A, the DC current is applied to reduce the stator magnetic saturation caused by PMs. For all the machines, the magnitudes of back-EMF can achieve the maximum value at the DC excitation of around 16A. Then the machines become saturated again due to the DC current over-excitation. The magnitude of 13-rotor pole machine remains less than those of other machines with the increasing DC current, and hence, the electromagnetic torque for the machine might be lower than those of other machines.

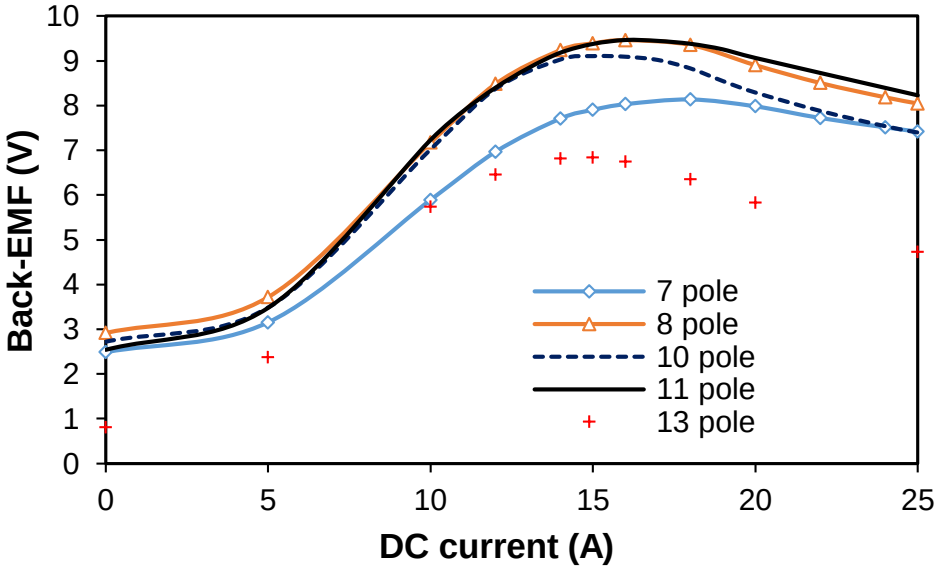

Fig. 2.23 Open-circuit phase A back-EMF fundamental harmonic against DC excitation current for F1A3 HSSPM machines.

2.7.4. Electromagnetic torque

According to Fig. 2.24, it shows that the F1A3 HSSPMMs with different numbers of rotor poles can achieve the maximum average electromagnetic torque when the current angle is 0. Thus, the machines have negligible reluctance torque. Fig. 2.25 shows the electromagnetic torque performance for the machines with different numbers of rotor poles. As the cogging torque waveforms, the odd rotor pole machines have small torque ripple and the even rotor pole machines have large torque ripple since the even rotor pole machines have dominant 3rd order harmonic. The 8- and 10-rotor pole machines have larger average torque compared with other machines, while the 13-rotor pole machine has the lowest average torque. The average torque, torque ripple for different rotor poles are displayed in Table 2.5. The torque ripple

(T_{ripple}) can be calculated by the percentage of dividing the difference of maximum electromagnetic torque (T_{max}) and minimum electromagnetic torque (T_{min}) with the average torque (T_{ave}). According to Table 2.5, it shows that the 11 rotor pole machine has the lowest torque ripple and the 10-rotor pole machine has the highest torque ripple. The 8-rotor pole machine has the highest average torque. While the 13 rotor pole machine has the lowest average torque which is more than half lower than that of the 8-rotor pole machine.

The average torque against copper loss in Fig. 2.26(a) shows that the machines except 13 rotor pole machine have increased significantly when the copper loss is less than 5W. The 8- and 10-rotor pole machines have almost similar electromagnetic torque with the increasing copper loss and remain larger than other machines. The torque difference becomes significant for the 7- and 11- rotor pole machines compared with 8- and 10-rotor pole machines when the copper loss is larger than 20W. In addition, the difference of electromagnetic torque becomes large between 7- and 11 rotor pole machines when the copper loss is higher than 40W. After 40W, the 7 rotor pole machine has lower average torque than the 11 rotor pole machine. The torque of the 13 rotor pole machine remains low with the increasing copper loss. Fig. 2.26(b) exhibited that the machines with odd rotor pole number will have less torque ripple than those with even rotor pole number. For the 8- and 10-rotor pole machines, the peak torque ripple will be achieved at 20W copper loss and then reduced significantly. The torque ripple for 7- and 13-rotor pole machine is reduced with the increasing copper loss, and when the total copper loss is 120W, the 7-rotor pole machine has the lowest toque ripple.

Table 2.5 Torque performance for the F1A3 HSSPMMs with different numbers of rotor poles @ copper loss of 60W

	7 pole	8 pole	10 pole	11 pole	13 pole
$T_{ave,}$ Nm	0.697	0.951	0.949	0.760	0.424
T_{max}, Nm	0.729	1.092	1.093	0.787	0.456
T_{min} Nm	0.666	0.823	0.827	0.734	0.393
T_{ripple}, %	9.02	28.27	27.96	6.97	14.73

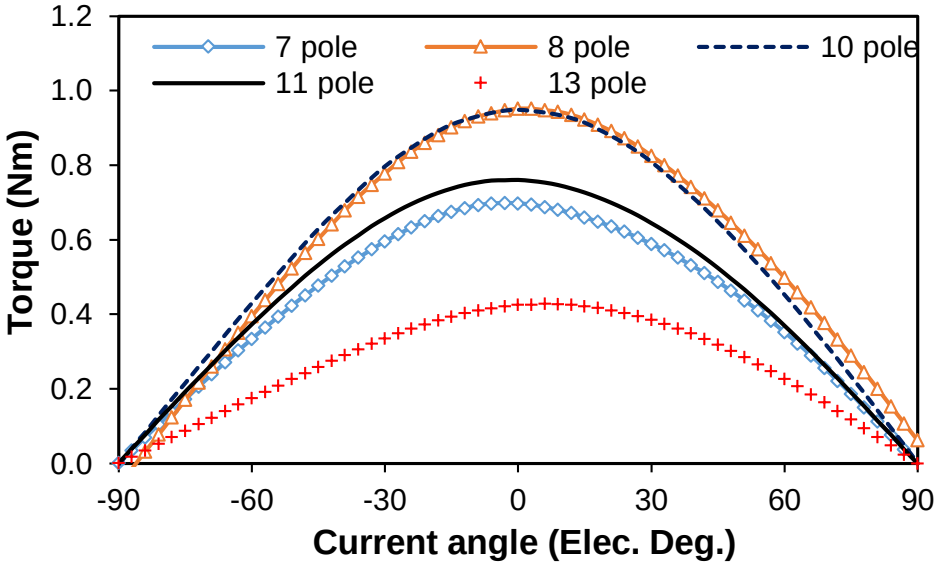

Fig. 2.24 Electromagnetic torque against current angle for F1A3-HSSPMMs with different numbers of rotor poles (total P_{Cu} = 60W).

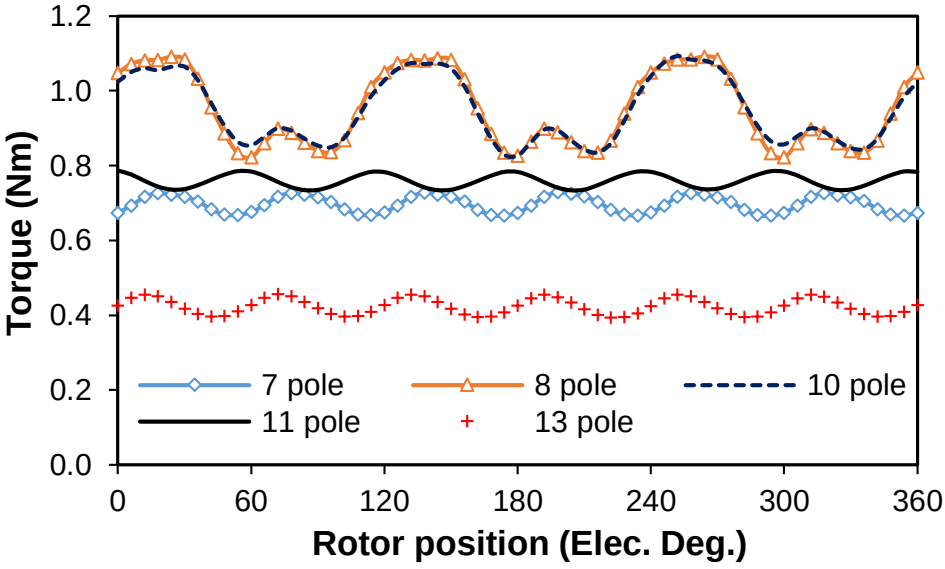

(a) Electromagnetic torque waveforms

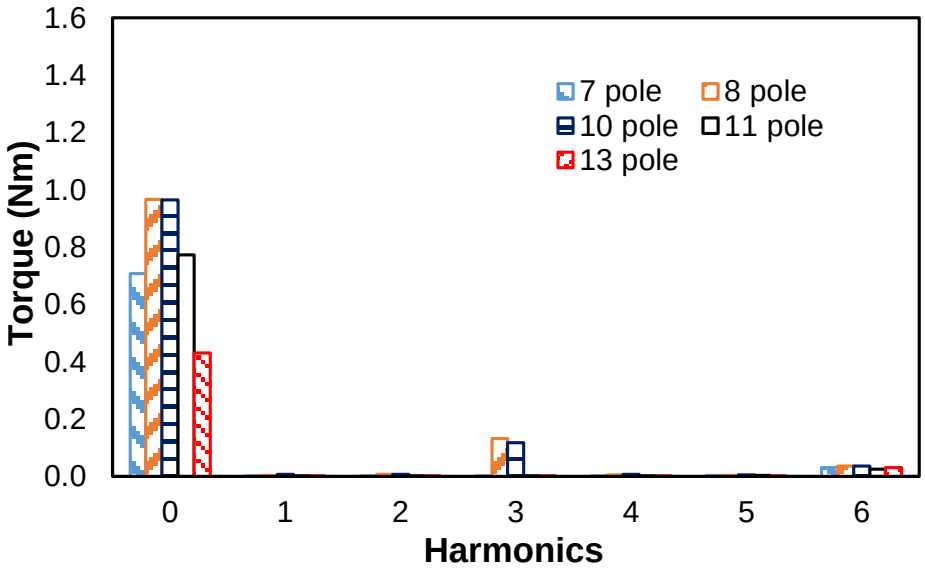

(b) Harmonics

Fig. 2.25 Electromagnetic torque for F1A3 HSSPMMs with different rotor poles.

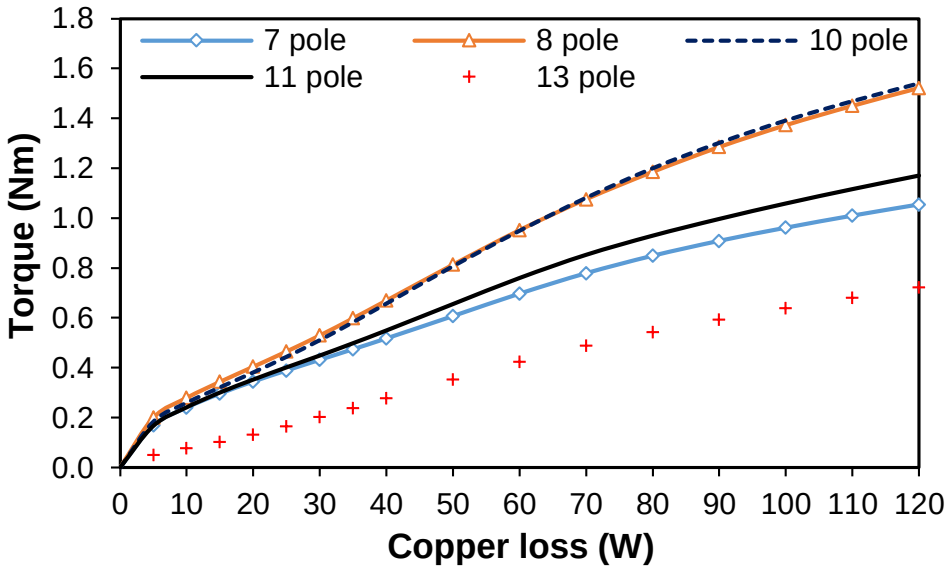

(a) Torque against copper loss

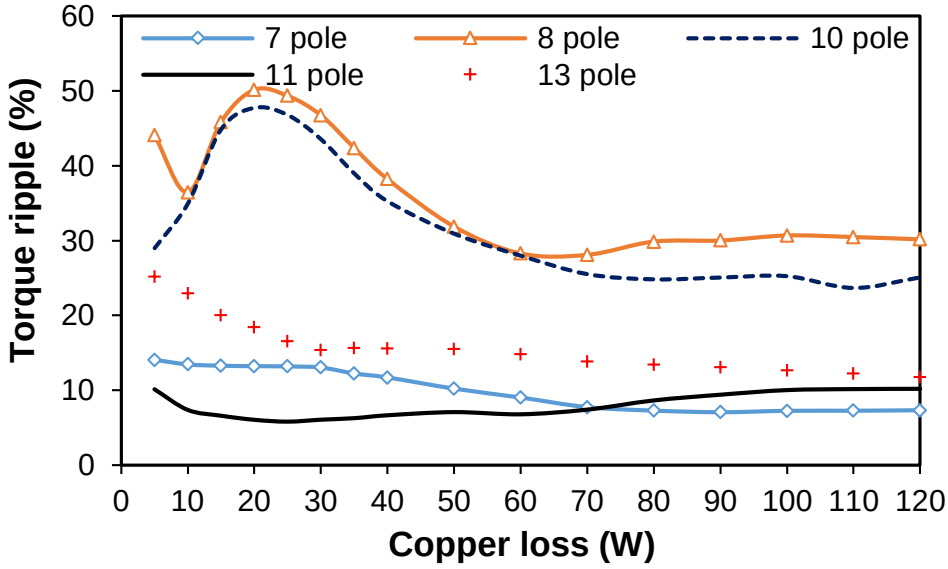

(b) Torque ripple against copper loss

Fig. 2.26 Variation of average torque and torque ripple against copper loss for F1A3-HSSPM machines.

2.8. Conclusion

In this chapter, a new type of F1A3 HSSPM machine has been introduced and compared with an existing F1A1 HSSPM machine at both open-circuit and on-load conditions. It shows that the F1A3 HSSPMM has almost 50% higher average electromagnetic torque than the F1A1 HSSPMM, albeit with higher torque ripple. The losses in the F1A3 HSSPMMs are much higher than those in the F1A1 HSSPMM at high rotor speed and high load. Also, the F1A3 machine has less magnetic saturation at higher DC excitation current. The F1A3 HSSPMMs with different rotor poles are designed and investigated. It is worth mentioning that the F1A3 HSSPMMs have a drawback of large flux-leakage which can cause large flux-linkage, back-EMF and cogging torque when the machines have no current excitation.

Chapter 3 Stator Hybrid-excited F3A2 Machine with Permanent Magnets Located on Slot Opening

3.1. Introduction

In Chapter 2, the F1A1 and F1A3 hybrid stator slot permanent magnet (HSSPM) machines were investigated and the electromagnetic performance were compared. The F1A3 HSSPM machine is a new topology of stator hybrid-excited double salient machine which places the PM in the slot opening area of DC slot of a F1A3 wound field synchronous machines (WFSM) to enhance the torque density. The field windings provide an additional degree of freedom to adjust the excitation flux in air-gap to improve the flux regulation capability of the machine by field weakening/strengthening, and the machine efficiency is improved by optimizing the field-armature flux ratio [111, 112]. Some hybrid machines are proposed based on the variable flux machine (VFM) and wound field synchronous machines (WFSM), and the PMs are located on the slot opening area [92, 93 and 110]. This type of hybrid stator slot opening PM machines (HSSPMMs) has higher torque density than WFSMs with good flux regulation capability due to parallel PM and field excitation. The working principle for HSSPMMs shows in [92] is revealed based on the stator slot opening PM machine [85]. Hybrid excited machines can be classified into parallel and series excitation machine topologies [113, 114], while the PM and field excitations can be both on stator or rotor, or separated onto stator and rotor, respectively [114-116]. When the PM and field excitations are both on stator, the machines have the structure of robust rotor without brushes and slip rings, which are similar to the stator PM machines [95, 96, 99, 101, and 102]. Most of the machines are directly modified from the switched flux PM machines (SFPMMs) [96, 99], thus can be called hybrid SFPMMs (HSFPMMS). In comparison with SFPMMs, the PM slots or locations of HSFPMMs are slightly modified by: (a) replacing a part of PMs with field windings [96, 99]; (b) by placing field windings on stator back-iron [101, 102]. However, the effectiveness of field excitation is limited by high PM reluctance for the type (a) machine, while the type (b) machine may cause a part of PM flux shunted in the stator back iron. In addition, a few other types of HSFPMMs are designed and investigated with the same PM volume of the SFPMMs, e.g. field windings in the same stator slots with armature windings [95] and E-core HSFPMMs [130] in which the field windings are wound around the redundant teeth of an E-core machine [43].

In this chapter, a new type of HSSPMM is designed and investigated. The chapter can be briefly summarized as:

- Machine structure and basic operation principle of the HSSPMM
- Investigations of different stator /rotor pole combinations
- Machine optimization and electromagnetic performance comparison with different stator/rotor pole combinations, i.e. open-circuit flux-linkage, back-EMF, cogging torque, on-load torque density and unbalance magnetic force.

3.2. Machine structure and operation principle

The new type of HSSPMMs, Fig. 3.1 (c), is based on the F3A2 WFSM which has a coil over three slot pitches for the field winding (F3) and a coil over two slot pitches for the armature windings (A2), as shown in Fig. 3.1 (a). The PMs are located in the slot openings of the field winding slots of the F3A2 WFSM machine, which is similar to that in [110]. The F3A2 HSSPM machine can also be derived from the E-core SFPMMs, Fig. 3.1 (b), of which the PMs are partly replaced by field windings. While the E-core SFPM machine has removed half of the PMs comparing with the conventional SFPM machine and allocated the PM alternatively to divide the stator as "E-shaped" laminated segments. The coils of the E-core SFPM machine are wound on the stator tooth with PM insert [43]. For the F3A2 HSSPM machine, the PMs and field windings are placed in the same slot, the optimization to distribute the armature, field winding and PM areas is difficult. Thus, for simplicity, the PM volume of the machine is fixed, and the field current density to armature current density ratio needs to be considered as a variable parameter during the optimization, which will be described in detail in section 3.3.

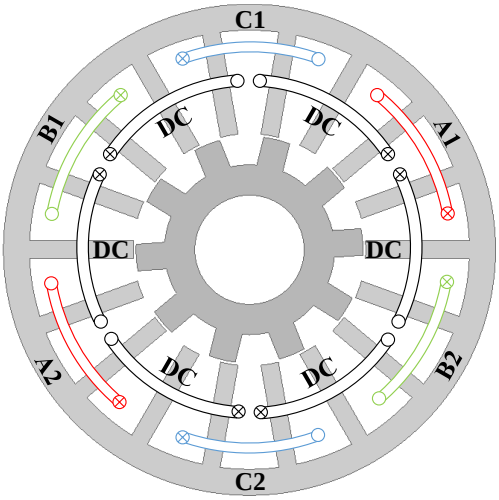

(a) F3A2 WFSM

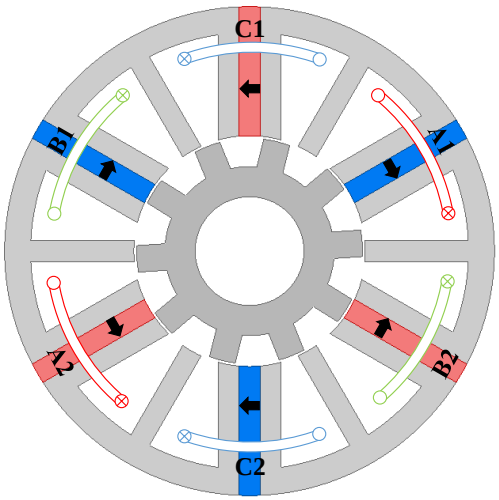

(b) E-core SFPMM

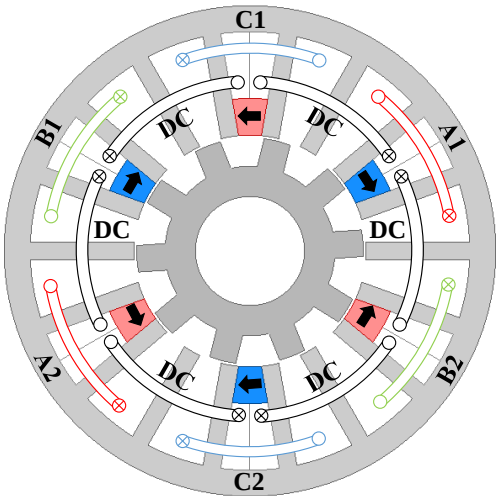

(c) F3A2 HSSPMMs

Fig. 3.1 Cross section of wound field machine, E-core SFPM machine and F3A2 HSSPM machine.

Fig. 3.2 shows the flux path at open circuit condition for the 11-rotor-pole F3A2 HSSPM machine. When no DC current excited in the machine, the flux path generated by PMs is mainly short-circuited in the stator area, only few path to the rotor via the air gap, as shown in Fig. 3.2 (a). Hence, the open-circuit performance of the machine without field excitation will be low. The short circuit path of PM flux is still available with field excitation when the DC current is not over-excited. The flux produced by DC current has opposite direction from the short-circuit PM flux. When the DC current achieves the over-excited value, Fig. 3.2 (c), the machine has no short circuit PM flux. Thus, the main effect of field excitation in this machine is to push the PM flux to the machine rotor via air gap, which will definitely increase the machine performance.

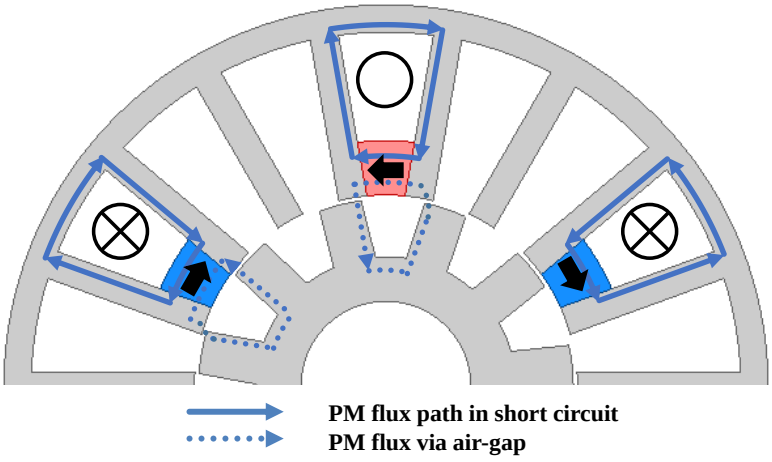

(a)

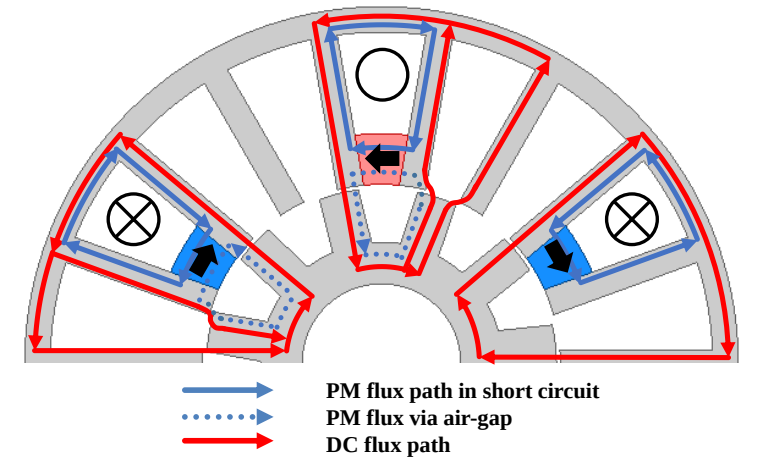

(b)

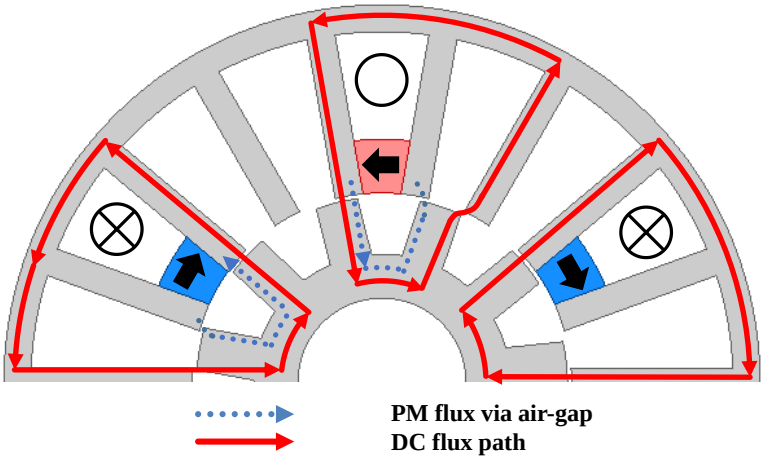

(c)

Fig. 3.2 DC and PM flux paths in half machine models at open-circuit for 11-rotor-pole F3A1 HSSPMMs. (a) I_{dc} = 0A. (b) 9A > I_{dc} > 0A. (c) I_{dc} = 9A (machine is over-excited).

Besides, the structure of the machine and the dual source excitation of the machine will cause the machine magnetically saturated with the increasing DC current. The influence of the DC current for F3A2 HSSPMMs with different numbers of rotor poles is shown in Fig. 3.3. This figure shows the variable fundamental harmonic of phase back-EMF with the raising DC current. It shows that when the DC currents are around 9A and 10A with both the armature and field turns per coil at 92, the magnitude of the phase back-EMF values achieve the peak value and then reduced. That means the machine can be over-excited when the DC current is 9-10A due to magnetic saturation.

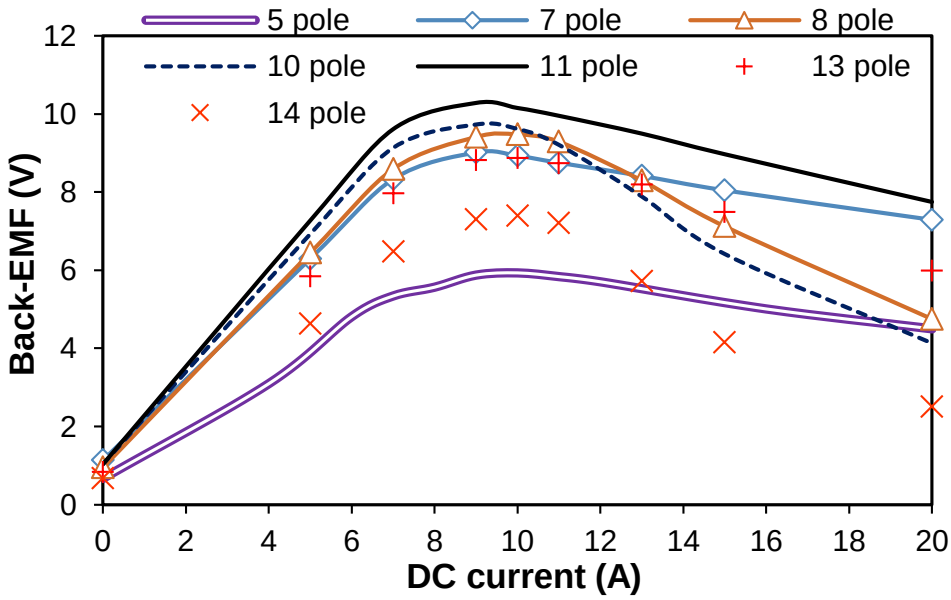

(a) Magnitude of back-EMF

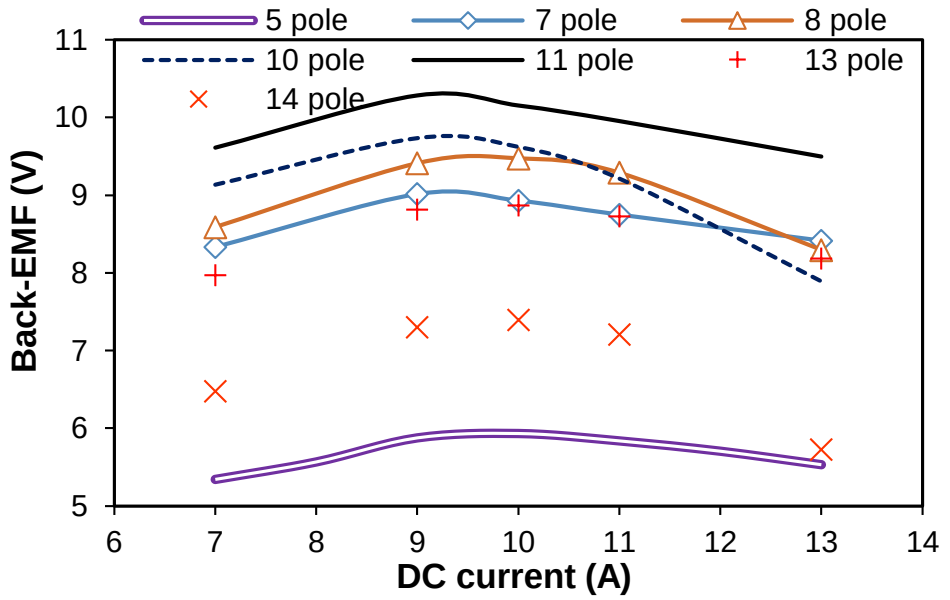

(b) Zoom in

Fig. 3.3 Open-circuit phase A back-EMF fundamental harmonic vs. DC current for different numbers of rotor poles

The flux distribution for the 11-rotor pole machine at open-circuit, Fig. 3.4, shows that when the magnitude of the phase back-EMF achieves the peak value, the machine has no short-circuit PM flux. In that case, the flux density of the machine shows the stator teeth ‘a’ and ‘b’ and the stator back iron ‘c’ is saturated. Meanwhile, the PM is demagnetized at the corners close to the air-gap, and some corners of stator and rotor teeth have high flux density because of the fringing flux.

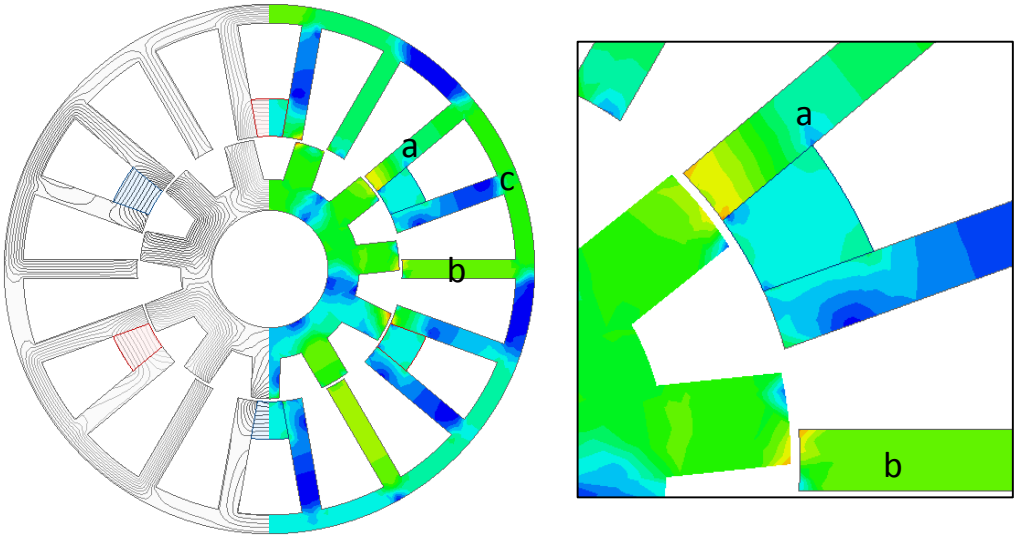

Fig. 3.4 Open-circuit flux density and flux distributions of the 11-rotor pole machine.

3.3. Stator-rotor pole combinations

3.3.1. Feasible stator and rotor pole combinations

Since the F3A2 HSSPM machines can be derived from the E-core SFPM machines, the combinations of stator/rotor pole for the two types of machines can be assumed to be similar. Thus, the feasible stator and rotor pole combinations of an N_{ph} phase F3A2 HSSPM machine are [43]:

$$N_s = k_1 N_{ph}, k_1 = 1,2, \ldots \tag{3.1}$$

$$N_r = 2N_s \pm k_2, k_2 = 1,2, \ldots \tag{3.2}$$

where N_s and N_r are the numbers of stator and rotor poles respectively, k_1 and k_2 are the integers while the number of stator poles must be even. In order to simplify the analysis in this chapter, the phase number is restricted to three and the stator pole number is 6, and according to (3.1) the rotor poles of the machines are chosen to be 5, 7, 8, 10, 11, 13, and 14.

3.3.2. Winding analysis

According to [43], the method to determine the coil EMF phasor for switched flux permanent magnet (SFPM) machine is displayed in detail. The HSSPM machine can be analysed by using the same method as well. From [43], the electrical degree between two adjacent coil back-

EMFs (α_e) can be obtained by multiplying the rotor pole number (N_r) and the mechanical degree between adjacent coils (α_m). For the F3A2 HSSPM machines with different numbers of rotor poles, the coil distributions are shown in Fig. 3.5. Assuming the coil EMF phasor for coil 1 has the positive direction, for coils 2, 4 and 6 which cover the magnets with opposite magnetization direction, the directions of coil EMF phasors will be opposite and indicated with an (’). The coil connections for different rotor pole machines are shown in Fig. 3.5 respectively, and the coils are grouped to form the phases.

The fundamental coil back-EMF phasors for the three phase HSSPM machines with 6-5/7/8/10/11/13/14 stator/rotor poles F3A2 HSSPMMs are shown in Fig. 3.6. The machine coil back-EMF phasors have one set of balanced three phase windings with 0 electrical degree phase shift.

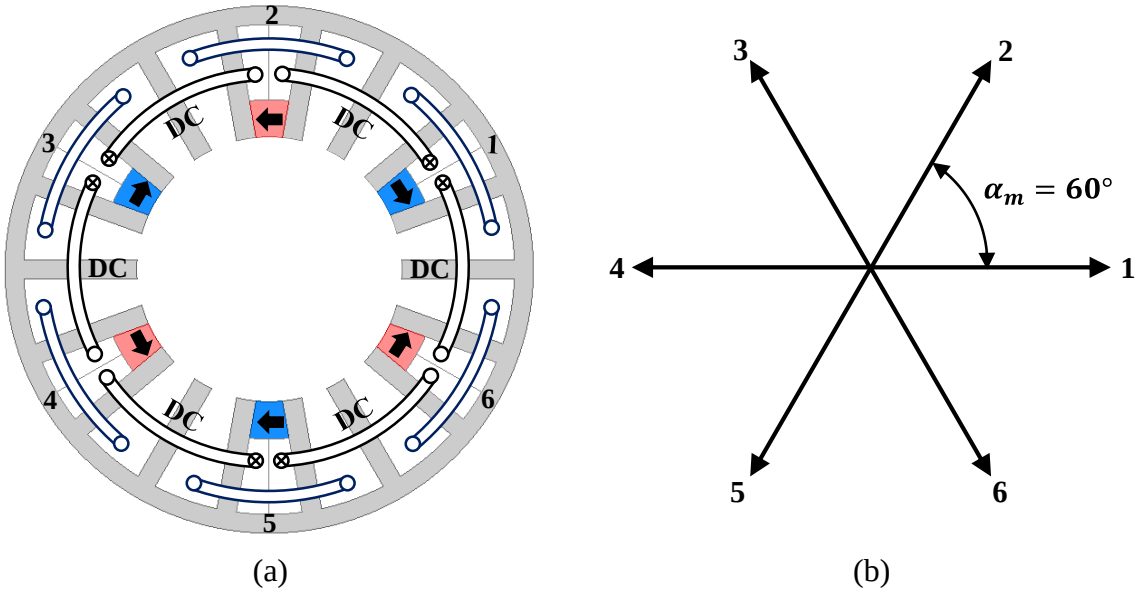

(a) (b)

Fig. 3.5 Stator for F3A2 HSSPM machine. (a) Schematic of stator armature coil position in mechanical degree for the machines. (b) Coil distribution in mechanical degree.

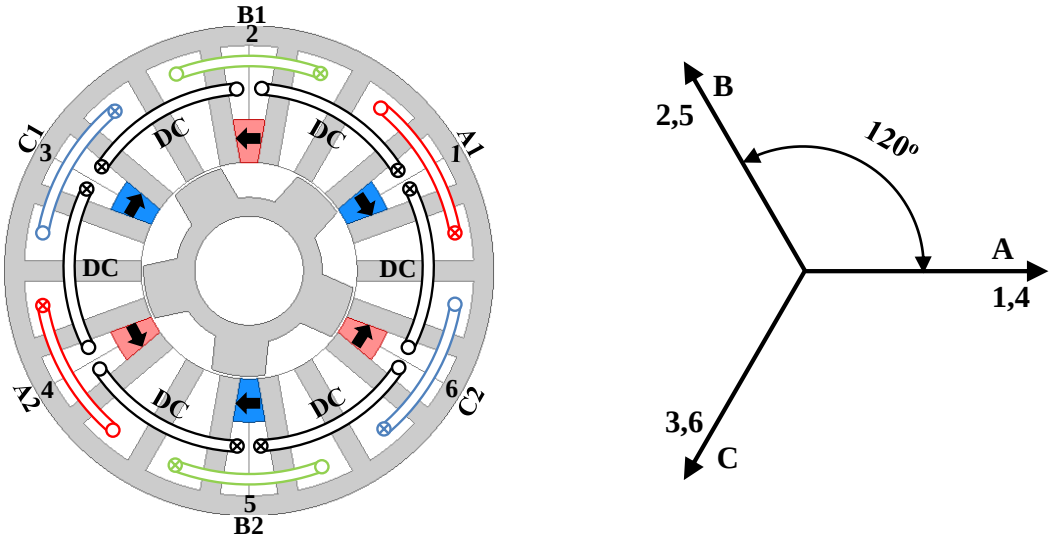

(a) 5 pole

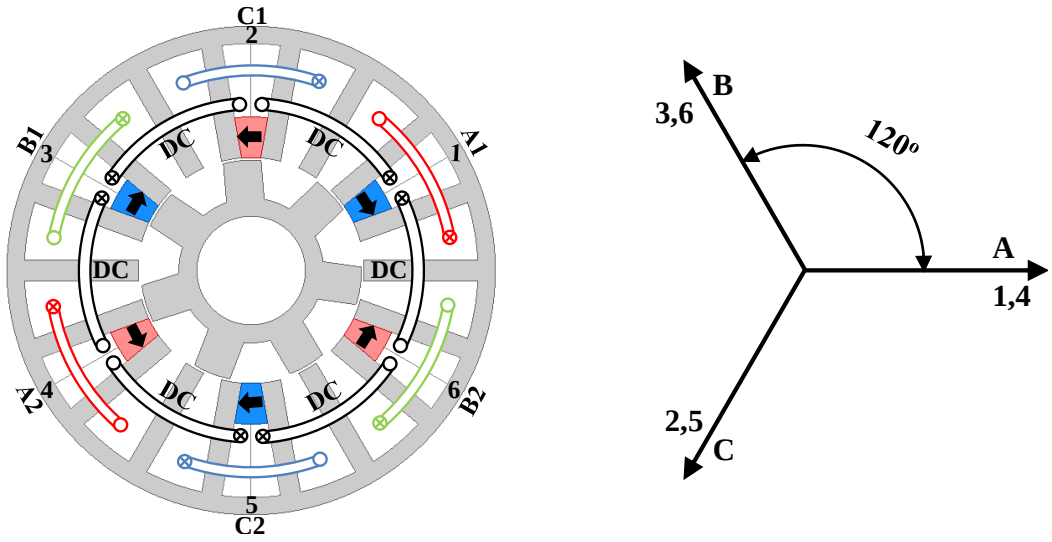

(b) 7 pole

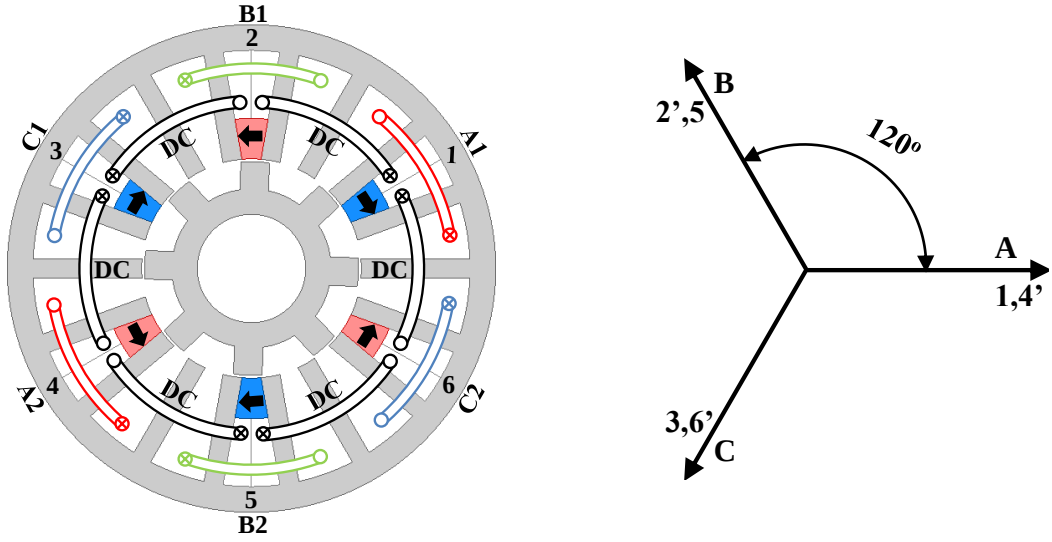

(c) 8 pole

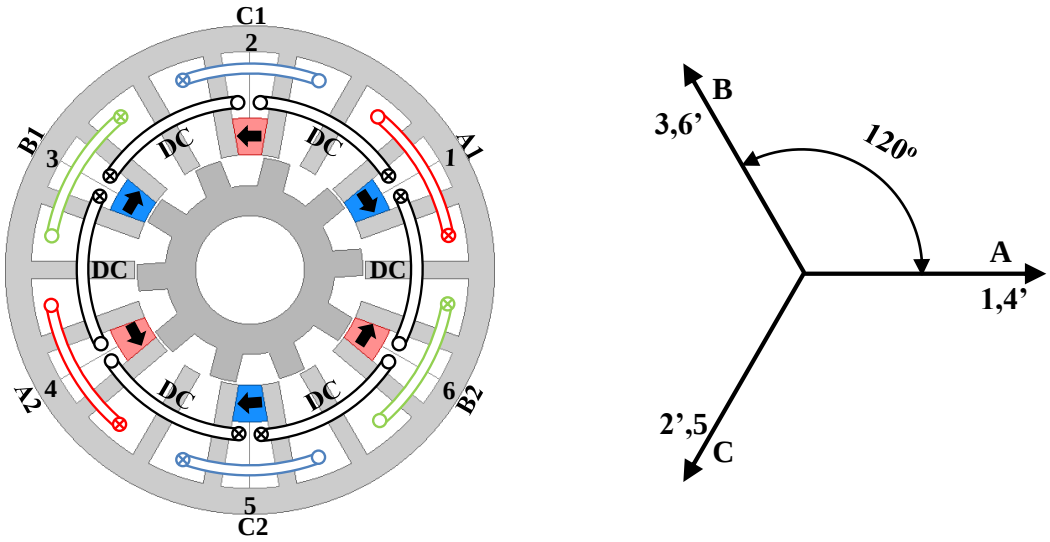

(d) 10 pole

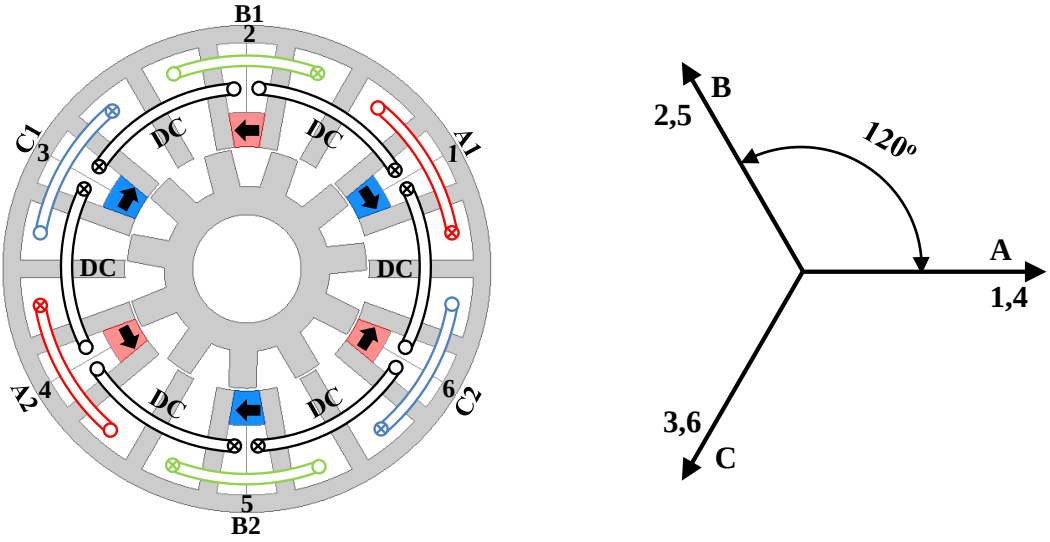

(e) 11 pole

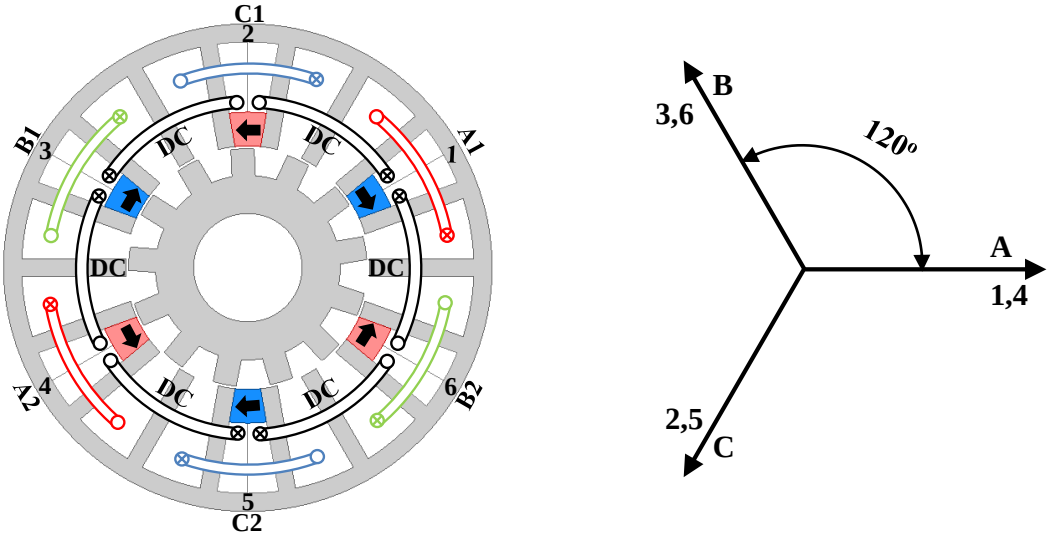

(f) 13 pole

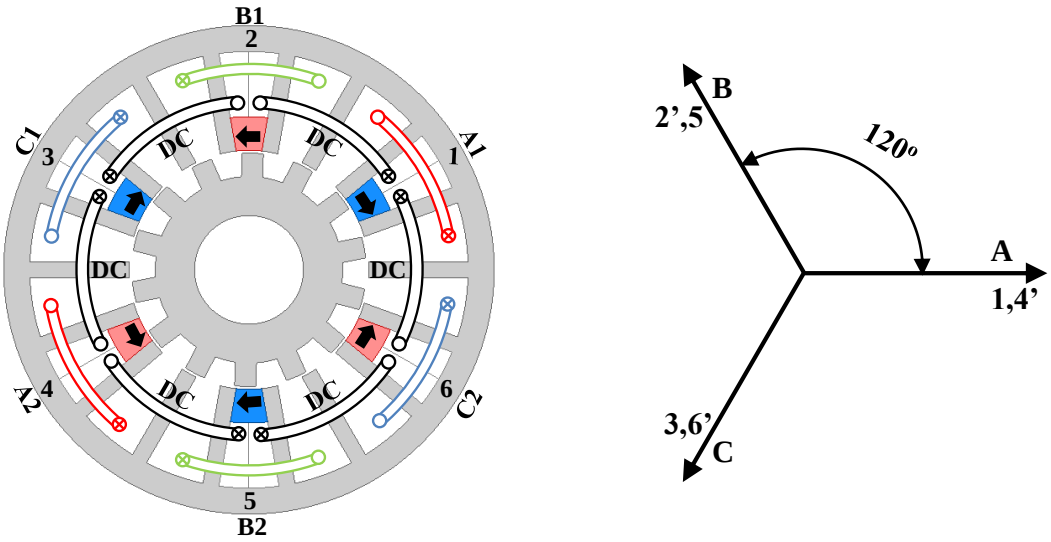

(g) 14 pole

Fig. 3.6 Winding connections and fundamental back-EMF phasors for F3A2 HSSPMMs with different numbers of rotor poles and the cross-sections.

The F3A2 machine has one middle teeth between two permanent magnets but with no magnets or coils on that, which is quite similar to the E-core SFPM machine [43]. However, for the E-core SFPM machine, because of the middle teeth, the winding factors of this machine for different numbers of rotor poles are difficult to define, as for some stator/rotor pole combinations, the electromagnetic torque density achieves the maximum value when the teeth are removed [43]. Thus, the full machine cross section needs to be modelled in 2D finite element analysis (FEA) to analyse the electromagnetic performance of the machines.

3.4. Electromagnetic performance comparison

3.4.1. Design optimization

The F3A2 HSSPM machines are optimized and investigated by using 2D FE method. The machine performance with different numbers of rotor poles are investigated and compared. Genetic algorithm is used to obtain the global optimization of the 5-, 7-, 8-. 10-. 11-. 13-, and 14-rotor pole machines aiming to achieve maximum average electromagnetic torque. To make a fair comparison, some critical parameters need to be fixed during optimization, such as: (a) total copper loss (60W), (b) stator outer radius (R_{SO}), (c) air-gap length (G), (d) stack length (l_{stack}), (e) number of turns per phase for armature/field winding, and (f) PM usage. Besides, the F3A2 HSSPM machines are optimized based on the F1A1 DL-HSSPM machine [92], the number of turns per phase for F1A1 machine is 184 for armature windings, and the F1A1 machine have four coils per phase, while the F3A2 machine have two coils per phase which means the machine has 92 turns per coil. The F3A2 HSSPM machines should be optimized with fixed PM volume for the machine having field winding and PM in one slot. The PM volume of the machines is similar to that in F1A1 DL-HSSPM machines. The restrictions for optimization are shown in Table 3.1, and the geometric parameters are shown in Fig 3.7.

To obtain the global optimization, the parameters to be optimized and the optimized geometric parameters are listed in Table 3.2.

Table 3.1 Restriction for optimization of the 6-stator pole F3A2 HSSPM machines

Parameters	**Unit**	**6-5/7/8/10/11/13/14**
Stator outer radius (R_{SO})	mm	45
Stack length (l_{stack})	mm	25
Air-gap length (G)	mm	0.5
Shaft radius (R_{Rshaft})	mm	10
Copper loss (P_{Cu})	W	60
PM volume (V_{PM})	mm^2	5403.8
Packing factor (k_p)		0.59
PM N38SH at 20 °C (Br/μ_r)		1.2T/1.05
Turns/coil (armature) (N_a)		92
Turns/coil (field) (N_f)		92
Total number of turns (armature)		552
Total number of turns for (field)		552
Rated speed	rpm	400

Table 3.2 Optimized F3A2 HSSPM machines optimized geometric parameters.

Parameters	**Unit**	**Rotor pole number**						
		5	**7**	**8**	**10**	**11**	**13**	**14**
Back-iron thickness (H_{BI})	mm	3.67	3.21	4.74	4.77	3.22	3.35	4.79
Stator pole arc (θ_{st})	Mech. Deg.	10.85	10.33	10.06	8.79	8.56	8.03	7.74
Stator tooth width (w_{st})	mm	3.76	3.75	3.55	3.26	3.37	3.15	2.97
Rotor pole arc (θ_{rt})	Mech. Deg.	29.37	19.75	15.33	13.55	13.17	11.26	10.40
Rotor tooth thickness (H_{Rt})	mm	6.24	7.16	5.11	5.25	6.86	4.97	4.34
Split ratio		0.43	0.45	0.44	0.46	0.49	0.49	0.48
PM thickness (H_{PM})	mm	7.901	7.469	7.474	6.75	6.41	6.23	6.22
Stator inner radius (R_{SI})	mm	19.89	20.82	20.23	21.25	22.56	22.46	22.00
Ratio of field to armature slot current density (J_{ratio})		1.042	1.022	1.032	0.935	0.904	0.874	0.667
Total armature slot area (S_a)	mm^3	1781	1806	1685	1701	1813	1851	1723
Total field slot area (S_f)	mm^3	674	687	626	634	691	709	645

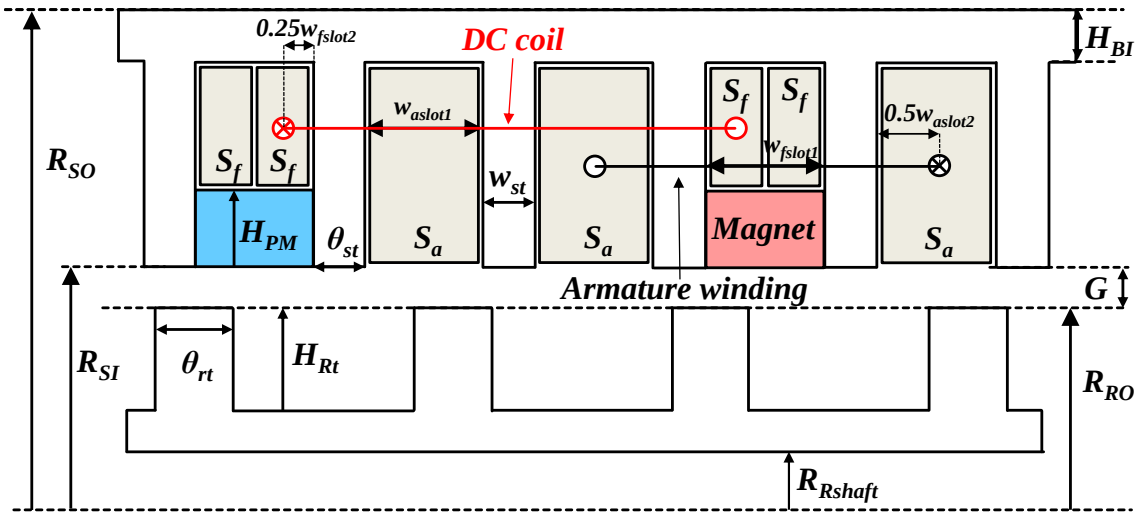

Fig. 3.7 Illustration of stator and rotor geometric parameters.

The optimization is implemented at a fixed rotor speed of 400 rpm. During the optimization, the copper loss of the machines is fixed. To reduce the quantity of parameters which needs to be optimized, the stator slots for the machines are equal. However, due to the PMs located in the slot opening area, the slot areas for armature winding (S_a) and field windings (S_f) are different and both slot areas are variable during optimization. In addition, the excited armature current and field current for the machines are different and variable during the optimization. Hence, the current densities in the equation (3.4) are employed to calculate the copper loss. The armature and field current densities are indeterminate, for that reason, the ratio of field to armature slot current density, J_{ratio}, is considered as an optimized parameter. Thus, the currents excited in the armature windings and field windings can be calculated as:

$$P_{Cu} = I_a^2 R_a + I_f^2 R_f \tag{3.3}$$

$$J_a = \frac{I_a N_a}{S_a k_p} \tag{3.4}$$

where J_a is the armature current density, I_a and I_f are the rms armature current and the DC current, respectively, R_a and R_f are the total armature and field winding resistances respectively. The end-winding has been considered in optimization and the coil end shape is assumed to be rectangle, and hence, the total armature and field end-winding lengths, l_{end_a} and l_{end_f}, can be expressed in (3.5) and (3.6), respectively.

$$l_{end\_a} = 2\left(\left((S_{SO} - H_{BI}) + S_{SI}\right)\pi - 6w_{st}\right) \tag{3.5}$$

$$l_{end\_f} = 2((S_{SO} - H_{BI}) + (S_{SI} + H_{PM}))\pi \quad (3.6)$$

Thus, the total armature winding resistance is given in (3.7) and the total field winding resistance is given in (3.8).

$$R_a = \frac{N_a^2 \rho_{Cu}(12 l_{stack} + l_{end\_a})}{S_a k_p} \quad (3.7)$$

$$R_f = \frac{N_f^2 \rho_{Cu}(12 l_{stack} + l_{end\_f})}{S_f k_p} \quad (3.8)$$

where, ρ_{Cu} is the electrical resistivity of copper.

3.4.2. Open circuit flux-linkage and back-EMF

The open-circuit flux linkages investigated for 6-stator pole / 5-, 7-, 8-, 10-, 11-, 13-, and 14-rotor pole F3A2 HSSPM machines are shown in Fig. 3.8. The fundamental phase flux linkages at I_{dc} = 0A are small when compared with the corresponding flux enhanced fundamentals at their rated DC currents, especially for the 13- and 14- rotor pole machines. The fundamental flux linkage for the 14-rotor pole machine has the lowest amplitude and increases slightly when the machine has field excitation. While for the 7-rotor pole machine, the amplitude is the highest. From Fig. 3.8 (b), it shows that the flux-linkage waveforms have a little DC bias, especially for the machine with even rotor poles. That is because of the DC field excitation.

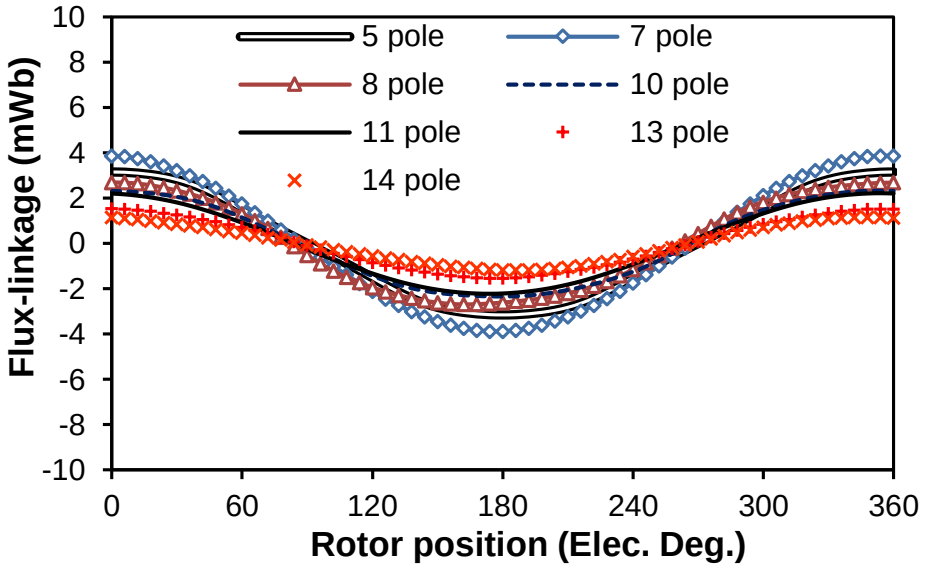

(a) Open-circuit flux linkage waveforms (non-linear stator /rotor material, I_{dc} = 0A)

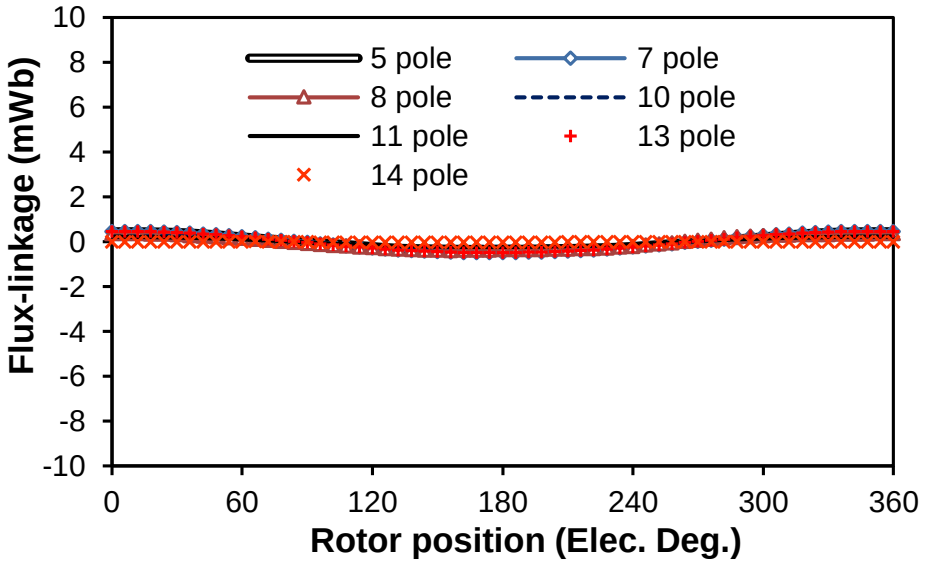

(b) Open-circuit flux linkage waveforms (linear stator /rotor material, I_{dc} = 0A)

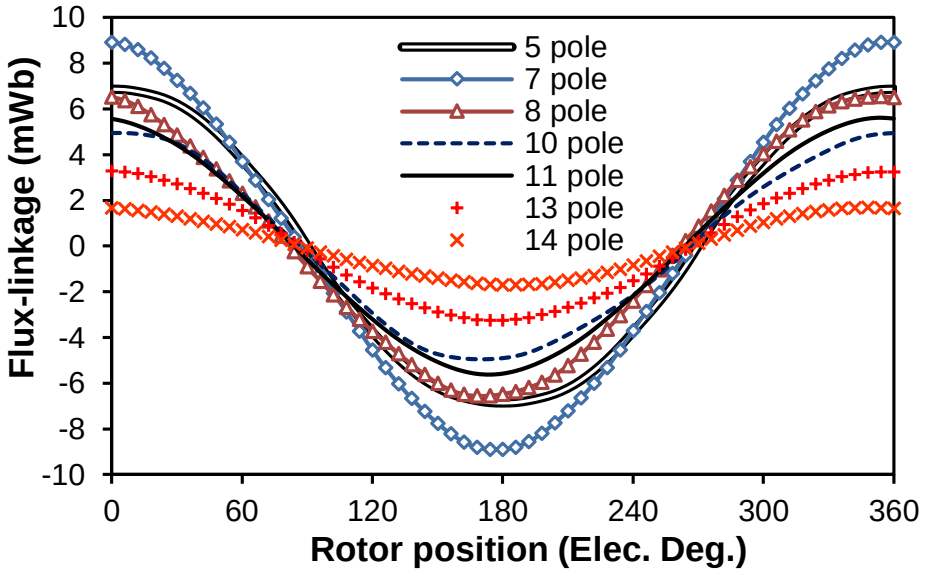

(c) Open-circuit flux linkage waveforms (non-linear stator /rotor material, rated DC current excitation)

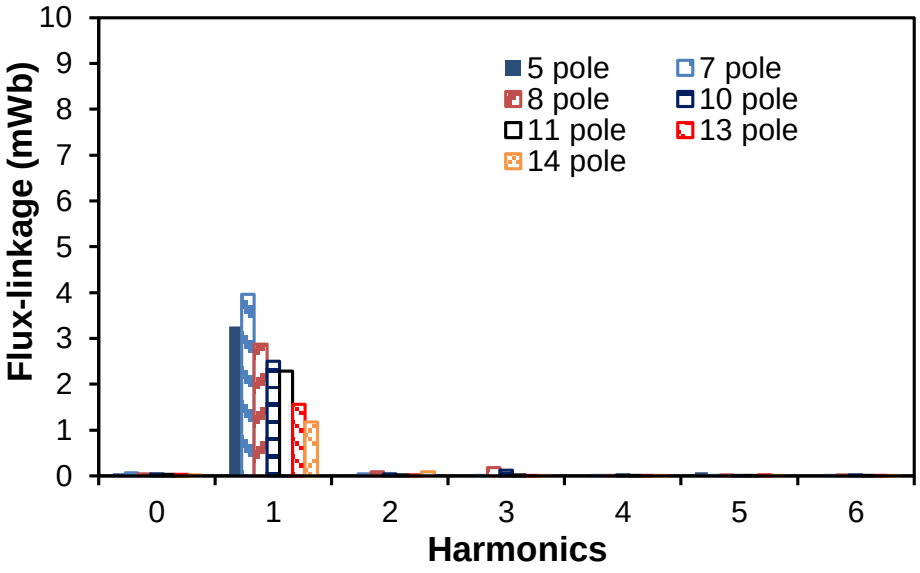

(d) Harmonics (non-linear stator /rotor material, I_{dc} = 0A)

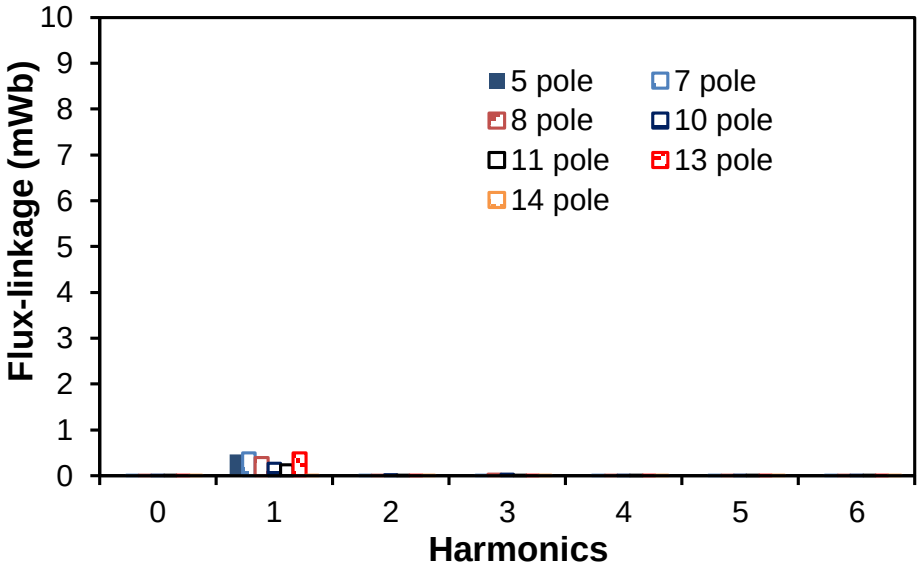

(e) Harmonics (linear stator /rotor material, I_{dc} = 0A)

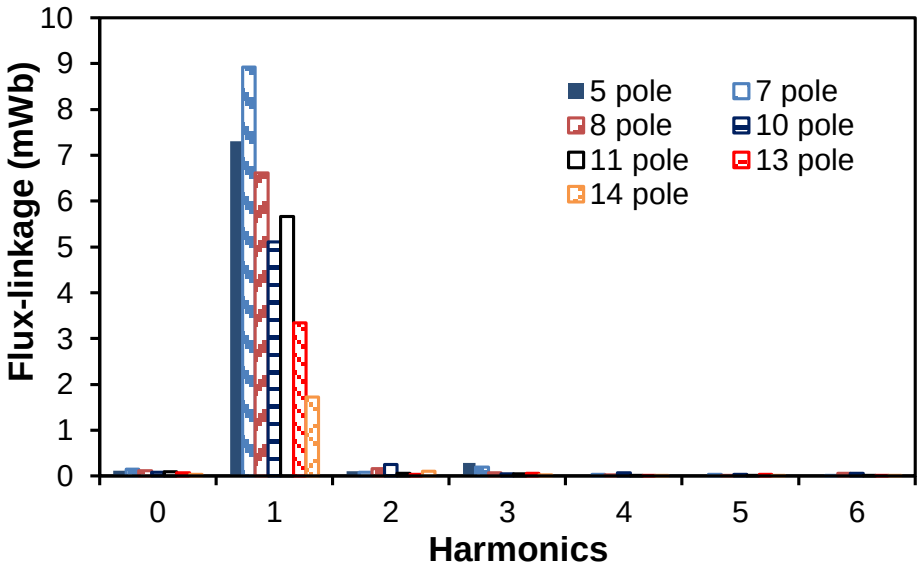

(f) Harmonics (rated DC current excitation)

Fig. 3.8 Open-circuit flux linkage for F3A2 HSSPM machines with different numbers of rotor poles

The PMs employed in the HSSPM machine are used to reduce the magnetic saturation caused by current [92]. From the machine operation principle, when the machine has no current excitation, the flux-linkage waveforms should be almost negligible. However, the PM may make the machine saturated to cause the flux-leakage. This can be proved by the machine flux distribution and flux density with linear or non-linear (laminated silicon steel) rotor and stator material which are shown in Fig. 3.9. The flux density distribution shows that when the excited DC current is 0, the stator teeth adjacent to PM and the corresponding stator yoke are magnetically saturated, and the flux will pass to the rotor via the middle tooth. That will produce the flux-linkage and back-EMF when the machine has no current excitation. When the stator and rotor material is linear material, it shows that the stator teeth and yoke around the PM slot are saturated, however, the middle teeth and rotor have no flux distribution. The amplitude and magnitude of the flux-linkage for the machines, as Fig. 3.8 (b) and (e) shows, are quite small, which proves that when the machines have no current excitation, the flux-linkage is negligible. When adding a DC current, the saturation will be reduced. With the increasing DC current, the machines will become magnetically saturated again and the magnitudes of back-EMF and flux-linkage are reduced due to the over loading DC current, which is proved in Fig. 3.3.

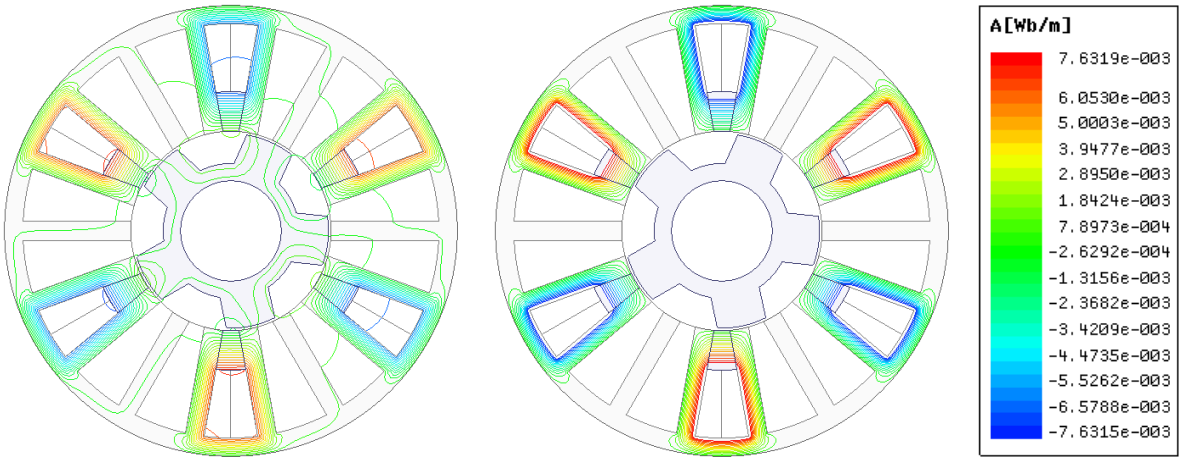

Flux line distribution

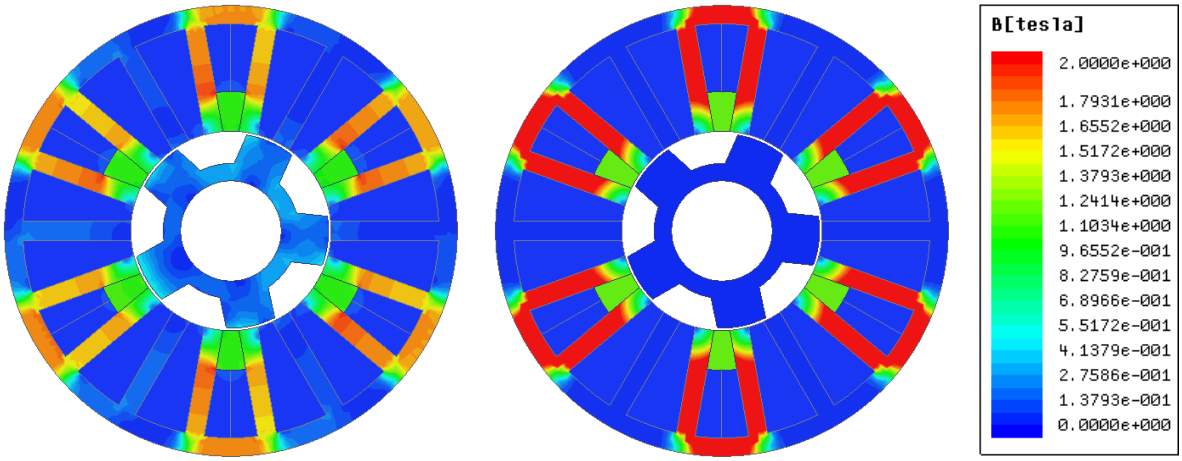

Flux density distribution

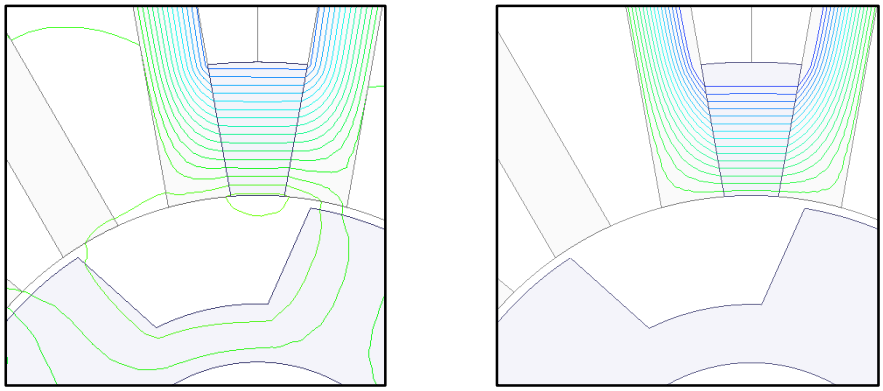

Zoom in

(a) Non-linear stator and rotor material

(b) Linear stator and rotor material

(I) 5 rotor pole

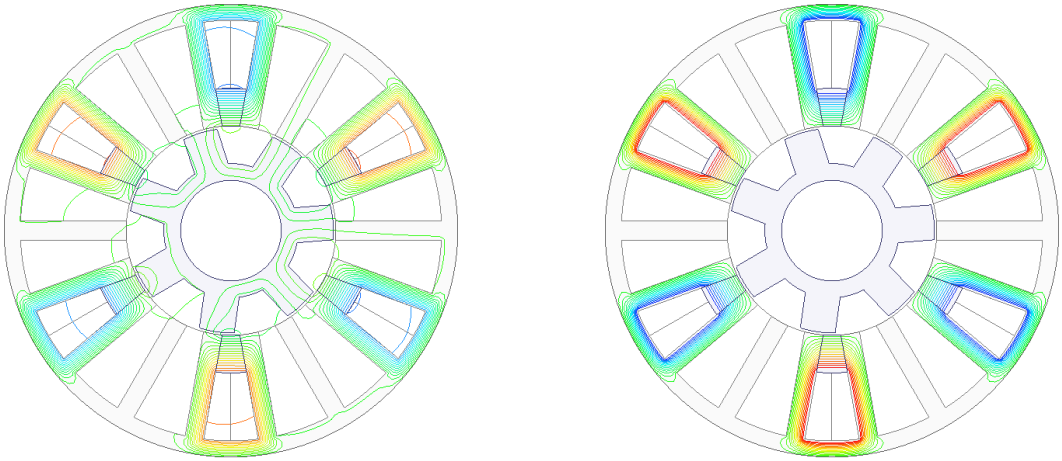

Flux line distribution

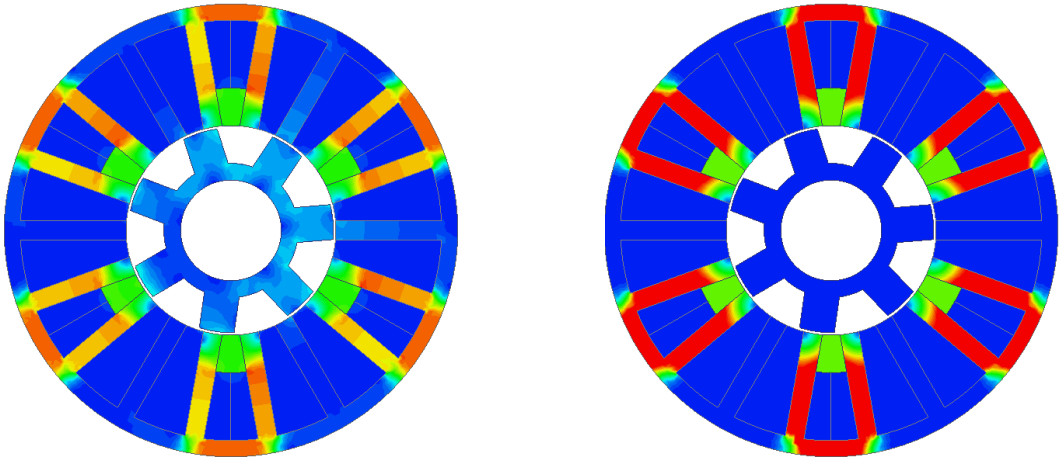

Flux density distribution

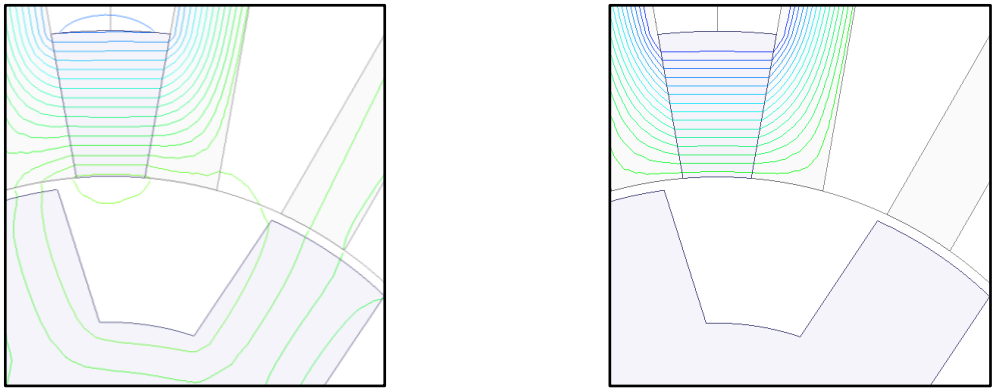

Zoom in

(a) Non-linear stator and rotor material (b) Linear stator and rotor material

(II) 7 rotor pole

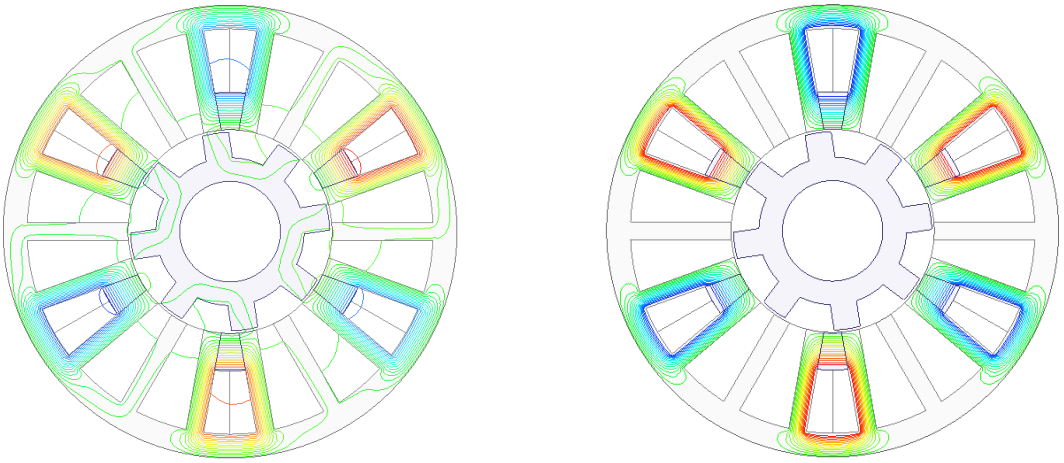

Flux line distribution

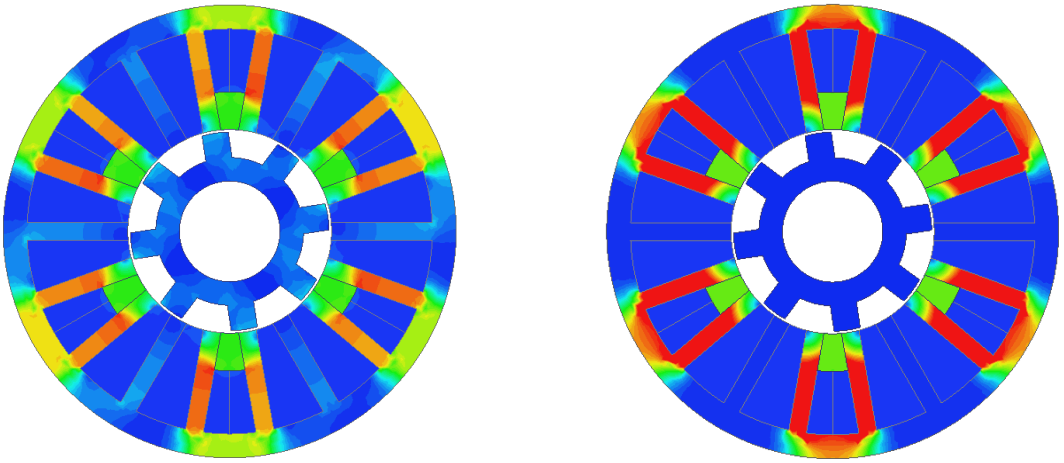

Flux density distribution

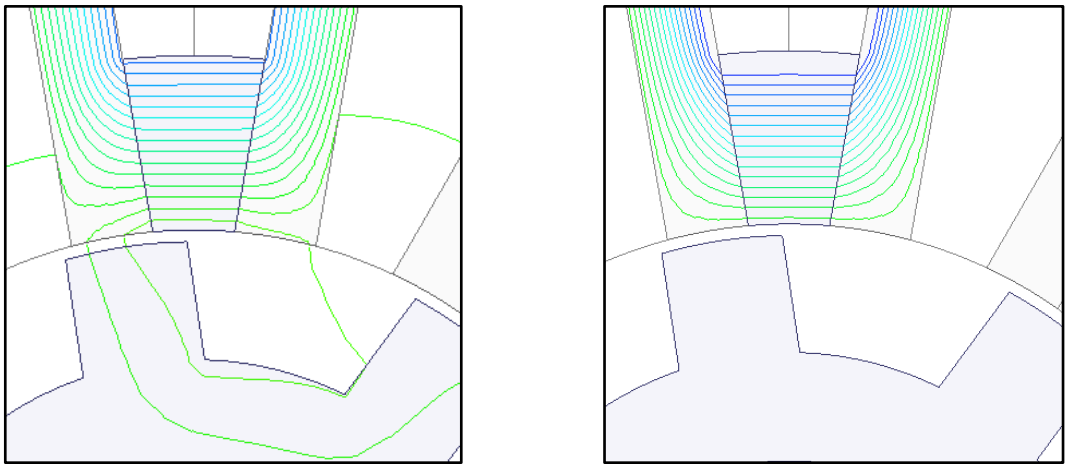

Zoom in

(a) Non-linear stator and rotor material (b) Linear stator and rotor material

(III) 8 rotor pole

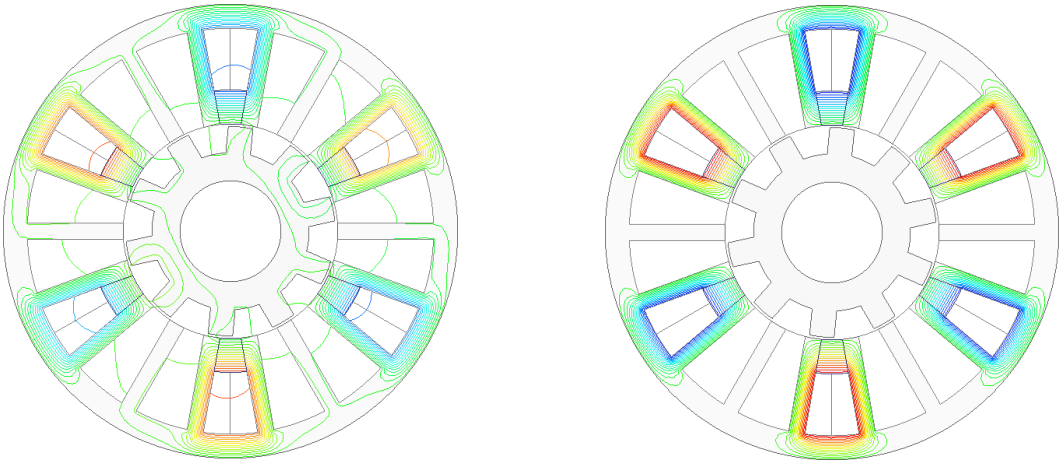

Flux line distribution

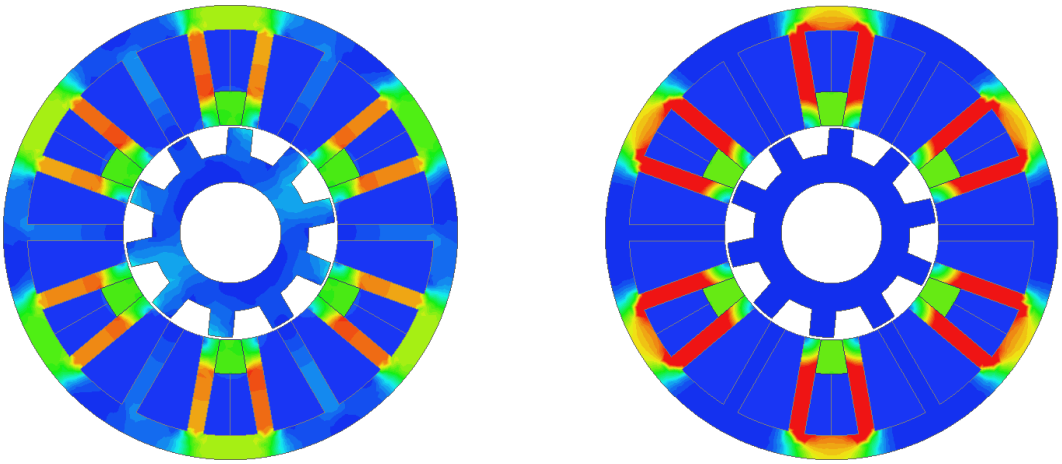

Flux density distribution

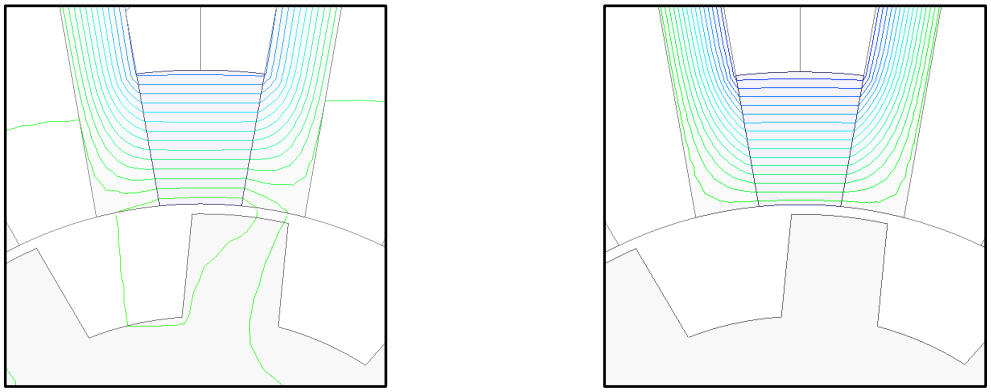

Zoom in

(a) Non-linear stator and rotor material (b) Linear stator and rotor material

(IV) 10 rotor pole

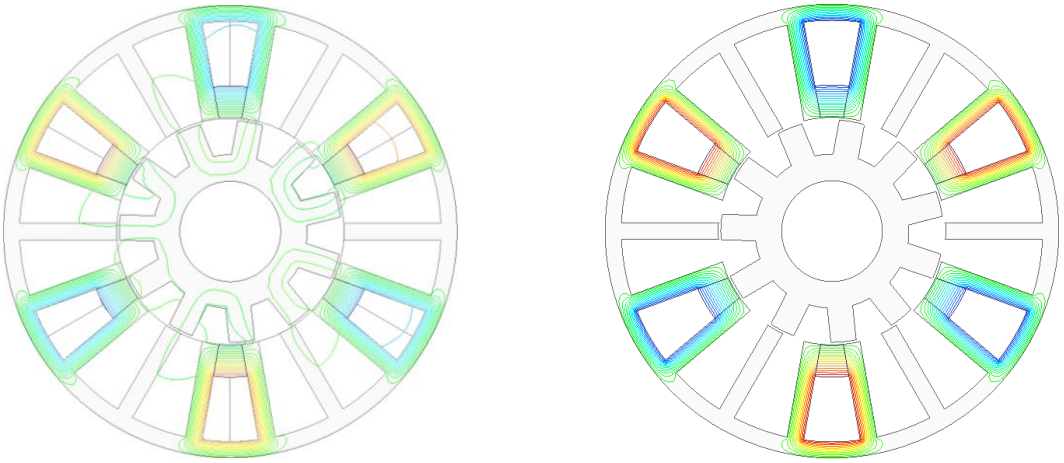

Flux line distribution

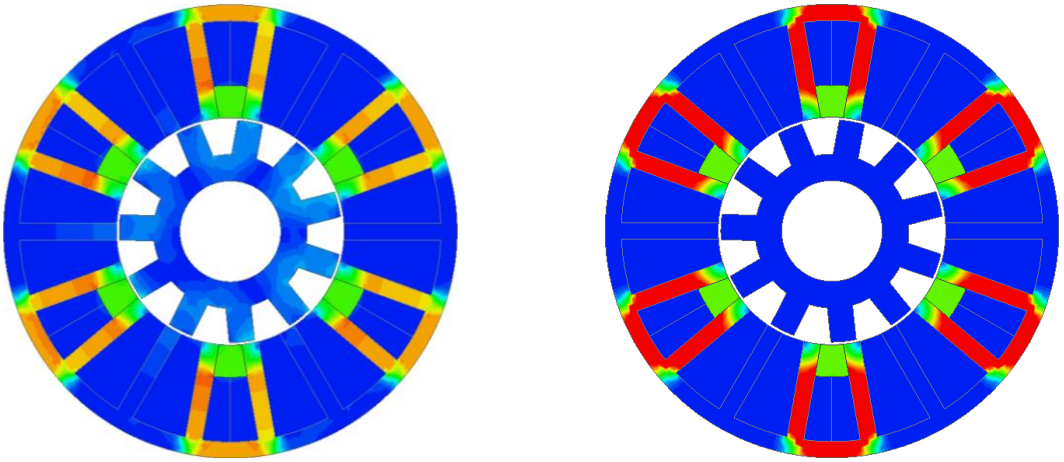

Flux density distribution

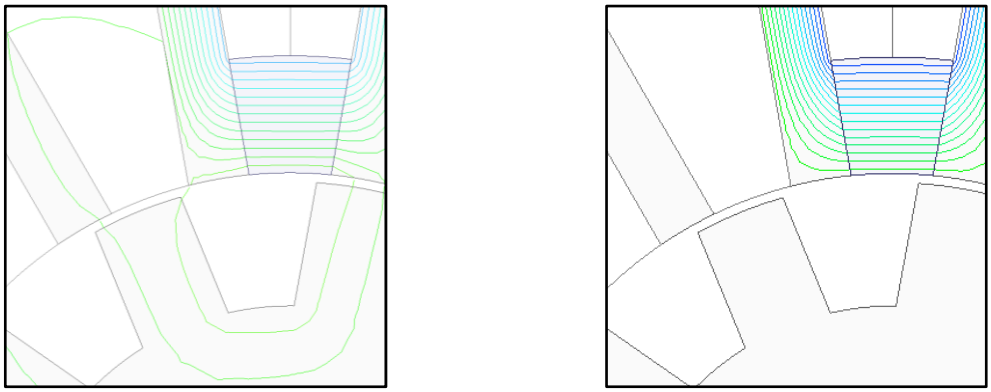

Zoom in

(a) Non-linear stator and rotor material (b) Linear stator and rotor material

(V) 11 rotor pole

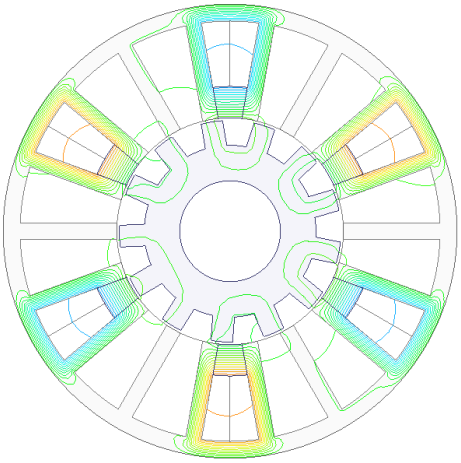
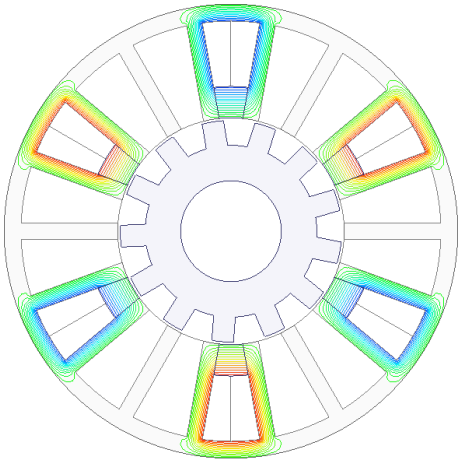

Flux line distribution

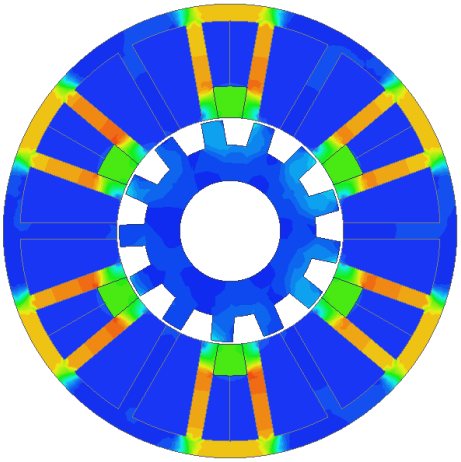
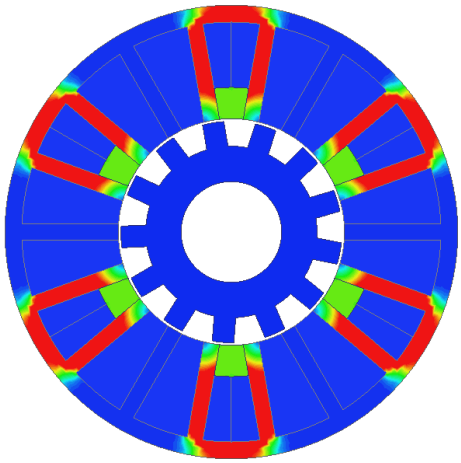

Flux density distribution

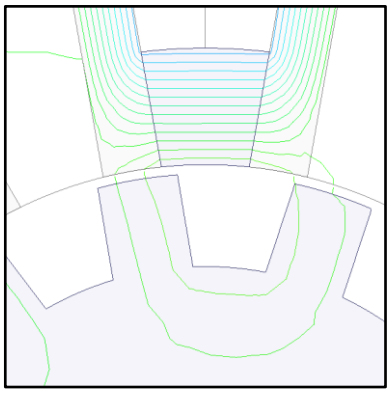
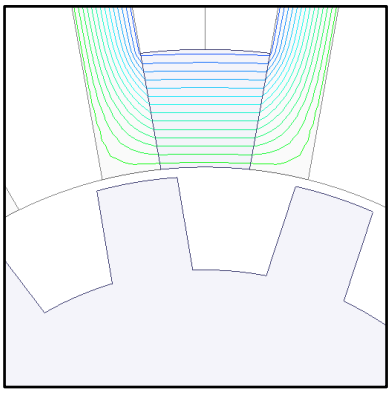

Zoom in

(a) Non-linear stator and rotor material (b) Linear stator and rotor material

(VI) 13 rotor pole

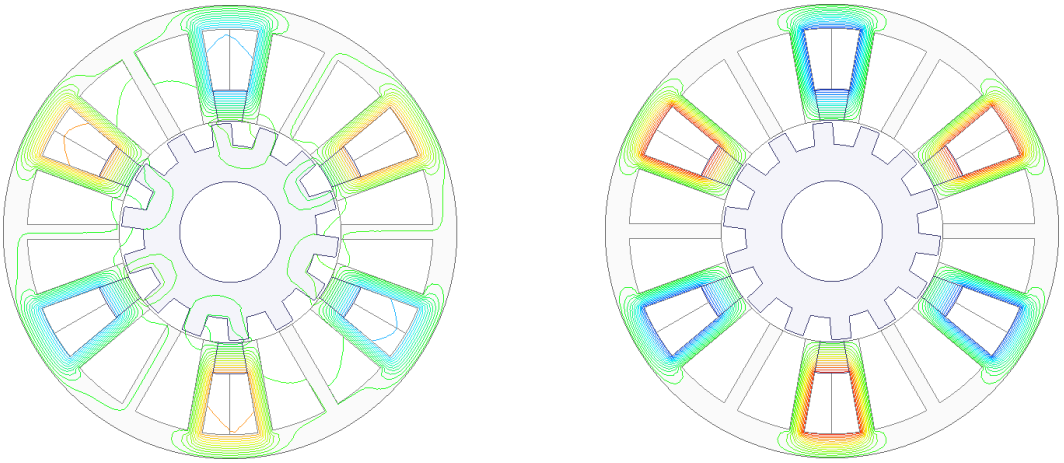

Flux line distribution

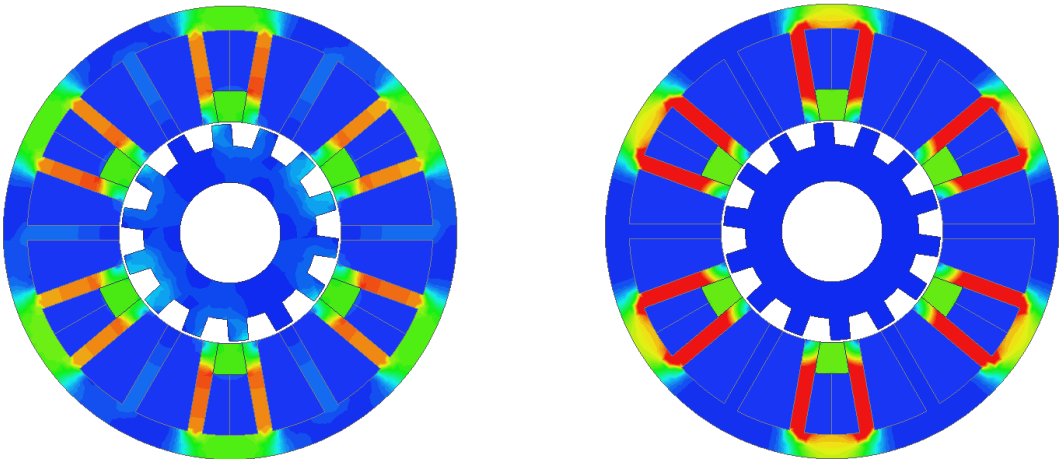

Flux density distribution

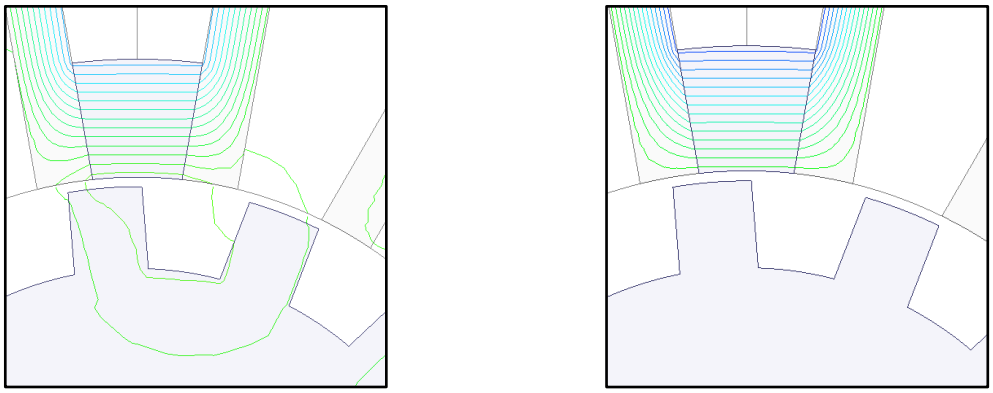

Zoom in

(a) Non-linear stator and rotor material (b) Linear stator and rotor material

(VII) 14 rotor pole

Fig. 3.9 The flux line and flux distributions of the machines having different numbers of rotor poles with linear and non-linear stator and rotor material.

When the F3A2 HSSPMMs with field excitation, the fundamental harmonics for the back-EMF are significantly increased when compared with the machine without field current, as shown in Fig. 8. The phase back EMF can be derived from the rate of change of phase flux-linkage, as [16]:

$$EMF = -\frac{d\psi_{phase}}{dt} \tag{3.9}$$

$$EMF \propto f\psi_{phase} \tag{3.10}$$

where ψ_{phase} is the phase flux-linkage, t is the time and f is the frequency. From (3.10), since the frequency dependent with rotor speed and rotor poles, and the rotor speeds for the machines are the same. Thus, the 14-rotor pole machine definitely has the lowest phase back-EMF magnitude due to quite low phase flux-linkage magnitude. Besides, the machines with even number of rotor poles have asymmetric waveforms which may have a larger ripple for torque performance. When the stator and rotor material is linear material, the back-EMFs of the machines are negligible. Thus, the machines are magnetically saturated and cause flux-leakage due to the PMs when the machines have no current excited.

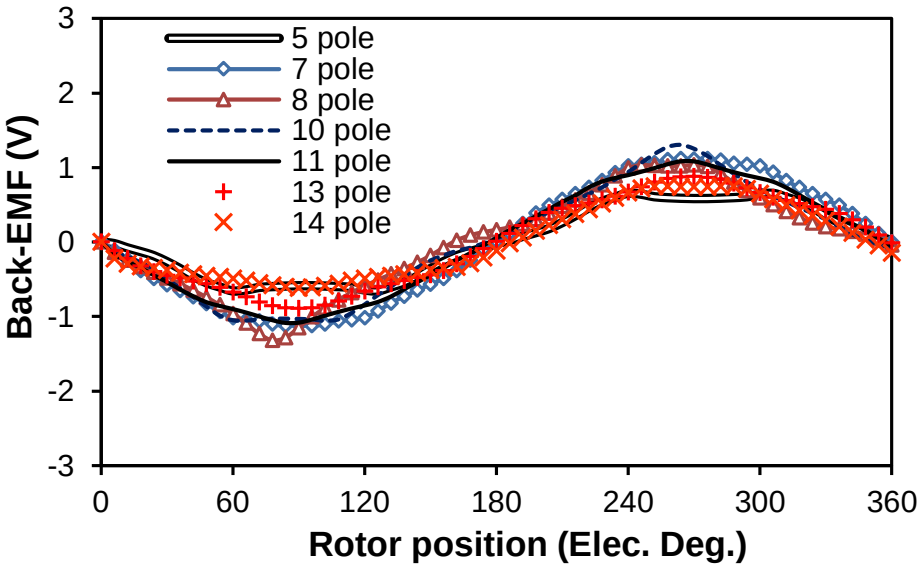

(a) Open-circuit back EMF waveforms (non-linear stator/rotor material, I_{dc} = 0A)

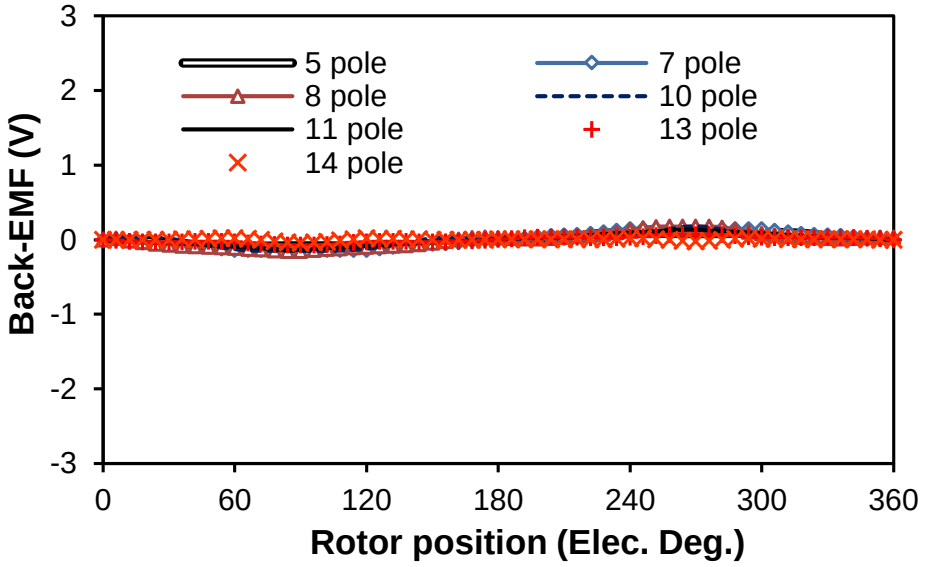

(b) Open-circuit back EMF waveforms (linear stator/rotor material, I_{dc} = 0A)

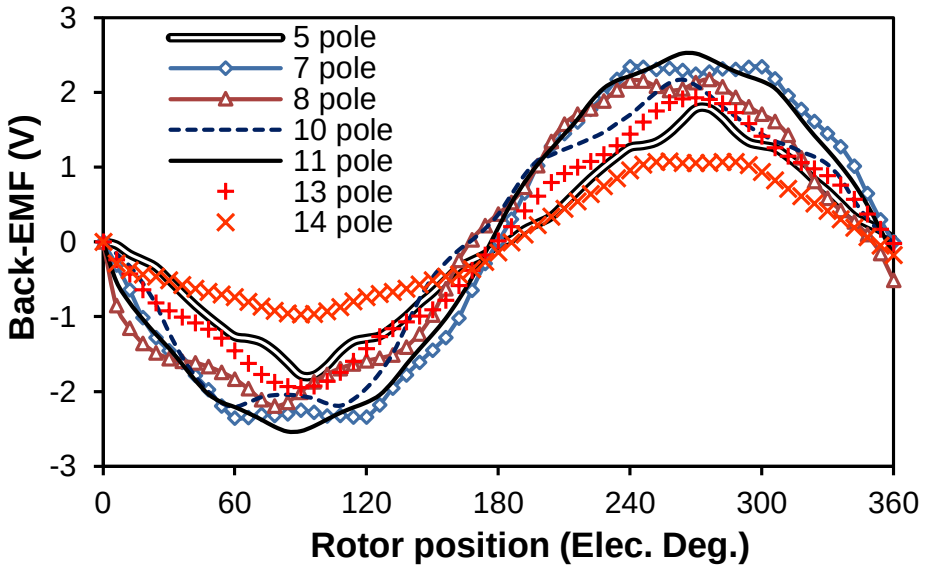

(c) Open-circuit back EMF waveforms (non-linear stator/rotor material, rated DC current excitation)

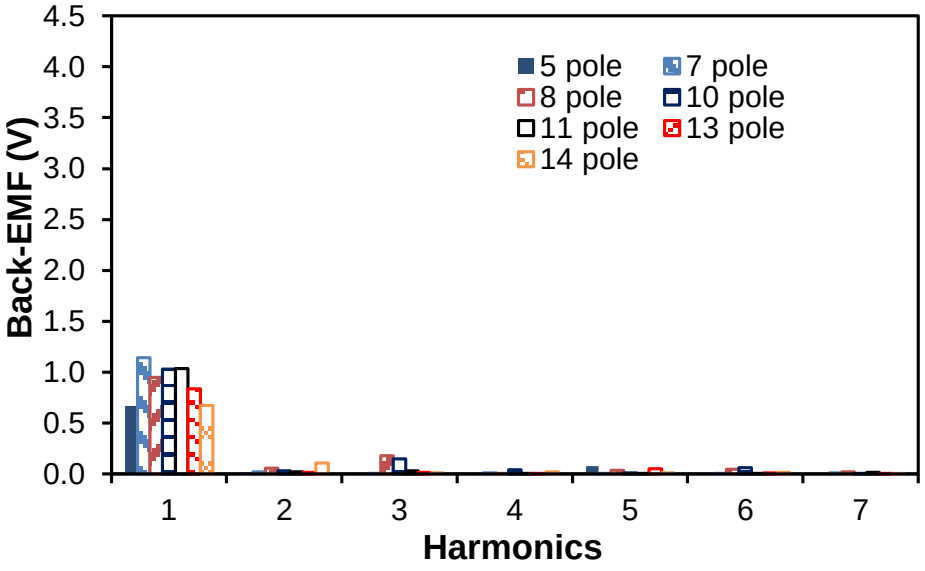

(d) Harmonics (non-linear stator/rotor material, I_{dc} = 0A)

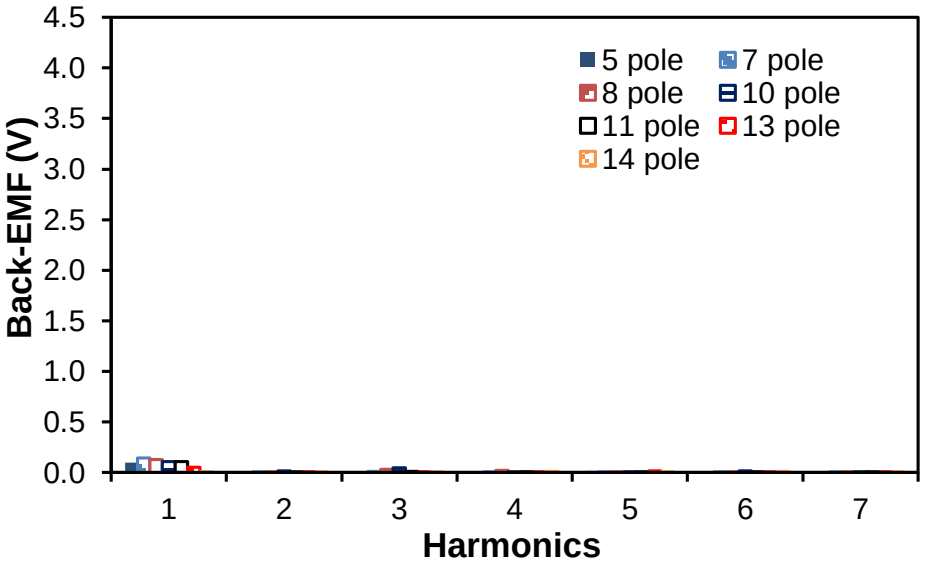

(e) Harmonics (linear stator/rotor material, I_{dc} = 0A)

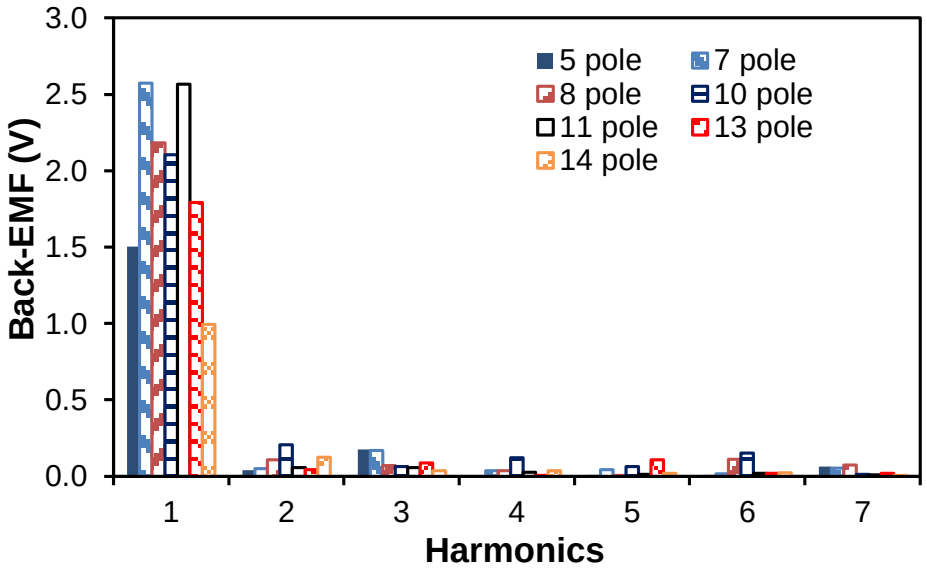

(f) Harmonics (non-linear stator/rotor material, rated DC current excitation)

Fig. 3.10 Open-circuit back-EMFs for F3A2 HSSPM machines with different numbers of rotor poles.

3.4.3. Torque performance

Open circuit cogging torque and on-load electromagnetic torque performance will be presented and analysed in this section. Fig. 3.11 shows that the F3A2 HSSPMMs with even number of rotor poles have larger torque ripple for open circuit cogging torque when compared with odd rotor pole number machines for both DC excitation conditions. The machine magnitude shows the even rotor pole number machines have higher 3^{rd}, 6^{th}, 9^{th} and 12^{th} harmonics, while the odd rotor pole number machines only have higher 6^{th} and 12^{th} harmonics but still have much lower magnitude than the even pole machines. The 10-rotor pole machine has significantly increased 9^{th} harmonic with field excitation. That determines the shape of the cogging torque waveform when the machine has field excitation. For the odd rotor pole machines, the magnitudes are increased when adding DC current. On the contrary, the even rotor pole machines have lower magnitude with the machine field excitation.

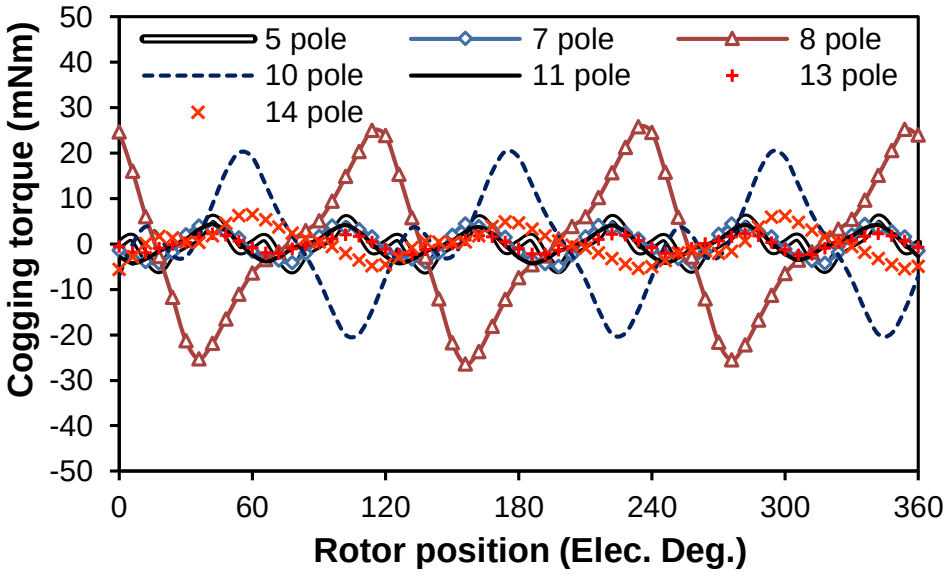

(a) Open-circuit cogging torque waveforms (I_{dc} = 0A)

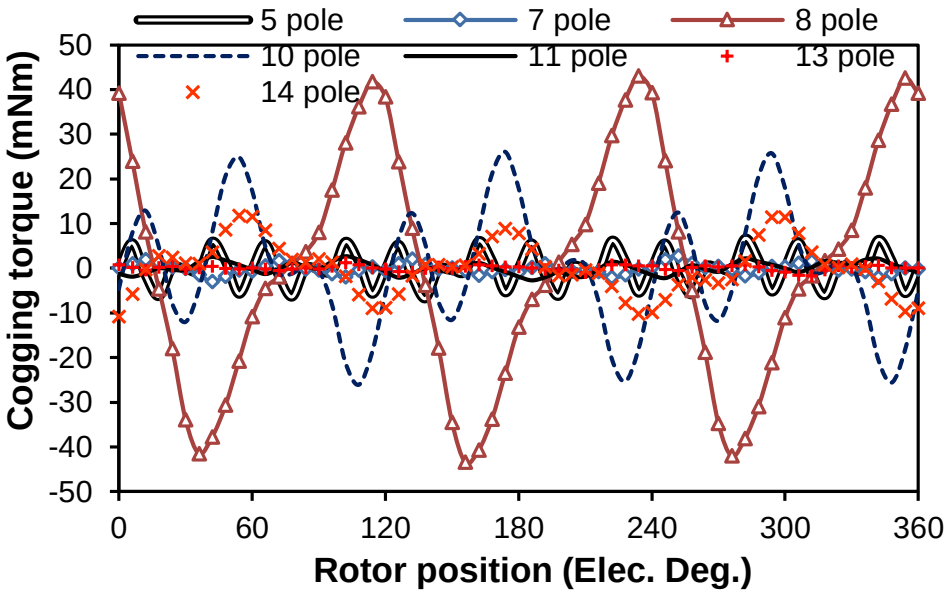

(b) Open-circuit cogging torque waveforms (rated DC current excitation)

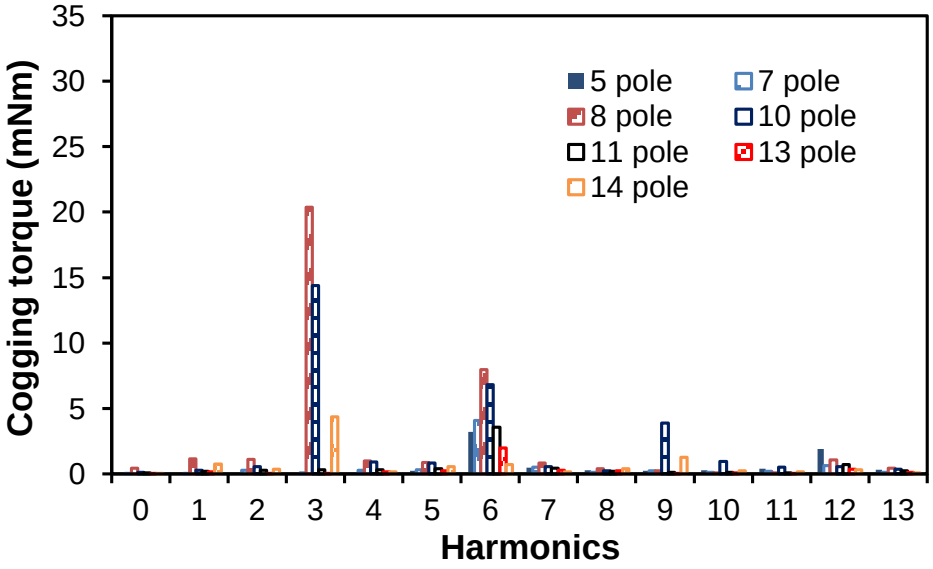

(c) Harmonics (I_{dc} = 0A)

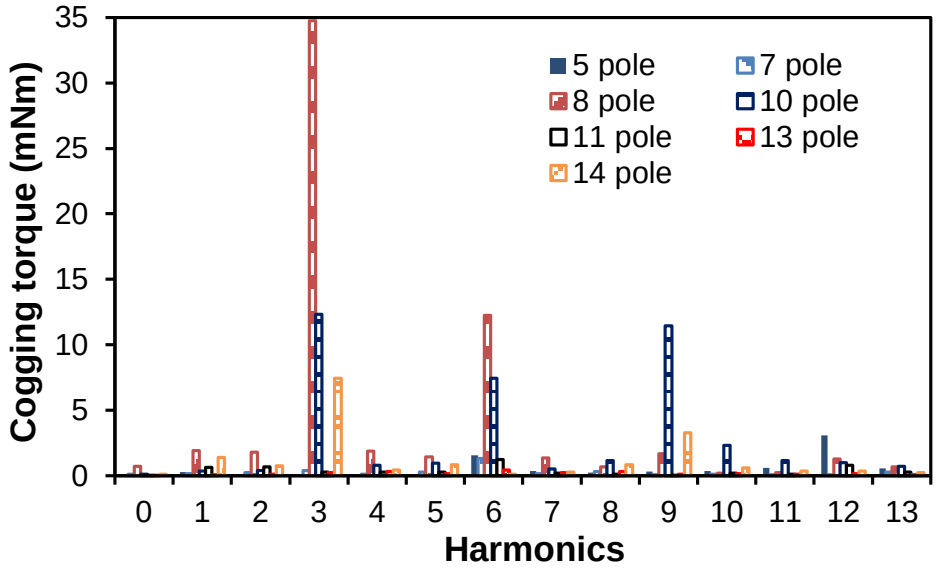

(d) Harmonics (rated DC current excitation)

Fig. 3.11 Open-circuit cogging torques for F3A2 HSSPM machines with different numbers of rotor poles.

The current angle for the machines can ensure the maximum average electromagnetic torque during the machine optimization. The average torques against current angle are shown in Fig. 3.12. The machines can achieve the maximum average torque within -10 to 10 electrical degree current angle. Thus, the machines have small or negligible reluctance torque. The DC bias of the curve is caused by the field excitation, which is mentioned in the open-circuit flux-linkage analysis.

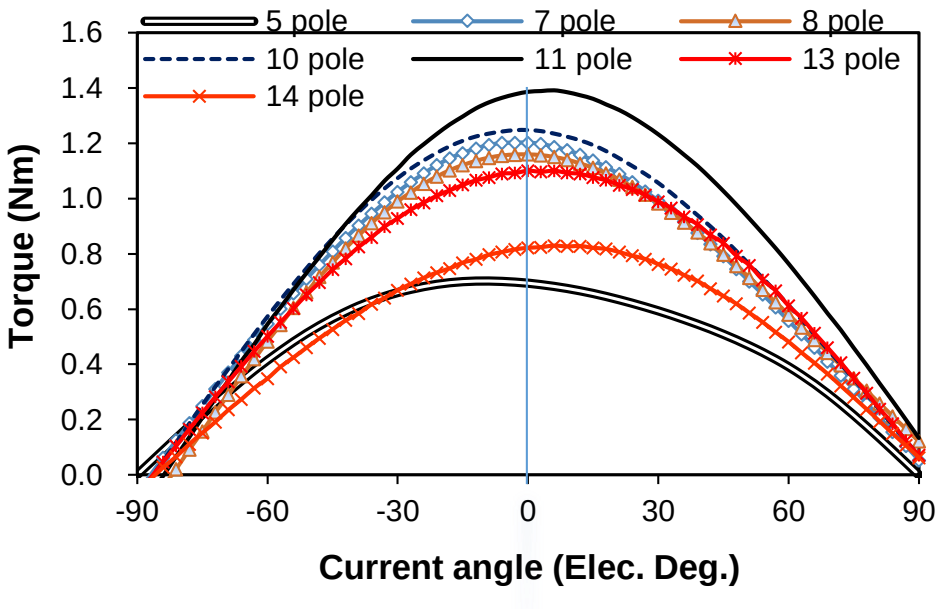

Fig. 3.12 Electromagnetic torque against current angle for F3A2 HSSPMMs with different numbers of rotor poles (total copper loss = 60W).

The electromagnetic torque for the F3A2 HSSPMMs are shown in Fig. 3.13. Fig. 3.13 (a) shows that the even rotor pole machines have large torque ripple and the 14-rotor pole machine has the worse torque performance, which is because of the lowest amplitude of the back-EMF and asymmetric waveform. Apart from the fundamental harmonic, the odd rotor pole machines have only the 6th harmonic without the 3rd harmonic, while the even rotor pole machines have a large 3rd harmonic which causes the large torque ripple. Especially for the 14-rotor pole machine, the 3rd harmonic of this machine is the largest, and thus, the torque ripple for the machine is the largest. The torque characteristics of the machine are shown in Table 3.3.

Table 3.4 Torque characteristics at rated armature and field currents

Parameters	**Unit**	**5 pole**	**7 pole**	**8 pole**	**10 pole**	**11 pole**	**13 pole**	**14 pole**
Average torque (T)	Nm	0.70	1.20	1.16	1.24	1.39	1.10	0.81
Torque ripple (T_{ripple})	%	19.37	4.22	33.79	24.83	3.82	15.09	143.57
Peak-to-peak torque ($T_{p\text{-}p}$)	Nm	0.13	0.05	0.39	0.31	0.05	0.17	1.16

According to Table 3.3, the values of torque ripple are small for the machines with odd number rotor pole. The 14-rotor pole machine has the worst torque performance while the 11-rotor pole

has the best torque performance. Meanwhile, the 5-rotor pole machine has the lowest average electromagnetic torque value.

The average toque rises with the increasing total copper loss, and it shows that at high copper loss, the machines will be saturated, but the 5-rotor pole machine exhibited gentle saturation with the increasing copper loss. Fig. 3.14. The 5-rotor pole machine has the lowest average torque with the variable total copper loss, and the 11-rotor pole machine has the highest average toque. Because of the severe magnetically saturation at high copper loss for the 14-rotor pole machine, the torque value of the machine is almost same as that for the 5-rotor pole machine. The 7- and 10-rotor pole machines and the 8- and 13-rotor pole machines have similar average torque values at low copper loss, respectively. When the copper loss is high, the 7- and 13-rotor pole machines have lower average torque than the 8- and 10-rotor pole machines.

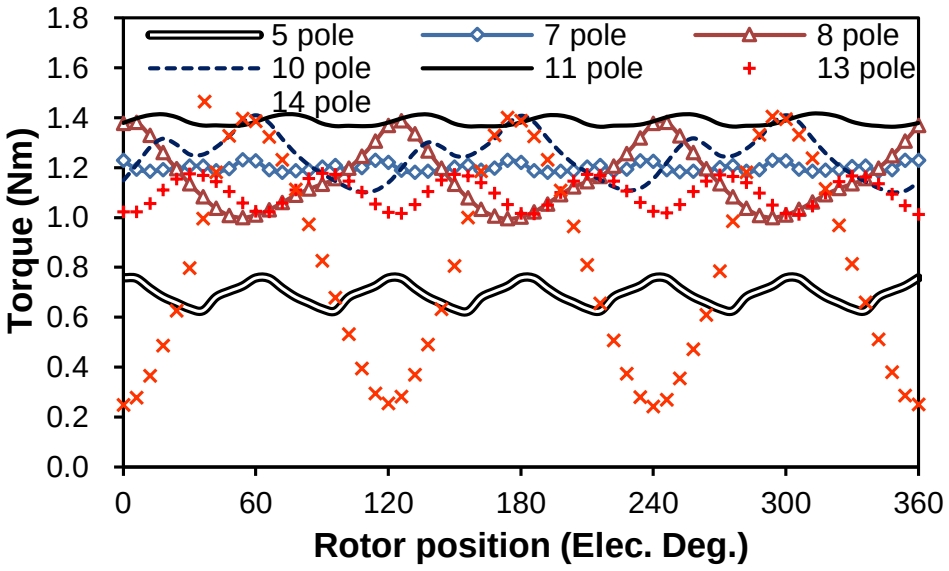

(a) Electromagnetic torque waveforms

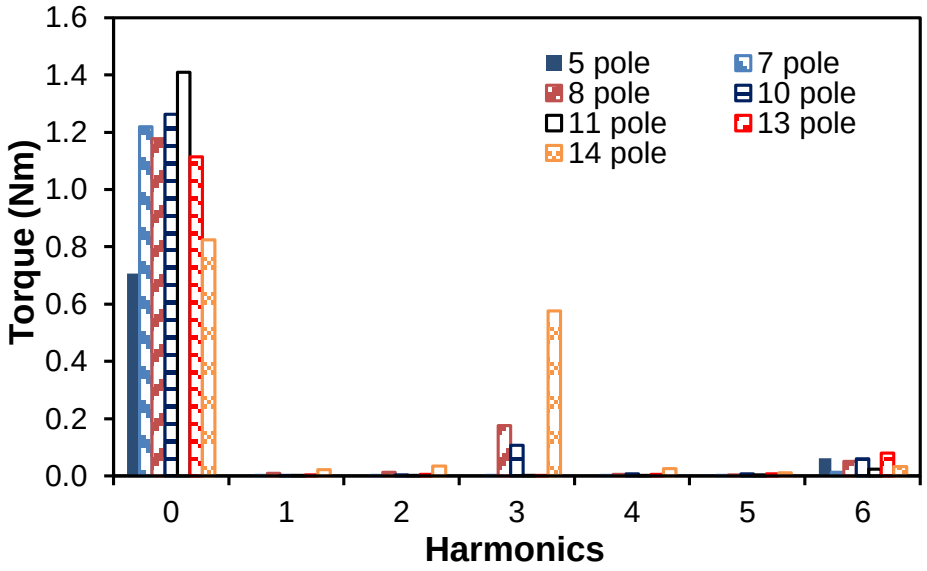

(b) Harmonics

Fig. 3.13 Electromagnetic torques for F3A2 HSSPMMs with different numbers of rotor poles (total copper loss = 60W).

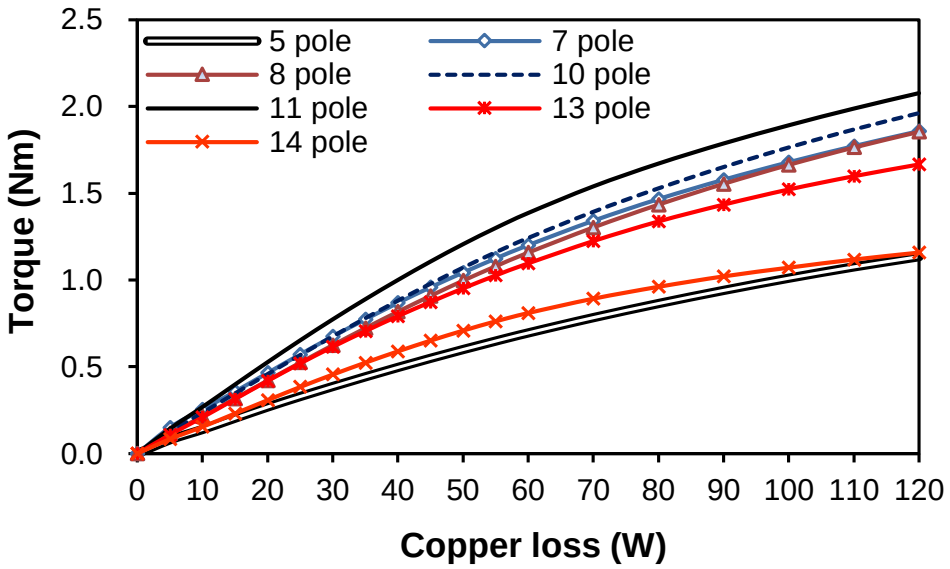

Fig. 3.14 Average electromagnetic torque against total copper loss for F3A2 HSSPMMs with different numbers of rotor poles.

3.5. Unbalanced magnetic force

The unbalanced magnetic force (UMF) can be calculated from the tangential and radial magnetic forces. Both tangential and radial magnetic forces can be transformed into x- and y-axes, F_x and F_y as:

$$F_x = F_{tx} + F_{rx} = \frac{r l_{stack}}{2\mu_0} \int_0^{2\pi} (2B_r B_\alpha \sin\alpha + (B_\alpha^2 - B_r^2)\cos\alpha) d\alpha \quad (3.11)$$

$$F_y = F_{ty} + F_{ry} = \frac{r l_{stack}}{2\mu_0} \int_0^{2\pi} (-2B_r B_\alpha \sin\alpha + (B_\alpha^2 - B_r^2)\cos\alpha) d\alpha \quad (3.12)$$

where F_{tx}, F_{ty}, F_{rx} and F_{ry} are the x- and y-axis components of tangential and radial magnetic forces, respectively. B_α and B_r are the circumferential and radial components of the air gap flux density, respectively, r is the air gap radius, and μ_0 is the permeability of the free space [39].

Fig. 3.15 (a) and (b) shows the UMF loci of the machines without and with field current at on-load situation for the F3A2 HSSPMMs with different numbers of rotor poles. It shows that the odd rotor pole number machines exhibit UMF, while the machines with even rotor pole have negligible UMF. Meanwhile, the 5-rotor pole machine have the largest UMF. The UMF might be caused from a difference in the air-gap flux densities on opposite sides of the machine. This can be found directly as the machine flux line distribution, which shows that the flux distribution of odd number rotor pole machines is unbalanced. The open circuit flux line distribution for the machines can be exhibited in Fig. 3.9.

Machine total UMF can be calculated as equation (3.13):

$$F = \sqrt{F_x^2 + F_y^2} \quad (3.13)$$

The peak UMF for the machines will increase with field excitation. Especially for the 11 pole machine, the peak force is increased by 20% when DC excited current at rated current. The UMF without field current will increase slightly with the increasing number of rotor poles. However, the UMF for 11 pole machine is the largest when the machines have field current.

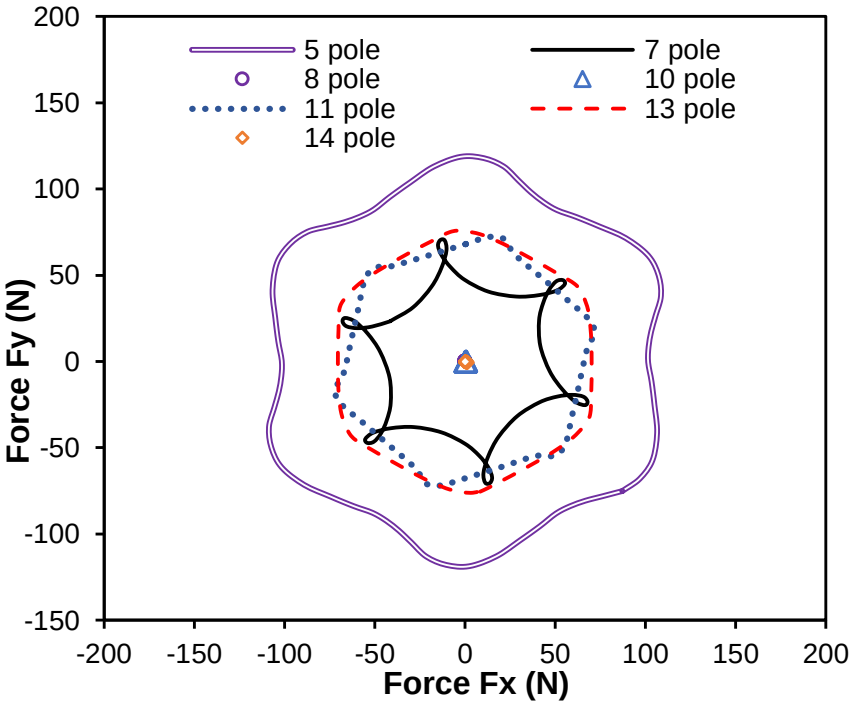

(a) UMF loci for F3A2 HSSPMMs at on-load situation with I_{dc} = 0A (total copper loss = 60W).

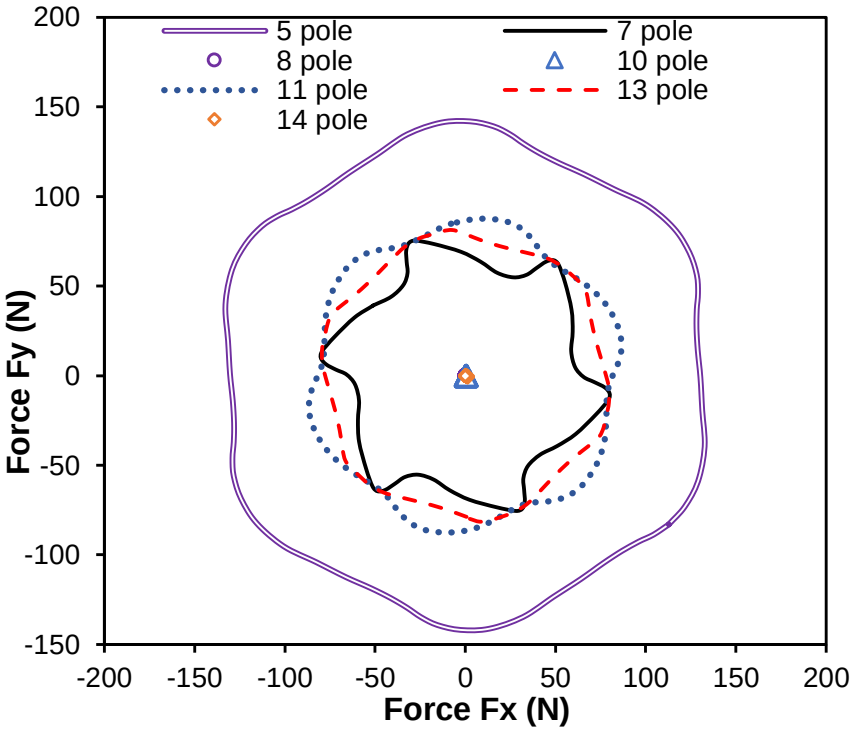

(b) UMF loci for F3A2 HSSPMMs at on-load situation with rated DC current excitation (total copper loss = 60W).

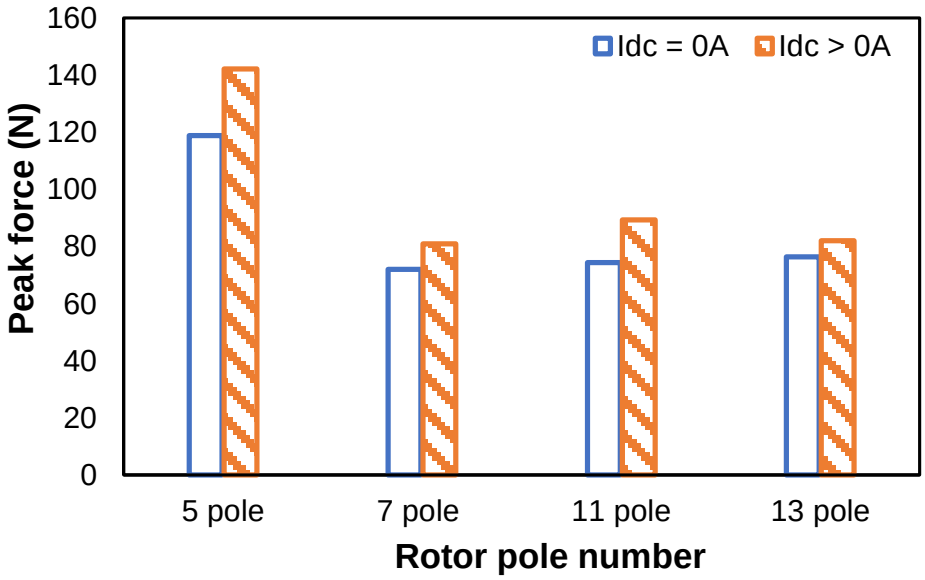

(c) Peak force for different numbers of rotor poles with and without I_{dc}.

Fig. 3.15 Machine UMF for F3A2 HSSPMMs at on-load situation.

The influence of the field and armature currents on the average UMF for 5-, 7-, 11- and 13-rotor pole F3A2 HSSPMMs is shown in Fig. 3.16. It shows that when the machines on open-circuit with I_{dc} = 2.5A, all the machines have the lowest average UMF. In addition, when the machines have no field current, the average UMF will be increased significantly when I_{rms} is lower than 10A and increasing smoothly to the highest force value, as expected for the 7-rotor pole machine. The 5- and 7-rotor pole machines have significantly increasing average UMF from 2.5A field current to the highest force value on open-circuit. Besides, when the field and armature currents are the same after 10A, the force values are the lowest. For 11- and 13-rotor pole machines on open-circuit, the force increased to the peak at I_{dc} = 10A and reduced till the maximum field current value.

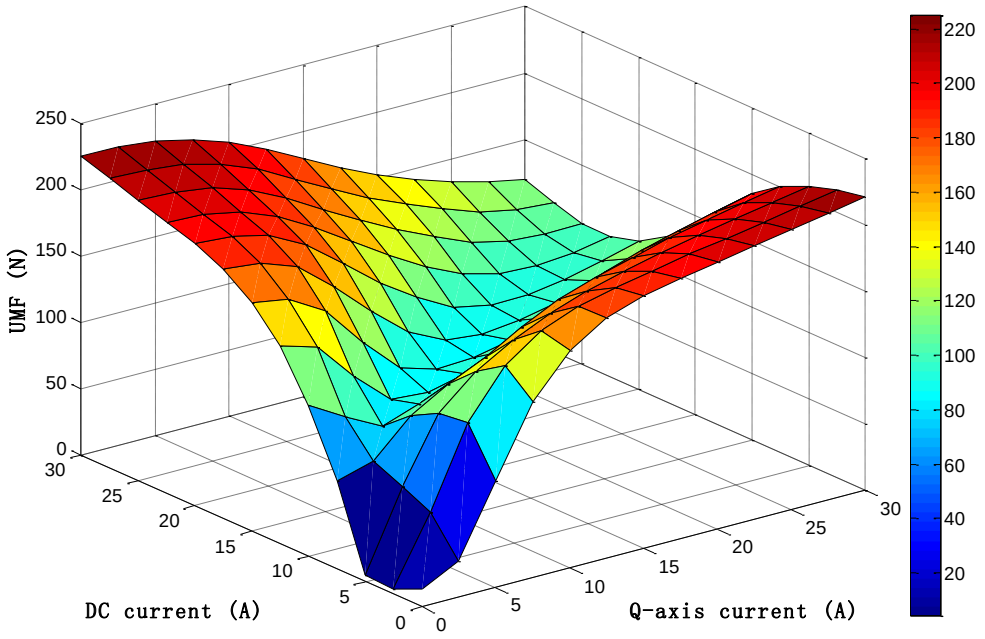

(a) 5-rotor pole

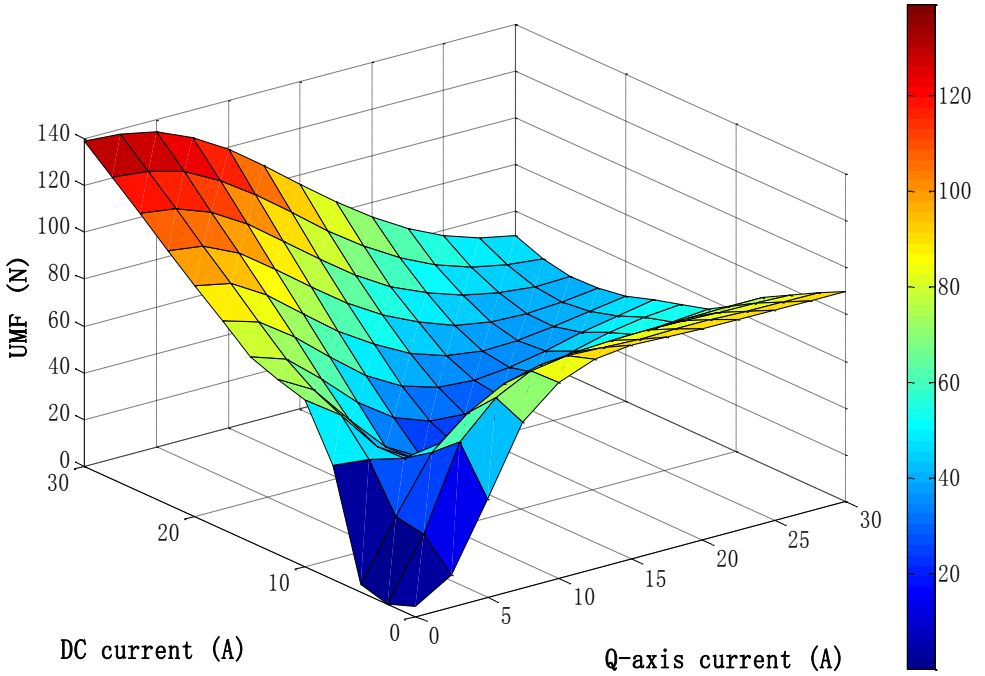

(b) 7-rotor pole

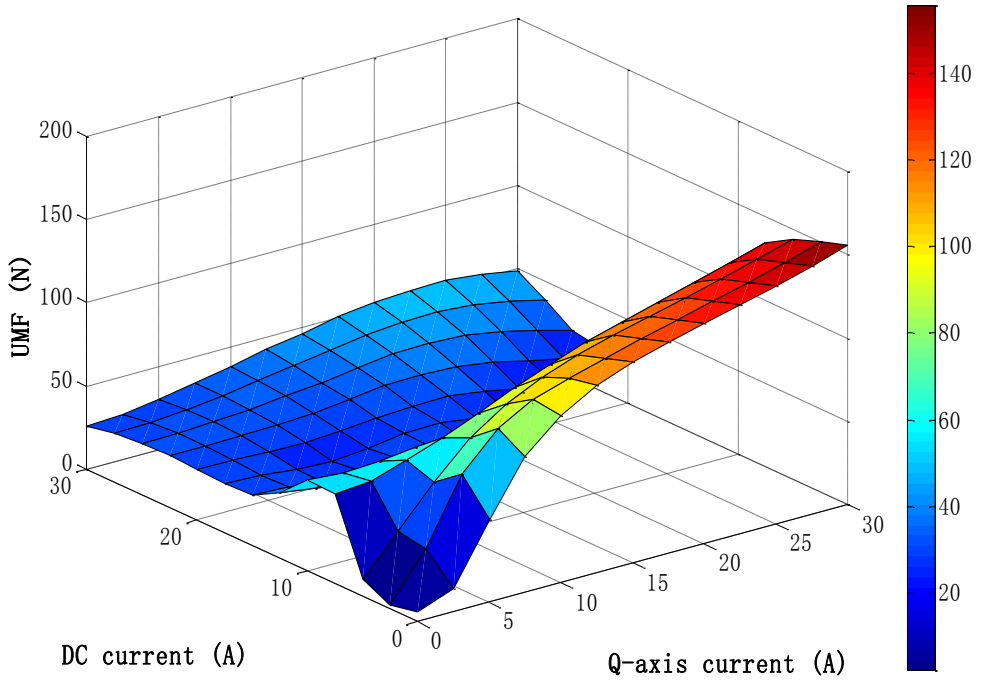

(c) 11-rotor pole

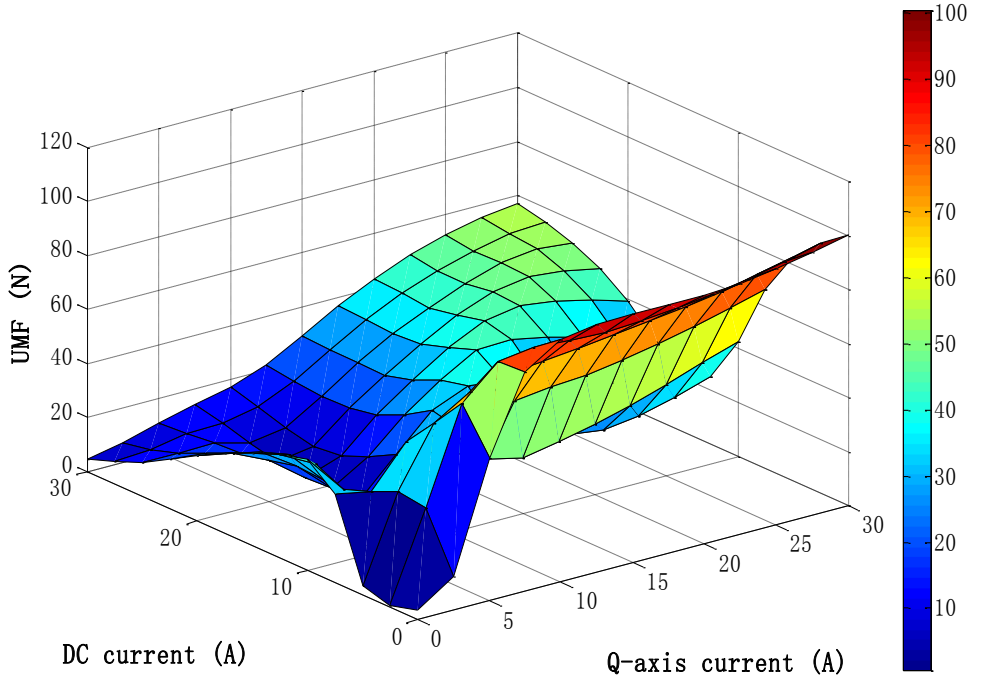

(d) 13-rotor pole

Fig. 3.16 Influence of the field and armature currents on the average UMF for F3A2 HSSPMMs.

3.6. Conclusions

In this chapter, the open-circuit and on-load electromagnetic performance of the 18-stator slot and 6-stator pole F3A2 HSSPMMs with 7/8/10/11/13/14-rotor poles are investigated and compared. The 14-rotor pole machine has the worst performance, while the 11-pole machine has the best. According to the back-EMF waveforms, the even rotor pole machines have asymmetric waveforms and high torque ripple due to high even harmonics in the back-EMF. The UMF of the machine has larger peak force value when the machine has field excitation and the 11-rotor pole machine exhibits the largest UMF value.

Chapter 4 Modular Stator Hybrid-excited Doubly Salient Machines with Permanent Magnets Located on Slot Openings

4.1. Introduction

Due to simplified manufacturing and winding processes, the application of modular machine structures is increased [117]. As modular coil configurations, the concentrated windings are employed on the modular segments or plug-in teeth, which also have the benefit for easy manufacturing and short end winding [12]. However, the modular machines will also have drawbacks of a reduction of torque performance and an increase in cogging torque and torque ripple due to manufacturing tolerances [118].

The modular stator machines can have the structure of PMs located on rotor [119-124] which can be achieved by adding flux gaps and removing part of the stator back-irons from a surface mounted PM or interior PM machine, and PMs located on stator [47, 86, 87, 105, and 125] which can be achieved by removing alternative PMs in switched flux PM machines (SFPMMs) and adding PMs on the slot openings of stator segments for a modular stator switched reluctance machine (SRM).

The operation principle of a 'U-shaped' modular stator coil machine with PMs located on rotor is investigated in [119] and the winding configuration of a 'U-shaped' stator segment machine has been introduced in [120]. According to [119], it is found that eddy current loss can be reduced by removing some section of stator yoke which changes the MMF harmonics. The influence of stator back-irons and teeth of a stator yoke flux gaped machine is shown in [121, 122]. It has demonstrated that the remaining stator back-irons should be increased to avoid over saturation, and the remaining stator back-irons thickness and tooth width in one stator segment can be similar. From [122], it shows that the flux gaps have significant effect on cogging torque. The papers in [123, 124] mainly report the 'E-core' stator segments.

The papers in [47, 105 and 125] describe a modular SFPM machine with two 'U-shaped' segments next to PMs. When compared with a conventional switched flux PM machine, the modular machine has a reduction of electromagnetic torque and an increase in the torque ripple due to the flux gap and half PMs removed. In addition, the modular machine has improved fault tolerant capability. Further, the demagnetization withstand capability of the modular machine may be improved.

The ‘U-shaped’ stator segment machine with PMs on stator slot openings can be modified from the SRM machine [86, 87]. This type of machine has higher torque and power density and efficiency than the conventional SRM. Besides, the modular machine with PMs on slots openings is fault tolerant and does not have open-circuit cogging torque which is different from other modular stator machines.

In this chapter, a hybrid-excited modular stator machine with PMs located on stator segment slot openings and field excitation also on stator will be designed and investigated, and a 10 rotor pole machine is shown in Fig. 4.2(c). This type of machine can be modified from a single layer (SL) F1A1 HSSPMMs or a SL-wound field synchronous machine (SL-WFSM) which will be shown later in this chapter. The research in this chapter can be summarized as:

- The introduction of hybrid excited modular stator machine structure and the modifications from the SL-F1A1 HSSPMM and SL-WFSM.
- The optimization of the modular machines with two sets of restriction parameters under different stator back-iron and tooth conditions, and comparison of the torque performance of the machines
- Investigation of different stator/rotor pole combinations with/without field windings.
- Comparison of torque performance on open-circuit and on-load conditions for the modular machines with/without field windings with different stator/rotor pole combinations

4.2. Machine structure

The modular stator slot opening permanent magnets (PMs) hybrid-excited machine (MS-HSSPMM) has segmented “U-shape” laminated stator with alternative armature winding and DC-excited winding on each stator segments. Circumferentially magnetized PMs are allocated in the slot area of each stator segment. This machine has short magnetic circuit and the “modular core” construction will eliminate the interaction between different phases [86, 119, and 126].

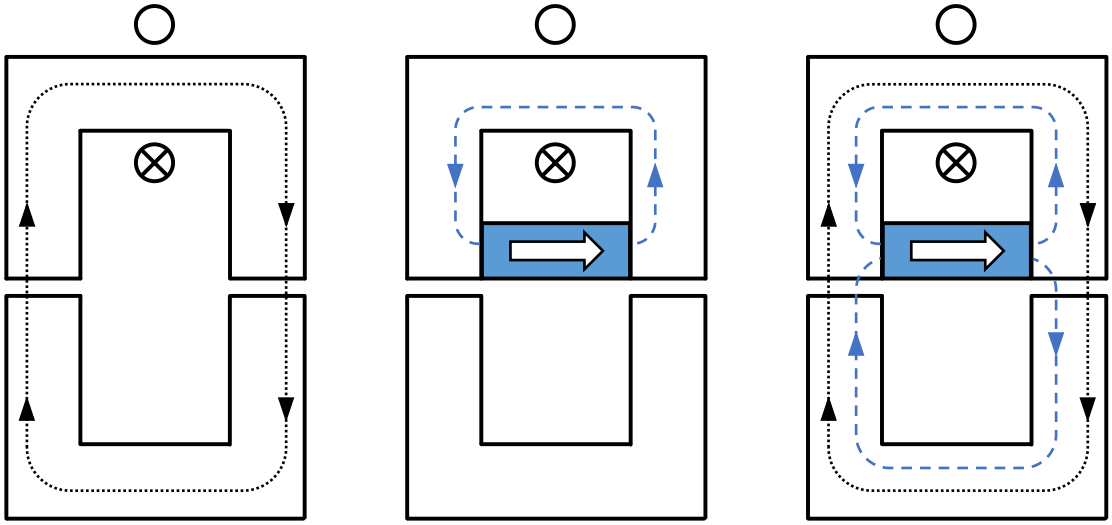

(a) No PM, I_{dc} > 0A (b) I_{dc} = 0A (c) I_{dc} > 0A

Fig. 4.1 Schematic diagram of DC and PM flux paths.

The basic operation principle of the machine can be explained by the illustration in Fig. 4.1. Fig. 4.1(a) shows when the magnets are removed and at on-load condition, the flux generated by coil will link both the rotor and stator via air-gap, and EMF will be induced in the coil. On open circuit condition, Fig. 4.1(b) shows that the flux produced by PMs is shunted in the stator part having opposite direction to the flux produced by coil. When both coil current and PM exist, the fluxes generated from both sources can pass via the air-gap to the rotor to induce the EMF in the coil. The flux produced by coil current will make partial PM flux pass the air-gap due to the magnetic pull between both excitation fields. The increasing current can cause the shunted flux reduced till the machine is magnetically saturated. Thus, the DC excited current can adjust the flux in hybrid excited machines.

The MS-HSSPMMs, which is shown in Fig. 4.2(c), can be modified from two existing machines: (1) the single layer wound field synchronous machine (SL-WFSM), as shown in Fig. 4.2(a); (2) the single layer hybrid-excited stator slot PM machines with a coil span of one slot pitch for the field windings (F1) and the armature windings (A1) (SL-F1A1 HSSPMMs), as shown in Fig. 4.2(b).

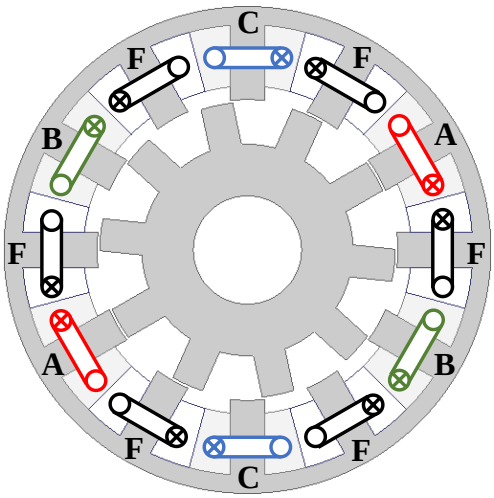

(a) SL-WFSM

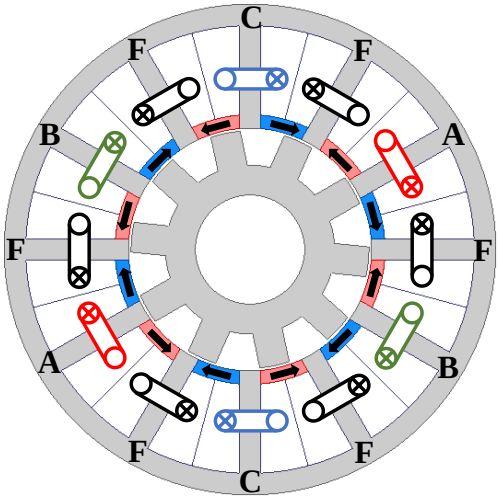

(b) SL-F1A1 HSSPMM

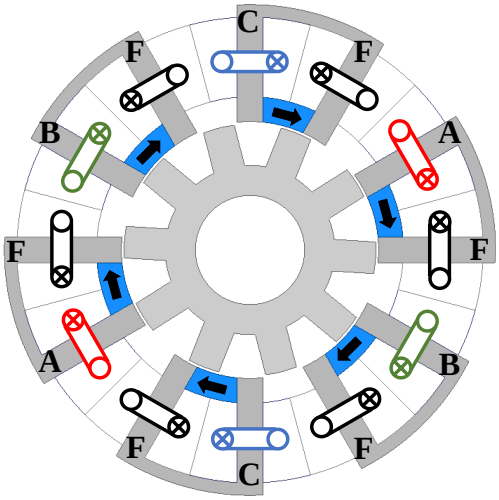

(c) MS-HSSPMM

Fig. 4.2 Cross sections for SL-WFSM, SL-F1A1 HSSPMM and MS-HSSPMM.

4.2.1. Modified from SL-WFSM

As shown in Fig. 4.2(a), the SL-WFSM has both field and armature coils alternatively disposed on the stator and the field coils have identical polarity. The machines have been described in detail in [127]. To create a MS-HSSPMM, the machine needs to remove half of the back-iron to make the stator segments non-interlocking, and a PM will be inserted in the slot opening area of the remained "U-shaped" stator segments. According to [76, 127], the field winding area and armature winding area are approximately similar. Thus, the WFSM can be optimized with (1) similar field and armature winding areas, (2) similar numbers of turns for field and armature windings, (3) similar current density for convenience. For other optimization parameters, the fixed copper loss, stator outer diameter and stator stack length are considered. Since PMs will be located in the slot opening areas to create the MS-HSSPMM, the slot

opening area spaces need to be reserved during the optimization to avoid the reducing of total copper loss.

4.2.2. Modified from SL-F1A1 HSSPMM

The conventional F1A1 HSSPM machine can be developed from the variable flux machine, which is a double layer F1A1 WFSM, by adding PMs between adjacent stator poles, and the machine is all stator poles wound machine [92]. The SL-F1A1 HSSPM machine is an alternative stator poles wound machine. The single layer HSSPM machines have high torque ripple when the rotor pole number is even. The design and investigation of the F1A1 HSSPM machines are described in detail in [92, 93]. In order to modify the SL-F1A1 HSSPMM to MS-HSSPMM, the alternative stator back-irons need to be removed and the corresponding PMs in the same slots of the corresponding stator back-irons are removed as well. The F1A1 HSSPM machine has a thin back-iron after optimization since the machine needs to be magnetically saturated by the magnetic field produced by coil current. Hence, the PMs allocated between adjacent stator poles are able to reduce the machine saturation. However, when the machine has removed alternate stator back-irons to make the stator modular, the thin back-iron will cause the torque density reduced significantly due to over saturation. In order to avoid this issue, the thickness of remaining stator back-irons can be increased or it is even possible to employ equal stator tooth width and stator back-iron thickness [121, 128]. Thus, during the optimization of SL-F1A1 HSSPMM, the stator tooth width and stator back-iron thickness can be assumed to be similar.

The design parameters and torque performance comparison of SL-WFSM, SL-F1A1 HSSPMM and MS-HSSPMM are displayed in Table 4.1. From Table 4.1, it shows that the MS-HSSPMM has less PM usage than the SL-F1A1 HSSPMM, but the average electromagnetic torque is reduced due to reduced slot area. However, the peak to peak value of cogging torque and the torque ripple for electromagnetic torque are reduced when the machine stator is modular. In addition, the MS-HSSPMM has less iron loss.

Table 4.1 Design parameters and electromagnetic torque performance of SL-WFSM, SL-F1A1 HSSPMM and MS-HSSPMM

	SL-WFSM	SL-F1A1 HSSPMM	MS-HSSPMM
Stator outer radius R_{SO}, mm	45		
Stator stack length l_{stack}, mm	25		
Air-gap length G, mm	0.5		
Copper loss P_{Cu}, W	60		
Back-iron thickness H_{BI}, mm	3.37	3.94	2.29
Stator tooth width w_{st}, mm	6.47	3.94	4.72
PM height (slot opening area thickness) H_{PM} ($H_{slot\ opening}$), mm	2.5	2.46	4.54
PM volume V_{PM}, mm^3	---	6172	5991
PM N38SH @ 20°C	---	1.2T/1.05	1.2T/1.05
Split ratio	0.607	0.484	0.512
Stator pole arc θ_{st}, deg.	13.36	10.15	11.51
Rotor pole arc θ_{rt}, deg.	12.53	14.48	14.48
Rotor tooth height H_{rt}, mm	7.84	6.35	7.62
Average torque @400rpm, Nm	0.75	0.92	0.80
Torque ripple @400rpm, %	119.5	120.6	69.4
Cogging T peak-peak, mNm	54.31	61.63	22.15
Average torque/PM volume @400rpm, Nm/m^3	---	148701.2	133547.2
Iron loss @4000rpm, W	28.25	27.85	19.51
Rotor loss @4000rpm, W	7.02	5.39	4.07
Stator loss @4000rpm, W	21.23	22.45	15.43
PM loss @4000rpm, W	---	1.48	0.88

4.3. MS-HSSPMMs with equal/unequal stator tooth width and stator back-iron thickness

4.3.1. Design optimization

The MS-HSSPMM has both field and armature windings on each stator segment with one PM located in slot opening area of the stator segment. The machine is designed to have three phases. The mechanical degree between each stator tooth is 30° for convenient machine topology design. The field slot area and armature slot area are assumed to be the same for optimization. A simplified model of the stator and rotor of MS-HSSPMM is shown in Fig. 4.3. The MS-HSSPMM has been globally optimized by employing the genetic algorithm to achieve the maximum average torque at 60 W total copper loss. The restrictions for optimization are listed in Table 4.2.

Table 4.2 Restrictions for optimization

Stator outer radius R_{SO}, mm	45
Stack length l_{Stack}, mm	25
Air-gap length G, mm	0.5
Total copper loss P_{Cu}, W	60
Turns/phase	184
Turns for DC windings	552
Packing factor	0.59
Rated speed, rpm	400

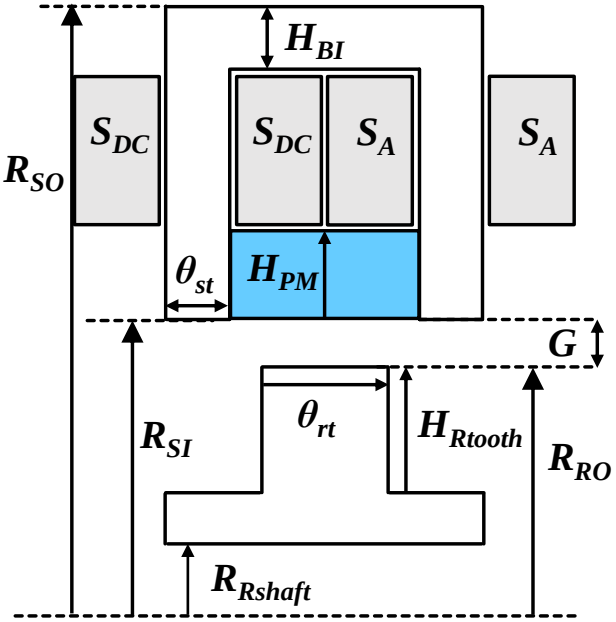

Fig. 4.3 Illustration of the stator and rotor geometric parameters

During the optimization, the split ratio, stator back-iron thickness, stator tooth width, rotor tooth width and height, and the PM volume are considered to be optimized and the optimized machine is shown in Fig. 4.4(a). According to [121], the stator back-iron thickness and stator tooth width for modular stator machine are better to be similar. Thus, the result of machine optimized with the constraint of equal stator back-iron thickness and tooth width is shown in Fig. 4.4(b).

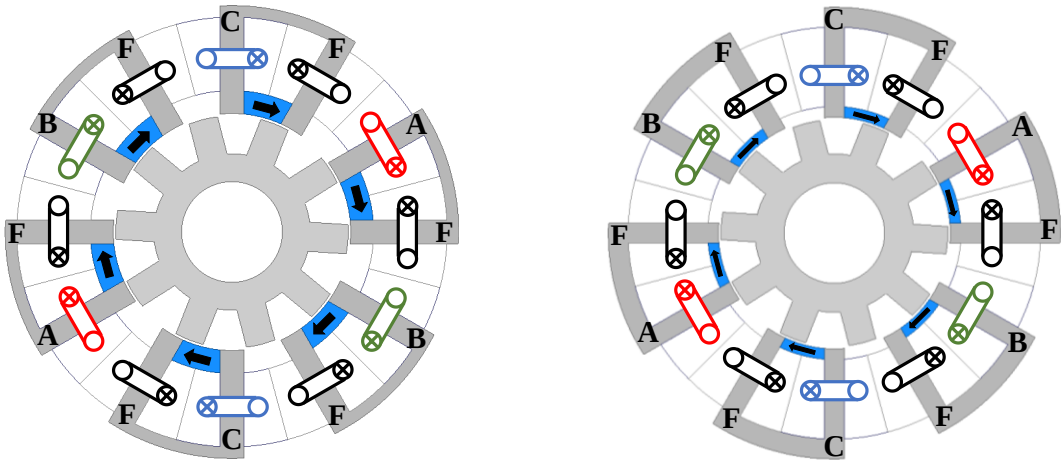

(a) $w_{st} \neq H_{BI}$ (b) $w_{st} = H_{BI}$

Fig. 4.4 Cross sections for MS-HSSPMMs with different stator back-iron thickness and stator tooth width restrictions.

It is obvious that when the machine with same stator back-iron thickness and tooth width, the PM volume of the machine is much lower than the machine optimized without the restricted condition. Table 4.3 shows the design parameters of the machines.

Table 4.3 Design parameters for MS-HSSPMMs

	MS-HSSPMMs	
	$w_{st} \neq H_{BI}$	$w_{st} = H_{BI}$
Back-iron thickness H_{BI}, mm	2.29	3.96
Stator tooth width w_{st}, mm	4.72	3.96
Stator pole arc θ_{st}, deg.	11.51	9.85
Rotor pole arc θ_{rt}, deg.	14.48	13.98
PM height H_{PM}, mm	4.54	2.12
PM volume V_{PM}, mm^3	5990.8	2762.9
Total slot area (AC), mm^2	1209.9	1271.4
Total slot area (DC), mm^2	1209.9	1271.4
Split ratio	0.512	0.501
Rotor outer radius R_{RO}, mm	23.06	22.57
Stator inner radius R_{SI}, mm	23.56	23.07
Rotor tooth height H_{rt}, mm	7.62	6.86

4.3.2. Electromagnetic performance comparison

In this section, the electromagnetic performance on both open circuit and load conditions are analysed. Flux-linkage, back-EMF, and cogging torque performance will be presented as open circuit electromagnetic performance. For on-load electromagnetic performance, the electromagnetic torque and loss performance are investigated. Fig. 4.5 shows the flux line and flux density distributions of MS-HSSPMMs when phase 'A' has been excited by a rated current with total DC field current excited at different rotor positions. The flux distributions at aligned position and non-aligned position are presented in Fig. 4.5(a) and (b), respectively. The angle

between these two positions is 18°. The difference from Fig. 4.5 between the two MS-HSSPMMs is due to the PM usage. At the aligned rotor position, because the PM volume of the MS-HSSPMM has different stator back-iron thickness and tooth width is large, the flux line generated by DC field current at the stator segment with coil A is offset by the flux line produced by PM which has opposite direction. This is also happened at non-aligned rotor position. For the MS-HSSPMM with equal stator back-iron thickness and tooth width at non-aligned rotor position, all the fluxes produced by PM and current are also offset.

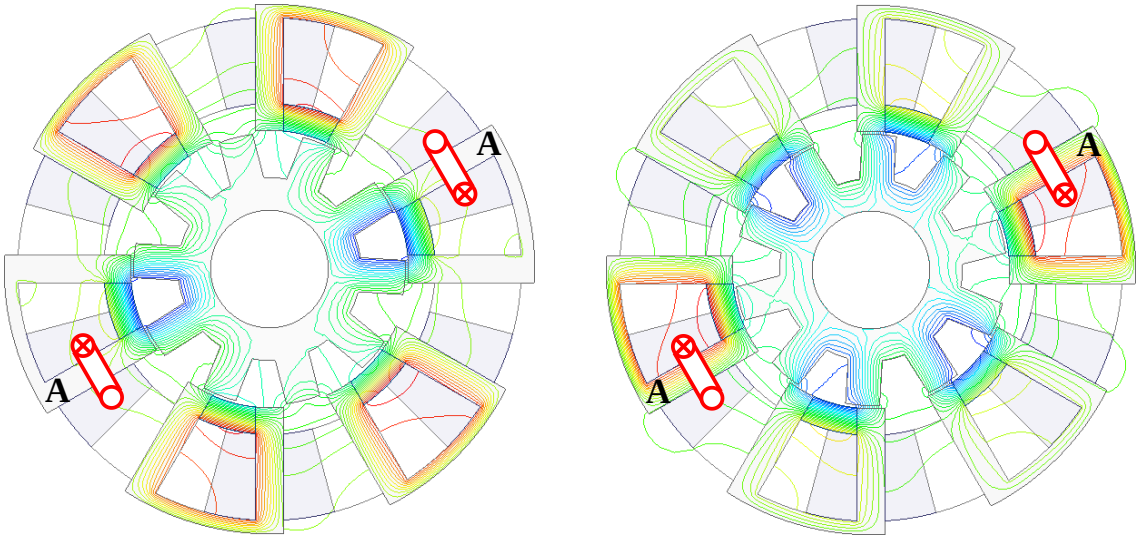

Flux line distributions for MS-HSSPMM with $w_{st} \neq H_{BI}$

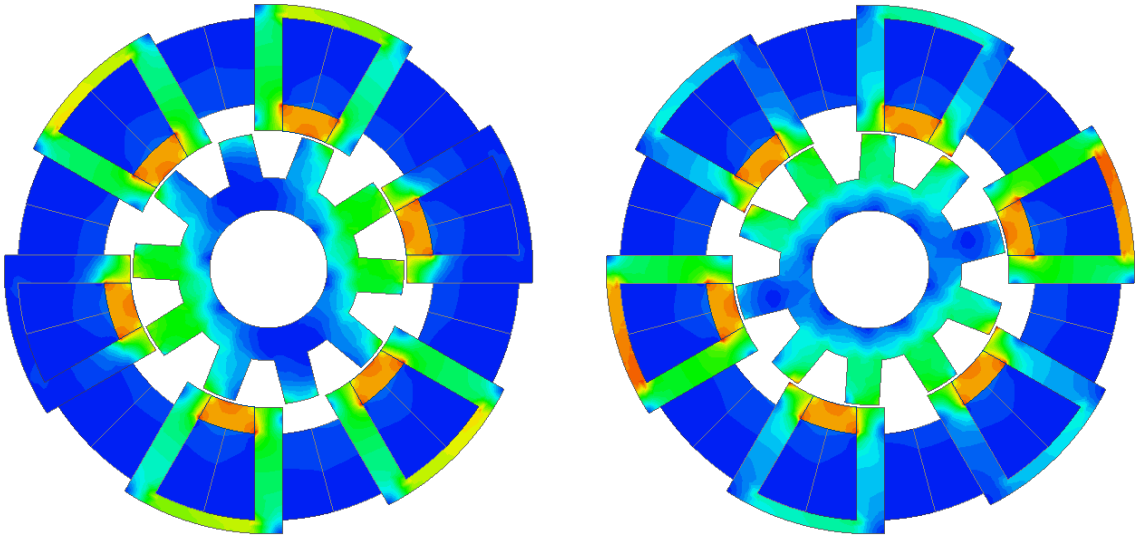

Flux density distributions for MS-HSSPMM with $w_{st} \neq H_{BI}$

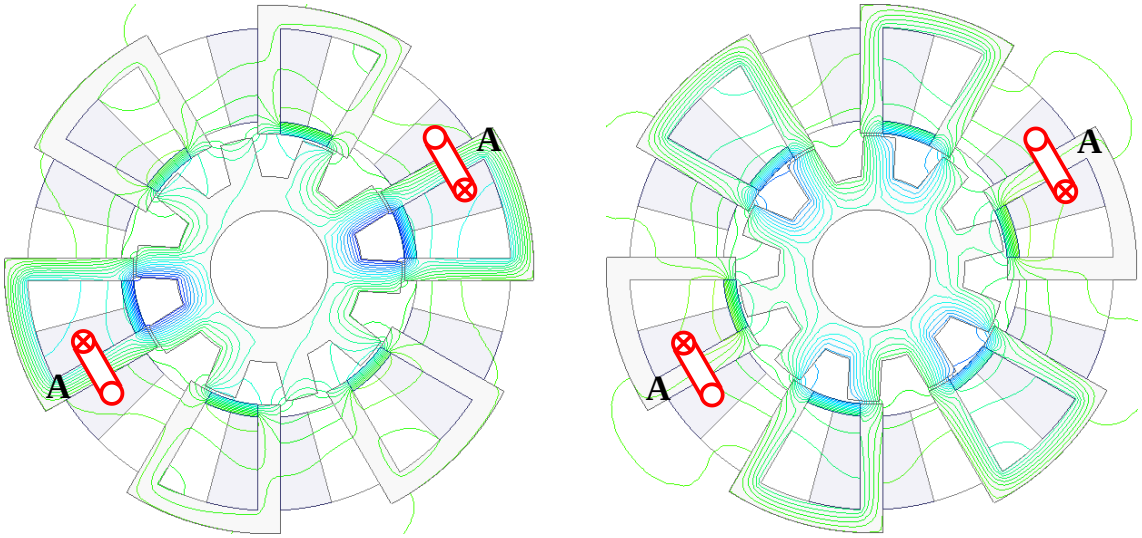

Flux line distributions for MS-HSSPMM with $w_{st} = H_{BI}$

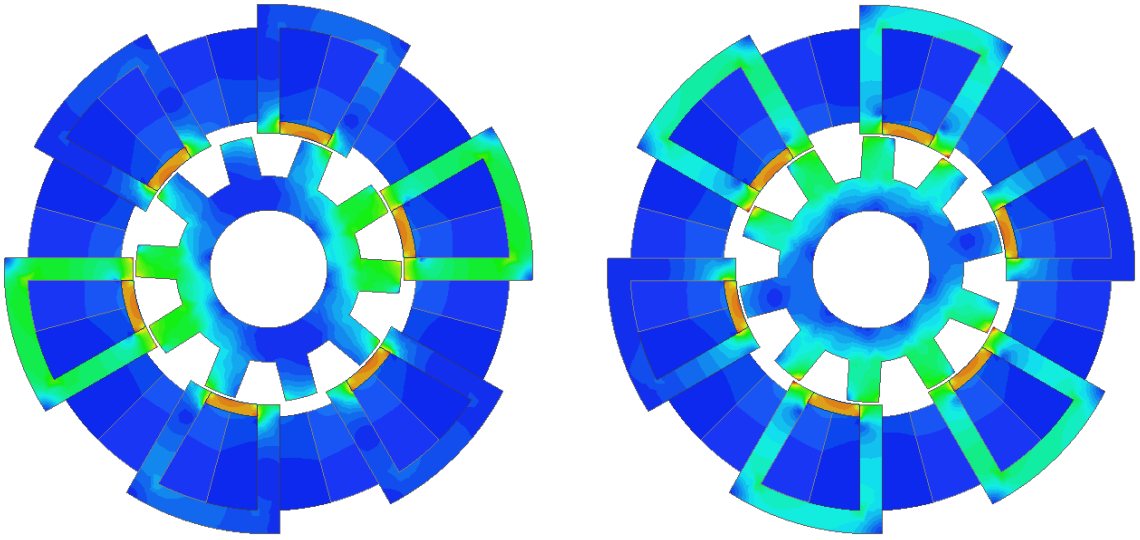

Flux line distributions for MS-HSSPMM with $w_{st} = H_{BI}$

(a) Aligned position (b) Non-aligned position

Fig. 4.5 Flux line and flux density distribution of the MS-HSSPMMs with total field current and phase 'A' current excited

A. Open-circuit flux distribution and phase flux-linkage

The flux line and flux density distributions for the two types of MS-HSSPMMs are shown in Fig. 4.6. According to the machine operation principle, the flux should be shunted in the stator segments when the DC current is 0A. For the machine with unequal w_{st} and H_{BI}, the stator back-irons of the stator segments are magnetically saturated due to the large volume of PMs when the DC current is 0A. This causes slightly flux leakage of this machine. The magnetic saturation of the stator segments is reduced when a rated DC current is excited. However, all

the flux produced by DC current is offset by the flux produced by PMs at both rotor positions. For the machine with equal w_{st} and H_{BI}, the PM usage is limited by the fixed w_{st} and H_{BI} and the flux is shunted without DC current excitation.

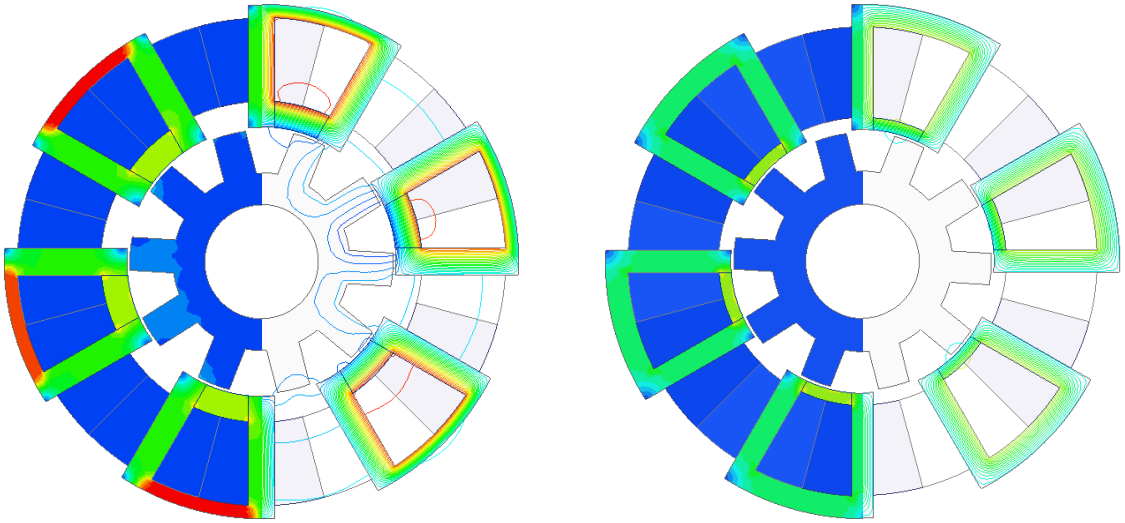

Aligned rotor position, I_{dc}=0A

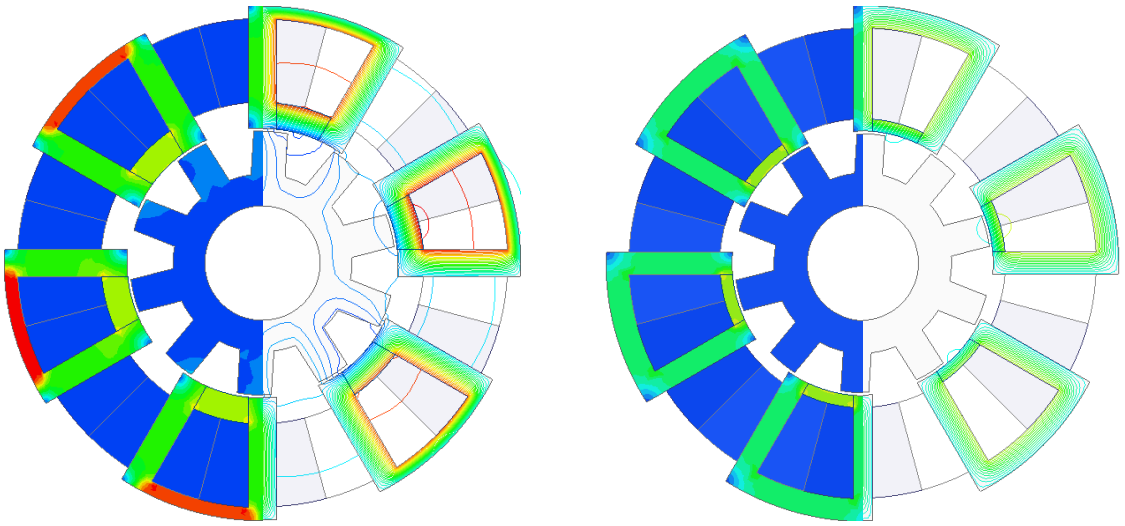

Non-aligned rotor position, I_{dc}=0A

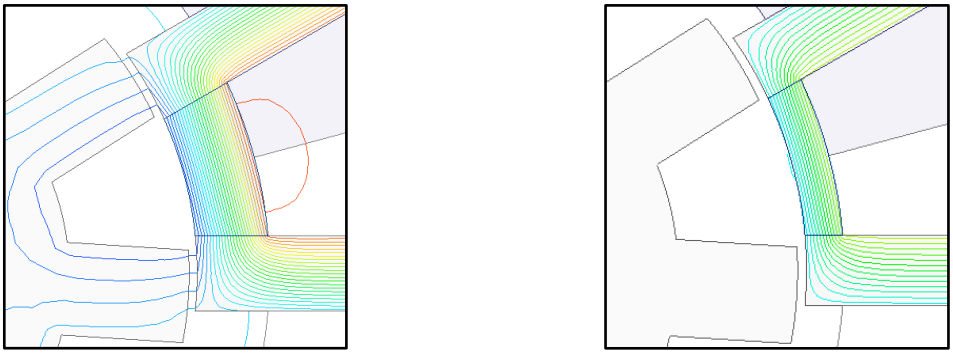

Zoom in at aligned rotor position, I_{dc}=0A

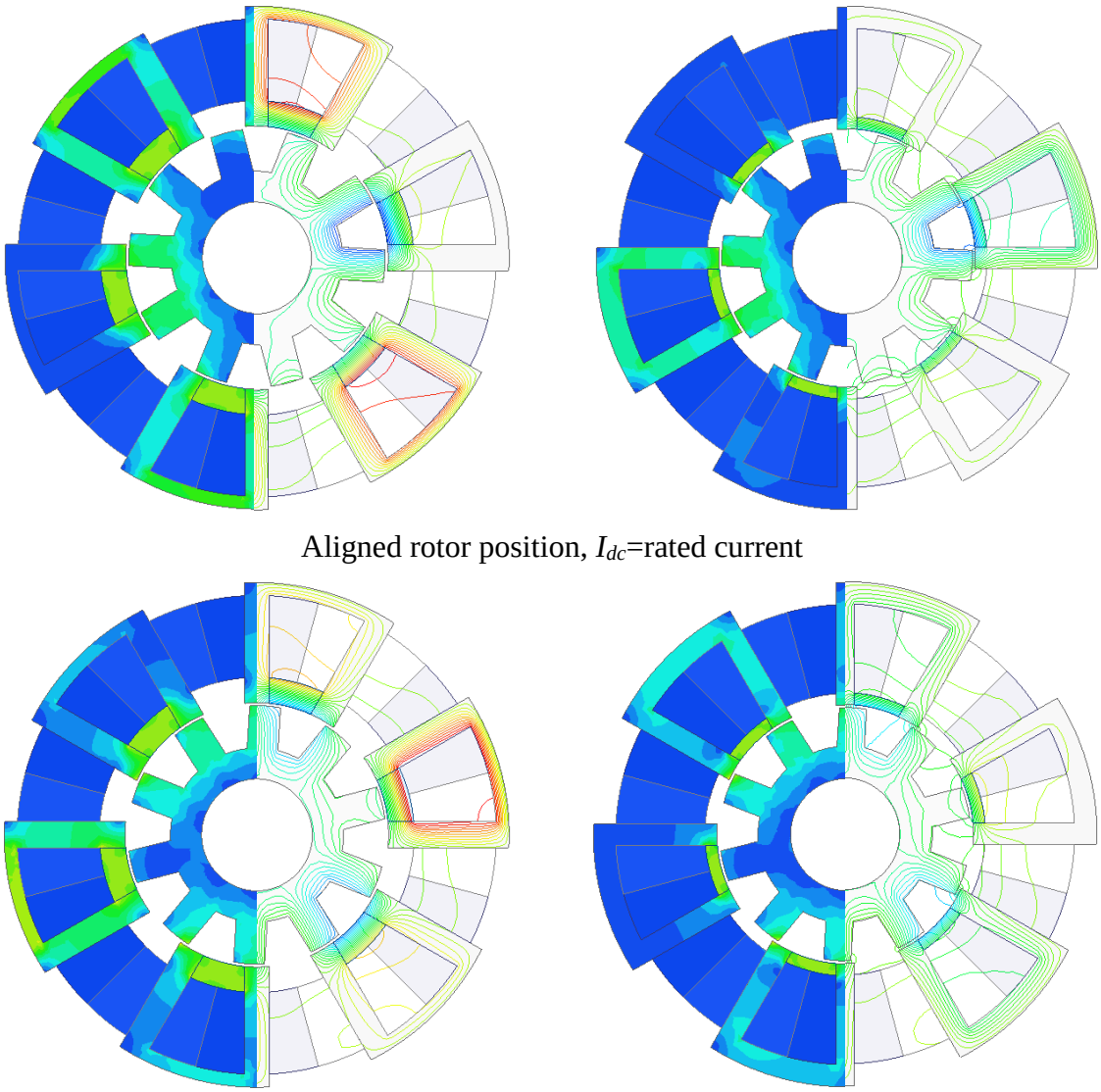

Aligned rotor position, I_{dc}=rated current

Non-aligned rotor position, I_{dc}=rated current

(a) MS-HAAPMM with $w_{st} \neq H_{BI}$ (b) MS-HAAPMM with $w_{st} = H_{BI}$

Fig. 4.6 Open circuit flux line and flux density distributions at different rotor positions with different DC current excitations for MS-HSSPMMs

Fig. 4.7 shows the comparison of flux linkages for MS-HSSPMMs with different stator tooth width and stator back-iron thickness relationship. From Fig. 4.7(a), it shows that the MS-HSSPMMs in phase winding are unipolar, and when DC current excitation is 0, the bias is more notable with the large amount of PM usage. Meanwhile, the flux linkage waveforms for both machines are negligible and have almost no variation. When the machines excited with a rated DC current, the biases of phase flux linkage for both machines are reduced.

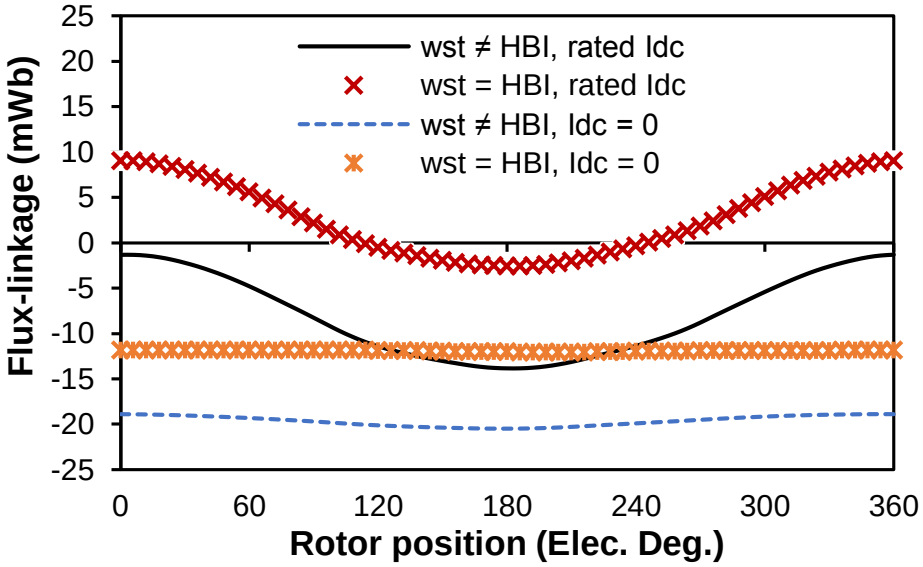

(a) Phase 'A' flux-linkage waveforms

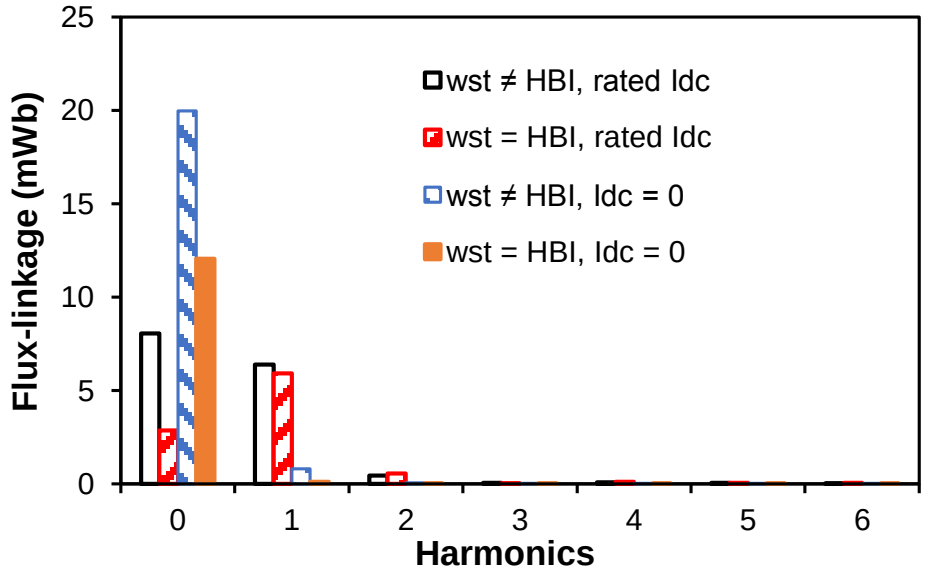

(b) Harmonics, Phase 'A'

Fig. 4.7 Phase flux linkage for MS-HSSPMMs with different stator tooth width and back-iron conditions (rotating speed = 400rpm)

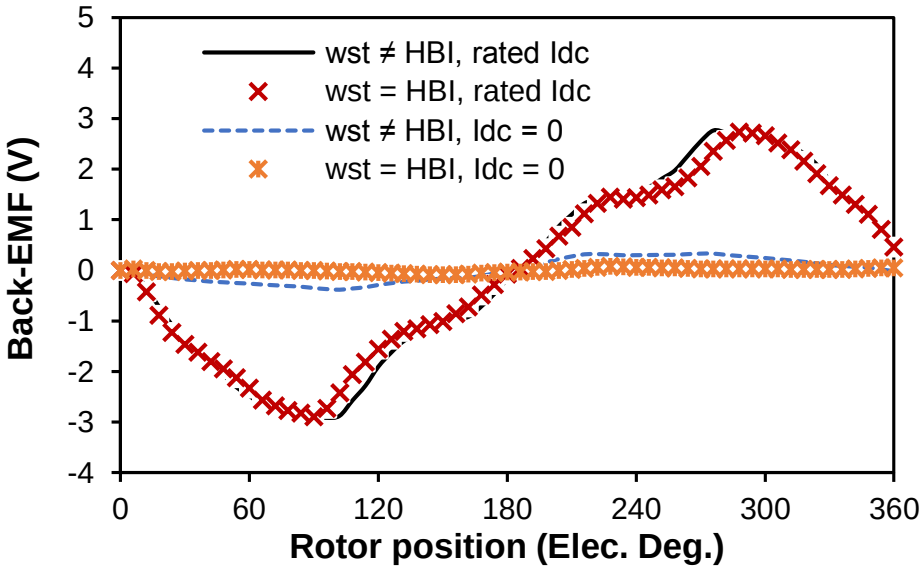

(a) Phase 'A' back-EMF waveforms

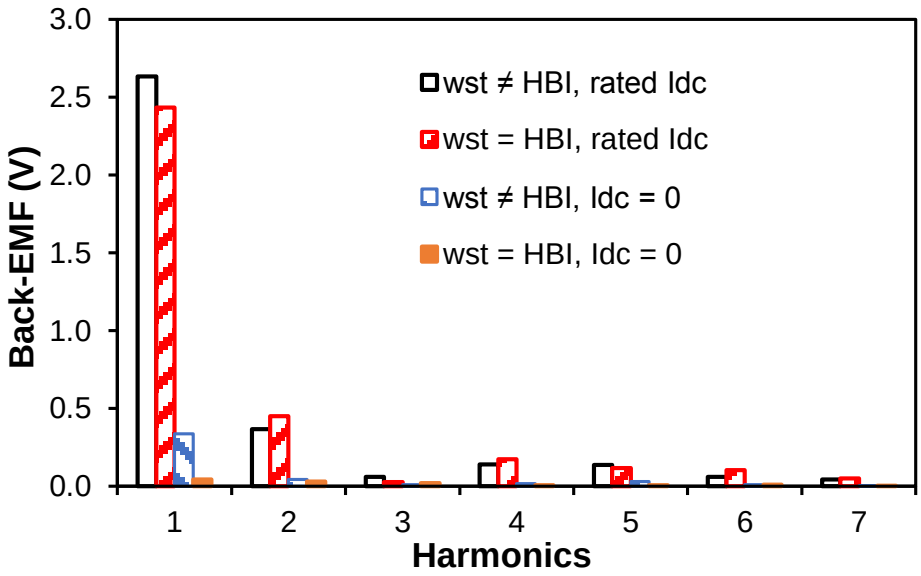

(b) Harmonics, Phase 'A'

Fig. 4.8 Phase back-EMF for MS-HSSPMMs with different stator tooth width and back-iron conditions (rotating speed = 400rpm)

B. Open-circuit phase back-EMF

The phase back-EMF waveforms for Phase 'A' of the machines are shown in Fig. 4.8. From Fig. 4.8(a), it shows that both MS-HSSPMMs have almost negligible back-EMF with 0A DC current excitation since the flux lines are almost shunted in the stator segments. However, from the harmonics shown in Fig. 4.8(b), the magnitude for Ms-HSSPM with different stator tooth and back-iron thickness is not negligible which is because the flux leakage as shown in Fig.

4.6. When the machines have a rated DC current excitation, the waveforms of the MS-HSSPMs are non-sinusoidal. Thus, the torque ripple of the machines might be large.

C. Torque performance

The cogging torque on open-circuit with no DC current excitation is caused by PM flux leakage, and is almost negligible for the Ms-HSSPMMs. When the machines are excited with rated DC current, the orders of harmonics in the cogging torque (N_k) can be calculated by (4.1)

$$N_k = \frac{LCM\{N_s, N_r\}}{N_r} k \ (k = 1,2,3 \dots) \tag{4.1}$$

where N_s, N_r, LCM are the number of stator poles, the number of rotor poles and the least common multiple, respectively.

The cogging torque waveforms and the frequencies of cogging torque are shown in Fig. 4.9(a) and (b), respectively. The MS-HSSPMMs remain to have small cogging torque, however, the machine with equal stator tooth and back-iron thickness has larger cogging torque. The 3rd and 6th harmonics for the machines are relatively large.

Fig. 4.10(a) shows the average torque waveforms of the two machines at rated armature current with rated DC current excitation. It is observed that the MS-HSSPM machines have large torque ripple due to the non-sinusoidal back-EMF waveforms. Fig. 4.10(c) shows the waveforms of average torque per PM volume. Due to the less usage of PMs, the machine with equal stator tooth and back-iron thickness has larger value for torque per PM volume, which is almost twice larger than the machine with unequal stator tooth and back-iron thickness. Due to the torque against current angle characteristics, as shown in Fig. 4.10(d), the machine with unequal stator tooth and back-iron thickness can achieve the maximum average torque when the current angle is 0. For the other machine, it may achieve the maximum average torque when the current angle is 6°. The bias can be caused by the interaction between PM and DC excitation and the DC excitation might be the main cause to cause flux distortion. Since the machines can achieve the maximum torque almost at 0° current angle, they have small/negligible reluctance torque. From the torque against copper loss waveforms which are shown in Fig. 4.10(e), it shows that when the copper loss is less than 60W, the torque of the machine with unequal stator tooth and back-iron thickness increases faster than that of the other machine, while over 60W, the torque increasing rates for both machines are slow down. Table 4.4 shows the torque performance for the MS-HSSPMMs.

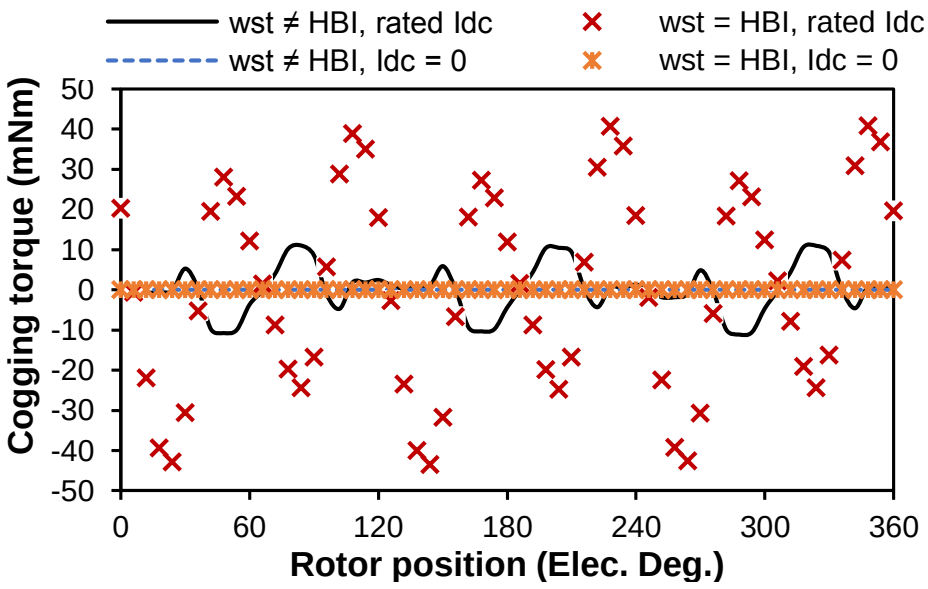

(a) Cogging torque waveforms

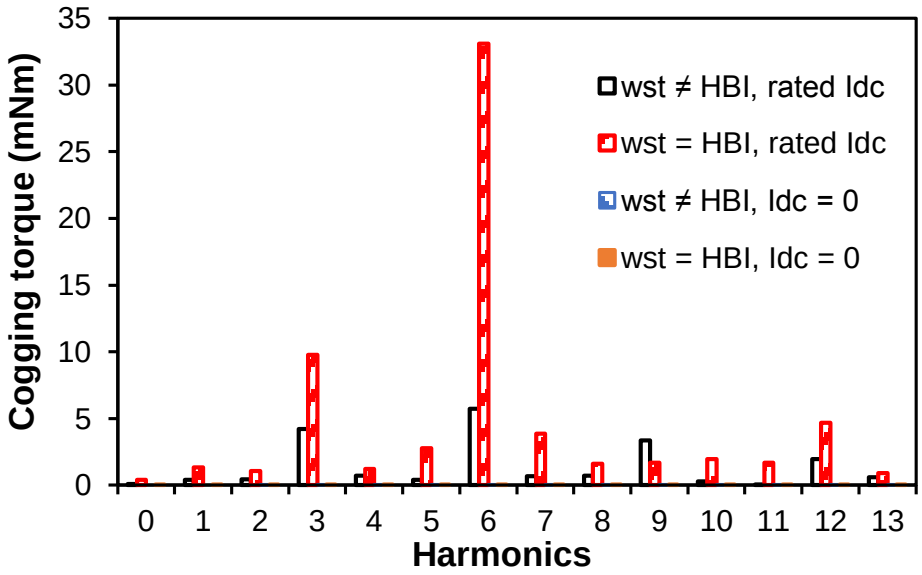

(b) Harmonics

Fig. 4.9 Cogging torque for MS-HSSPMMs with different stator tooth width and back-iron condition

Table 4.4 Torque performance for MS-HSSPMMs at rated DC current excitation

	$w_{st} \neq H_{BI}$	$w_{st} = H_{BI}$
Copper loss (W)	60	60
Current, I_{rated}/I_{dc} (A)	6.34	6.49
Average torque (Nm)	0.80	0.74
Torque ripple (%)	69.36	80.38
Average torque/PM volume Nm/m^3	133547.2	266261.5

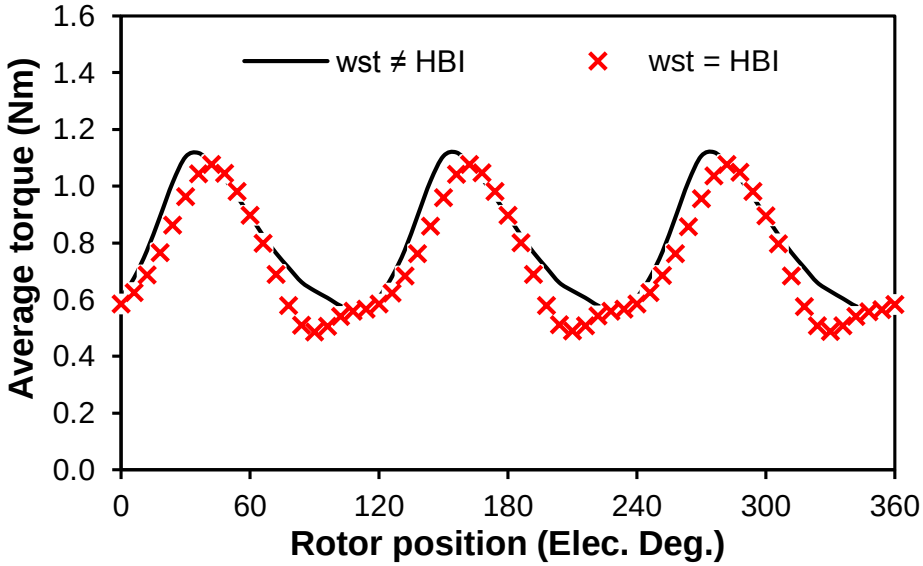

(a) Electromagnetic torque waveforms

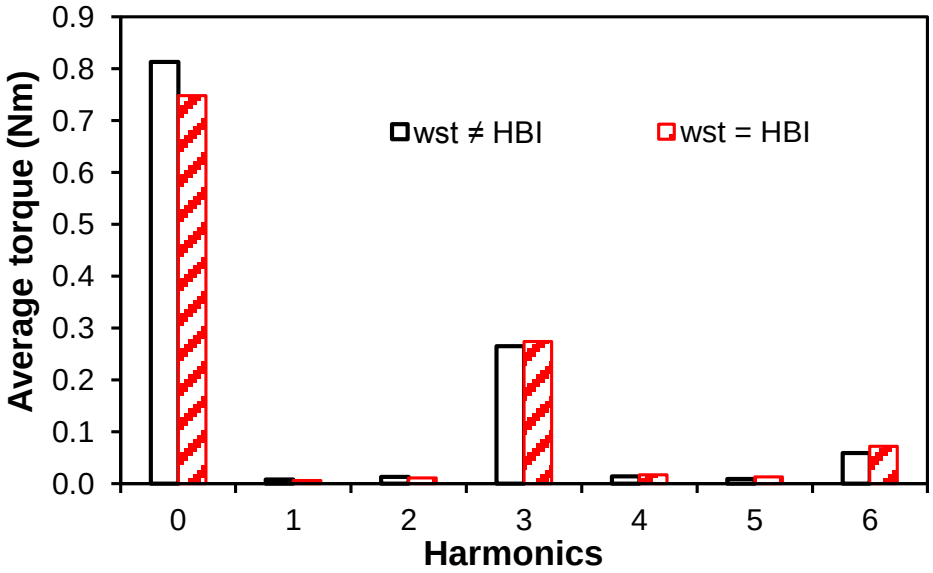

(b) Harmonics

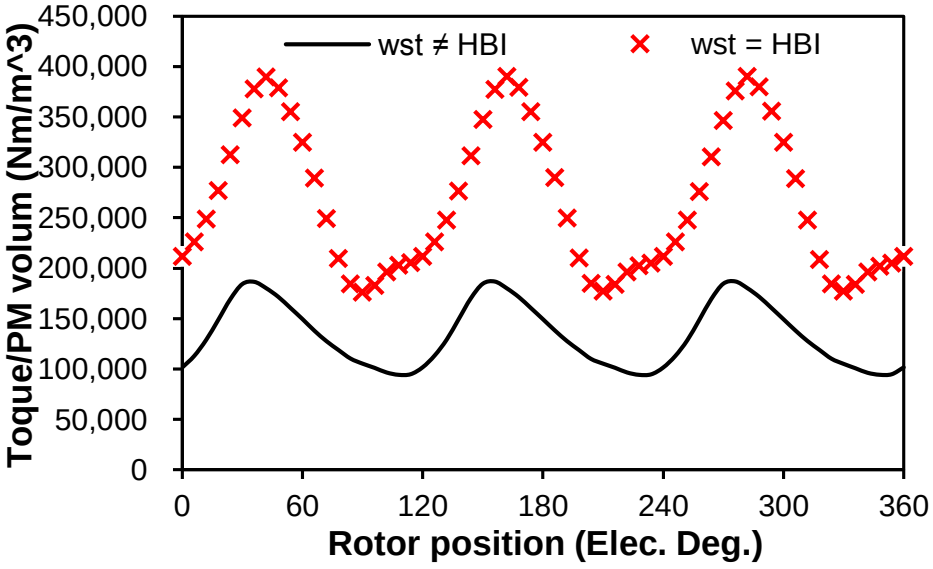

(c) Electromagnetic torque per PM volume waveforms

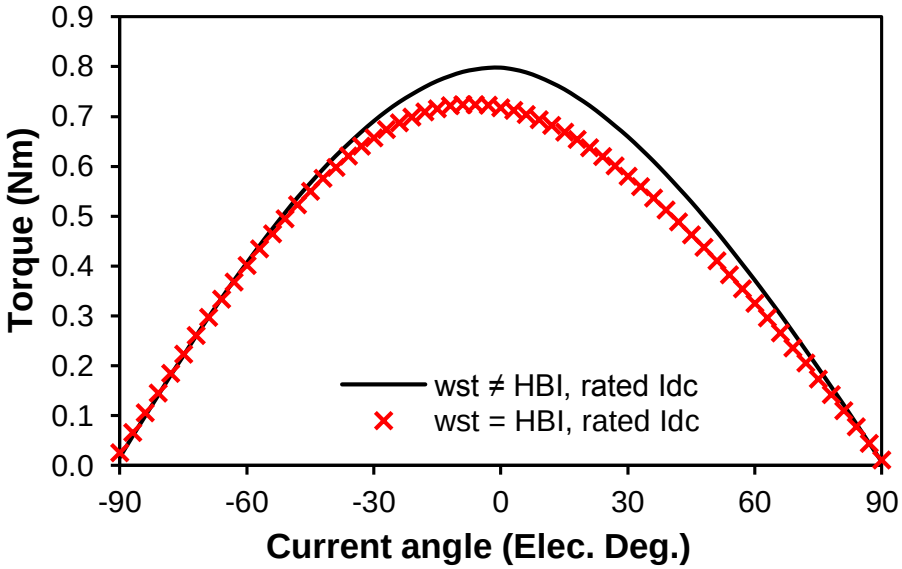

(d) Electromagnetic torque and current angle characteristics

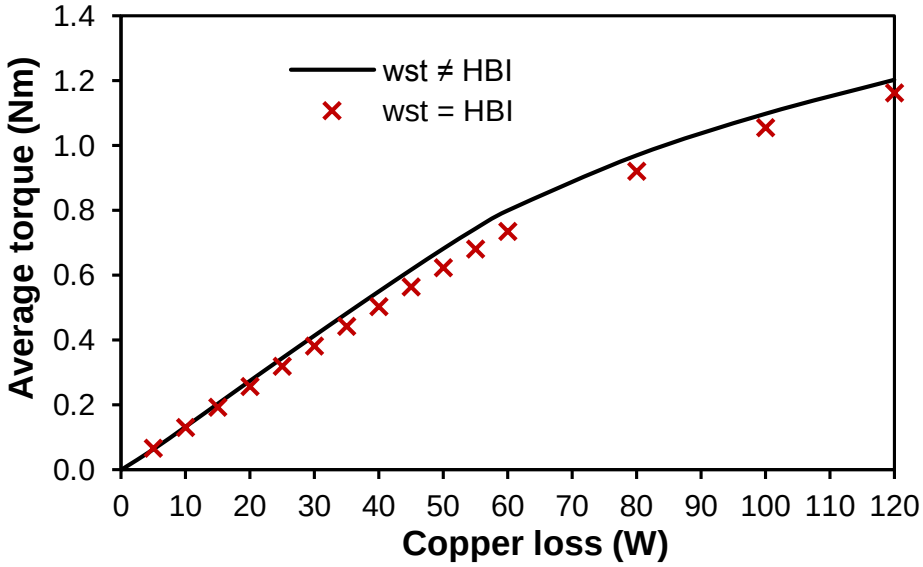

(e) Average torque against copper loss waveforms

Fig. 4.10 Electromagnetic torque performance for MS-HSSPMMs with equal/unequal stator tooth width and back-iron thickness

4.3.3. Losses

The variations of iron losses and PM eddy current loss with rotor speed at total machine copper loss of 60W are shown in Fig. 4.11. Fig. 4.11 shows that for all the iron losses, the MS-HSSPMM with unequal stator tooth width and back-iron thickness is slightly higher than the other machine. While, due to the large difference of PM volume for the two machines, the PM eddy current loss for the machine with unequal stator tooth width and back-iron thickness is much higher than that for the other machine. The difference between losses for both machines increases with the raising rotor rotating speed. About the variations of iron losses and PM eddy current losses with total copper losses for both machines, the MS-HSSPMM with equal stator tooth width and back-iron thickness has slightly higher total iron loss than the other machine when the machine is over 60W, which is shown in Fig. 4.12(a). From Fig. 4.12(a), both machines have fast increasing iron loss when the copper loss is lower than 100W. The PM eddy current loss for the machine with equal stator tooth width and back-iron thickness remains low with the increasing copper loss because of the less PM usage, which is shown in Fig. 4.12(b).

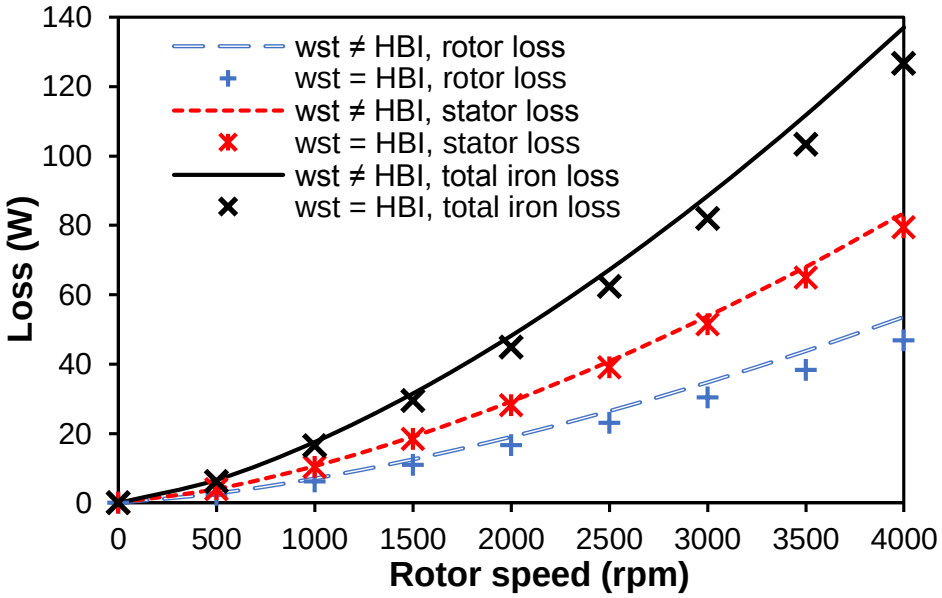

(a) Iron losses (total copper loss = 60W)

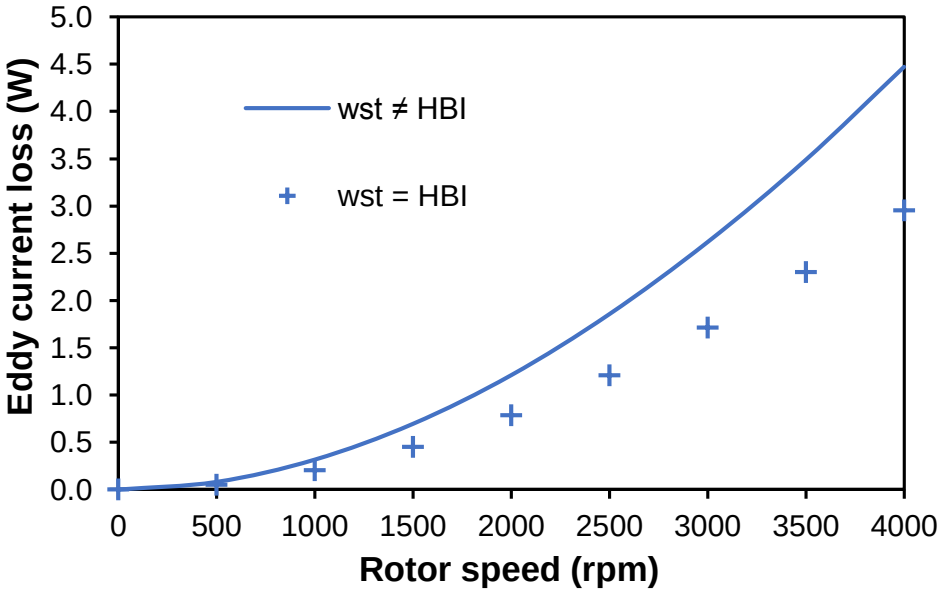

(b) PM Eddy current losses

Fig. 4.11 Average iron losses and PM eddy current losses for MS-HSSPMMs.

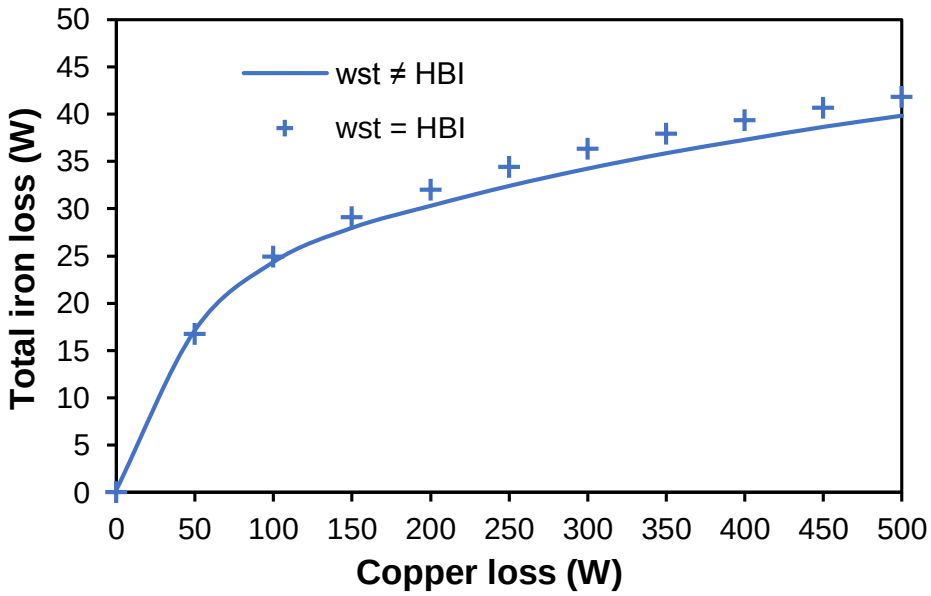

(a) Iron loss

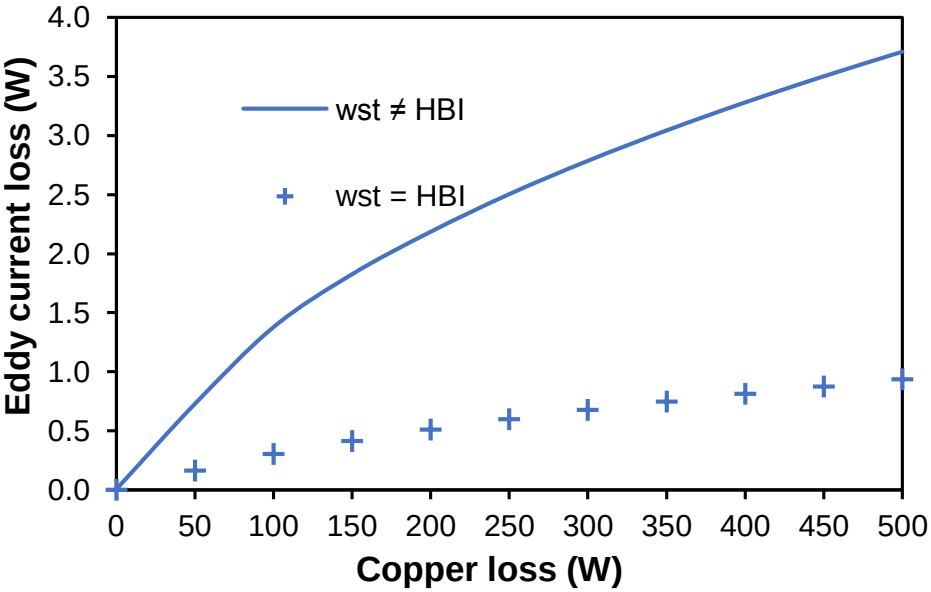

(b) PM eddy current loss

Fig. 4.12 Loss characteristics against copper loss for MS-HSSPMMs

4.4. Stator-rotor pole combinations of the machines with/without DC excitation

4.4.1. Feasible stator and rotor pole combination

Since the modular stator machines in this chapter can be modified form the SL-F1A1 HSSPMM, the determination of stator pole and rotor pole combinations can follow the method in [93, 129], which is given by (4.2)

$$\frac{N_s}{GCD(N_r, N_s)} = kN_{ph} \tag{4.2}$$

$$N_s = k_1 N_{phase} \quad k_1 = 1,2, \ldots \tag{4.3}$$

$$N_r = N_s \pm k_2 \quad k_2 = 1,2, \ldots \tag{4.4}$$

where N_s, N_r, N_{ph}, *GCD()* are the number of stator pole, the number of rotor pole, the number of phase and the greatest common driver, respectively. For the SL-F1A1 HSSPMMs, the phase number of the machines is 3 and the number of stator poles is fixed to 12. Thus, the feasible stator pole and rotor pole combinations can be obtained as 12/8, 12/10, 12/11, 12/13, 12/14, 12/16 stator /rotor poles etc. Meanwhile, the MS-HSSPMMs can have the rotor pole number of 8, 10, 11, 13, 14, 16 and etc.

When the DC windings in the MS-HSSPMMs are removed, the stator/rotor pole combinations remain the same as the HSSPMMs with DC excitation which is used to adjust the PM flux. The MS- stator slot PM machines (SSPMMs), the machine can be modified form the MS-HSSPMMs by removing DC coils. Thus, the MS-SSPMMs have similar feasible stator/rotor combinations as the MS-HSSPMMs.

4.4.2. Winding analysis

As the MS-HSSPMMs can be modified from the HSSPMMs and the MS-SSPMMs can be modified from the MS-HSSPMMs, the method of determining the EMF and phase coil phasors can be followed according to that presented in [93, 129] as well. Fig. 4.13(a) shows the coil position along the stator circumference, where α_m (in mechanical degree) is the angle between adjacent coil positions. Fig. 4.13(b) gives an example of coil back-EMF (α_e in mechanical degree) for the 11-rotor pole modular stator machine. While the relationship between coil back-EMF and coil position can be calculated as α_e equals α_m multiplied by N_r (rotor pole number). According to the coil back-EMF positon, the coils for phases can be grouped as shown in Fig. 4.14. Since the magnetization direction of the PMs has influence on the phase shift of the coil back-EMF, an (') is used to identify the coils with reversed polarity. In addition, since the machines have the concentrated armature winding connections on alternative stator tooth, only one armature coil is located in one slot area. Hence, the coil back-EMF phasors have only one set of balanced three phase windings. Meanwhile, for all the machines, the total numbers of turns are the same.

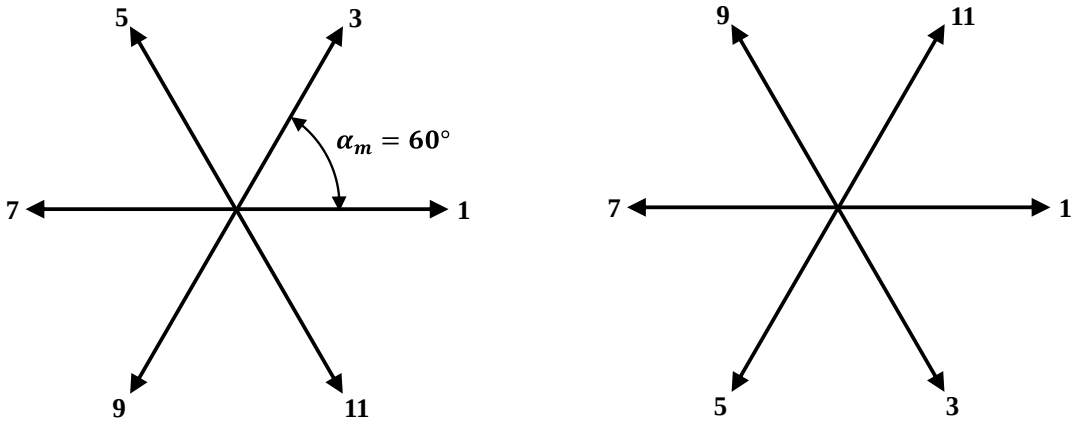

(a) coil position (b) coil back-EMF position

Fig. 4.13 Back-EMF and phase coil phasors for modular stator machines.

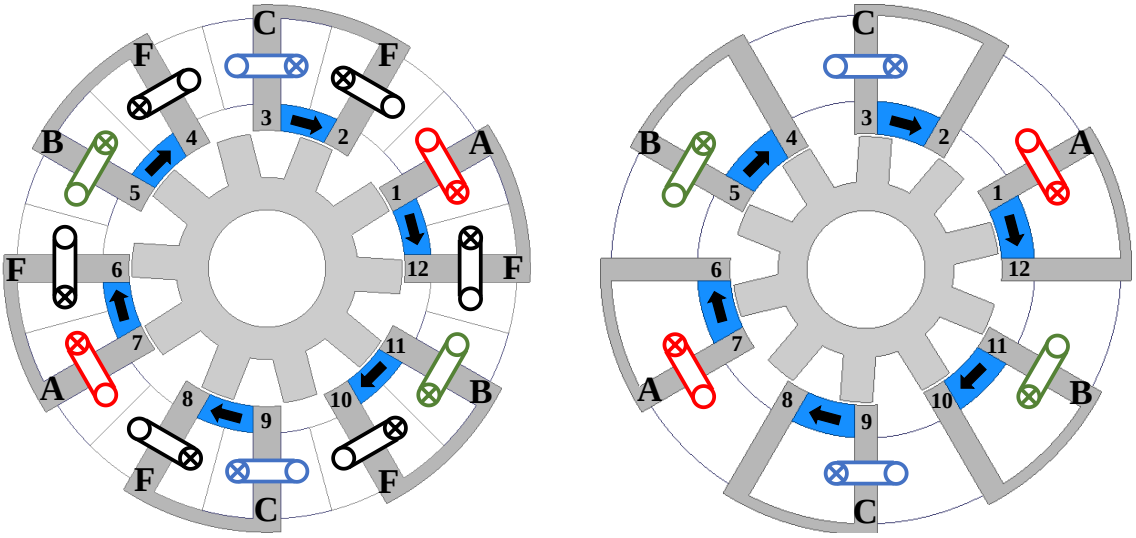

(a) MS-HSSPMM (b) MS-SSPMM

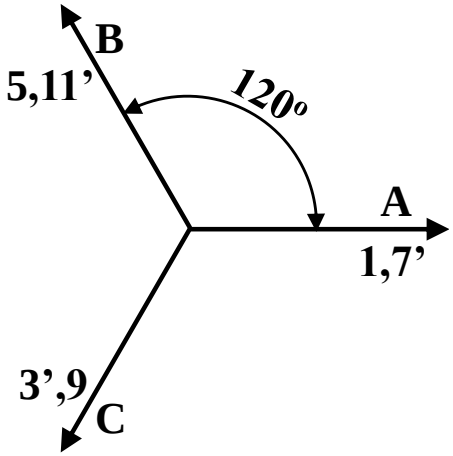

Fundamental back-EMF phasors

(I) 10-rotor pole machine

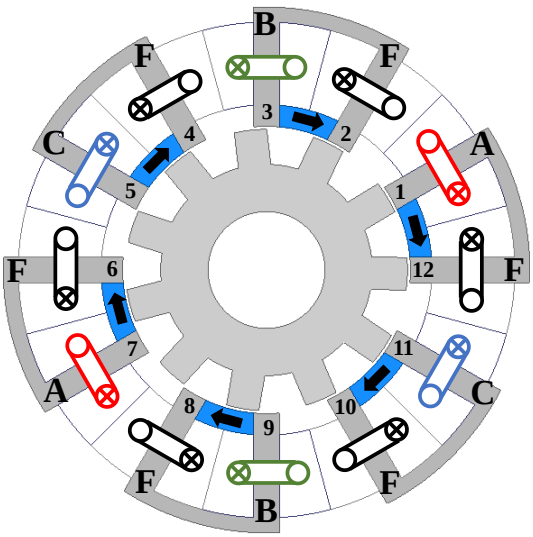

(a) MS-HSSPMM

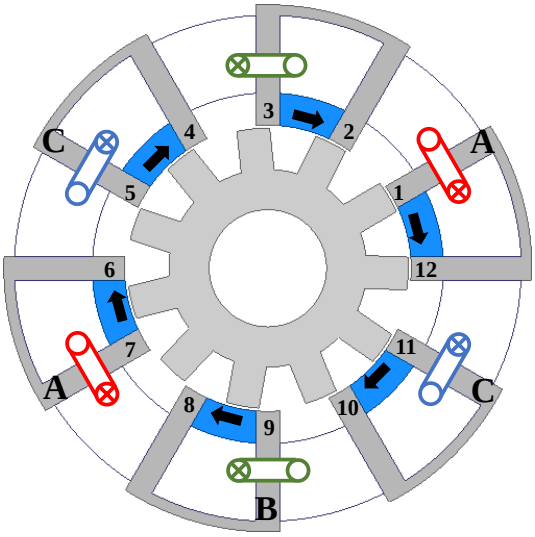

(b) MS-SSPMM

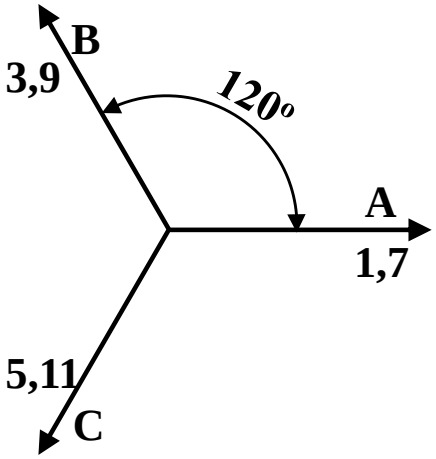

Fundamental back-EMF phasors

(II) 11-rotor pole machine

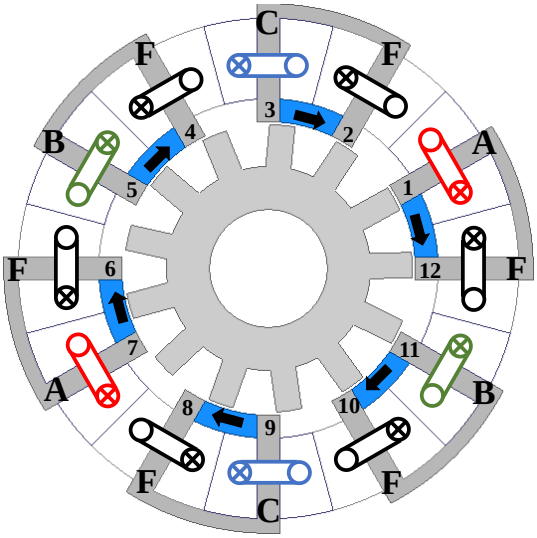

(a) MS-HSSPMM

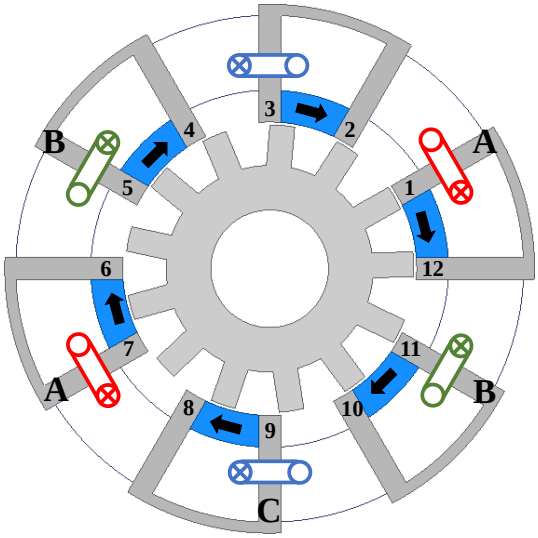

(b) MS-SSPMM

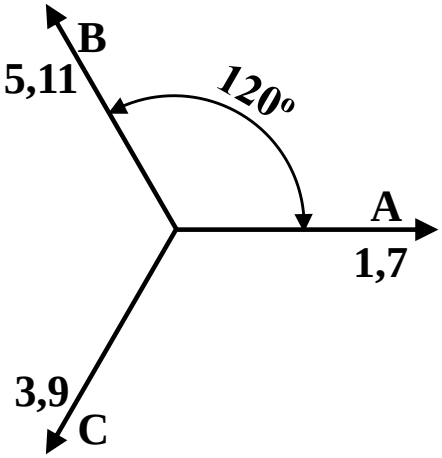

Fundamental back-EMF phasors

(III) 13-rotor pole machine

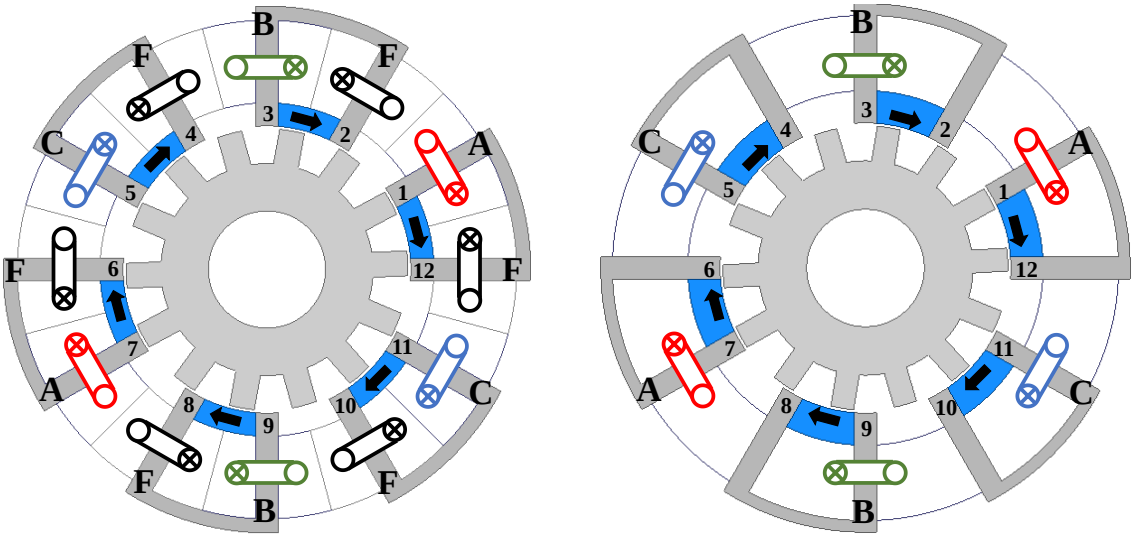

(a) MS-HSSPMM (b) MS-SSPMM

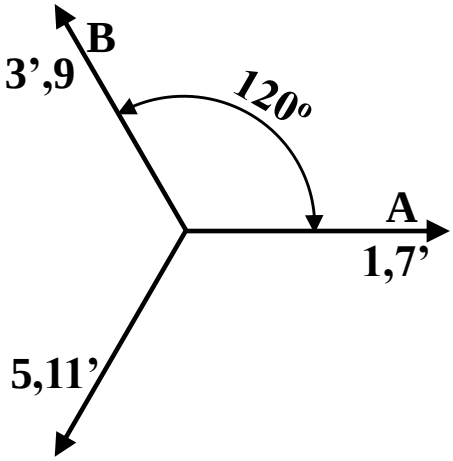

Fundamental back-EMF phasors

(IV) 14-rotor pole machine

Fig. 4.13 Cross sections with winding connections and fundamental back-EMF phasors of MS-HSSPMMs and MS-SSPMMs with different stator/rotor pole combinations.

The winding factor (k_w) of the machines can be calculated by multiplying the pitch factor (k_p) and the distribution factor (k_d). The distribution factor for multiple harmonics can be calculated by

$$k_{di} = \frac{\sin(\frac{q\sigma i}{2})}{q\sin(\frac{\sigma i}{2})} \tag{4.5}$$

where i, q and σ are harmonic order, the number of coil per phase and angular phase angle between adjacent EMF phasors on one phase, respectively. The pitch factor of the 'E-core'

stator segmented modular stator machine can be determined by (4.6) which is described in detail in [124].

$$k_{pi} = \sin(\frac{(\tau_s - \Delta)}{\tau_r}\frac{\pi}{2}i) \tag{4.6}$$

$$\Delta = \sin^{-1}(\frac{Flux\ gap}{2 \times R_{SI}}) \tag{4.7}$$

$$\tau_s = \frac{2\pi}{N_s} \tag{4.8}$$

$$\tau_p = \frac{2\pi}{N_r} \tag{4.9}$$

where τ_r, τ_p, R_{SI}, N_s and N_r are the rotor pole pitch, stator coil pitch, stator inner radius, number of stator pole and number of rotor pole, respectively.

However, in this chapter, the modular stator machines have 'U-shaped' stator segments, and for convenience in design, the gap between two adjacent stator segments equals to one stator slot. Thus, the pitch factor of the machines is similar to that in the non-modular machine which is shown in (4.10). Hence, the winding factor of the machines are calculated by (4.11).

$$k_{pi} = \sin(\frac{\tau_s}{\tau_r}\frac{\pi}{2}i) = \sin(\frac{N_r}{N_s}\frac{\pi}{2}i) = \cos(\pi i\left(1 - \frac{N_r}{N_s}\right)) \tag{4.10}$$

$$k_{wi} = k_{di}k_{pi} \tag{4.11}$$

The harmonic winding factors for the MS-HSSPMMs and MS-SSPMMs are displayed in Table 4.5. Since the winding factors for MS-HSSPMM and MS-SSPM with the same stator/rotor pole combination are the same, the values of the winding factor can be shown in one table. According to Table 4.5, it shows that the machines with 10-, 11-, 13-, 14-rotor pole have high fundamental winding factor. In this case, the machines are modelled and investigated for these four stator/rotor pole combinations. For all the machines, since the single layer windings have 120° in elec. From the distribution of adjacent coil EMF phasors, the distribution factor of the machines is equal to 1. The 10- and 14-rotor pole machines and 11- and 13- rotor pole machines have similar winding factor, respectively. The fundamental harmonics for the 11-and 13-rotor pole machines are higher than those for the 10- and 14- rotor pole machines, which might lead to the higher electromagnetic torque for the 11- and 13-rotor pole machines. The 11- and 13-rotor pole machines have very low winding factors for the 5th and 7th harmonics and have no 3rd harmonics. The 10- and 14-rotor pole machines have no 6th harmonics in winding factor.

However, since the machines have modular stator, the harmonic winding factors except the fundamental harmonics might be affected by the flux gap.

Table 4.5 Harmonic winding factors for MS-HSSPMMs and MS-SSPMMs machines with single layer armature windings

N_r		i = 1	i = 2	i = 3	i = 4	i = 5	i = 6	i = 7
10	k_{di}	1	1	1	1	1	1	1
	k_{pi}	0.87	0.5	0	-0.5	0.87	-1	-0.87
	k_{wi}	0.87	0.5	0	-0.5	0.87	-1	-0.87
11	k_{di}	1	1	1	1	1	1	1
	k_{pi}	0.97	0.87	0.71	0.5	0.26	0	-0.26
	k_{wi}	0.97	0.87	0.71	0.5	0.26	0	-0.26
13	k_{di}	1	1	1	1	1	1	1
	k_{pi}	0.97	0.87	0.71	0.5	0.26	0	-0.26
	k_{wi}	0.97	0.87	0.71	0.5	0.26	0	-0.26
14	k_{di}	1	1	1	1	1	1	1
	k_{pi}	0.87	0.5	0	-0.5	0.87	-1	-0.87
	k_{wi}	0.87	0.5	0	-0.5	0.87	-1	-0.87

4.4.3. Design parameters and optimal designs

The restriction conditions and the design optimisation parameters for the Genetic Algorithm global optimization are described in detail in section 4.3. As the optimization for the different stator/rotor pole combinations, the stator tooth width and stator back-iron thickness do not have to be fixed. The total numbers of turns of armature and field windings for MS-HSSPMMs with different rotor poles are the same. For the MS-SSPMMs, since the field winding is removed, and the slot area for armature winding is twice than the MS-HSSPMMs. Also, the total numbers of turns of windings for different stator/rotor pole combinations are kept the same. The optimized design parameters are given in Table 4.6 and Table 4.7. From the tables, it shows that the MS-HSSPMMs have larger stator back-iron thickness than the MS-SSPMMs, while the PM volume of the MS-HSSPMMs are less than that of the MS-SSPMMs.

Table 4.6 Optimized design parameters for MS-HSSPMMs

	10 pole	11 pole	13 pole	14 pole
Back-iron thickness H_{BI}, mm	2.29	2.57	2.46	2.41
Stator tooth width w_{st}, mm	4.72	4.37	3.91	3.85
Stator pole arc θ_{st}, deg.	11.51	10.19	8.99	9.00
Rotor pole arc θ_{rt}, deg.	14.48	13.33	10.16	10.19
PM height H_{PM}, mm	4.54	3.70	3.90	3.94
PM volume V_{PM}, mm^3	5990.8	5249.7	5948.0	5932.2
Total slot area (AC), mm^2	1209.9	1200.6	1214.2	1248.2
Total slot area (DC), mm^2	1209.9	1200.6	1214.2	1248.2
Split ratio	0.512	0.535	0.543	0.534
Rotor outer radius R_{RO}, mm	23.06	24.09	24.44	24.05
Stator inner radius R_{SI}, mm	23.56	24.59	24.94	24.55
Rotor tooth height H_{rt}, mm	7.62	6.06	7.15	5.96
Turn/phase (armature)	184			
Turns for DC windings	552			

Table 4.7 Optimized design parameters for MS-SSPMMs

	10 pole	11 pole	13 pole	14 pole
Back-iron thickness H_{BI}, mm	1.84	1.81	1.87	1.98
Stator tooth width w_{st}, mm	3.98	4.19	3.77	3.78
Stator pole arc θ_{st}, deg.	9.90	9.83	8.67	8.78
Rotor pole arc θ_{rt}, deg.	14.02	13.49	9.91	9.30
PM height H_{PM}, mm	5.56	5.50	5.41	5.48
PM volume V_{PM}, mm^3	7959.7	8278.9	8696	8698.2
Total slot area, mm^2	2586.4	2380.9	2365.9	2367.0
Split ratio	0.501	0.532	0.544	0.538
Rotor outer radius R_{RO}, mm	22.54	23.93	24.47	24.21
Stator inner radius R_{SI}, mm	23.04	24.43	24.97	24.71
Rotor tooth height H_{rt}, mm	7.74	7.14	6.93	5.98
Turn/phase (armature)	184			

4.5. Electromagnetic performance comparison

4.5.1. Open-circuit analysis

A. Flux distribution

The open-circuit flux distributions of both MS-HSSPMMs and MS-SSPMMs are shown in Fig. 4.14. From Fig. 4.14, it shows that the flux lines produced by PMs are almost shunted in the stator segments for the MS-HSSPMMs, while the MS-SSPMMs have large flux-leakage due to the stator magnetic saturation. When the MS-HSSPMMs are supplied by a rated DC current excitation, the flux distributions are enhanced obviously, as shown in Fig. 4.15. For the 11- and 13-rotor pole machines, the flux distributions are asymmetric.

MS-HSSPMMs MS-SSPMMs

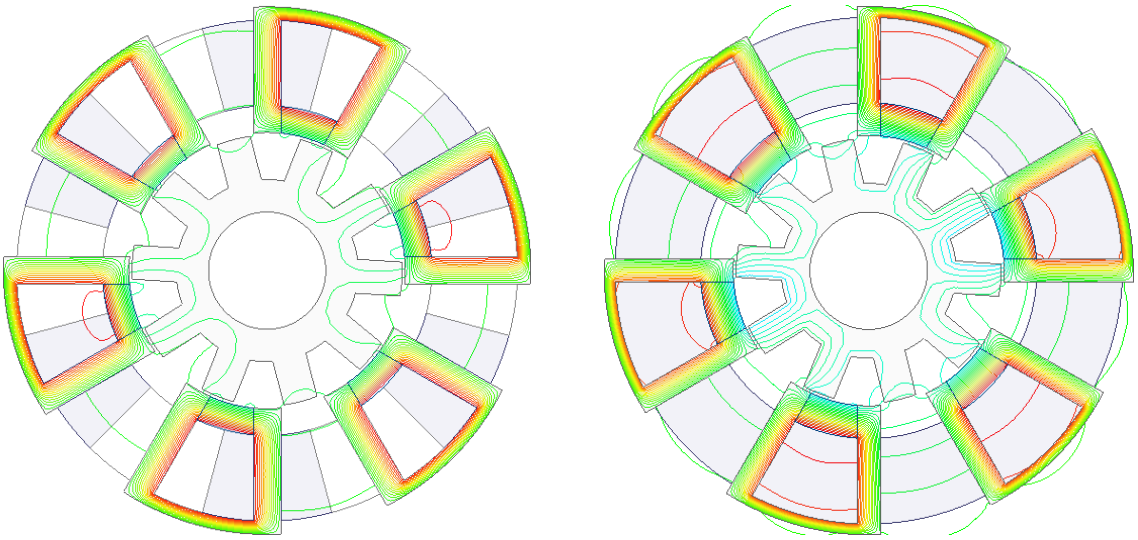

(a) Open-circuit flux distribution

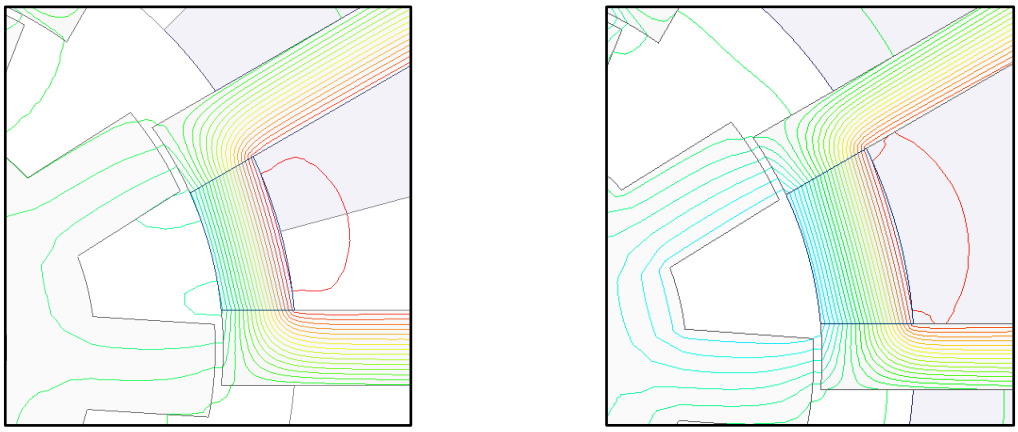

(b) Zoom in

(I) 10 rotor pole

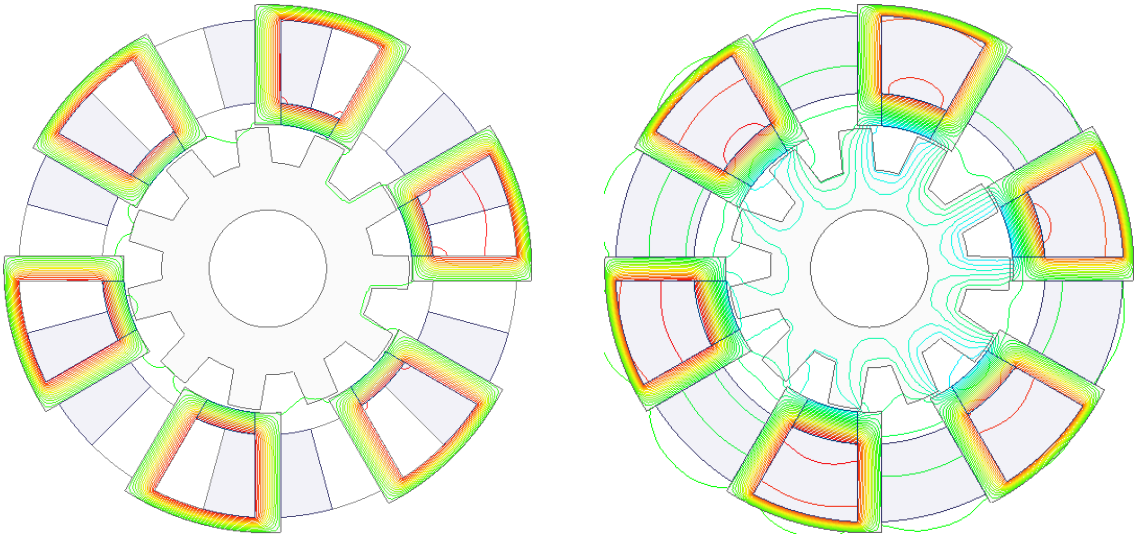

(a) Open-circuit flux distribution

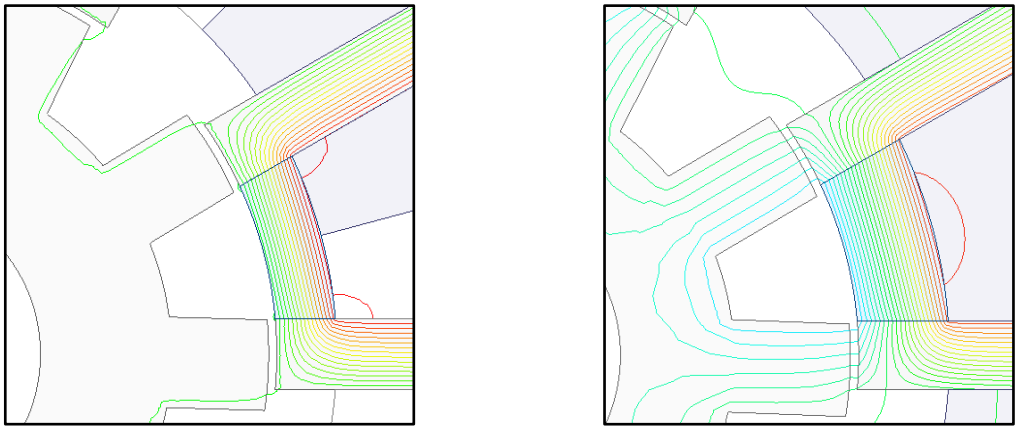

(b) Zoom in

(II) 11 rotor pole

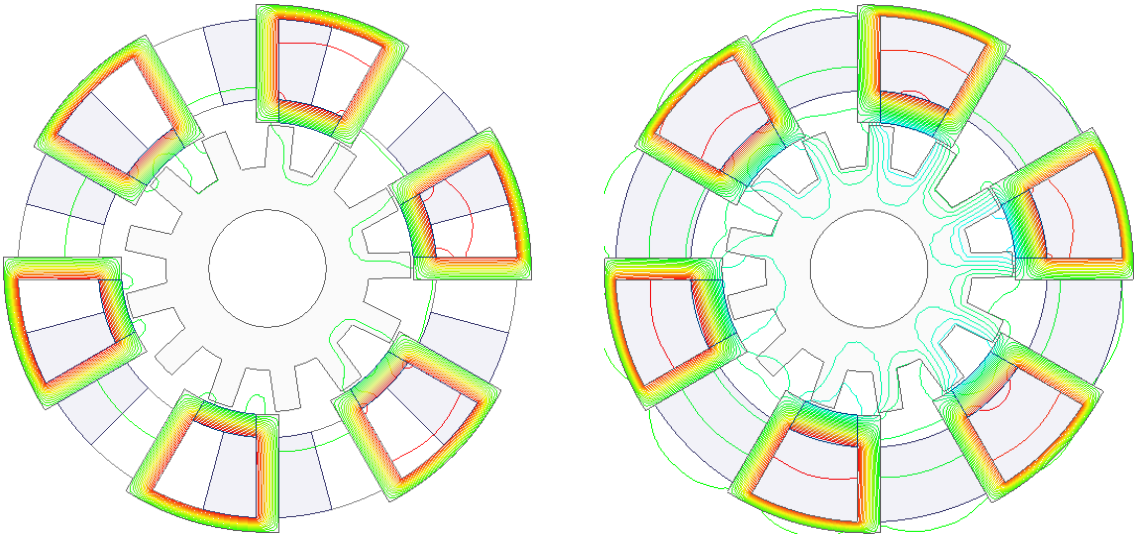

(a) Open-circuit flux distribution

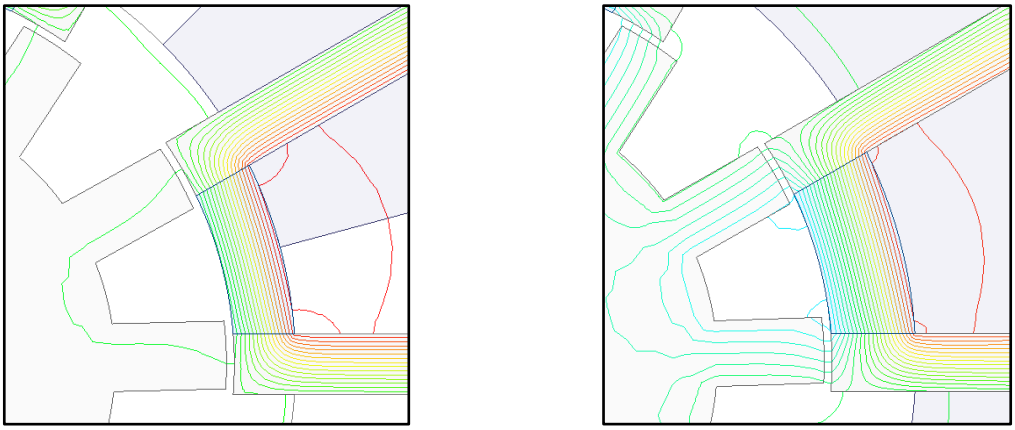

(b) Zoom in

(III) 13 rotor pole

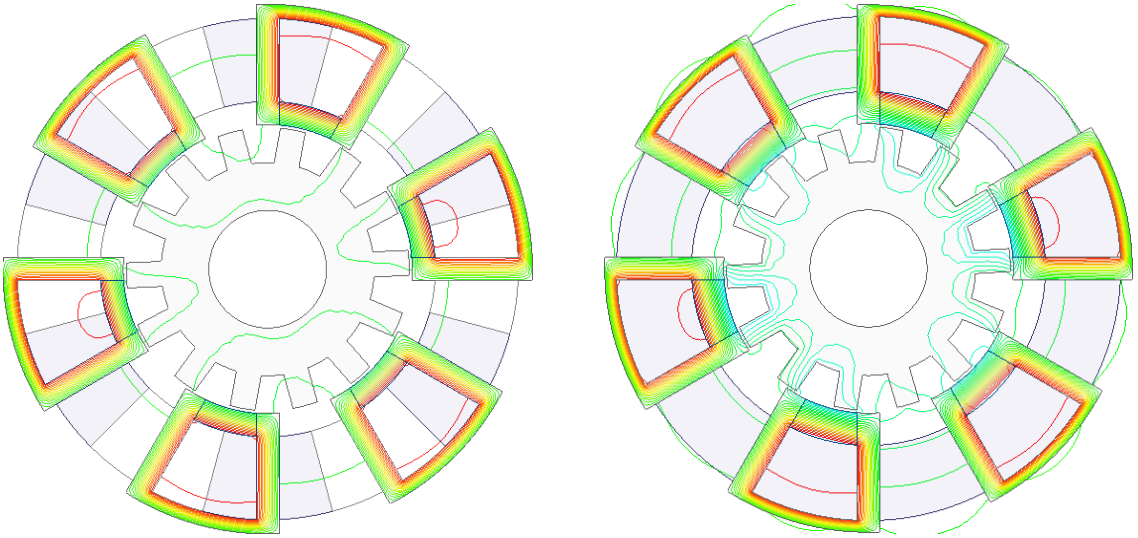

(a) Open-circuit flux distribution

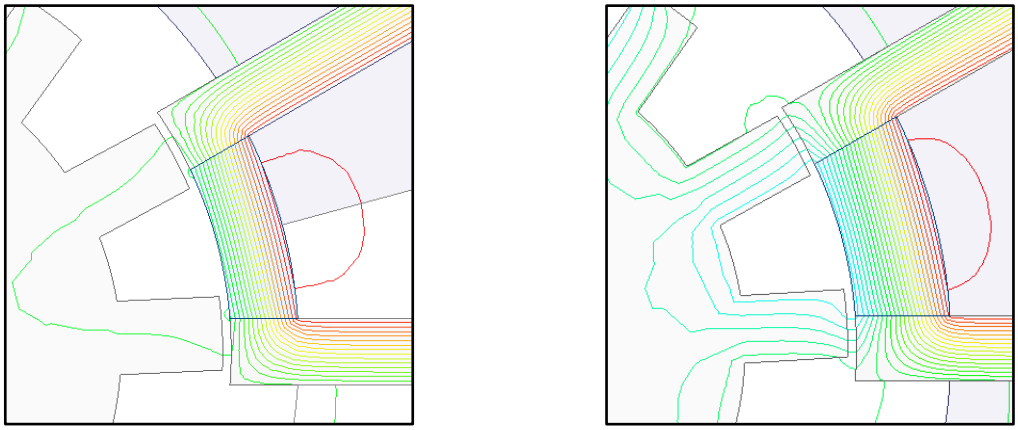

(b) Zoom in

(IV) 14 rotor pole

Fig. 4.14 Open circuit flux distributions for MS-HSSPMMs (I_{dc} = 0A) and MS-SSPMMs with different rotor poles.

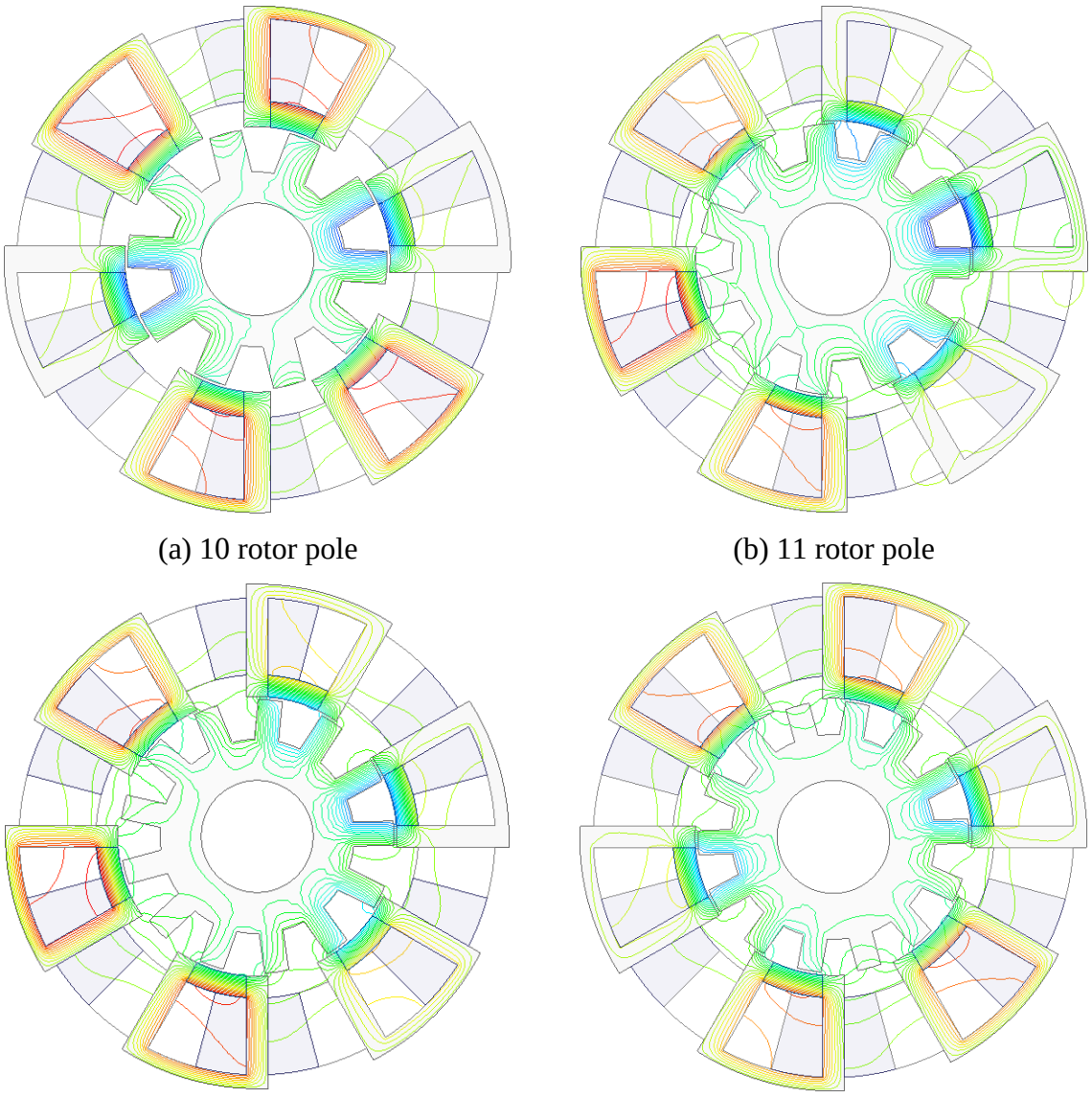

(a) 10 rotor pole (b) 11 rotor pole

(c) 13 rotor pole (d) 14 rotor pole

Fig. 4.15 Flux distributions of MS-HSSPMMs with I_{dc} = rated current.

B. Phase flux-linkage and back-EMF

According to Fig. 4.14, the flux-leakages in all MS-HSSPMMs are small. Thus, the open-circuit phase flux-linkage waveforms and phase back-EMF waveforms of the MS-HSSPMMs at no DC excitation condition are almost negligible, as shown in Fig. 4.16(a) and Fig. 4.17(a). When a rated DC current is supplied to the MS-HSSPMMs, the amplitudes of the flux-linkage waveforms and back-EMF waveforms are significantly increased. For the MS-SSPMMs, due to the large flux-leakage as shown in Fig. 4.14, the phase flux-linkage waveforms and the phase back-EMF waveforms are not negligible any more, as shown in Fig. 4.16(c) and Fig. 4.17(c). The flux-linkages of 10- and 14-rotor pole MS-HSSPMMs and MS-SSPMMs are unipolar.

This might be caused by the symmetry of the flux distribution which makes the fluxes in coils with the same magnetic polarity. The back-EMF waveforms of the 10- and 14-rotor pole MS-HSSPMMs are non-sinusoidal and asymmetric which might be because of the flux path restriction of the modular machines, which might lead to high torque ripple.

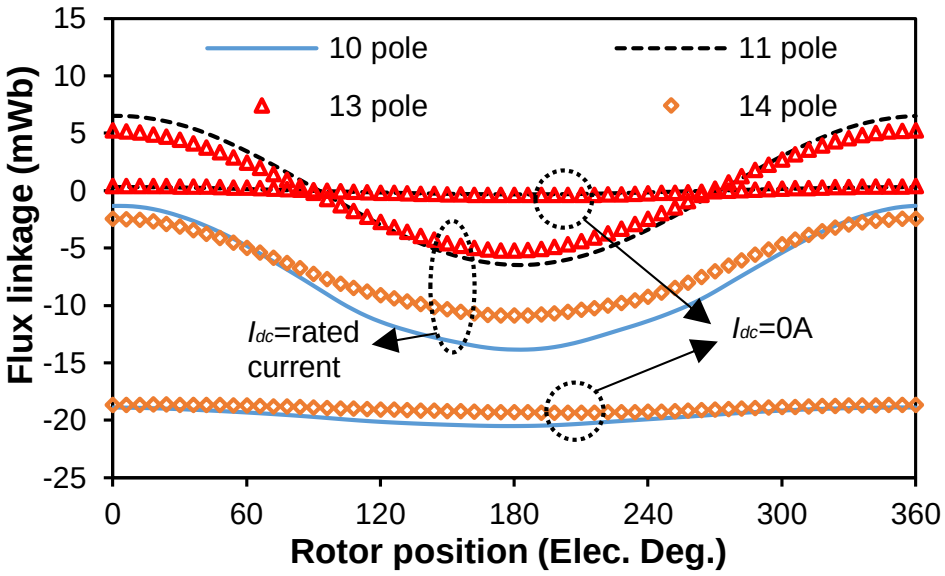

(a) Phase 'A' flux-linkage of MS-HSSPM with/without current excitation

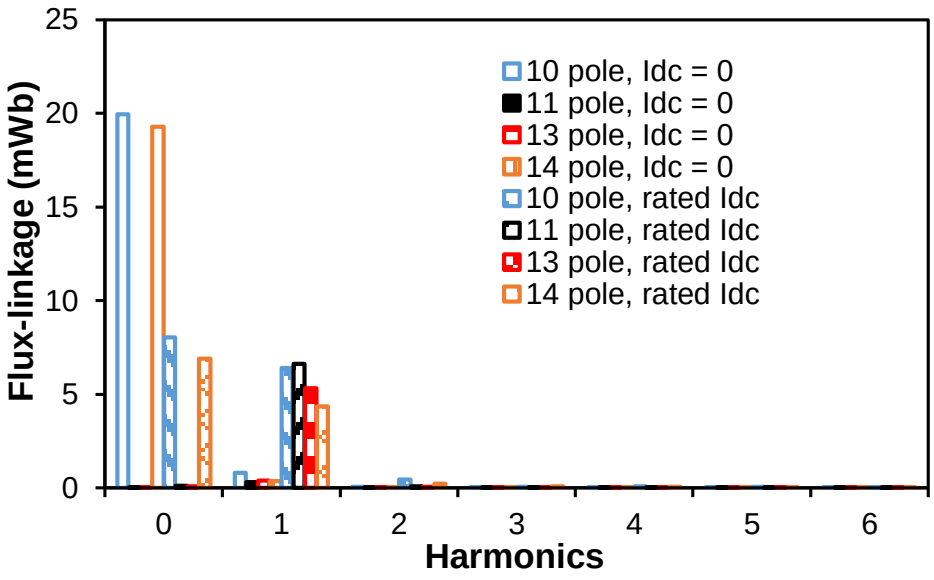

(b) Harmonics

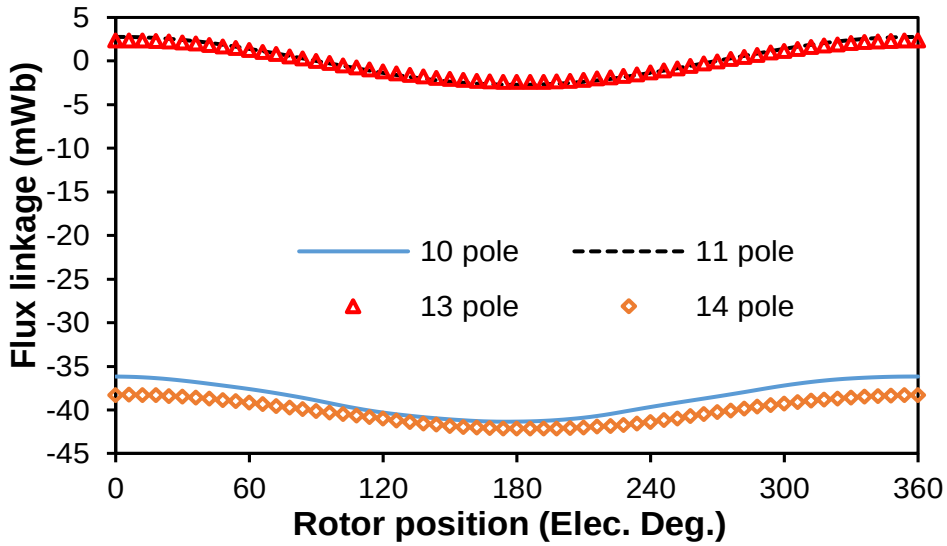

(c) Phase 'A' flux-linkage for MS-SSPM

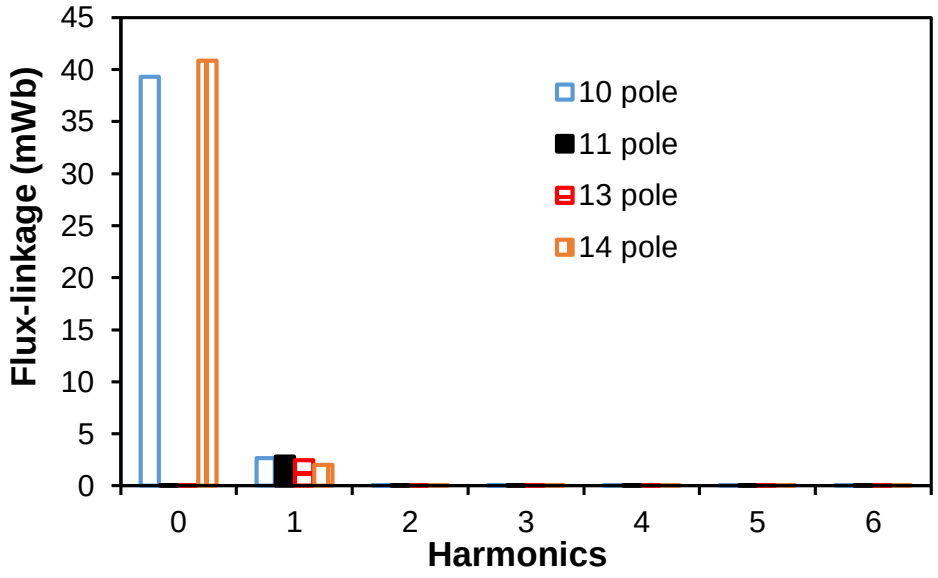

(d) Harmonics

Fig. 4.16 Open-circuit phase flux-linkages of MS-HSSPMMs and MS-SSPMMs with different stator/rotor pole combinations.

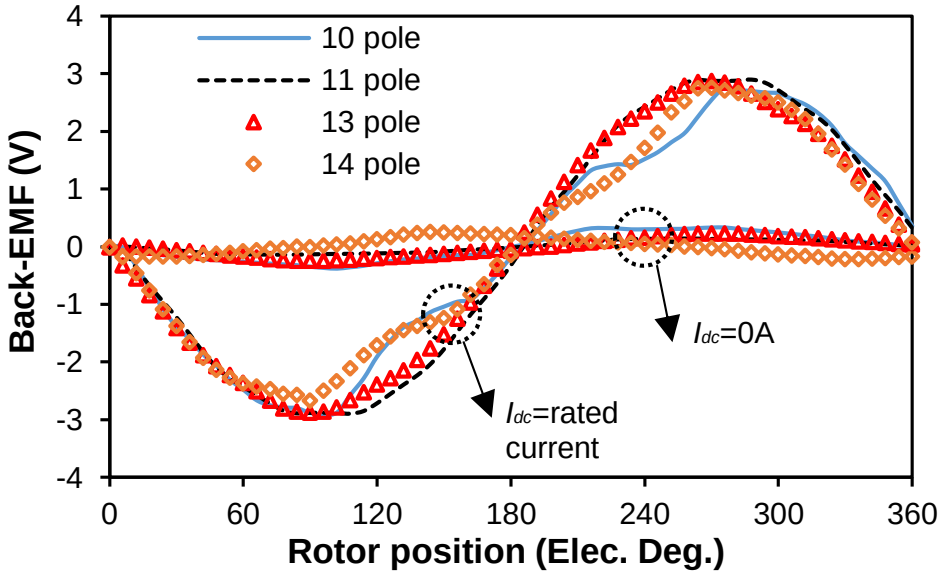

(a) Phase 'A' back-EMF for MS-HSSPM with/without current excitation

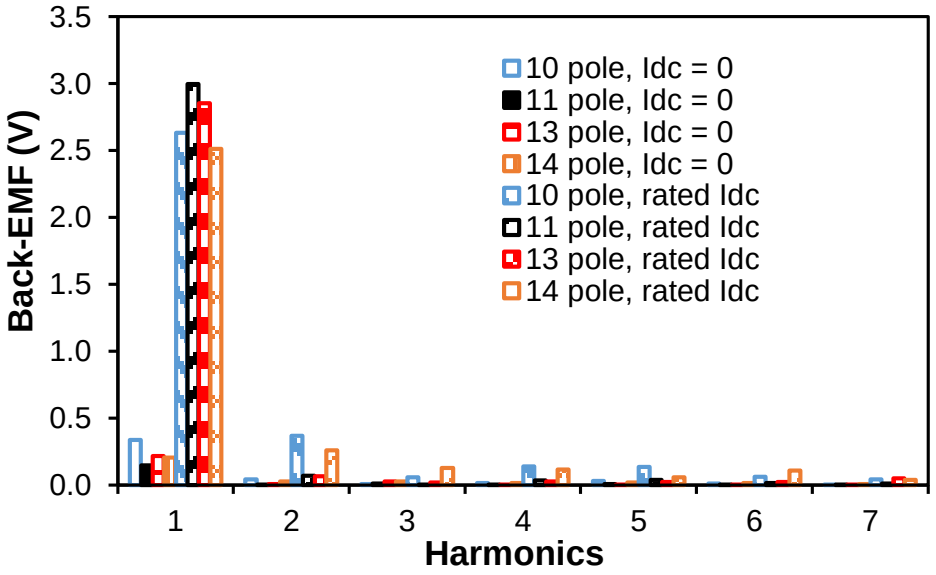

(b) Harmonics

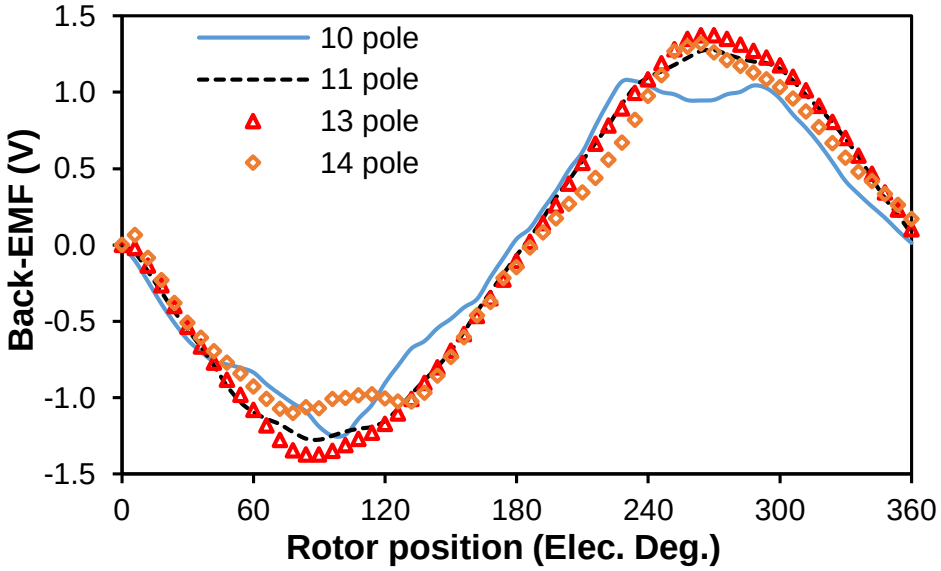

(c) Phase 'A' flux-linkage for MS-SSPM

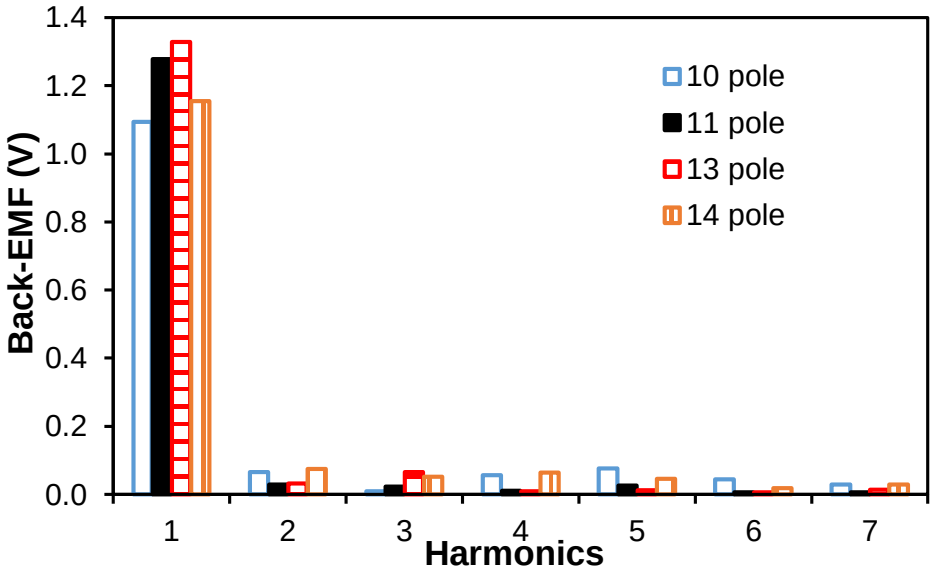

(d) Harmonics

Fig. 4.16 Open-circuit phase back-EMFs of MS-HSSPMMs and MS-SSPMMs with different stator/rotor pole combinations.

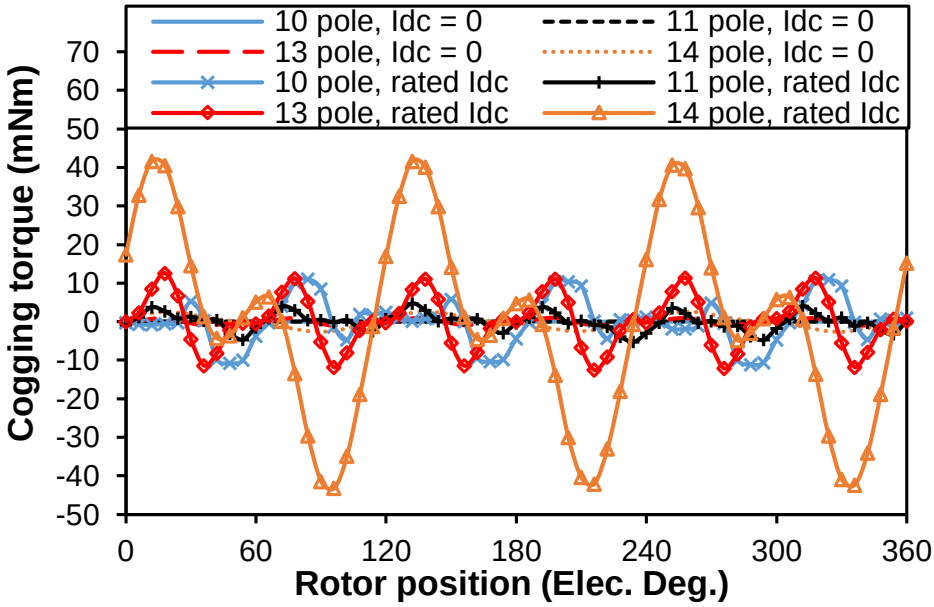

(a) Cogging torque for MS-HSSPMMs with/without current excitation

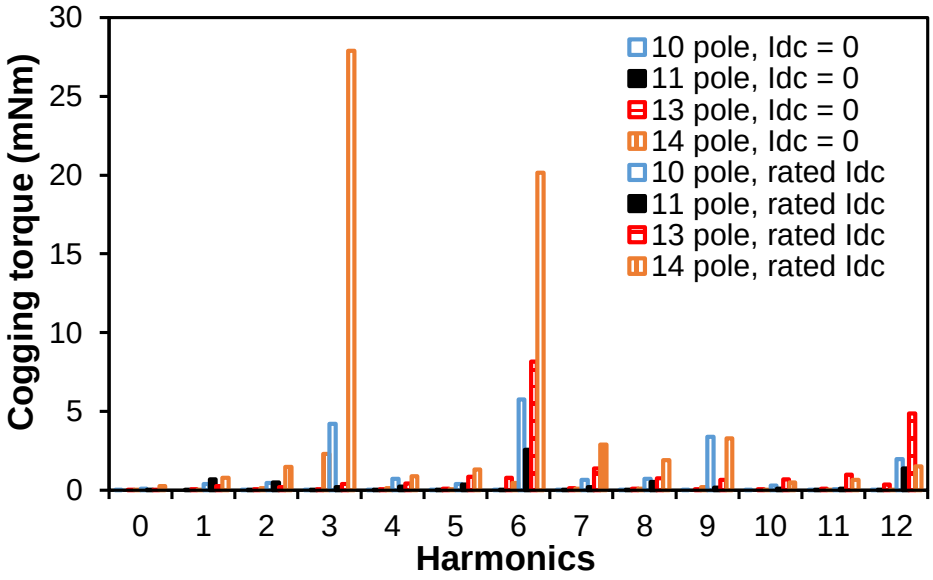

(b) Harmonics

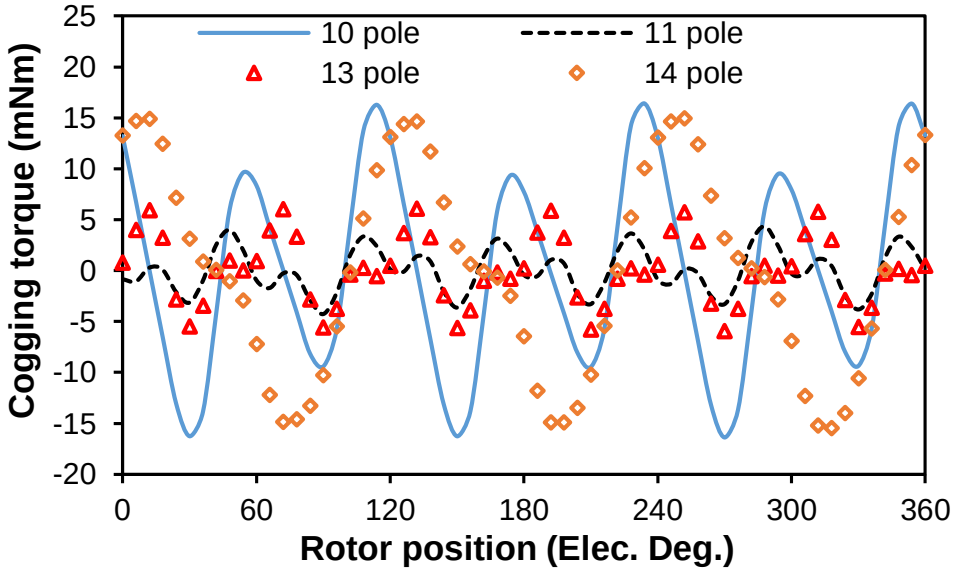

(c) Cogging torque for MS-SSPMMs

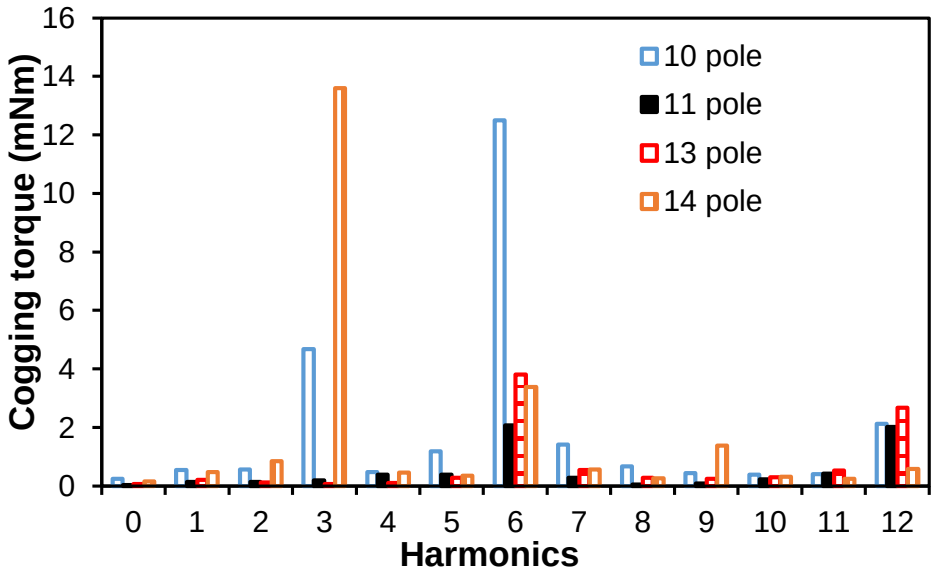

(d) Harmonics

Fig. 4.17 Open-circuit cogging torques of MS-HSSPMMs and MS-SSPMMs with different stator/rotor pole combinations.

C. Cogging torque

Fig. 4.17(a) shows that when the DC current is 0, the cogging torque waveforms for the MS-HSSPMMs are negligible. When the machines excited with a rated DC current, the cogging torque raised, especially for the 14-rotor pole machine. For a non-modular machine, the fundamental frequency of cogging torque is independent of the winding layer number. However, for the modular stator machines, half of the stator slots are removed, the fundamental frequency of cogging torque is halved compared with the corresponding non-modular machines, which should be 3 and 6 for the 10/14 rotor pole machine and the 11/13 rotor pole machine, respectively. This applies to the MS-SSPMMs as well. The 3 and 6 periods of cogging torque make a dominant 3rd order harmonic for the 10/14 rotor pole machine, and a dominant 6th order harmonic for 11/13 rotor pole machine.

For the MS-HSSPMMs, the machines have small cogging torque, but the 14 rotor pole machine has relatively high cogging torque compared to other machines. This might be because of the fluxes produced by DC coils in the stator slots are more concentrated on the stator segment. Besides, the fluxes produced by DC coils in the flux gap is blocked due to the modular stator structure. In addition, when the machine stator is segmented, the cogging torque will be increased, and more significant high effect will be observed in the machines with $N_r > N_s$. This can be seen in the 13-rotor pole machine when compared with the 11-rotor pole machine. For the MS-SSPMMs, the cogging torques remain small as they are generated due to the flux-leakage.

4.5.2. Torque performance analysis

Fig. 4.18(a) shows the torque and current angle characteristics of the MS-HSSPMMs with different numbers of rotor poles. It shows that the values of average torque for machines with different rotor poles can achieve the maximum value when the current angle is around 0. Thus, the MS-HSSPMMs have negligible reluctance torque, and the average electromagnetic torque can be calculated by (4.12), and the machines can be modified to take into account the PM flux-linkage and the DC flux-linkage, where the DC current flux is used to adjust the PM flux.

$$T_e = \frac{3}{2} N_r (\psi_d i_q - \psi_q i_d) \approx \frac{3}{2} (\psi_{DC} + \psi_{PM}) i_q \tag{4.12}$$

where T_e, N_r, ψ_d, ψ_q, ψ_{DC}, ψ_{PM}, i_d and i_q are the average electromagnetic torque, the number of rotor poles, the dq-axis flux linkages, the DC flux-linkage, the PM flux linkage, the dq-axis inductances, respectively.

The MS-SSPMMs have a slight bias which might be caused by larger volume of PMs and without DC excitation. The maximum torques of the MS-SSPMMs can be obtained by the current angle of almost 0. The electromagnetic torque can be calculated by (4.13) as shown in [87].

$$T_{ave} = \frac{N_{ph} N_r}{2\pi} W \tag{4.13}$$

where T_{ave}, N_{ph} and W are the average electromagnetic torque, the number of phases, and the magnetic co-energy change.

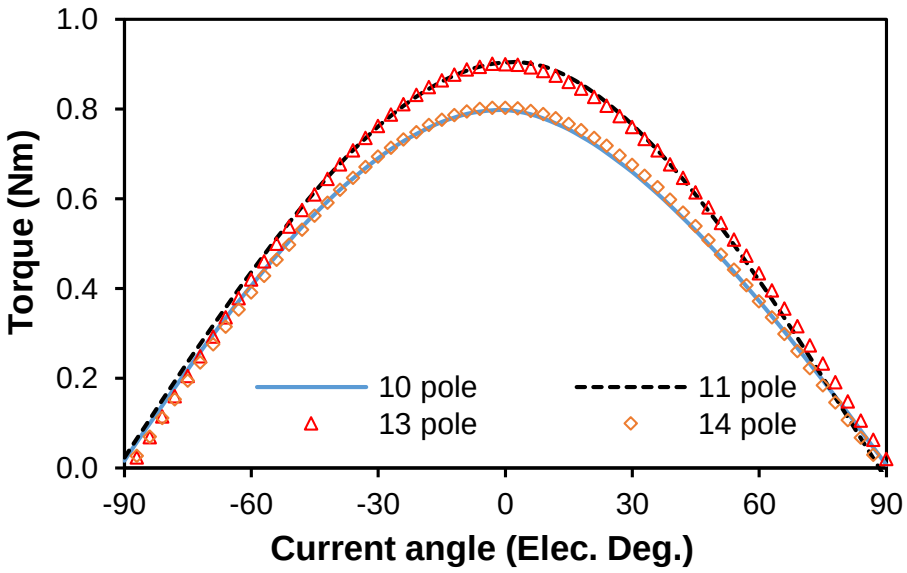

(a) MS-HSSPMMs

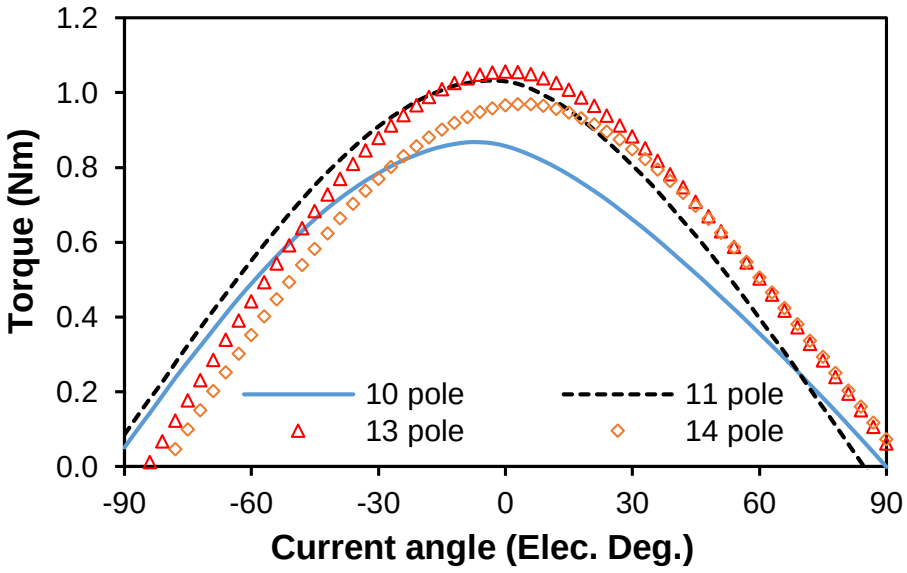

(b) MS-SSPMMs

Fig. 4.18 Electromagnetic torque against current angle for modular stator machines.

Fig. 4.19 shows the electromagnetic torques of MS-HSSPMMs and MS-SSPMMs. The electromagnetic torques of MS-SSPMMs are larger than those of the MS-HSSPMMs albeit with larger torque ripples as well. For both types of machines, the 11- and 13-rotor pole machines have larger average torque and small torque ripple. These machines have a dominant 6^{th} order harmonic, while the 10- and 14-rotor pole machines have significant 3^{rd} order harmonic. The torque ripples for 13- and 14-rotor pole MS-HSSPMMs decrease with the increasing copper loss, while the 10- and 11-rotor pole machines have the increasing torque ripple till the copper loss of 25W and 35W, respectively, as shown in Fig. 4.20(b). From Fig. 4.20(d), the torque ripples of the 10- and 14-rotor pole MS-SSPMMs are significantly increasing till the copper loss of 20W, and smoothly increasing till the copper loss of around 45W and then reducing. The average torques and the torque ripples for these machines with rated current excitation are shown in Table 4.8.

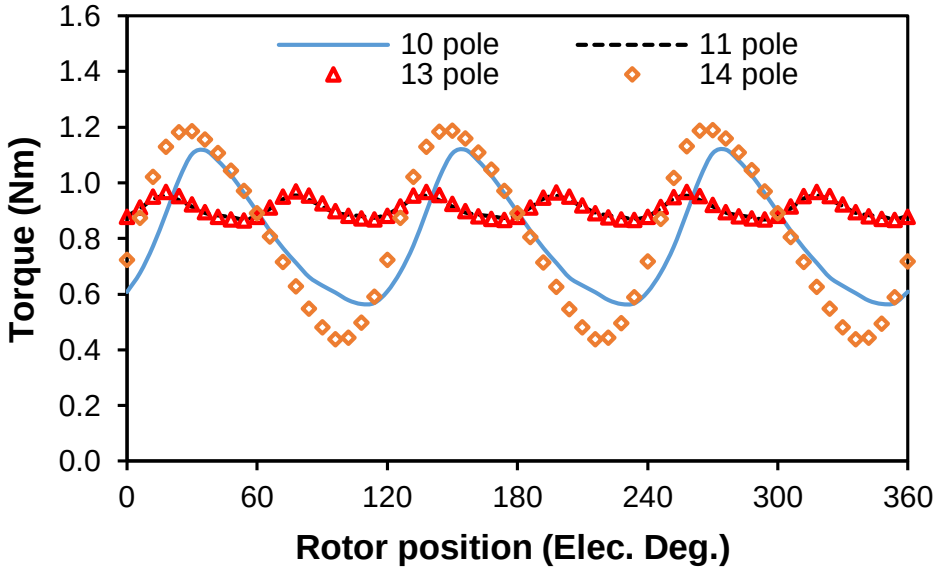

(a) Torque waveforms of MS-HSSPMMs

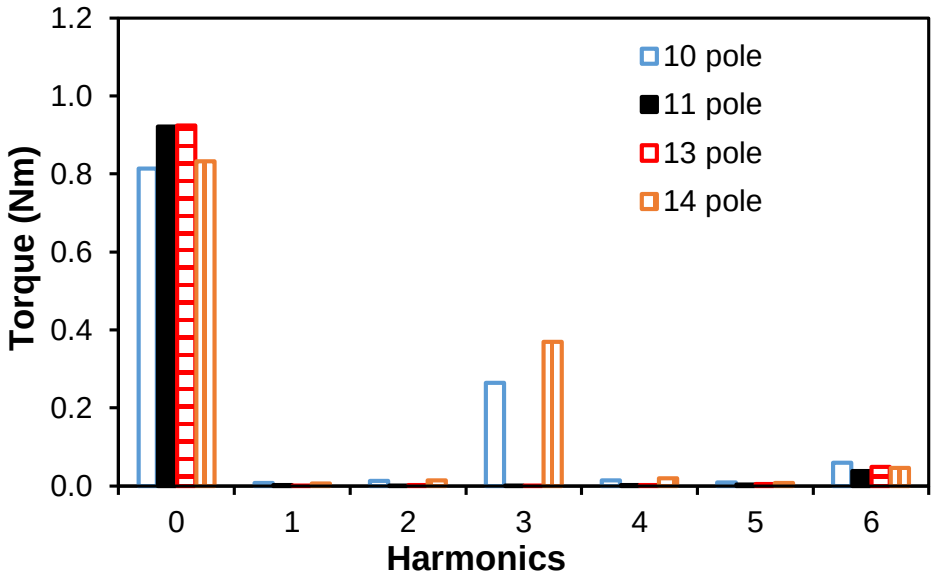

(b) Harmonics of MS-HSSPMMs

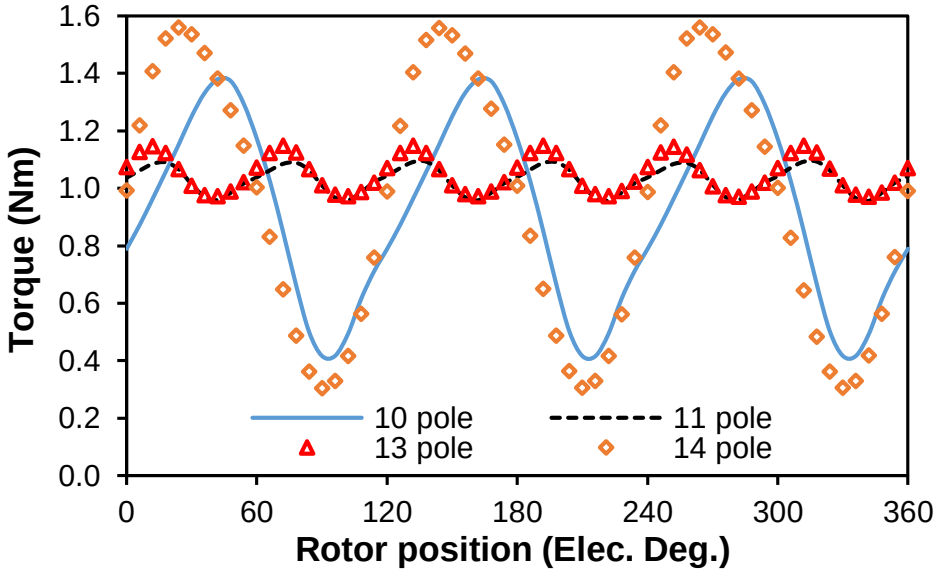

(c) Torque waveforms of MS-SSPMMs

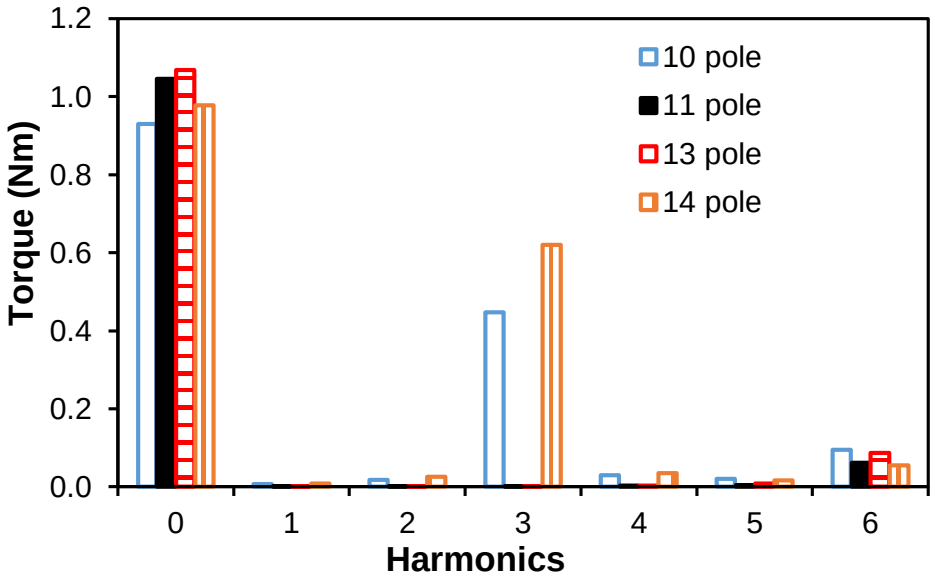

(d) Harmonics of MS-SSPMMs

Fig. 4.19 Electromagnetic torque waveforms of modular stator machines.

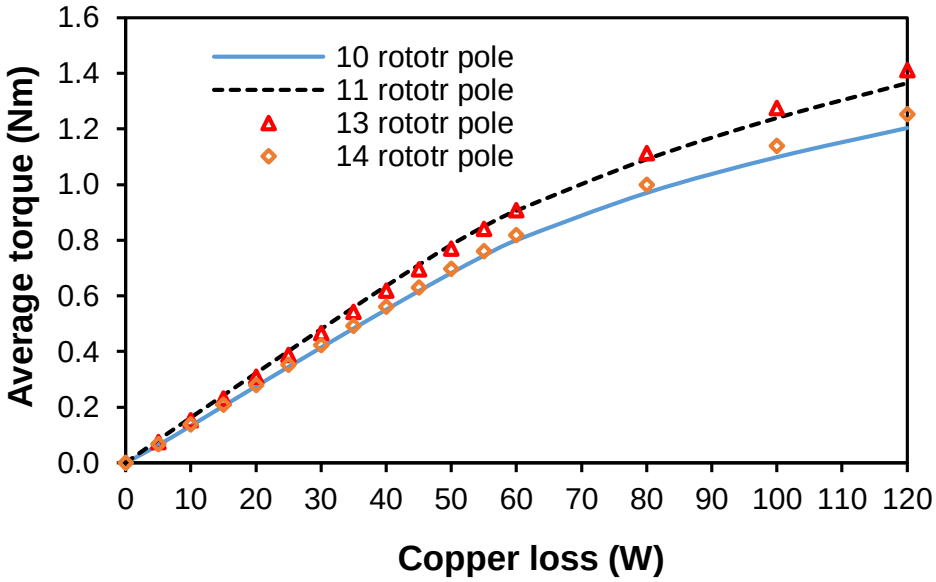

(a) Average torque against copper loss

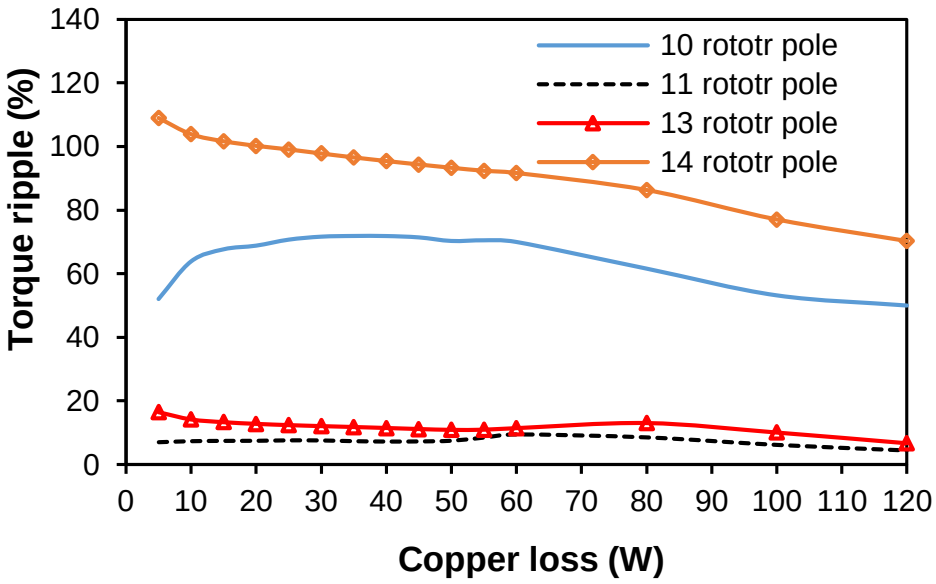

(b) Torque ripple against copper loss

(I) MS-HSSPMMs

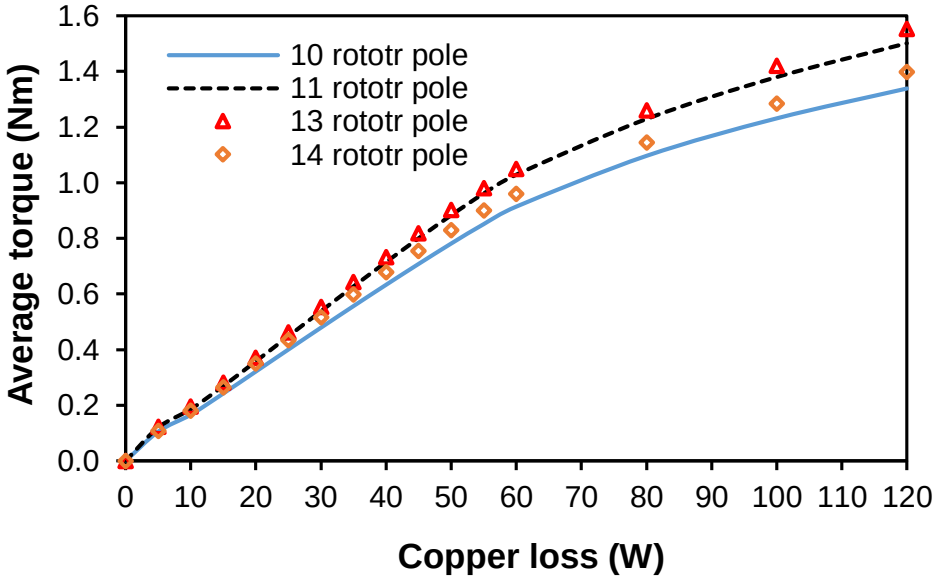

(c) Average torque against copper loss

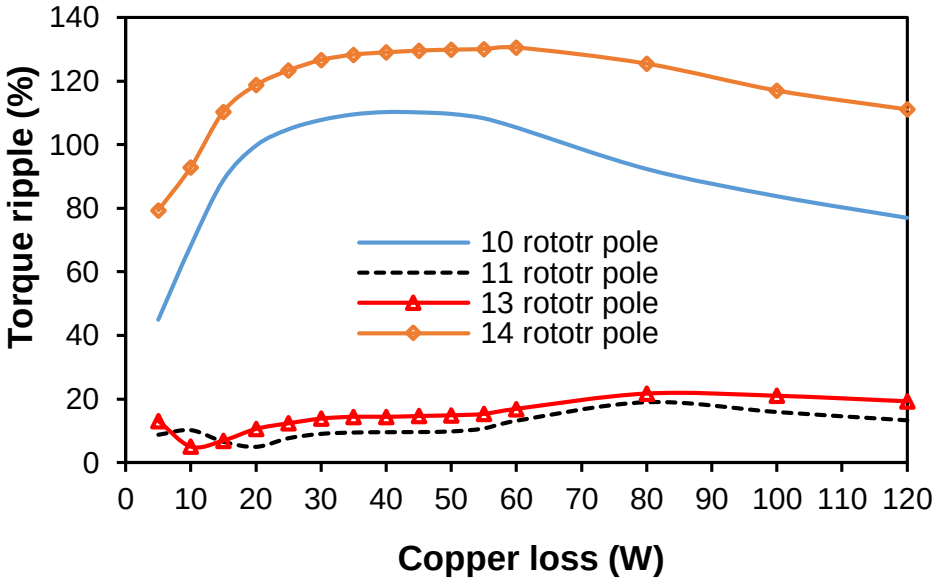

(d) Torque ripple against copper loss

(II) MS-SSPMMs

Fig. 4.20 Variation of electromagnetic torque and torque ripple with copper loss for modular stator machines.

Table 4.8 Electromagnetic torque performance at rated current excitation

	MS-HSSPMMs				MS-SSPMMS			
Number of rotor poles	10	11	13	14	10	11	13	14
Average torque (Nm)	0.800	0.906	0.908	0.819	0.914	1.029	1.051	0.961
Torque ripple (%)	69.3	9.5	11.4	91.7	105.4	13.2	16.9	130.6
Maximum torque (Nm)	1.119	0.955	0.968	1.188	1.380	1.092	1.149	1.561
Minimum torque (Nm)	0.565	0.868	0.864	0.437	0.416	0.956	0.971	0.306

4.6. Conclusions

This chapter has introduced and investigated the modular stator machines with PMs located on the slot openings. The MS-HSSPMMs can be modified from the SL-F1A1 HSSPMMs and the SL-F1A1 WFSMMs with a lower iron loss. When the machines have the restriction condition of fixed equal stator tooth width and stator back-iron thickness, the PM volumes of the machines are reduced. The MS-SSPMMs can be modified from the MS-HSSPMMMs by removing the DC coils. Both types of machine have high torque ripple for the 10- and 14 rotor poles, and the 11- and 13-rotor pole machines have the higher electromagnetic torque.

Chapter 5 Experimental Validation

5.1. Introduction

This chapter provides the experimental results of the F1A3 and F3A2 HSSPM machines to validate the FEA analyses in the former chapters, together with analyses of the test results. The F3A2 HSSPM machine is tested with different stator/rotor pole number combinations, including open-circuit back-EMF and on-load static torque. However, since the F1A3 HSPPM machine has been found with some design and manufacture problems, the focus will be on the analysis of the test results.

First of all, the measurement methods for back-EMF and static torque will be described.

A. Back-EMF measurement

The stator is fixed tightly in the jaws of the lathe machine and the rotor can be rotated easily. The three phase armature windings are connected to the oscilloscope probes. To provide a continuously and constant rotating speed, a hand drill is connected to the rotor shaft to rotate the rotor. The measured back-EMF waveform can be observed and recorded using the oscilloscope. The experimental rigs for open-circuit back-EMF test are shown in Fig. 5.1(a). Since the rotating speed given by the hand drill is difficult to control, thus the measured data for the back-EMF should be converted to obtain the same rotating speed as the simulation model which is 400 rpm.

B. Static torque measurement

The static torque measurement with and without current excitation is described in [131]. When no current excited, the cogging torque is measured. The machine stator with frame is fixed into the jaws of the lathe machine. The balanced beam is tightly fixed on the rotor shaft and one of its end with extrusive pin is rested on the surface of a digital scale. Meanwhile, a spirit level is used to keep the total balanced beam and the surface of the digital scale horizontality. A weight should be added and located above the pin which is connected to the scale in order to make the readings on the digital scale always unidirectional. The experimental rigs for static torque test are shown in Fig. 5.1(b). During the measurement, the rotor position is fixed and the stator position can be changed, and a variable force can be recorded on the digital weight scale. Thus, the torque can be calculated from the equation of: (measured force- added weight) × beam arm length × gravitational acceleration. For the static torque measurement, the machine needs two

DC power supplies to provide currents to field and armature windings respectively. The three phase armature windings are excited with DC current as $I_a = -2I_b = -2I_c$.

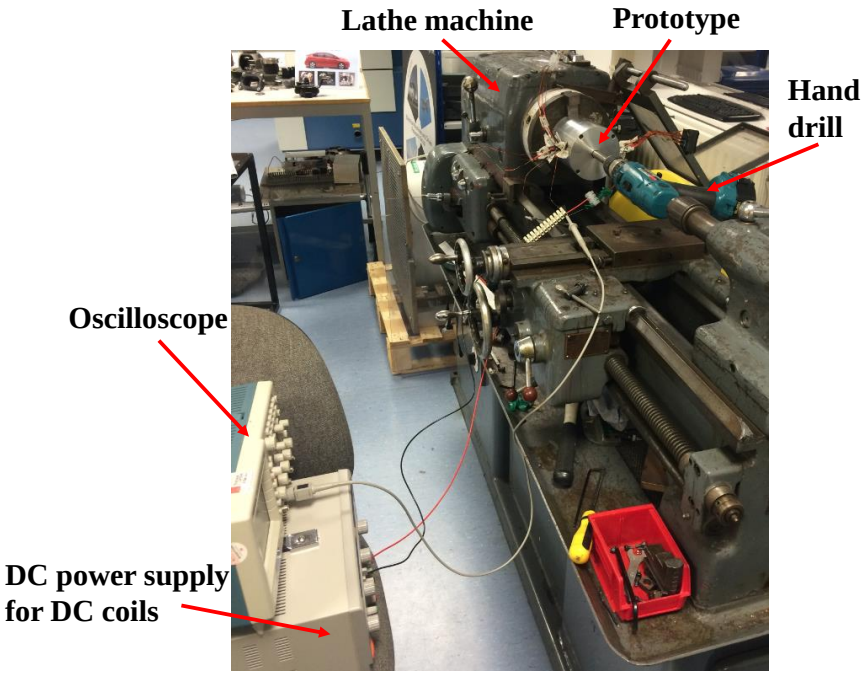

(a) Open-circuit back-EMF test stand

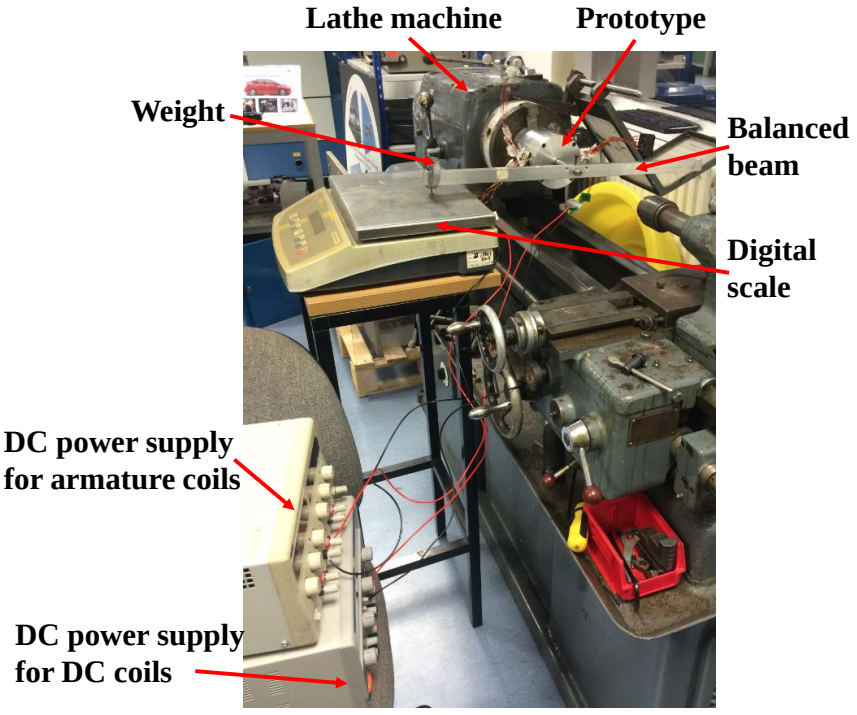

(b) Static torque test stand

Fig. 5.1 Experimental rigs for open-circuit back-EMF and static torque test.

5.2. F3A2 HSSPM machine

The prototypes of F3A2 HSSPM machines with 6-7/8/10/11 stator/rotor poles to be used to validate the analyses are shown in Fig. 5.2. The machine prototypes have been optimized with the total copper loss of 30W and a winding packing factor of 0.4. The stator of the machines for different stator/rotor pole combinations is designed to be identical, and thus, the design parameters are only considered to be the rotor pole arc and the rotor tooth height. The design parameters are given in Table 5.1.

Table 5.1 Optimized parameters for machine prototypes

Parameters	**Unit**	**7-pole**	**8-pole**	**10-pole**	**11-pole**
Stator outer radius (R_{SO})	mm	45			
Lamination stack length (l_{stack})	mm	25			
Air-gap length (G)	mm	0.5			
Copper loss (P_{Cu})	W	30			
PM volume (V_{PM})	mm^3	5403.8			
Packing factor (k_p)		0.4			
Turns/coil (armature winding) (N_a)		46			
Turns/coil (field winding) (N_f)		46			
Back-iron thickness (H_{BI})	mm	2.97			
Stator inner radius (R_{SI})	mm	21.96			
Stator pole arc (θ_{st})	Mech. Deg.	8.93			
Stator tooth width (w_{st})	mm	3.42			
Split ratio (R_{SI} /R_{SO})		0.477			
PM thickness (H_{PM})	mm	6.66			
Rotor outer radius (R_{RO})	mm	21.46			
Rotor pole arc (θ_{rt})	Mech. Deg.	20.95	15.96	12.94	12.96
Rotor tooth height (H_{Rtooth})	mm	7.51	6.74	7.54	7.00
Ratio of field to armature slot current density (J_{ratio})		0.90	1.07	1.07	0.94

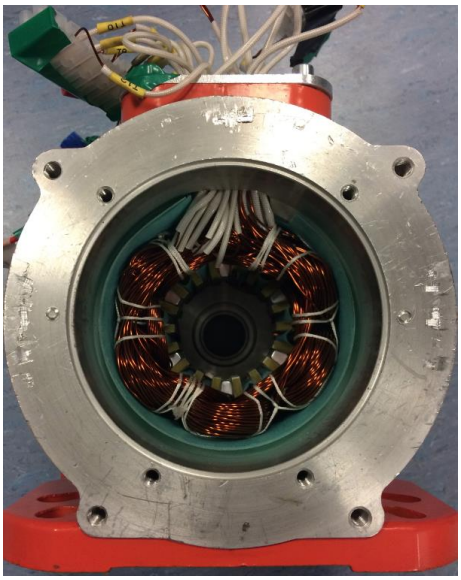

(a1) 6 pole stator

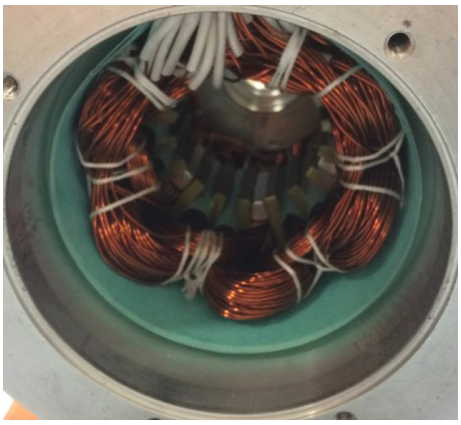

(a2) 6 pole stator

(b) 7-, 8-, 10-, and 11-rotor poles (left to right)

Fig. 5.2 Prototype machines with 6-7/8/10/11 stator/rotor poles.

Since the value of ratio of field to armature slot current density is around 1 [64], during the experiments, the field slot current density and armature slot current density can be assumed to be the same.

5.2.1. Test results

The measured and 2D FEA predicted back-EMF waveforms of the 6-7/8/10/11 stator/rotor pole F3A2 HSSPM machines at 400 rpm rotor speed are shown in Fig. 5.3-Fig. 5.6, respectively. The back-EMF waveforms are measured for DC current excitation at 0A, 1A. 2A and 3A, which correspond to the DC current density of 0, 2A/mm^2, 4A/mm^2 and 6A/mm^2, respectively. Good agreement is observed with the FEA predicted values for all DC currents. However, with the increasing DC current, the differences between the magnitudes of the FEA predicted back-EMF and measured back-EMF become larger. The machines with even rotor pole numbers have asymmetric back-EMF waveforms, which might lead to the non-symmetrical static torque waveforms.

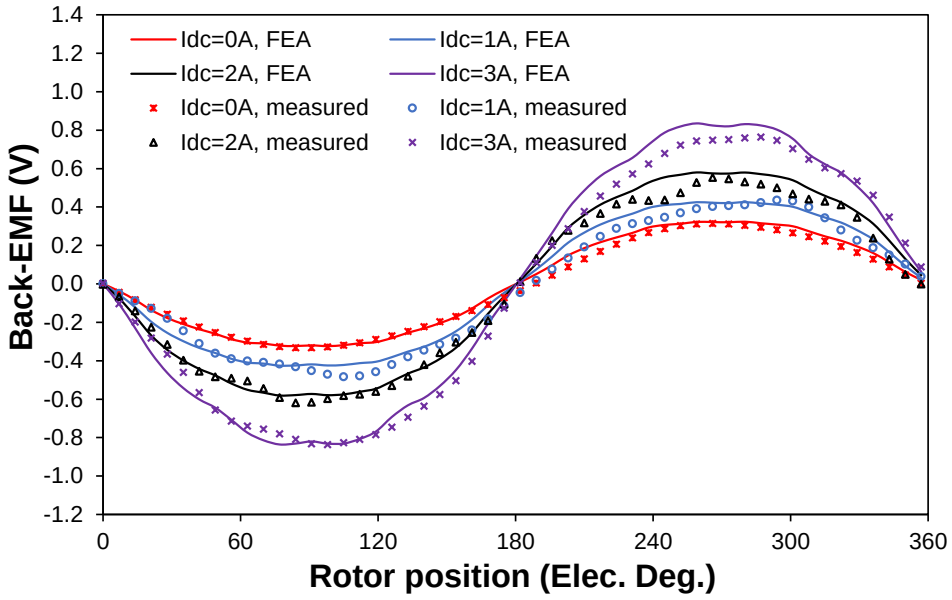

(a) Back-EMF waveforms

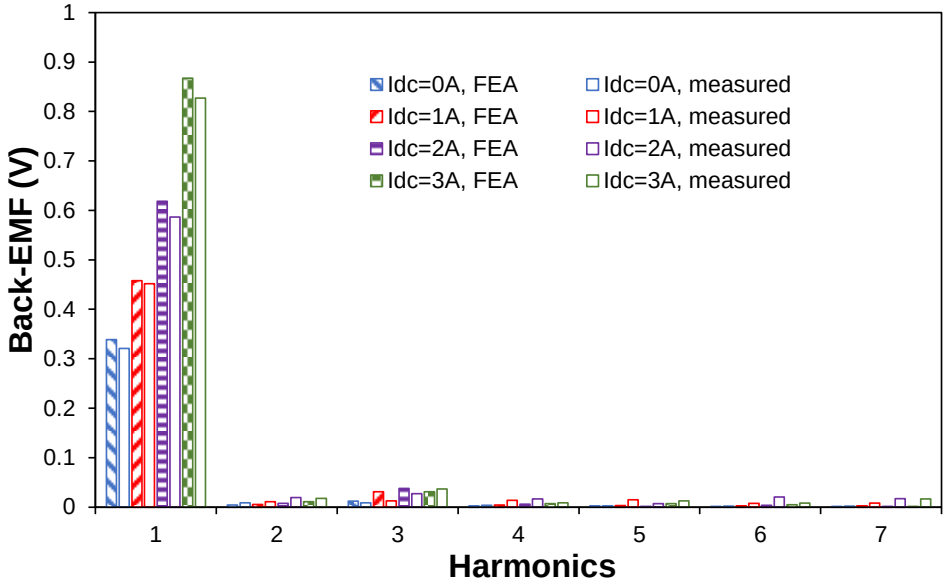

(b) Harmonics

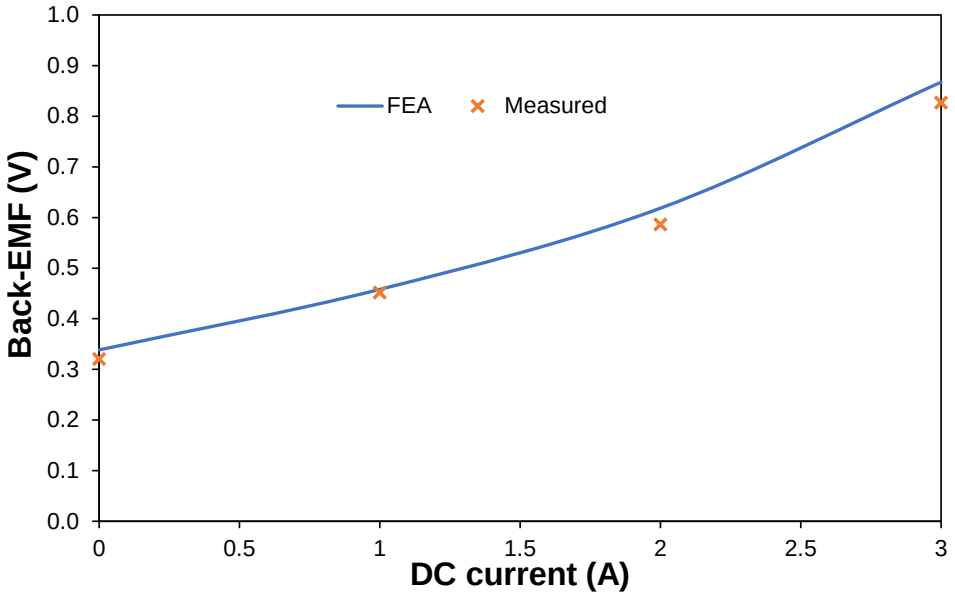

(c) Fundamental magnitude of back-EMF

Fig. 5.3 Back-EMFs of 6-7 stator/rotor pole F3A2 HSSPM machine at 400rpm rotor speed.

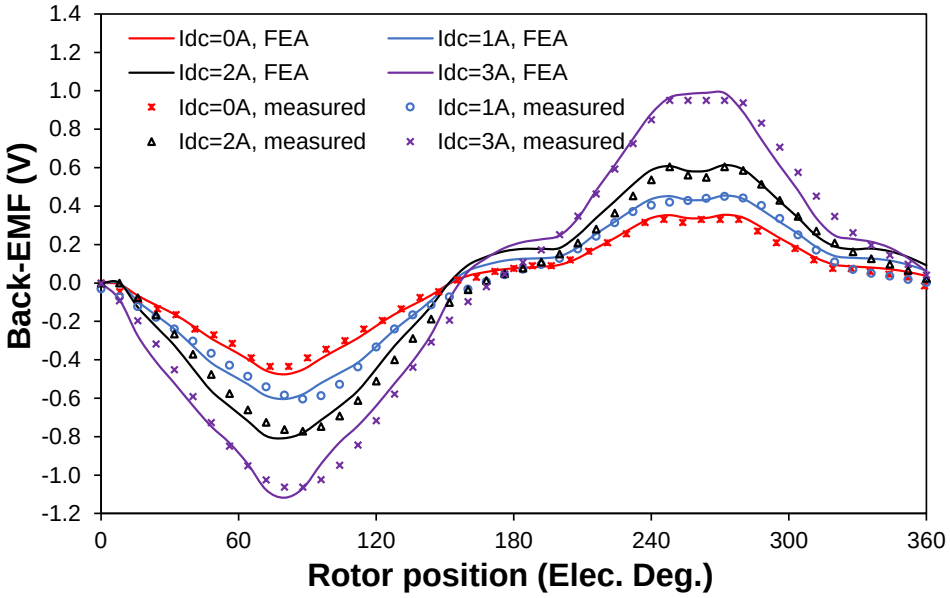

(a) Back-EMF waveforms

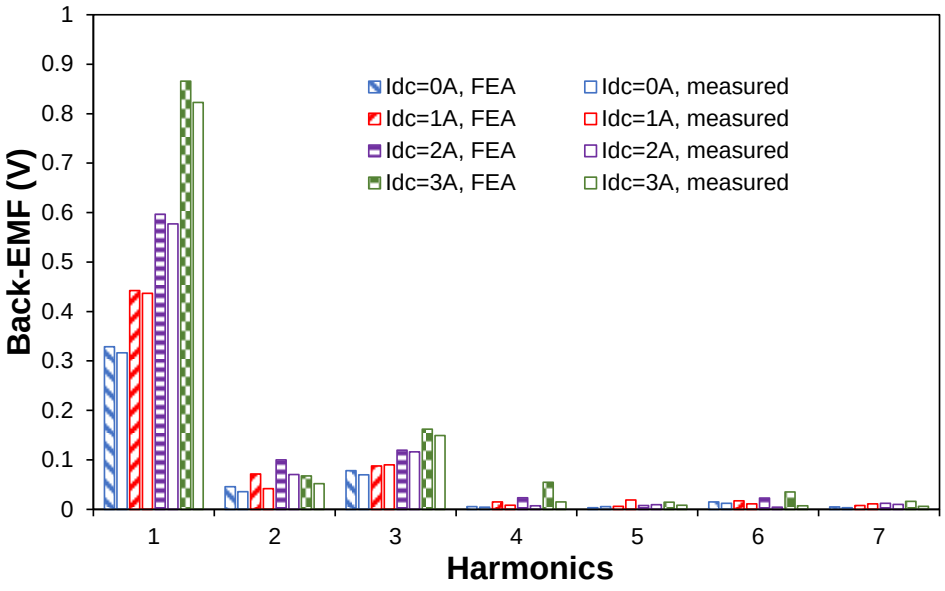

(b) Harmonics

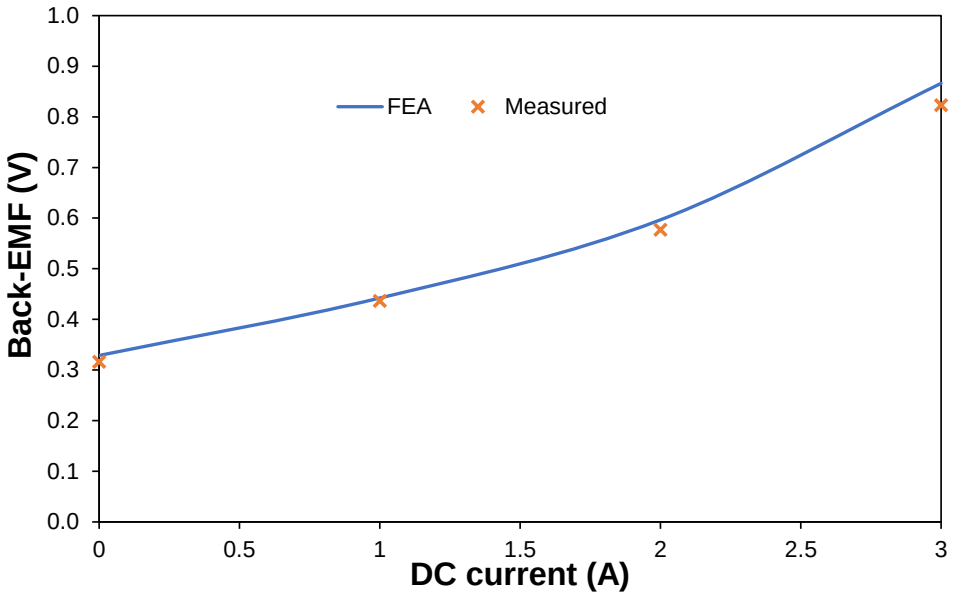

(c) Fundamental magnitude of back-EMF

Fig. 5.4 Back-EMFs of 6-8 stator/rotor pole F3A2 HSSPM machine at 400rpm rotor speed.

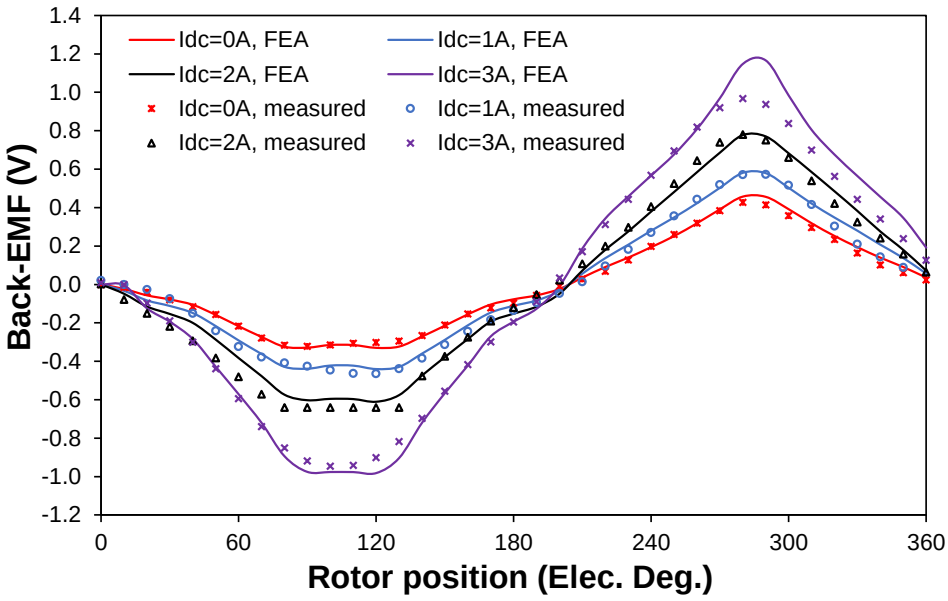

(a) Back-EMF waveforms

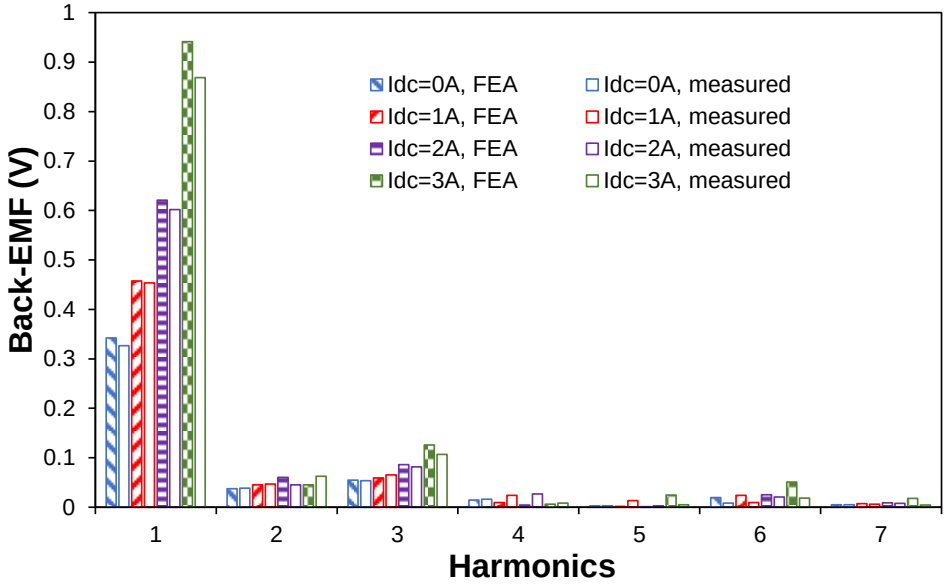

(b) Harmonics

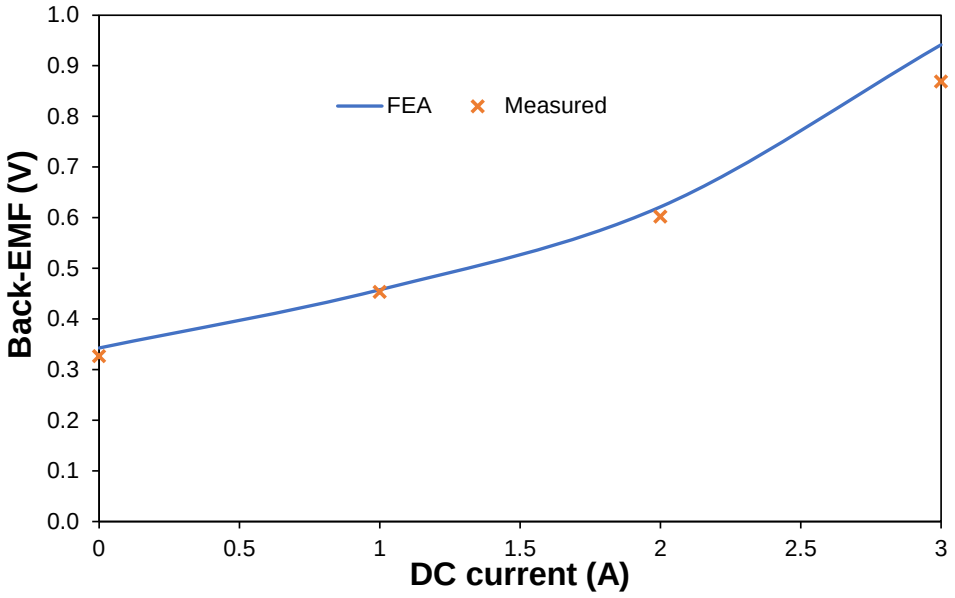

(c) Fundamental magnitude of back-EMF

Fig. 5.5 Back-EMFs of 6-10 stator/rotor pole F3A2 HSSPM machine at 400rpm rotor speed.

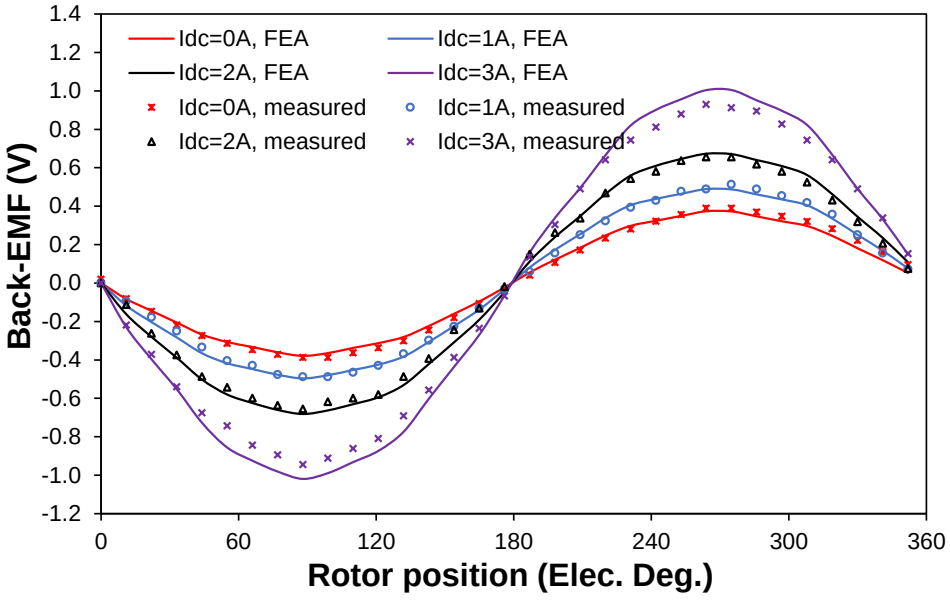

(a) Back-EMF waveforms

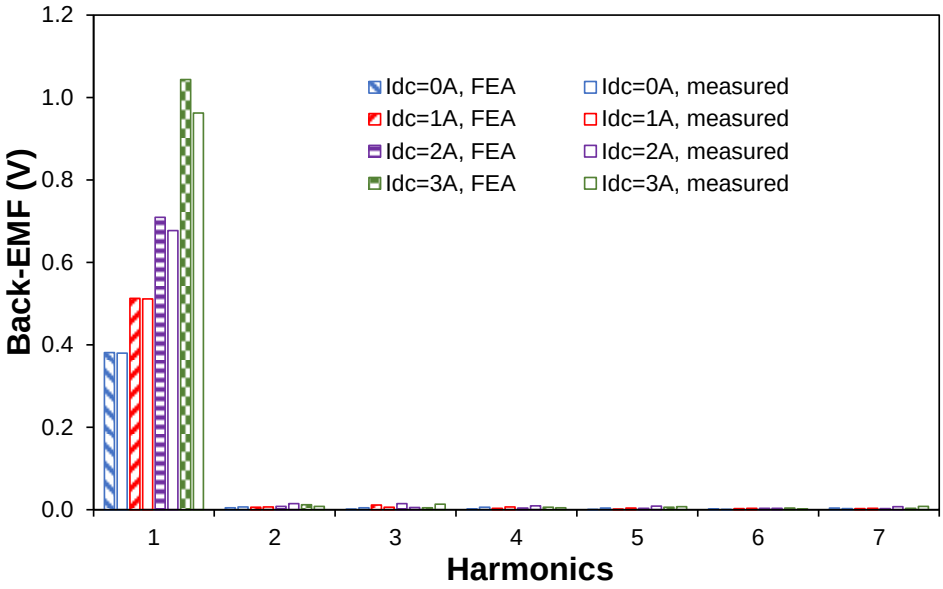

(b) Harmonics

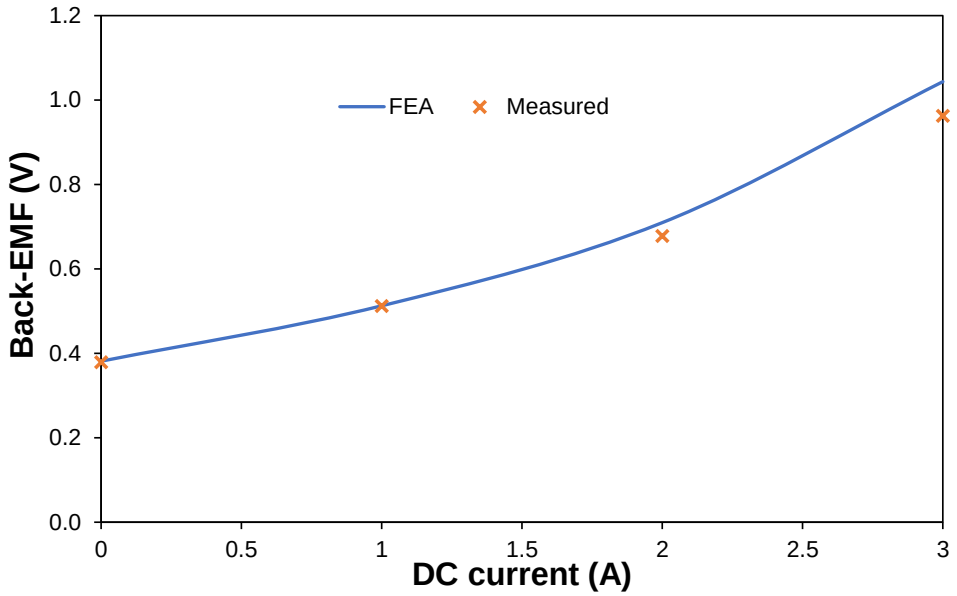

(c) Fundamental magnitude of back-EMF

Fig. 5.6 Back-EMFs of 6-10 stator/rotor pole F3A2 HSSPM machine at 400rpm rotor speed.

The variations of measured and FEA predicted static torques and cogging torques with rotor position for different DC and armature current densities for 6-7/8/10/11 stator/rotor pole F3A2 HSSPM machines are compared in Fig. 5.7 to Fig. 5.10, respectively. The static torques are measured under the field and armature current densities of 0, 2, 4 and 6A/mm^2 and the armature current is in peak value. Generally, good agreement is achieved between the measured and 2D FEA predicted static torques. As for the back-EMF waveforms, the machines with even rotor pole numbers have non-symmetrical static torque waveforms. Meanwhile, with the increasing current density, the differences between the measured and predicted static torques increase.

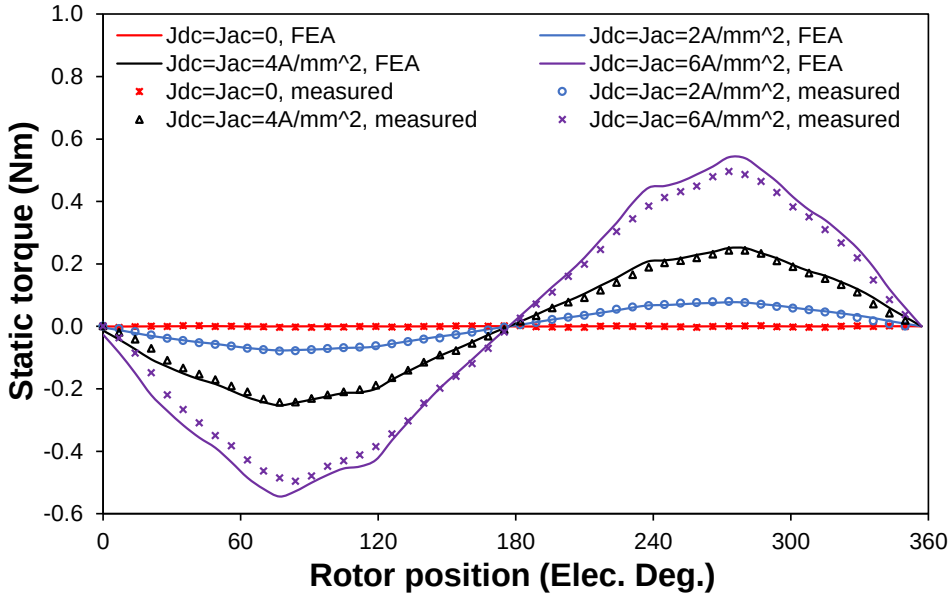

(a) Cogging torque and static torque with different DC and AC current densities

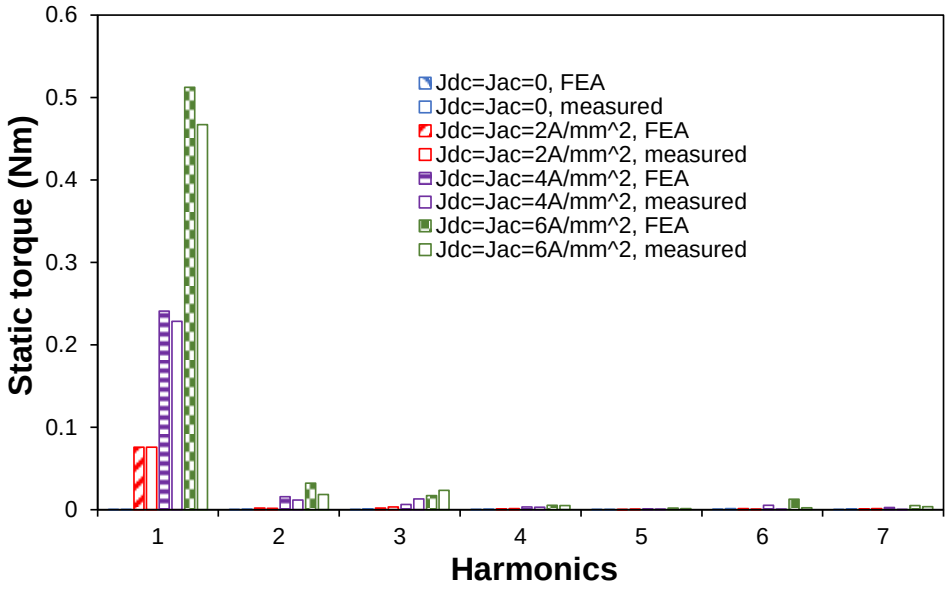

(b) Harmonics

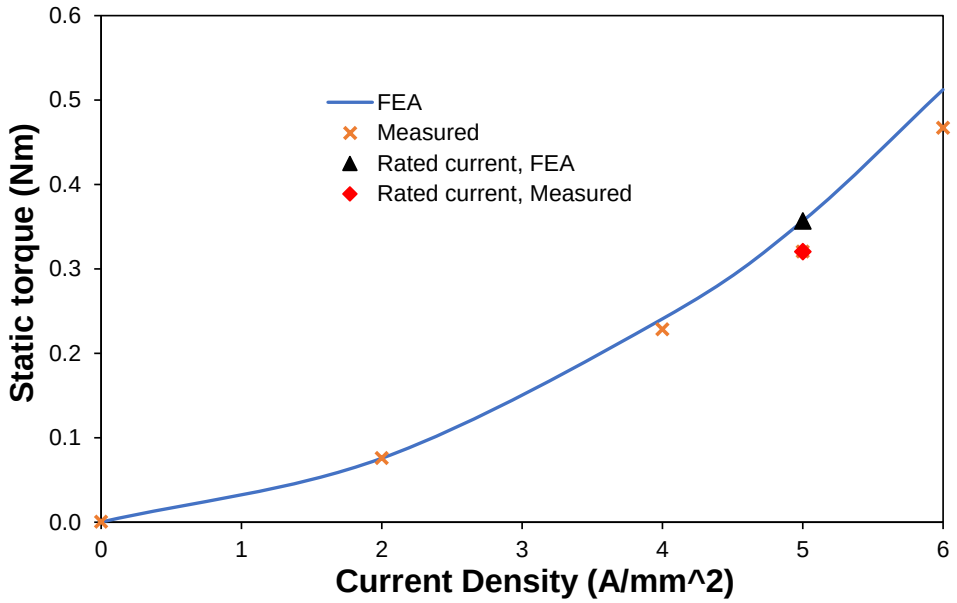

(c) First harmonic magnitude of cogging torque and static torque

Fig. 5.7 Static torque and cogging torque of 6-7 stator/rotor pole F3A2 HSSPM machine.

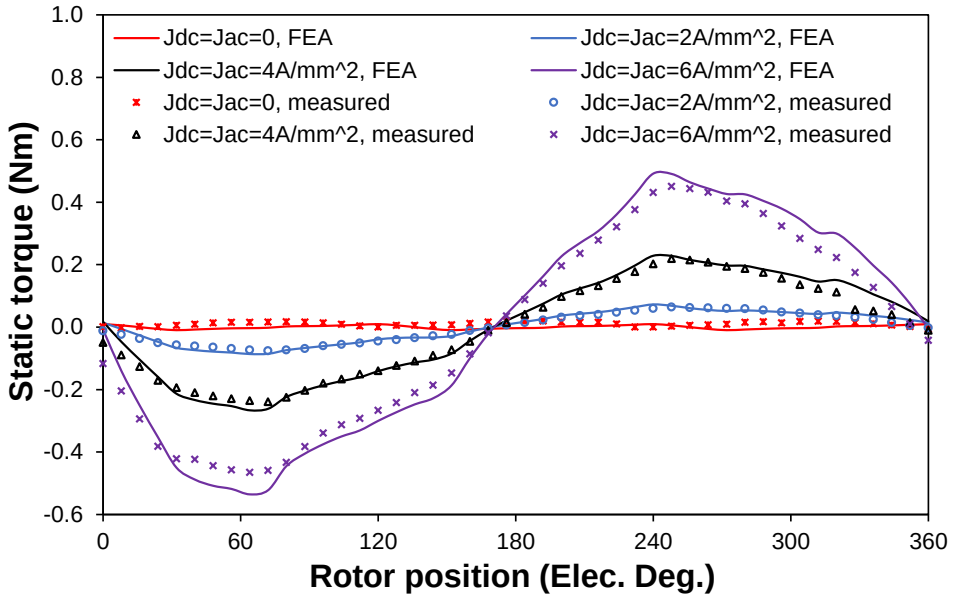

(a) Cogging torque and static torque with different DC and AC current densities

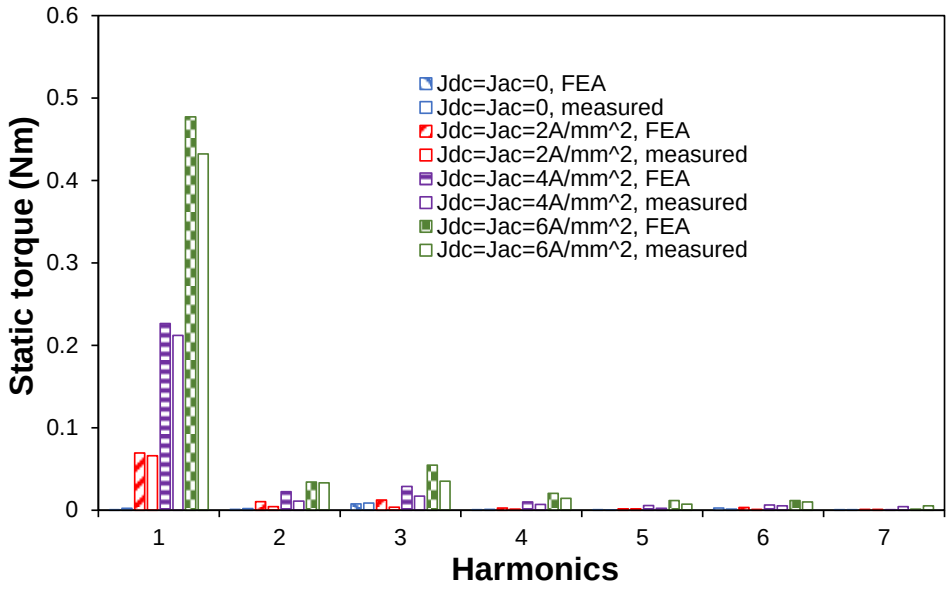

(b) Harmonics

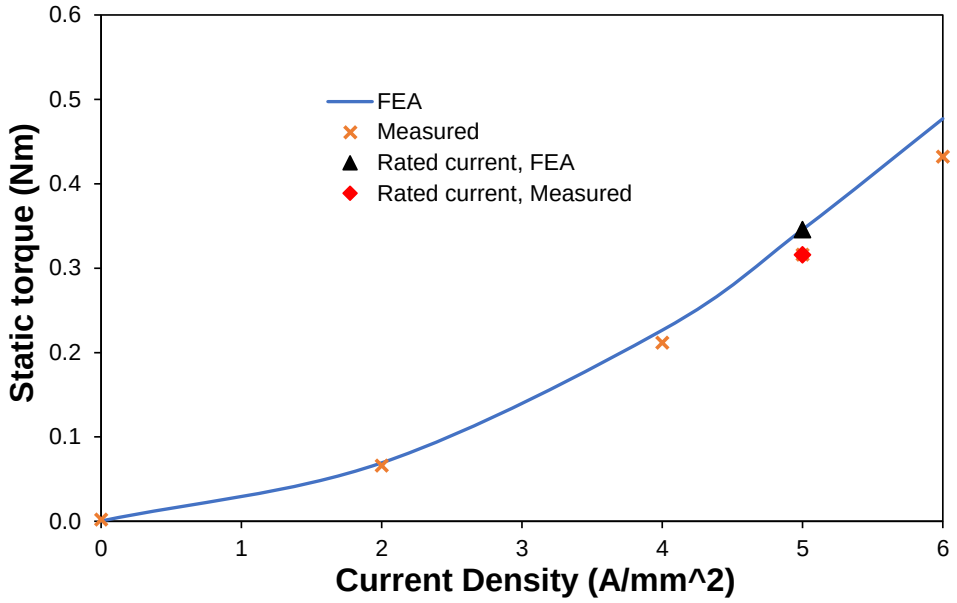

(c) First harmonic magnitude of cogging torque and static torque

Fig. 5.8 Static torque and cogging torque of 6-8 stator/rotor pole F3A2 HSSPM machine.

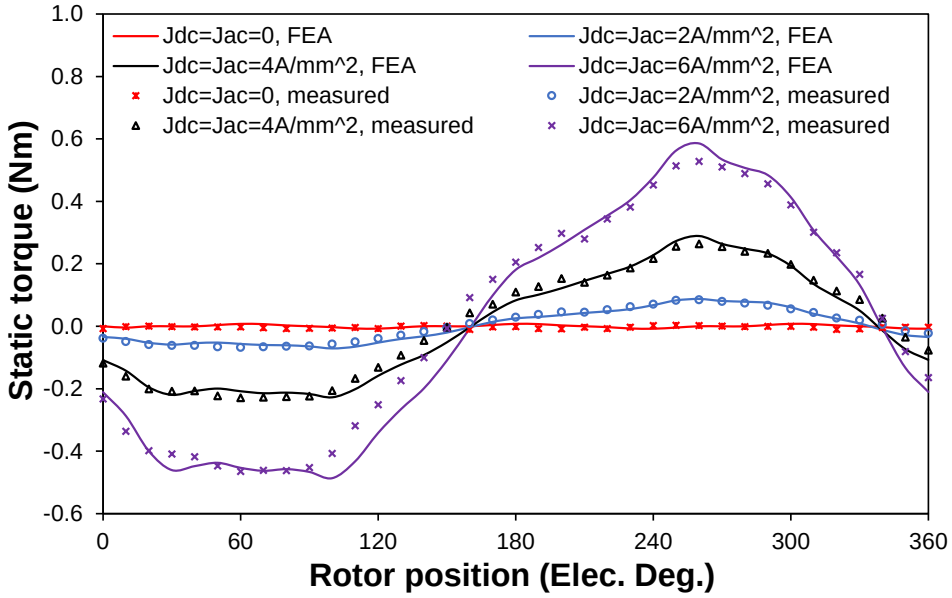

(a) Cogging torque and static torque with different DC and AC current densities

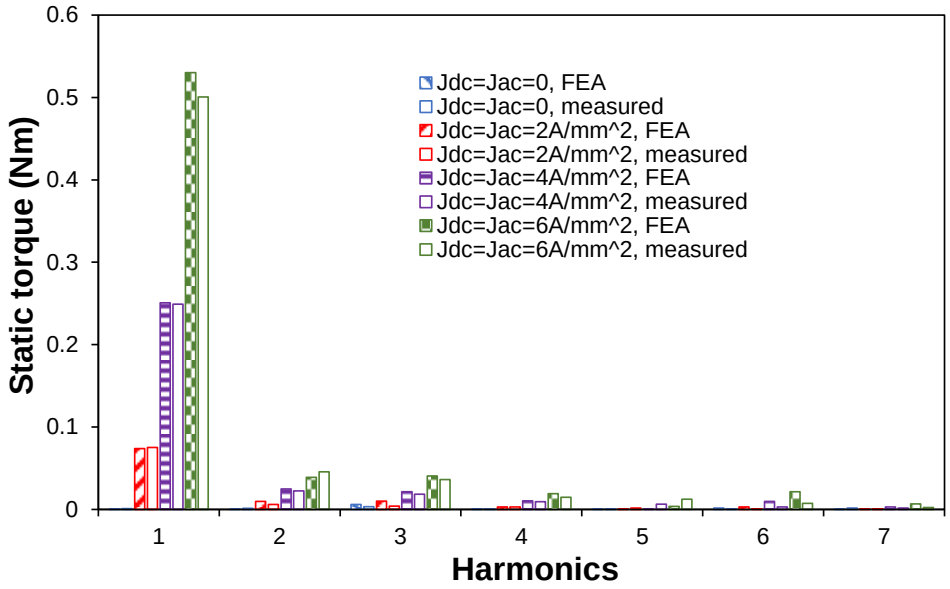

(b) Harmonics

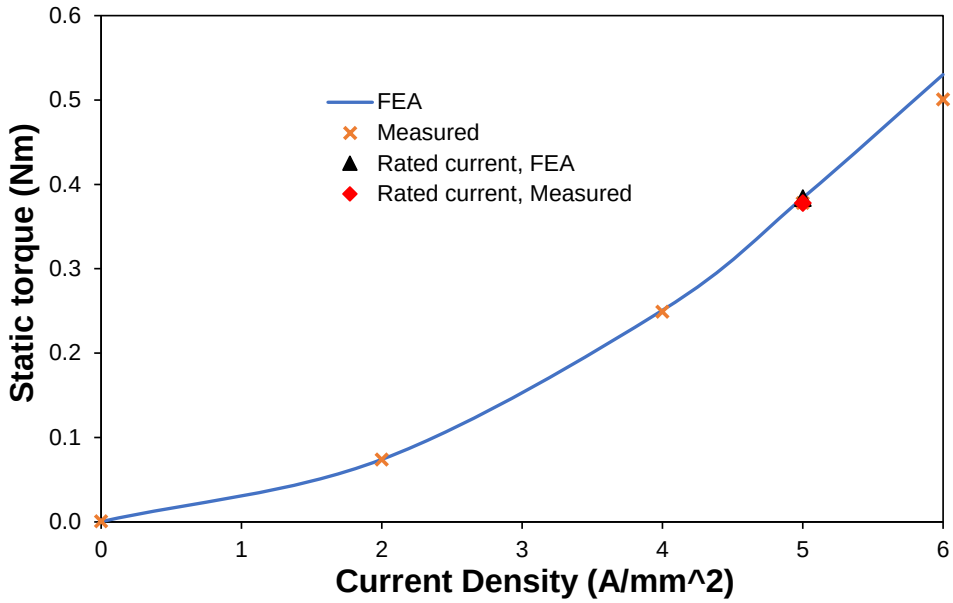

(c) First harmonic magnitude of cogging torque and static torque

Fig. 5.9 Static torque and cogging torque of 6-10 stator/rotor pole F3A2 HSSPM machine.

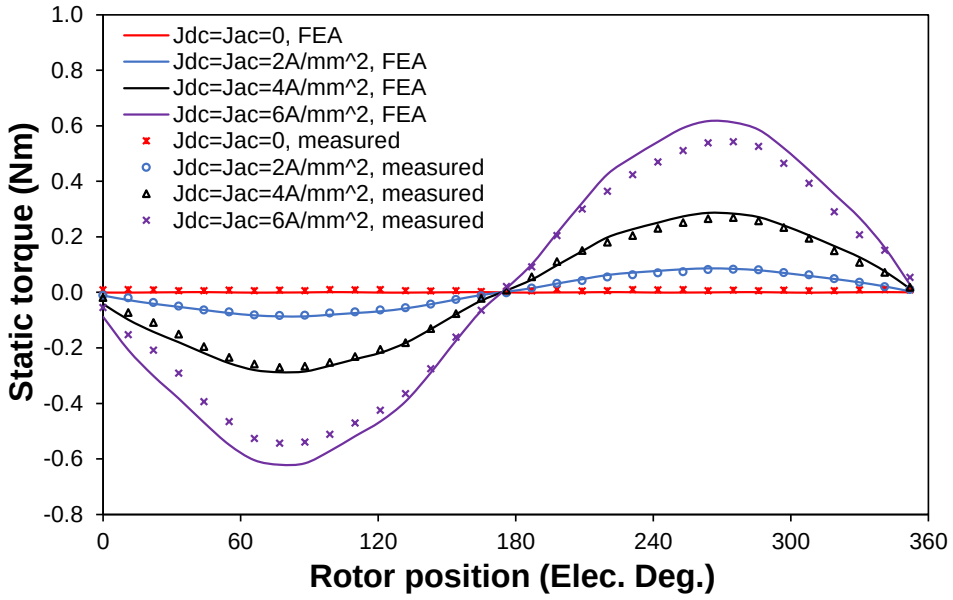

(a) Cogging torque and static torque with different DC and AC current densities

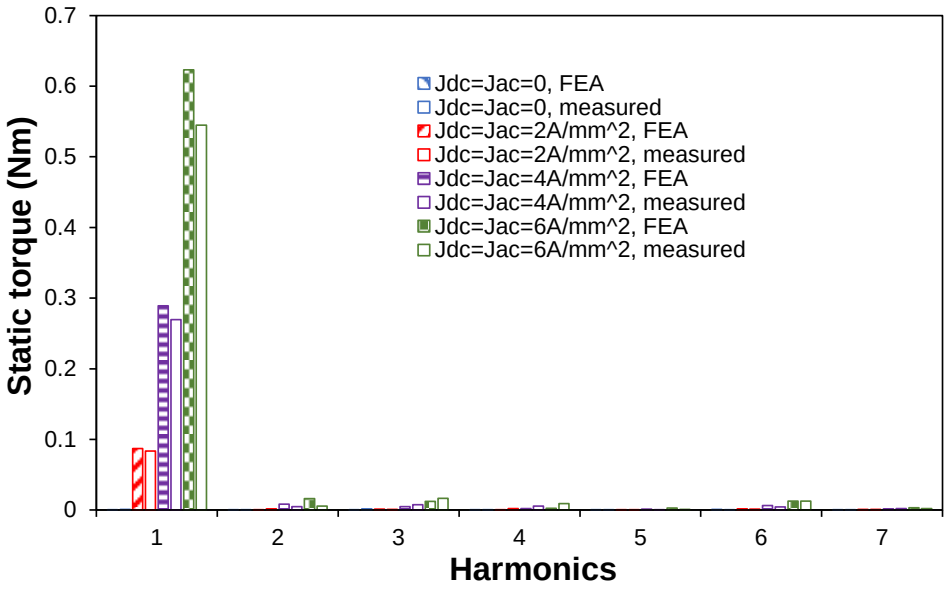

(b) Harmonics

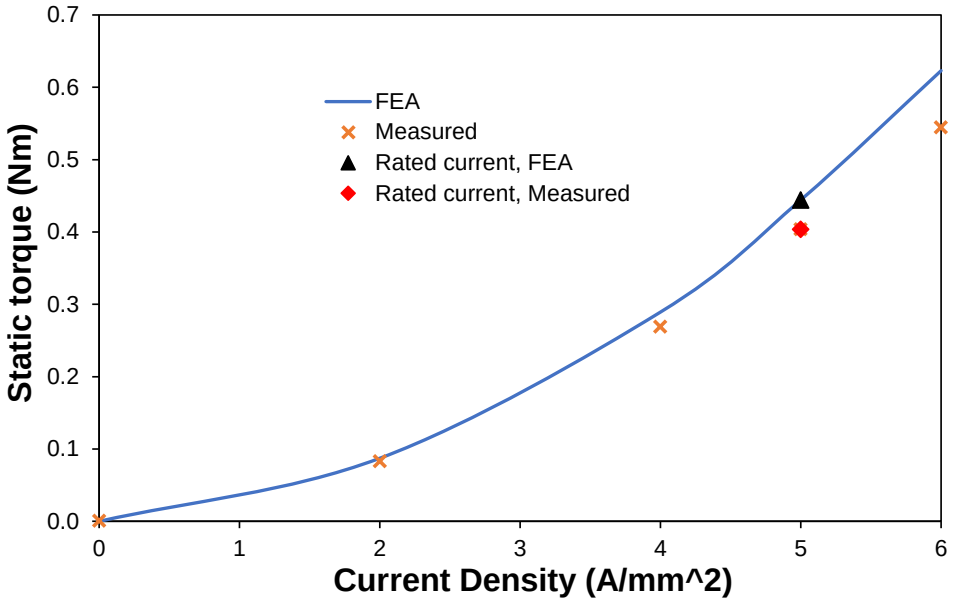

(c) First harmonic magnitude of cogging torque and static torque

Fig. 5.10 Static torque and cogging torque of 6-11 stator/rotor pole F3A2 HSSPM machine.

5.2.2. Analyses of experimental results

From the experiments, it shows that when there is no DC current excitation, the back-EMF waveforms for different rotor poles are not negligible, which is not expected from the machine basic operating principle. From chapter 3, these back-EMFs might be caused by the flux-leakage caused by stator magnetic saturation due to the PM. Hence, the comparison of back-EMF waveforms between non-linear and linear stator and rotor lamination materials is shown in Fig. 5.11, and the flux line and flux density distributions for 0°, 90°, 180° and 270° rotor positions (electrical degree) are shown in Fig. 5.12. According to these figures, the back-EMF waveforms of the machines with linear materials for the stator and rotor are truly negligible. Thus, it confirms that the back-EMF waveforms for the non-linear material machine is caused by flux-leakage due to magnetic saturation.

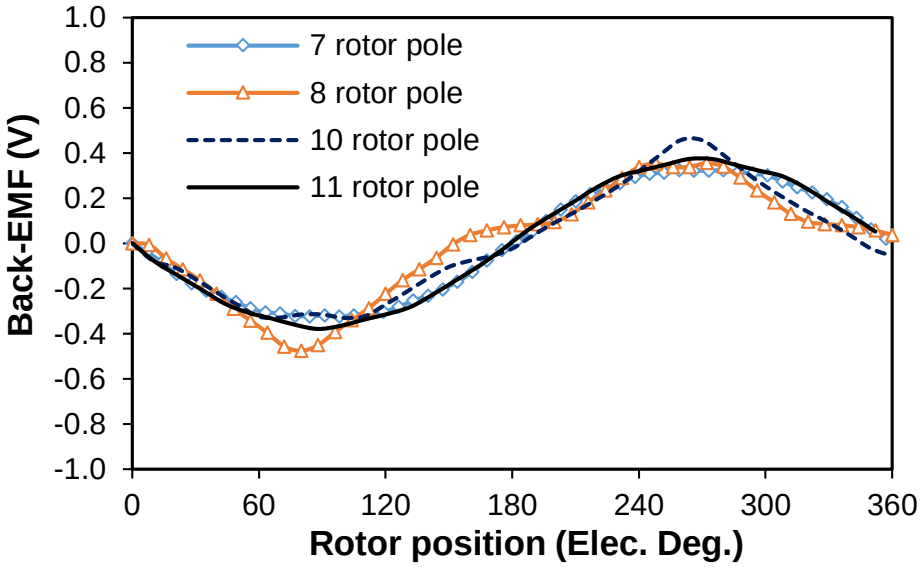

(a) Back-EMF waveforms for machines with non-linear material stator and rotor

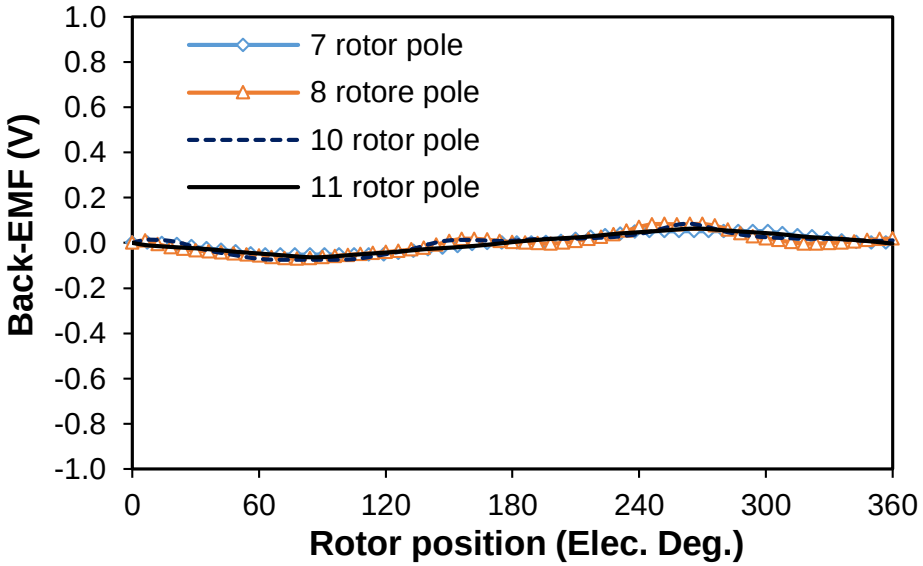

(b) Back-EMF waveforms for machines with linear material stator and rotor (relative permeability = 4000)

Fig. 5.11 FEA predicted phase back-EMF waveforms of F3A2 HSSPM prototypes with different rotor poles at 400 rpm.

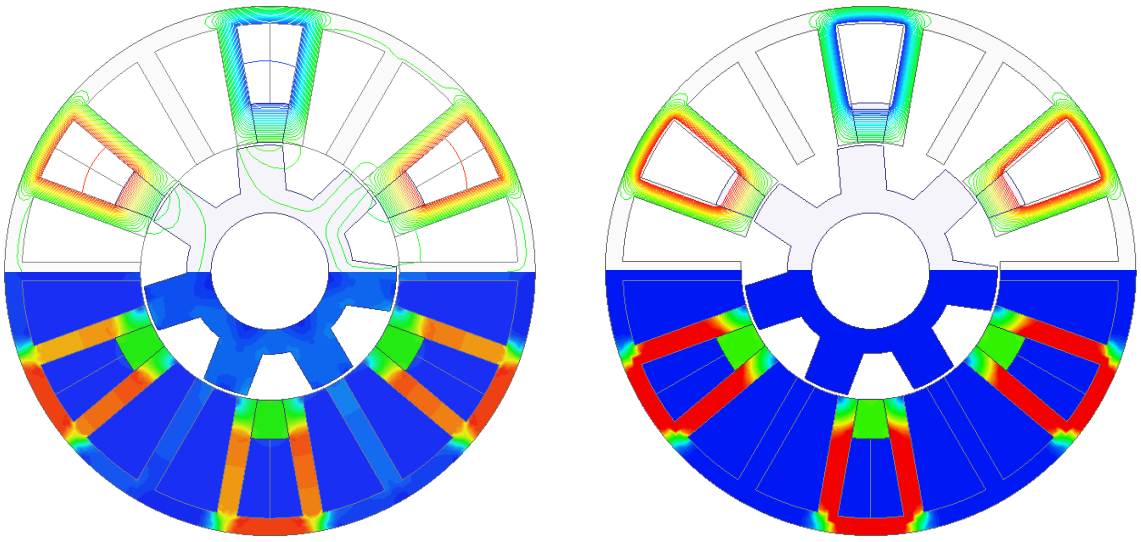

0° electrical degree

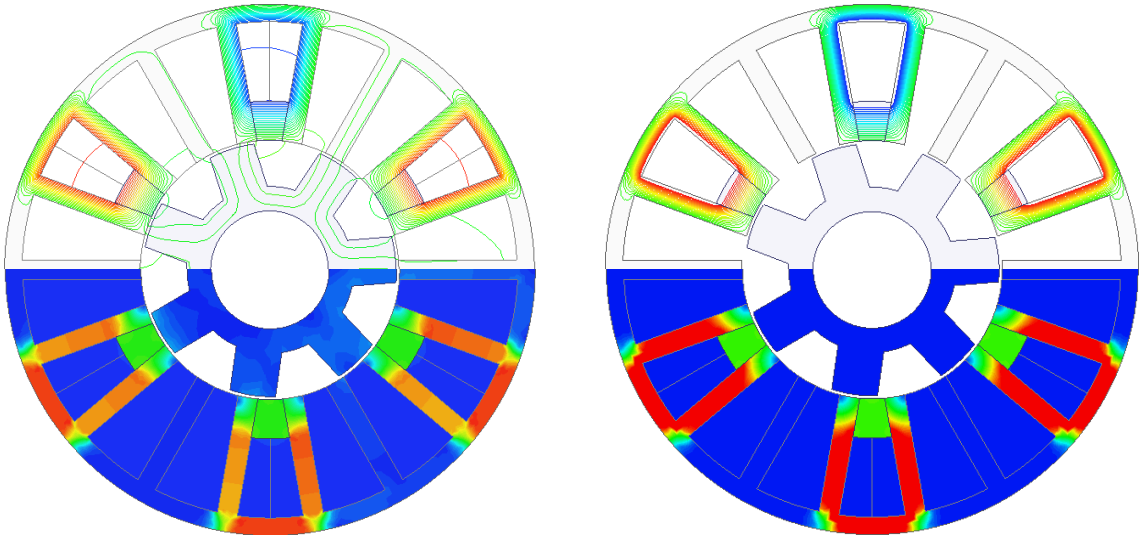

90° electrical degrees

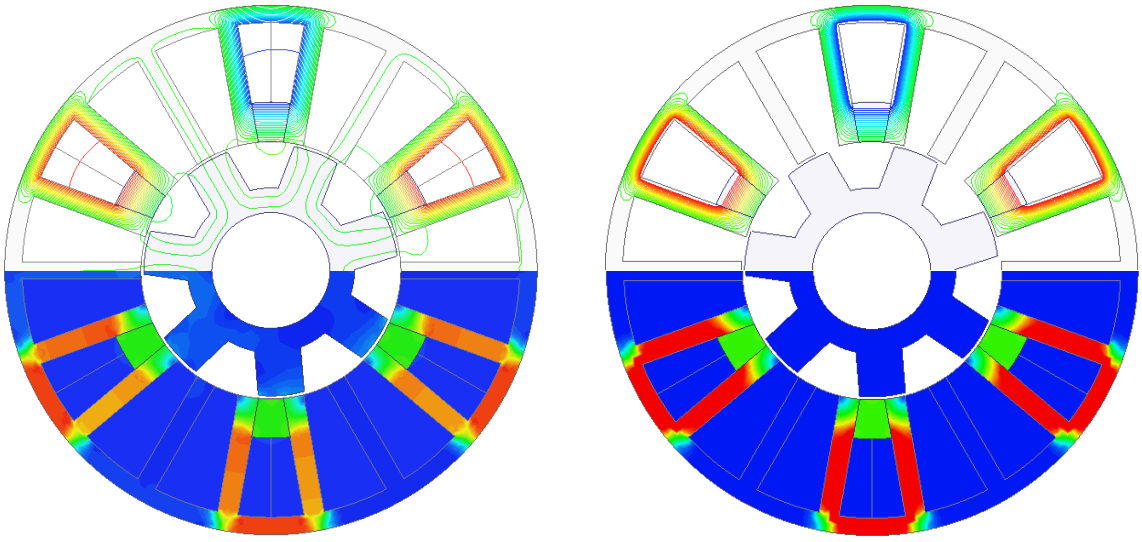

180° electrical degrees

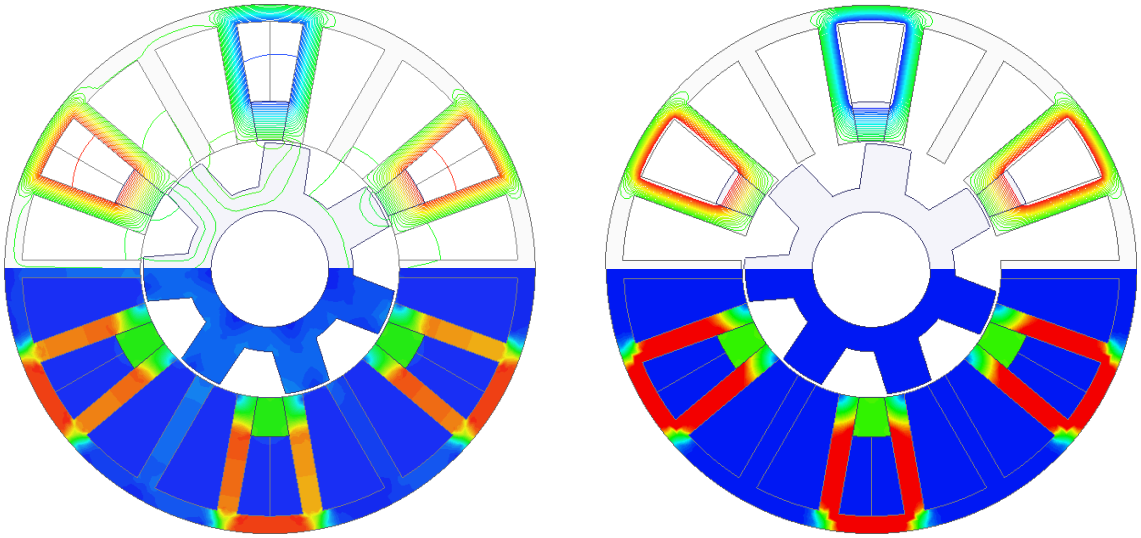

270° electrical degrees

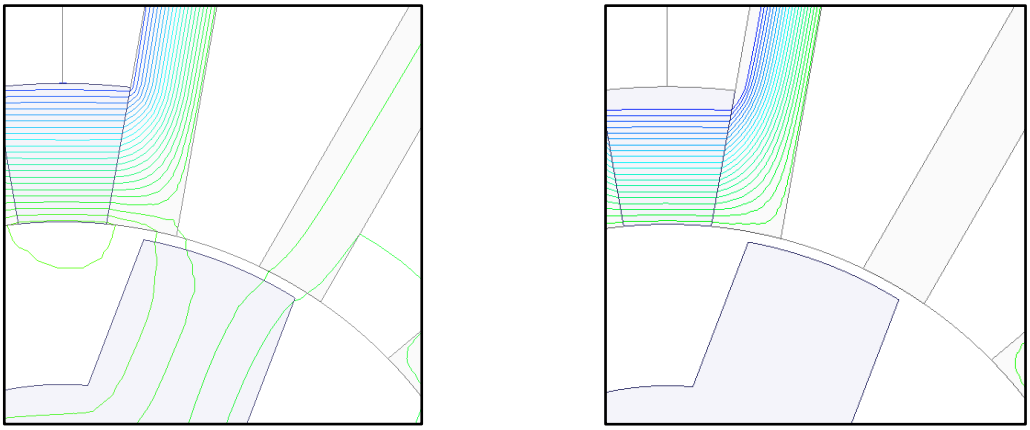

Zoon in

(a) non-linear stator and rotor material (b) linear stator and rotor material

(I) 7 rotor pole

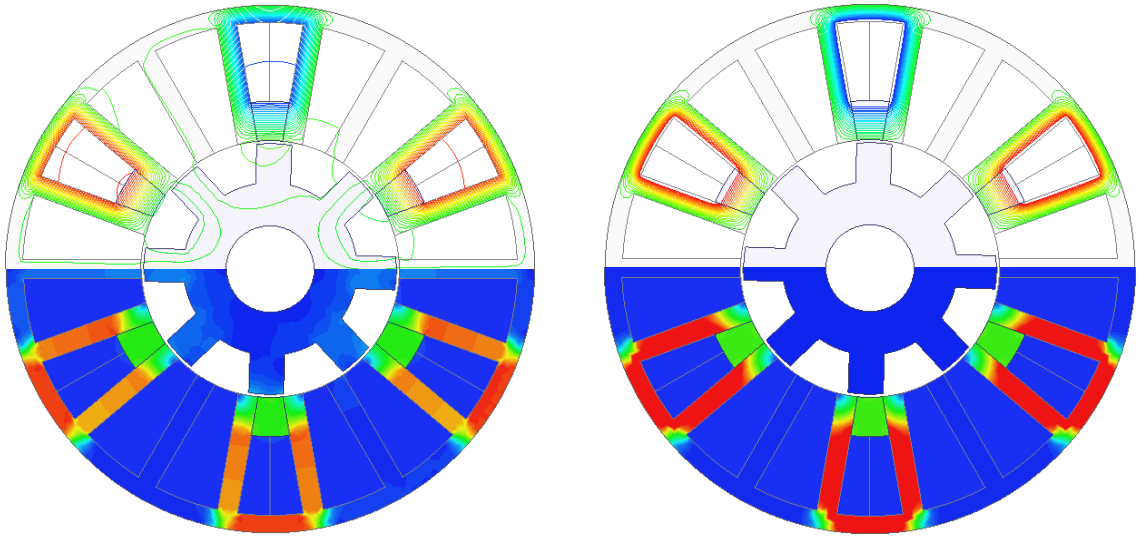

0° electrical degree

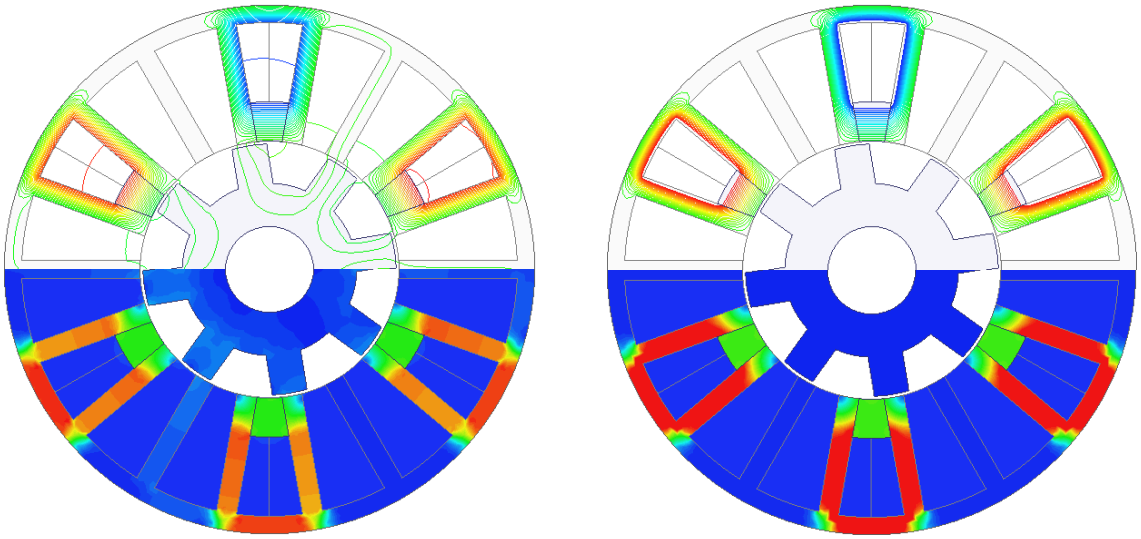

90° electrical degrees

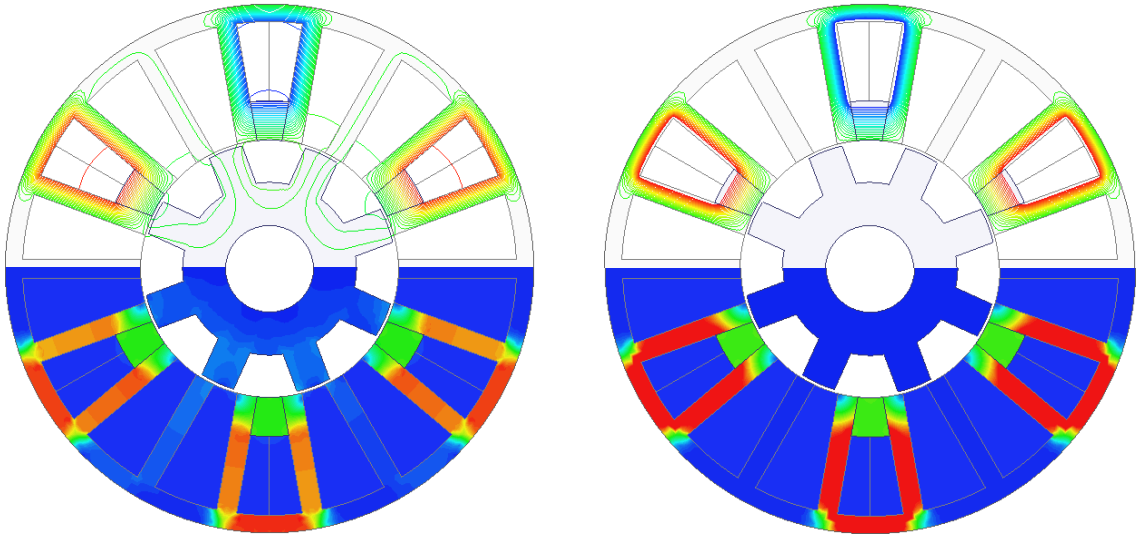

180° electrical degrees

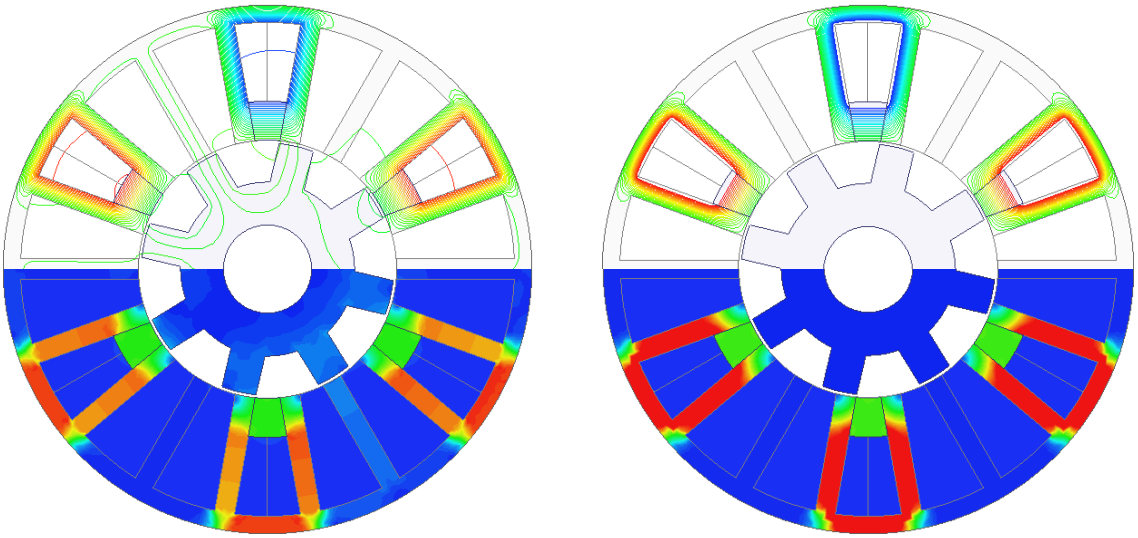

270° electrical degrees

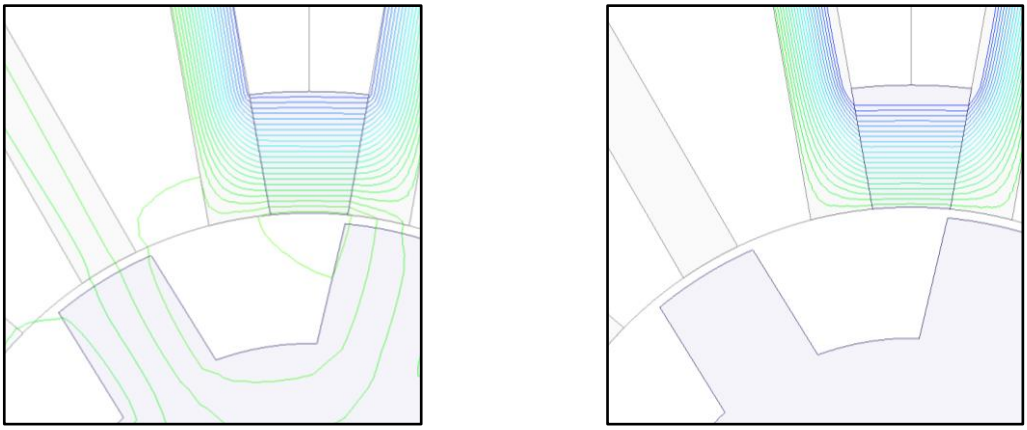

Zoon in

(a) non-linear stator and rotor material (b) linear stator and rotor material

(II) 8 rotor pole

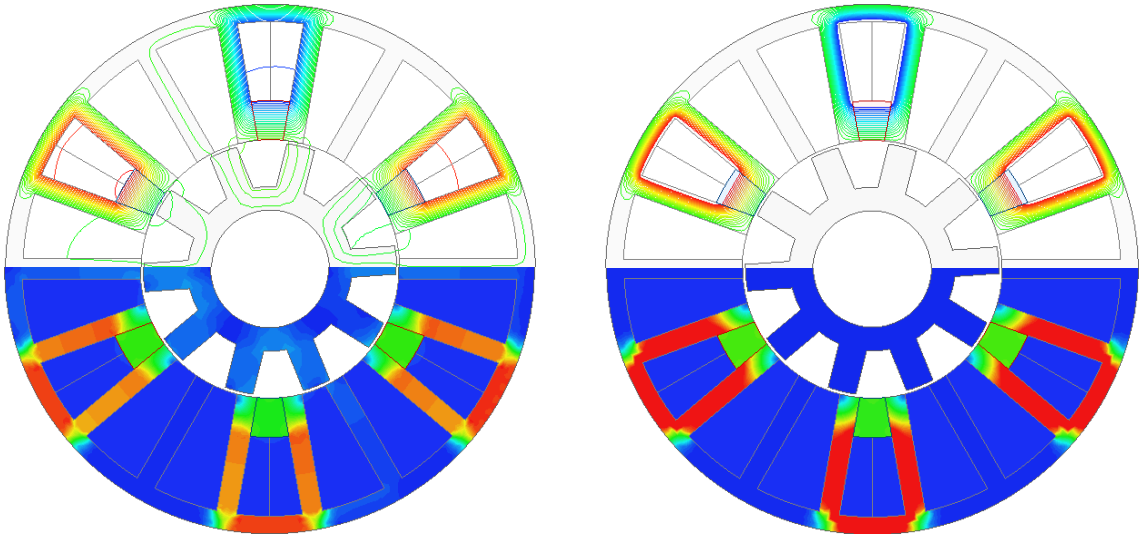

0° electrical degree

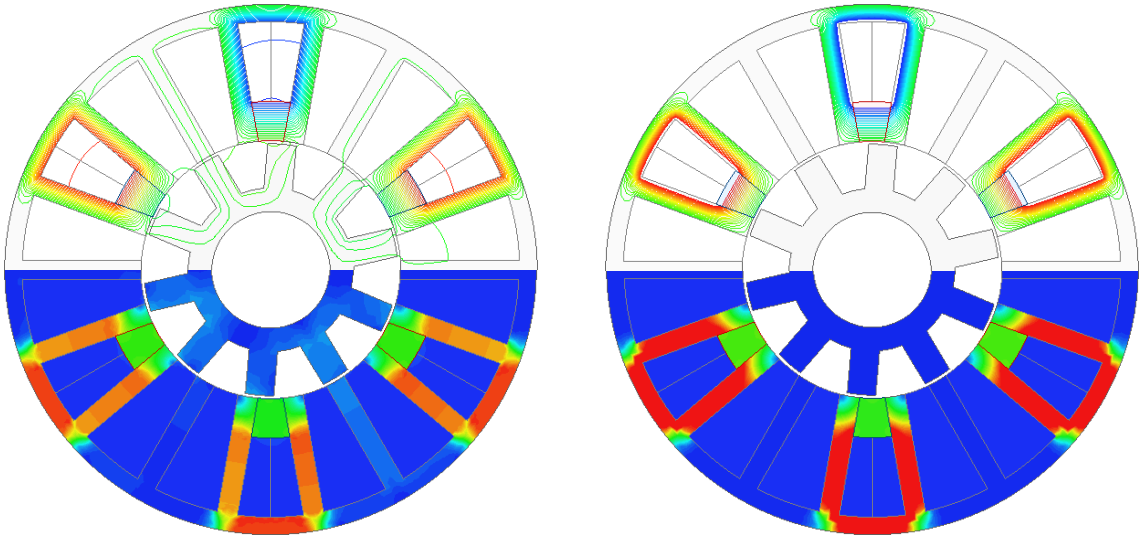

90° electrical degrees

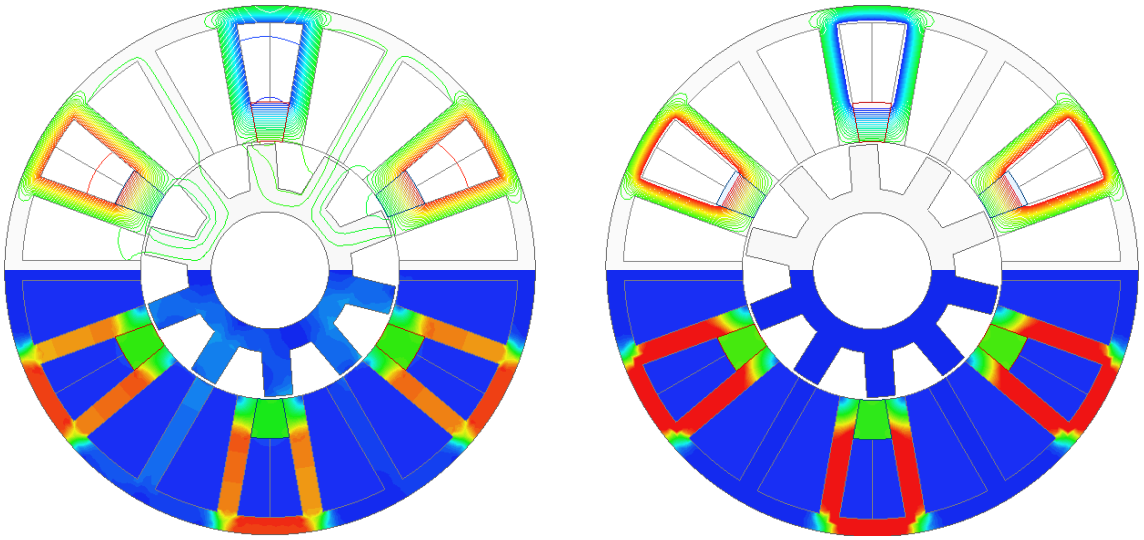

180° electrical degrees

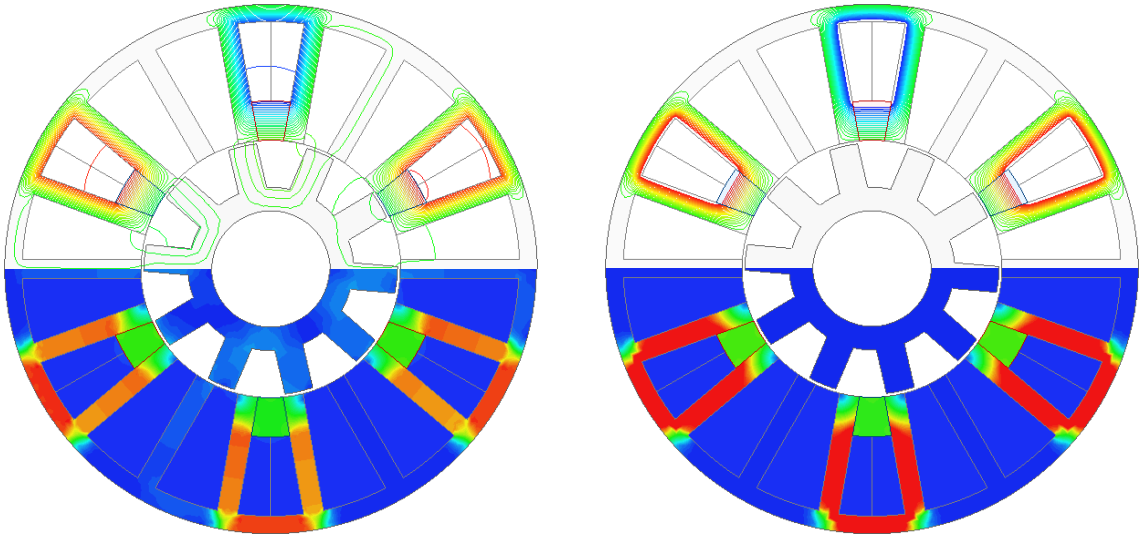

270° electrical degrees

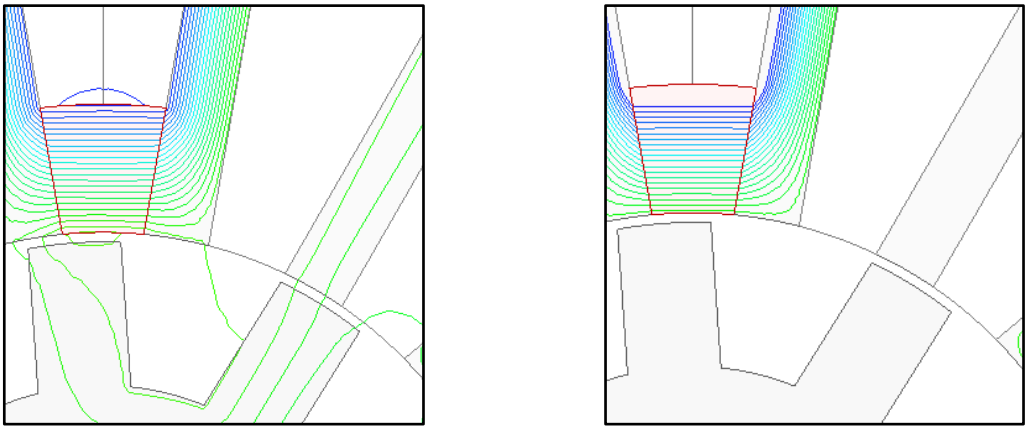

Zoon in

(a) non-linear stator and rotor material (b) linear stator and rotor material

(III) 10 rotor pole

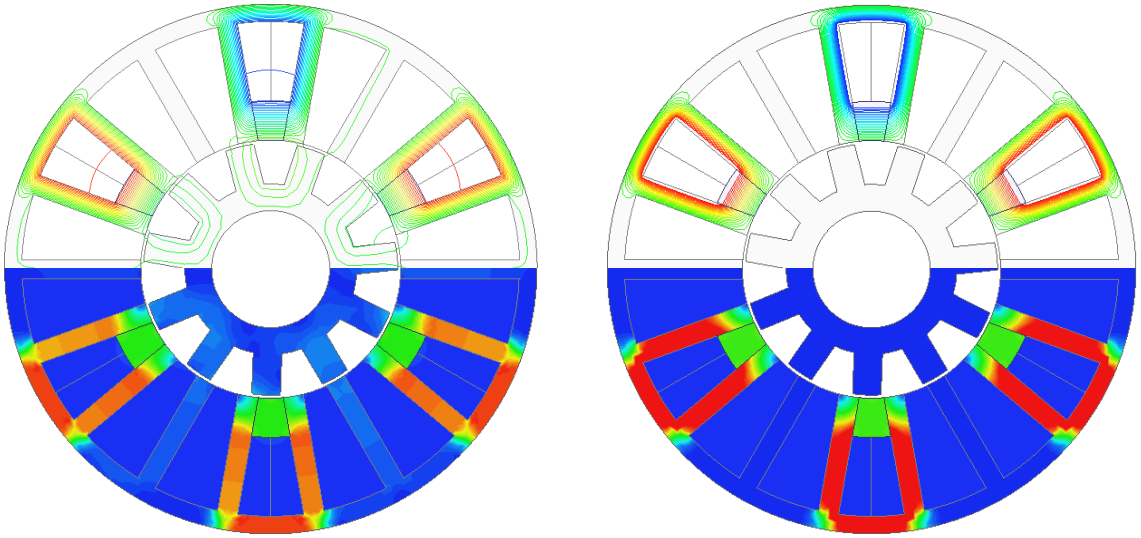

0° electrical degree

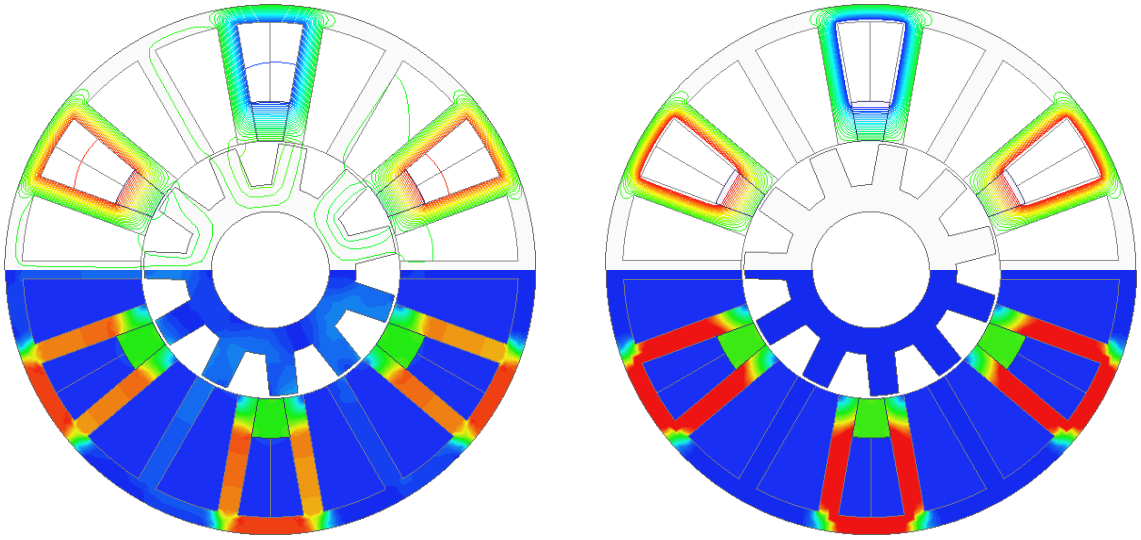

90° electrical degrees

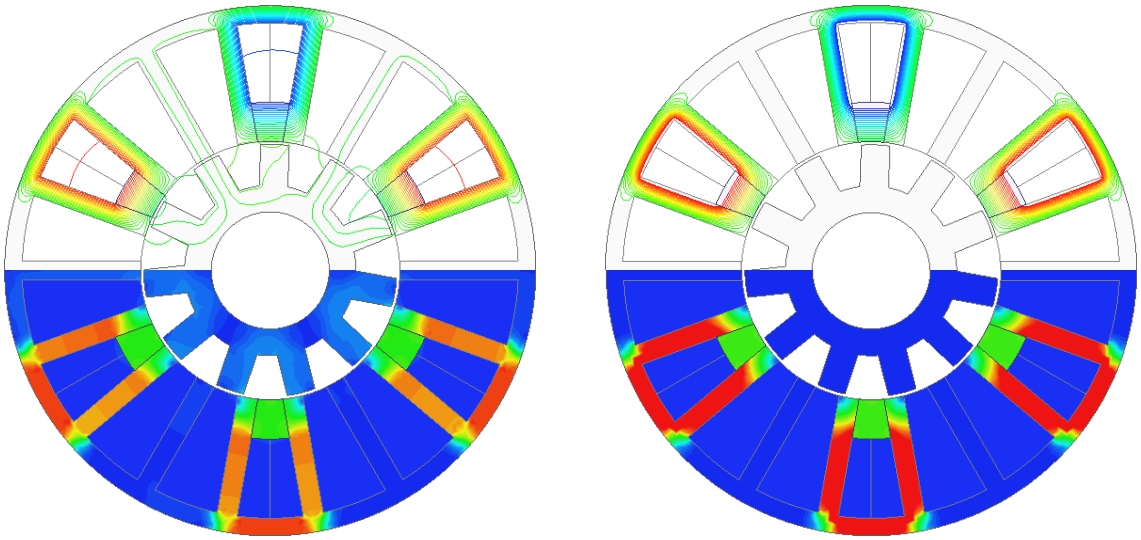

180° electrical degrees

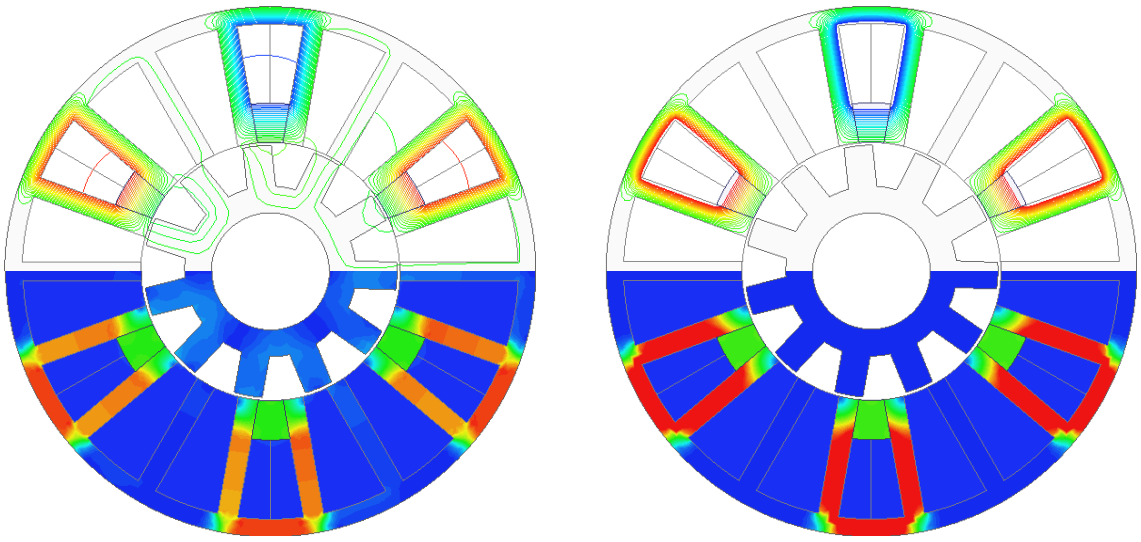

270° electrical degrees

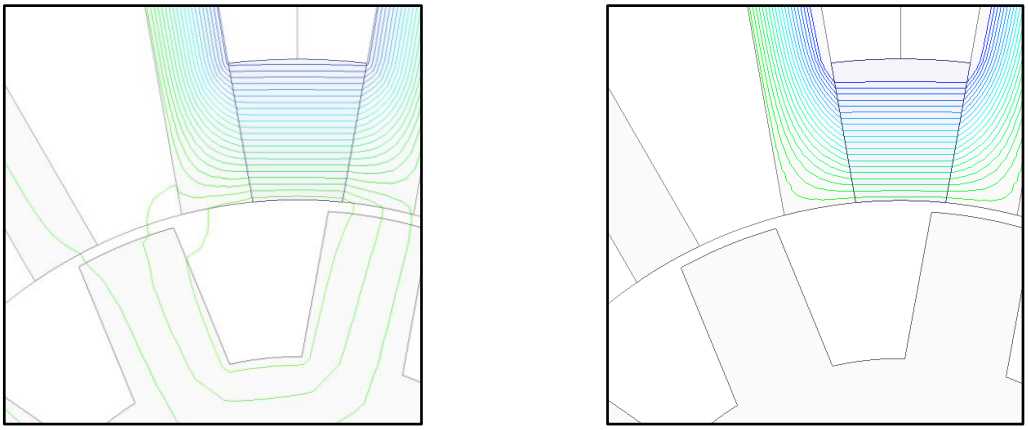

Zoon in

(a) non-linear stator and rotor material (b) linear stator and rotor material

(IV) 11 rotor pole

Fig. 5.12 Open-circuit flux line and flux density distributions of F3A2 HSSPM machines with different rotor poles at different rotor positions for non-linear/linear stator and rotor material.

According to Chapter 3, it shows that the back-EMF magnitude will be increased with the raised DC current, since the magnetic saturation will be reduced and then the PM flux will be pulled to the rotor via air gap, till all the PM fluxes are pulled to the rotor part at a specific DC current. When the DC current is further increased, the machine will become saturated again due to the flux caused by DC excitation. The back-EMF magnitude against DC current/DC current density for F3A2 HSSPM machines with different rotor poles are shown in Fig. 5.13. From Fig. 5.13, it shows that when the current density is less than 5A/mm^2 (rated current

density), the trend of magnitude of back-EMF increasing is smooth since the magnetic saturation caused by PMs is reducing. When the current density is increased from 5A/mm^2 to 30 A/mm^2, the air-gap flux is mainly produced by the DC current excitation which pulls the flux produced by PM to the rotor part via air-gap, and thus, the magnitude of back-EMF is raising significantly. Also, the machines tend to become magnetically saturated. When the DC current is at 30 A/mm^2, the magnitude of the phase back-EMF achieves the peak value, and then will be reduced if the DC current is further increased, which means the machine is over-excited due to magnetic saturation. The variation of magnetic saturation can be observed in Fig. 5.14. It is worth mentioning that the maximum DC current density chosen to test the prototype machine is 6A/mm^2. Thus, the test results are raising with the increasing DC current based on Fig. 5.13. In this case, the static torque will keep increasing with the increasing current density as the maximum torque requires a quite high current density.

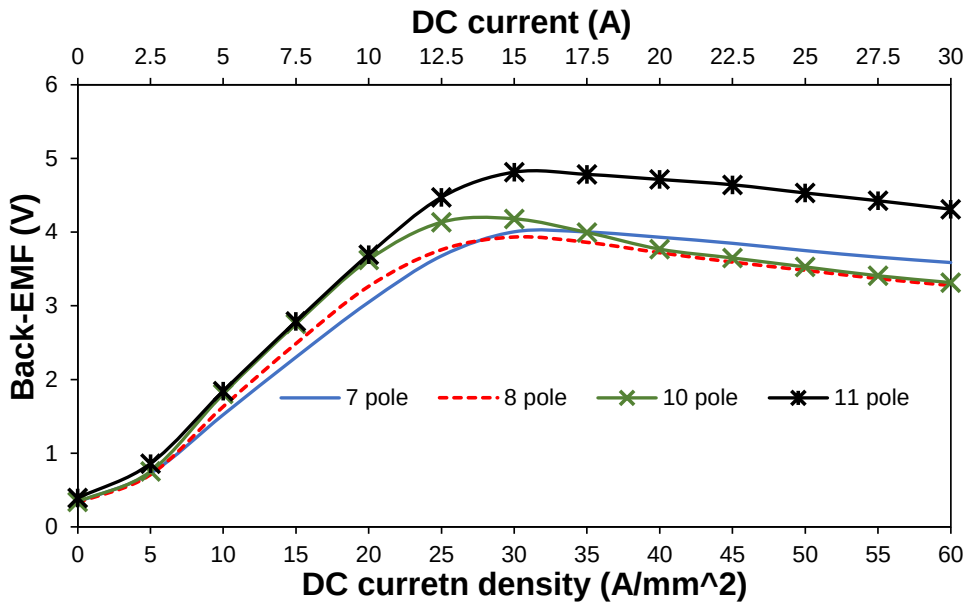

Fig. 5.13 Variation of phase back-EMF magnitudes of the F3A2 HSSPM machines with different rotor poles with the increasing DC current and DC current density.

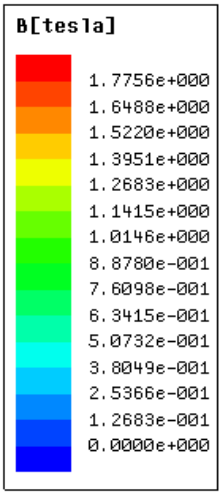

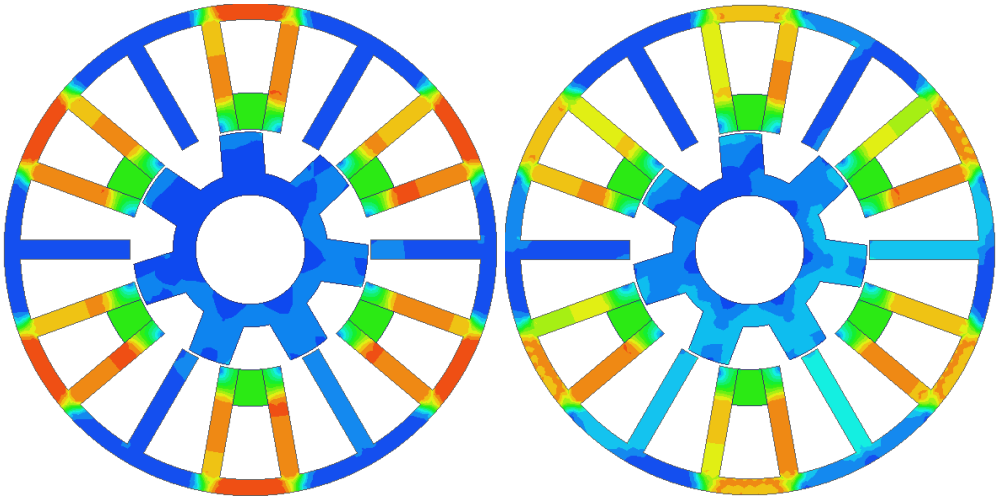

(a) J_{dc} = 0 (b) J_{dc} = 5A/mm^2 (rated)

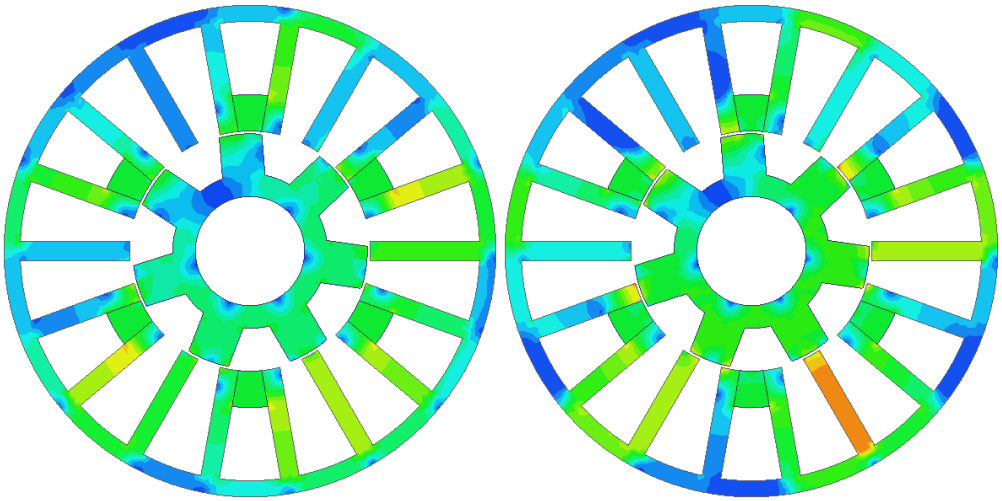

(c) J_{dc} = 15A/mm^2 (d) J_{dc} = 20A/mm^2

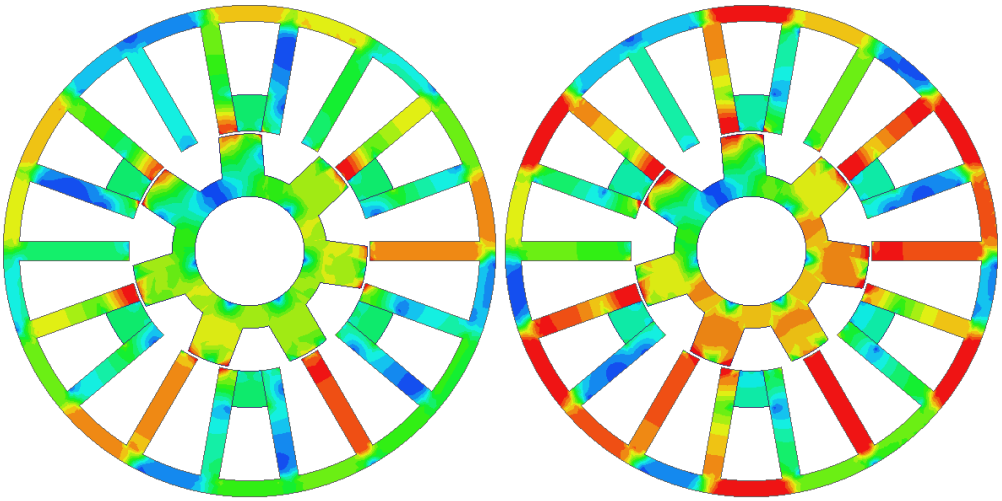

(e) J_{dc} = 30A/mm^2 (f) J_{dc} = 50A/mm^2

(I) 7 rotor pole

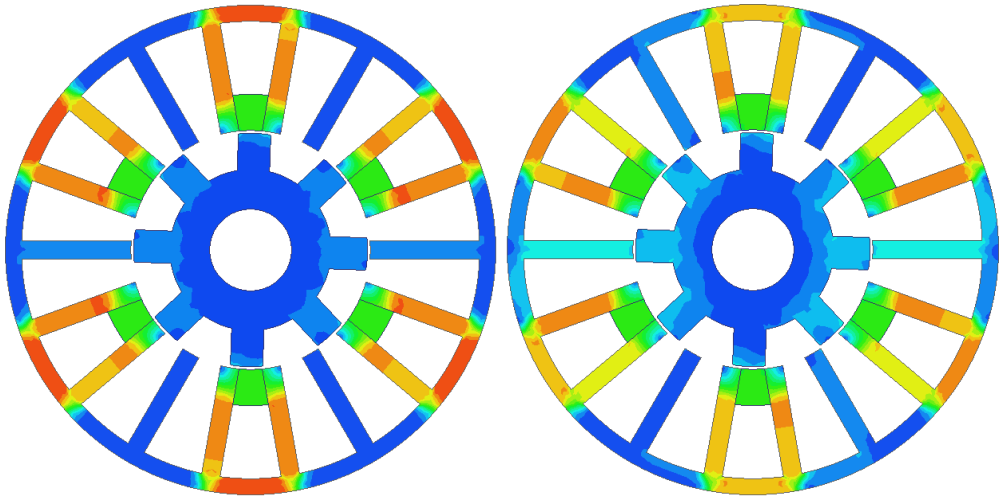

(a) J_{dc} = 0 (b) J_{dc} = 5A/mm^2 (rated)

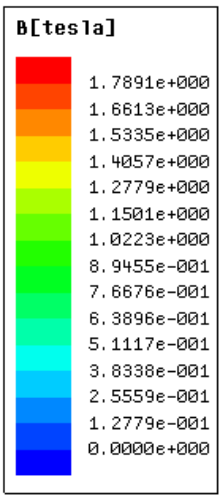

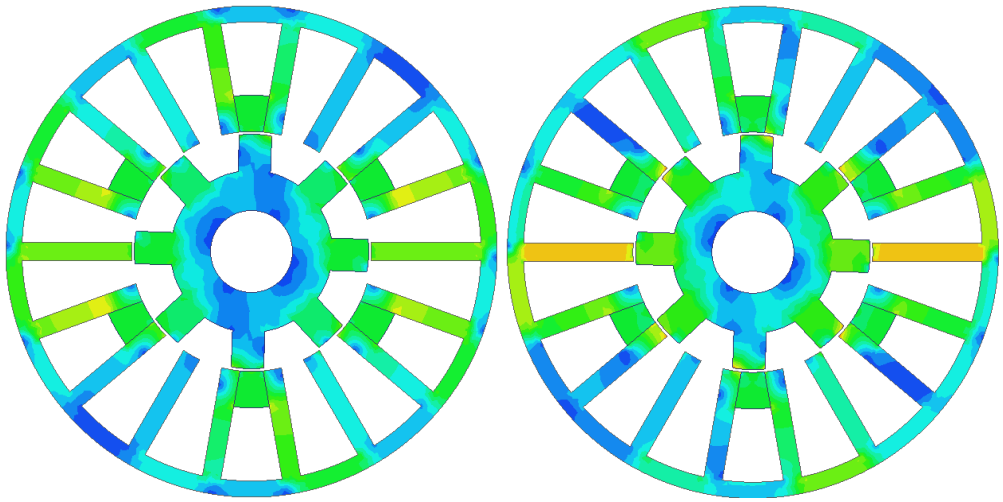

(c) J_{dc} = 15A/mm^2 (d) J_{dc} = 20A/mm^2

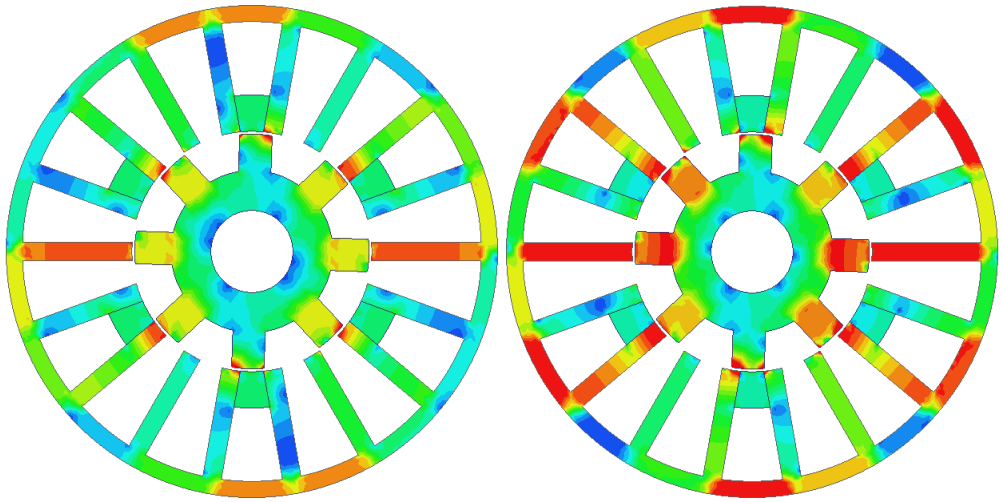

(e) J_{dc} = 30A/mm^2 (f) J_{dc} = 50A/mm^2

(II) 8 rotor pole

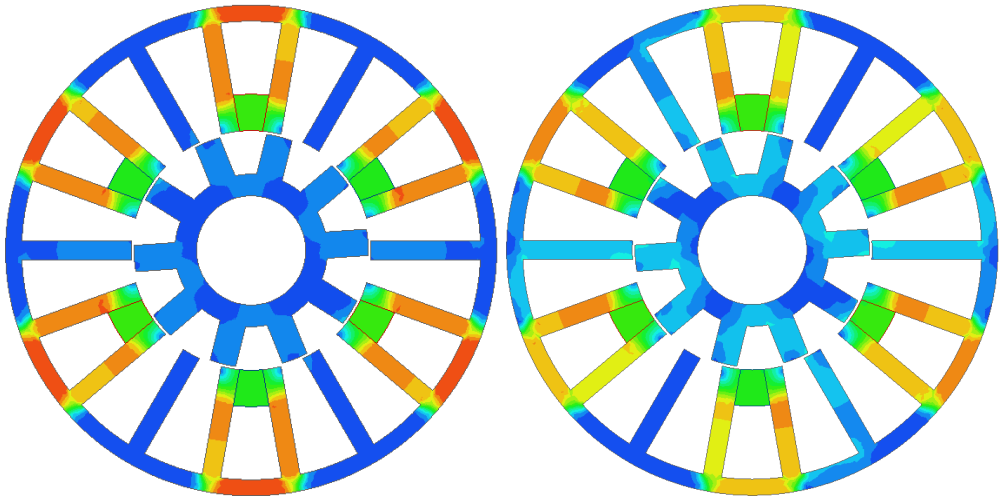

(a) J_{dc} = 0 (b) J_{dc} = 5A/mm^2 (rated)

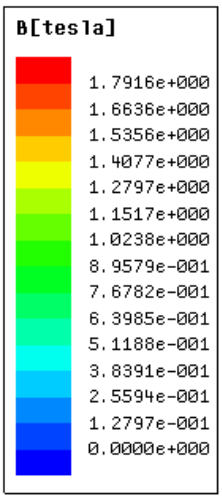

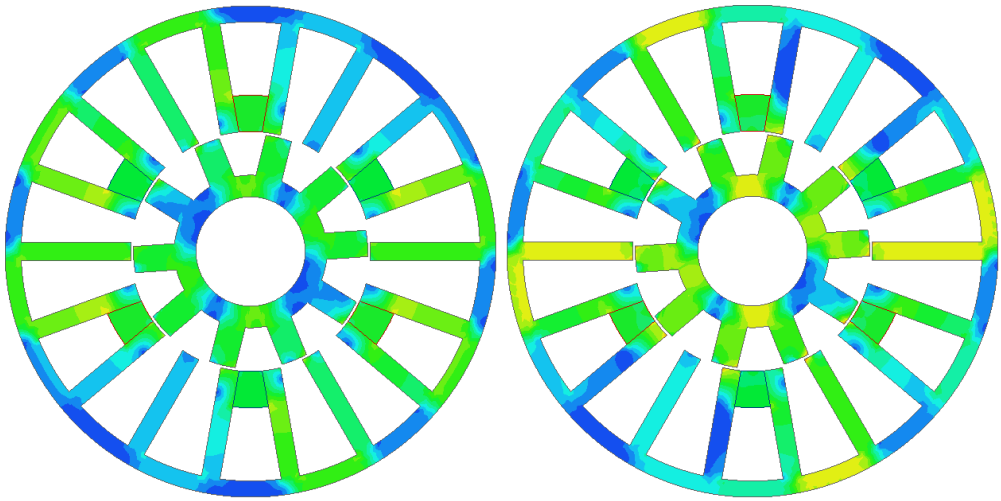

(c) J_{dc} = 15A/mm^2 (d) J_{dc} = 20A/mm^2

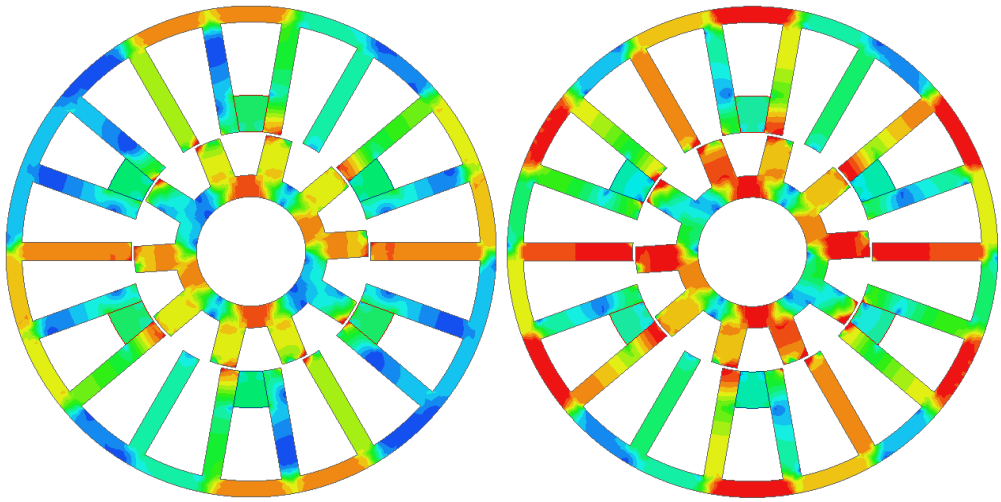

(e) J_{dc} = 30A/mm^2 (f) J_{dc} = 50A/mm^2

(III) 10 rotor pole

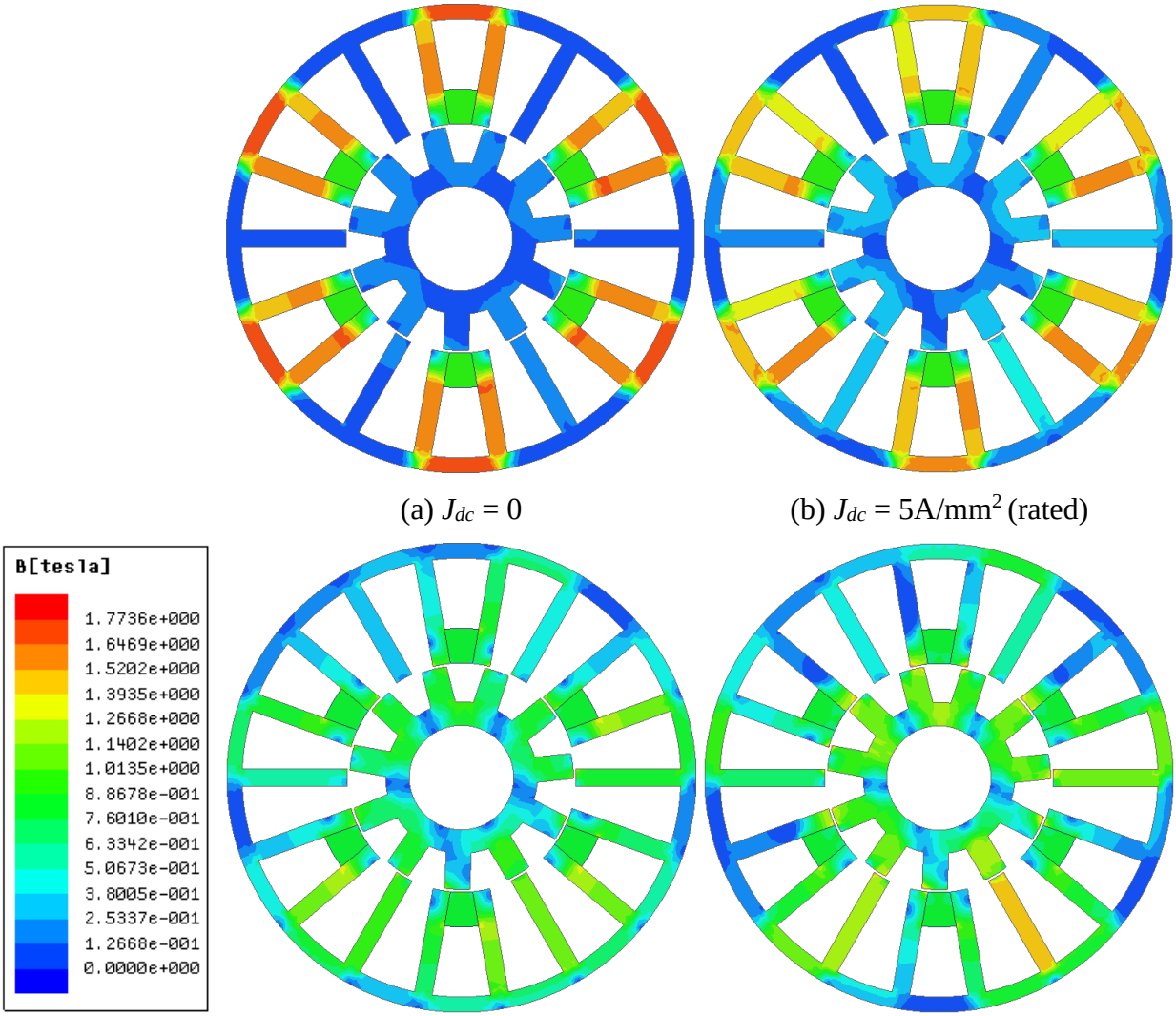

(a) J_{dc} = 0 (b) J_{dc} = 5A/mm^2 (rated)

(c) J_{dc} = 15A/mm^2 (d) J_{dc} = 20A/mm^2

(e) J_{dc} = 30A/mm^2 (f) J_{dc} = 50A/mm^2

(IV) 11 rotor pole

Fig. 5.14 Flux density distributions of F3A2 HSSPM machines with different rotor poles under different DC current density at initial rotor position.

5.3 F1A3 HSSPM machine

The electromagnetic performance of the 6-10 stator/rotor pole F1A3 HSSPM machine is planned to be validated using the prototype shown in Fig. 5.15. The prototype design parameters are shown in Table 5.2. During the open-circuit back-EMF measurement, some problems have been found due to the shortages in the machine design (such as too heavy magnetic saturation on open-circuit and too high required DC current vs. PM excitation) and also the tolerances in machine manufacture and assembly. These will be shown in details later in the experimental analysis part.

Table 5.2 Prototype design parameters

Parameters	**Unit**	**F1A3 HSSPMMs**
Stator outer radius (R_{SO})	mm	45
Stack length (l_{stack})	mm	25
Air-gap length (G)	mm	0.5
Copper loss (P_{Cu})	W	60
PM volume (V_{PM})	mm^2	6396
Packing factor (k_p)		0.4
Back-iron thickness (H_{BI})	mm	4.23
Stator inner radius (R_{SI})	mm	20.14
Stator pole arc (θ_{st})	Mech. Deg.	6.78
Stator tooth width (w_{st})	mm	2.38
Split ratio (R_{SI} / R_{SO})		0.436
PM thickness (H_{PM})	mm	3.99
Rotor outer radius (R_{RO})	mm	19.64
Rotor pole arc (θ_{rt})	Mech. Deg.	15.68
Rotor tooth width (H_{Rtooth})	mm	5.03
Ratio of field to armature slot current density (J_{ratio})		0.5

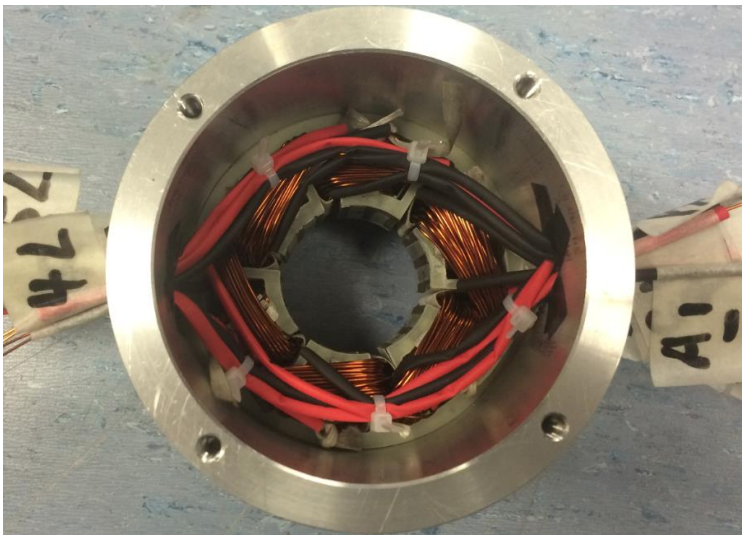

(a1) Stator

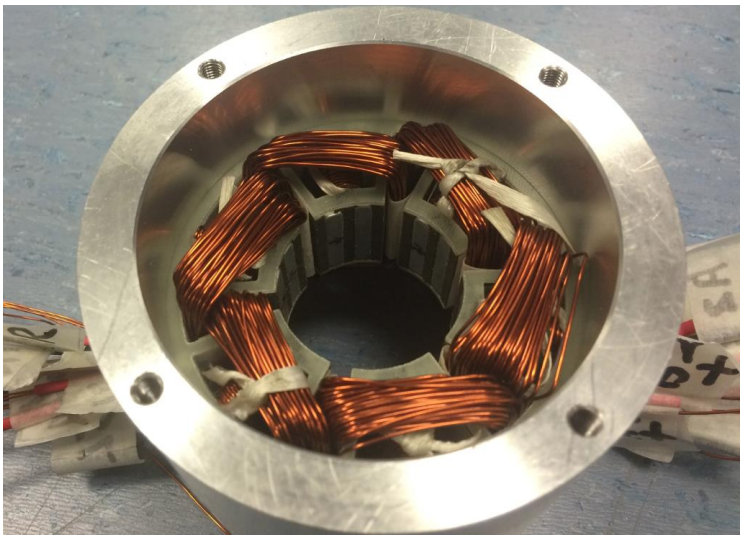

(a2) Stator

(b) Rotor (10-rotor pole)

Fig. 5.15 Prototype machine with 6-10 stator/rotor poles.

5.3.1 Open-circuit back-EMF test results

Due to the restriction of oscilloscope probes, the three phases of the machine are measured separately. The back-EMFs for both phase windings and each coil have been measured as well. The measured results are filtered and converted to the same rotor rotating speed of 400 rpm. The display for three phases on Fig. 5.16 did not consider the phase difference for three phases which are measured separately, while they are deliberately shown without phase shifts which are normally 120 degrees in order to reveal the difference amongst three phases. From Fig. 5.16, it shows that the amplitudes and waveforms of three phases are different, especially for phase 'A'. For the coil back-EMF waveforms, the coil back-EMF waveforms in phase 'A' have slightly difference, while the amplitudes of the coil back-EMF waveforms for coil B1 and coil C1 are twice larger than those of coil B2 and C2, respectively.

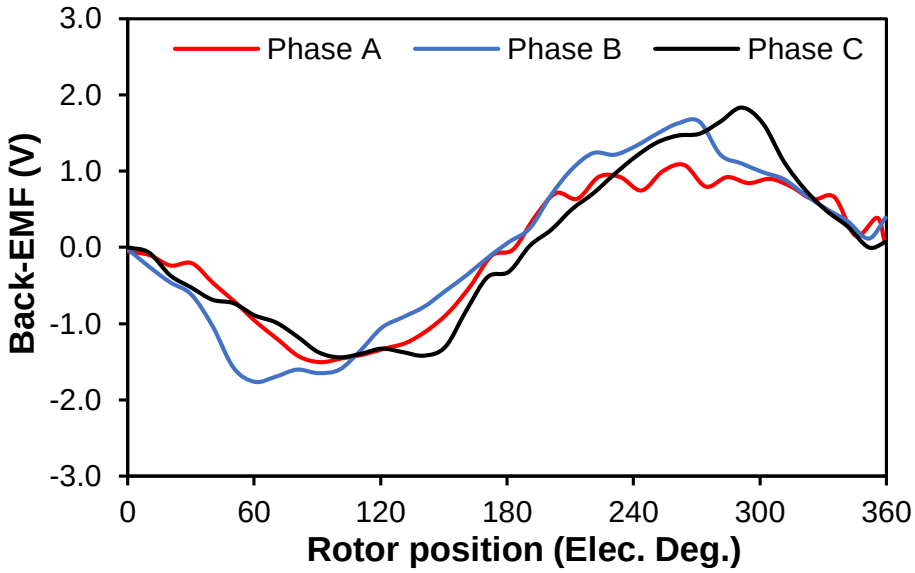

(a) Phase back-EMF waveforms (the actual three phase back-EMFs are shifted by 120 degrees electrically, but for easy comparison they are drawn in phase)

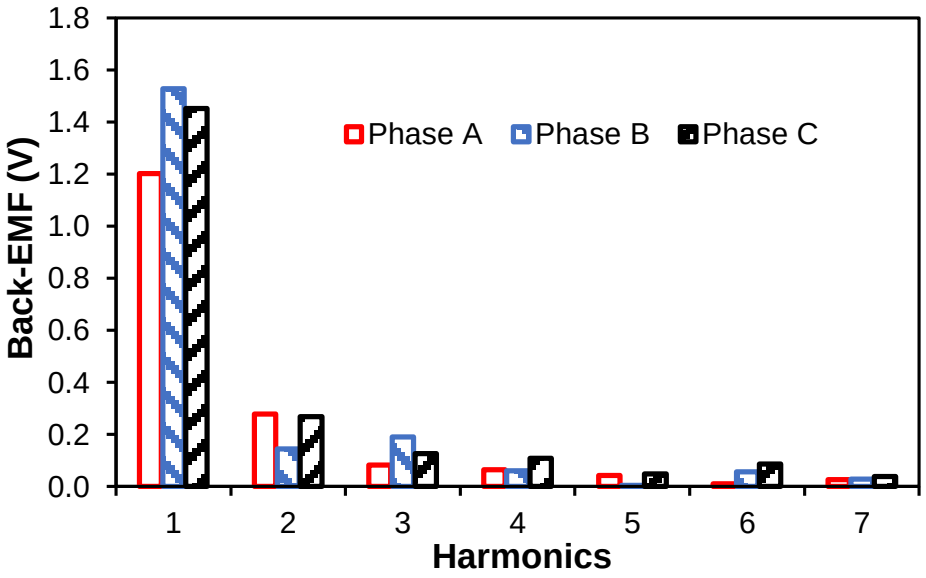

(b) Spectra

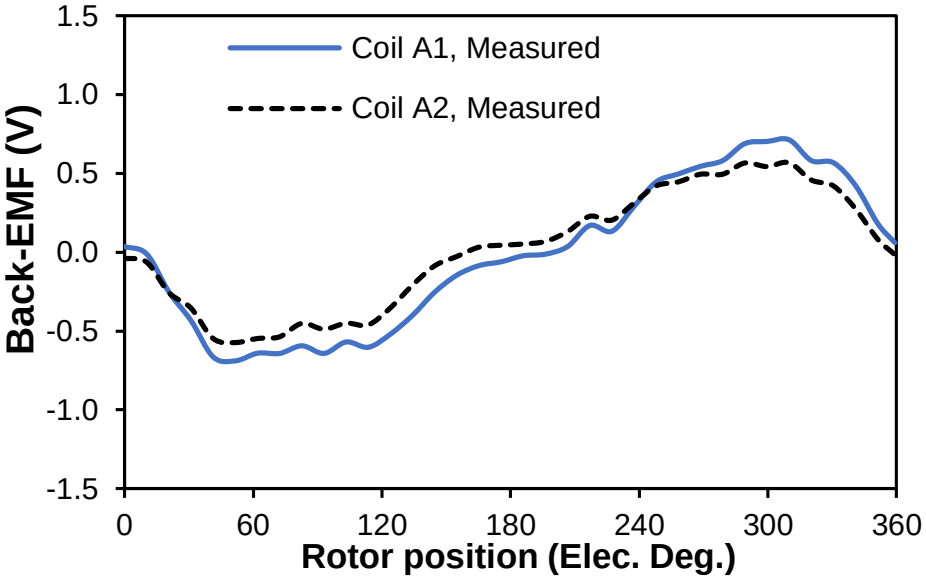

(d) Back-EMF waveforms for coil A1 and A2, Phase A

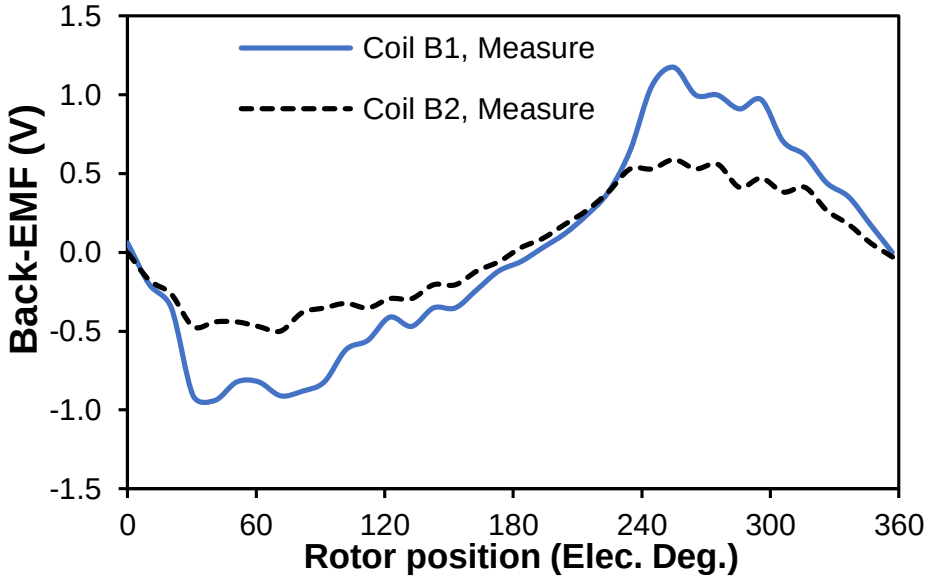

(e) Back-EMF waveforms for coils B1 and B2, Phase B

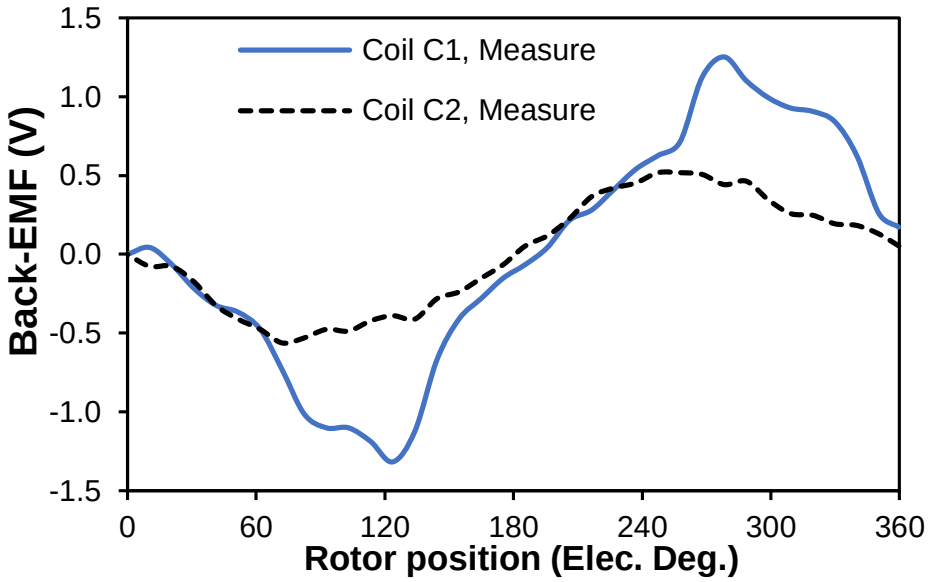

(f) Back-EMF waveforms for coils C1 and C2, Phase C

Fig. 5.16 Measured back-EMF waveforms for phases and coils. (Rotating speed=400rpm, I_{dc}=0, I_{ac}=0)

5.3.2 Test result analysis

According to the machine basic operation principle, the open-circuit back-EMF at no DC excitation should be almost negligible. However, the test results from Figs. 5.16 (a)-(c) show that the amplitudes of phase back-EMFs are larger than 1V. Thus, the prototype machine is simulated by FEA with non-linear and linear lamination materials for machine stator and rotor, and the no DC current excitation back-EMF waveforms are shown in Fig. 5.17. Fig. 5.17 shows that when the stator and rotor employ linear material, the back-EMFs are almost negligible. This means that the machine is magnetically saturated without DC current excitation, which can be proved by the flux density distributions displayed in Fig. 5.18. From the figure, it shows that the stator tooth between two adjacent PMs is magnetically saturated due to the flux produced by PMs. Thus, the phase back-EMFs of the machine are produced by flux-leakage.

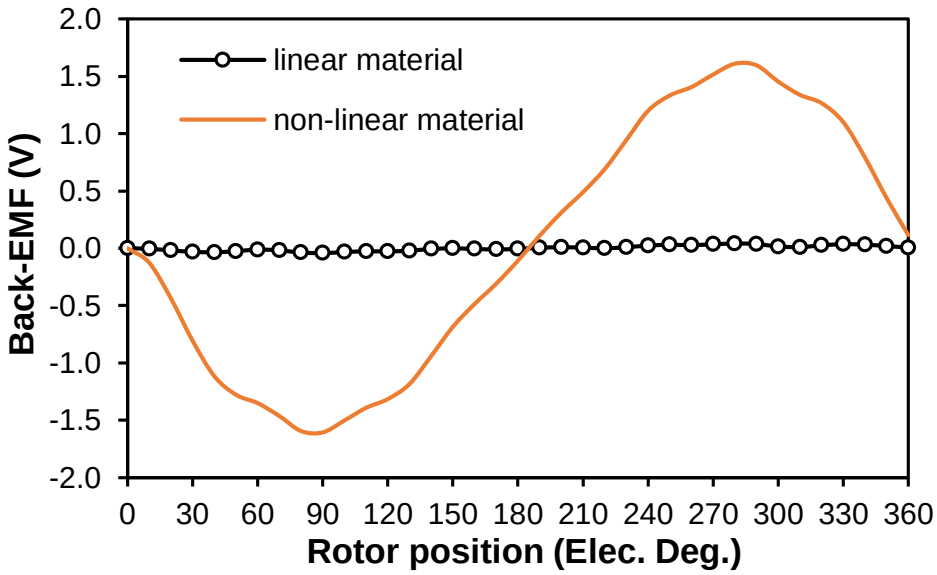

Fig. 5.17 Open-circuit Phase ‘A’ back-EMF waveforms for non-linear and linear material stator and rotor.

Rotor position (Elec. Deg.)	Non-linear material stator and rotor	Linear material stator and rotor
(a) 0°	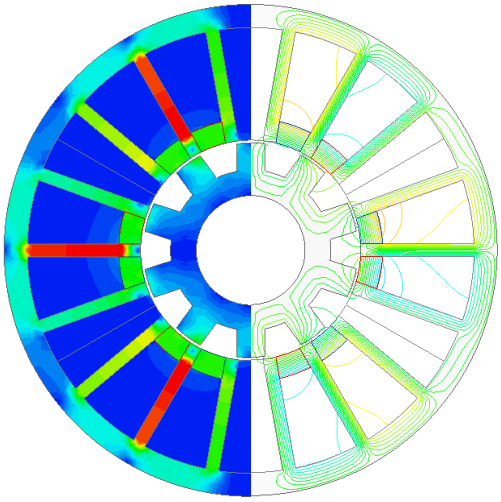	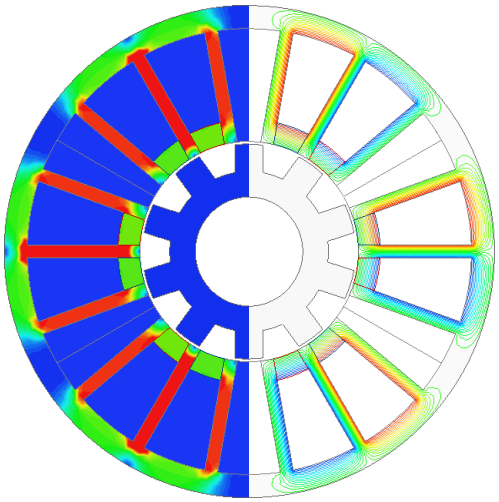
(b) 90°	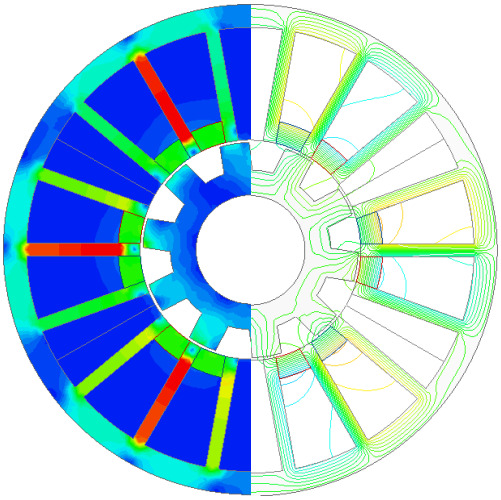	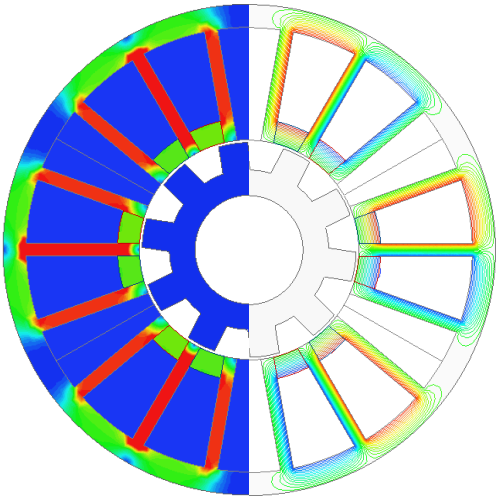
(c) 180°	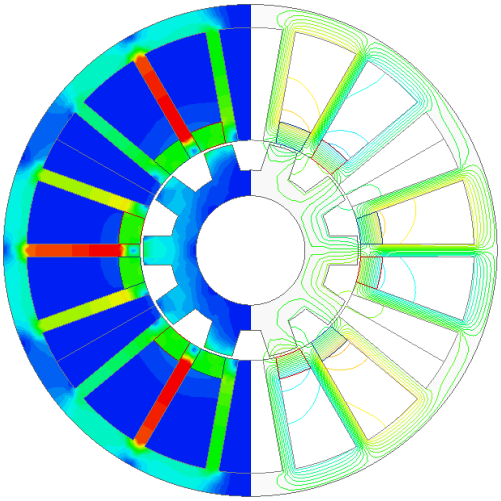	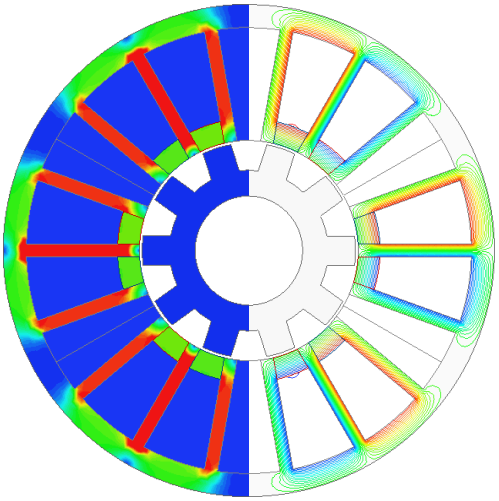

(d) 270°

(e) Zoon in

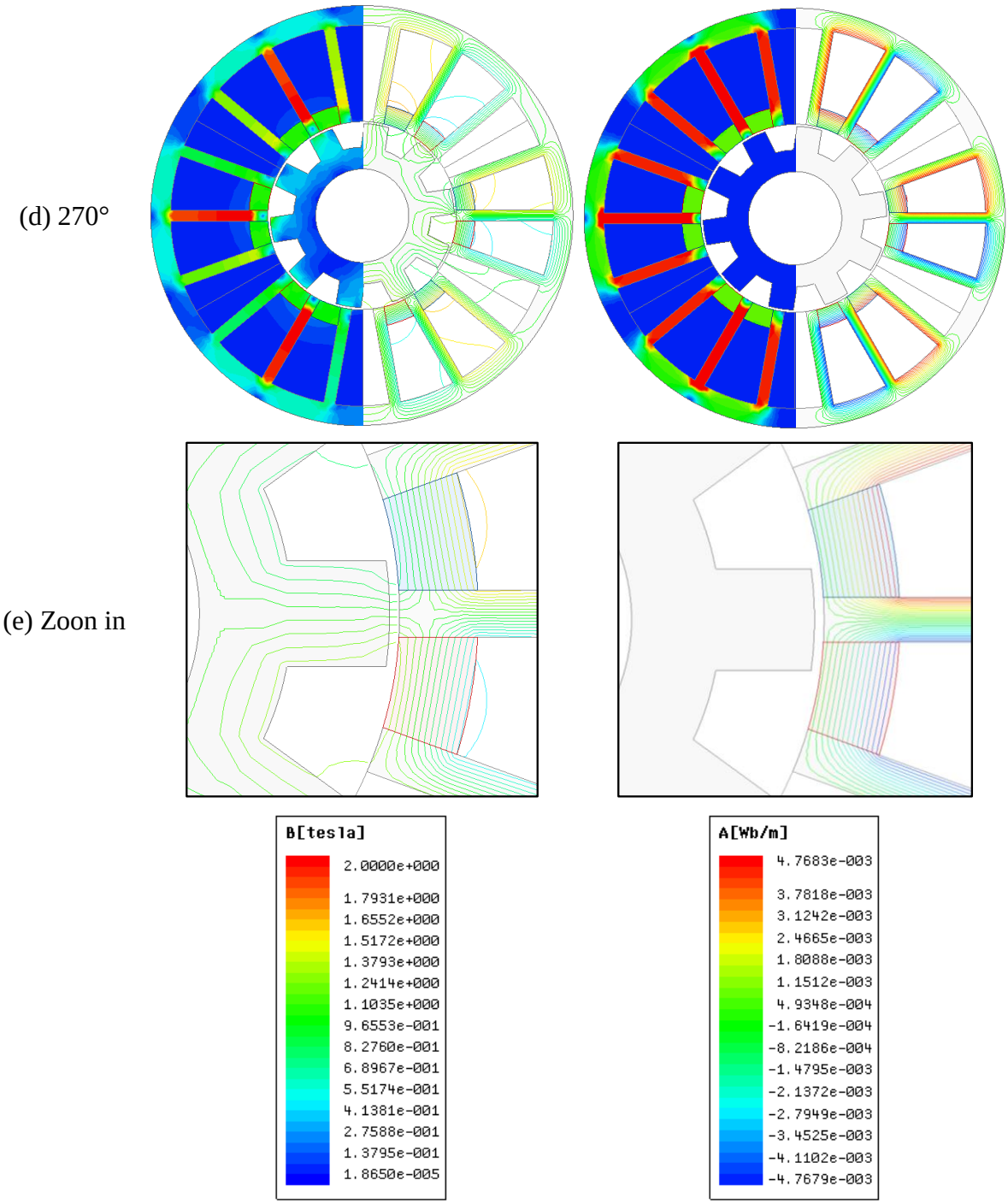

Fig. 5.18 Open-circuit flux density distributions for non-linear and linear material stator and rotor at different rotor positions (in electrical degree).

Similar to the F3A2 HSSPM machine, the magnitude of back-EMF can be varied by the increasing DC current excitation, Fig. 5.19. Due to the lack experience of coil winding (this was the very first prototype wound), the practical packing factor of the machine is nearly 0.3, and thus, the maximum DC current density for experiment should be 15 A/mm^2. However, the magnitudes of back-EMF for the non-linear material stator/rotor variation curve show that

when the DC current density is less than 25 A/mm^2, the DC excitation is used to reduce the saturation caused by PMs. Due to the adjacent two PMs are magnetized in opposite direction, the magnetic saturation can be reduced by applying a higher DC current excitation. For the DC current density from 25 to 50 A/mm^2, the flux produced by DC excitation will contribute more significantly to the phase back-EMF. Then, the machine tends to magnetically saturation again after the DC current density over 60 A/mm^2, as the machine is over excited. The flux density distributions at DC current density of 0, 15, 40, 60 and 80 A/mm^2 are shown in Fig. 5.20 to prove the variation of the back-EMF curve for non-linear material stator and rotor machine.

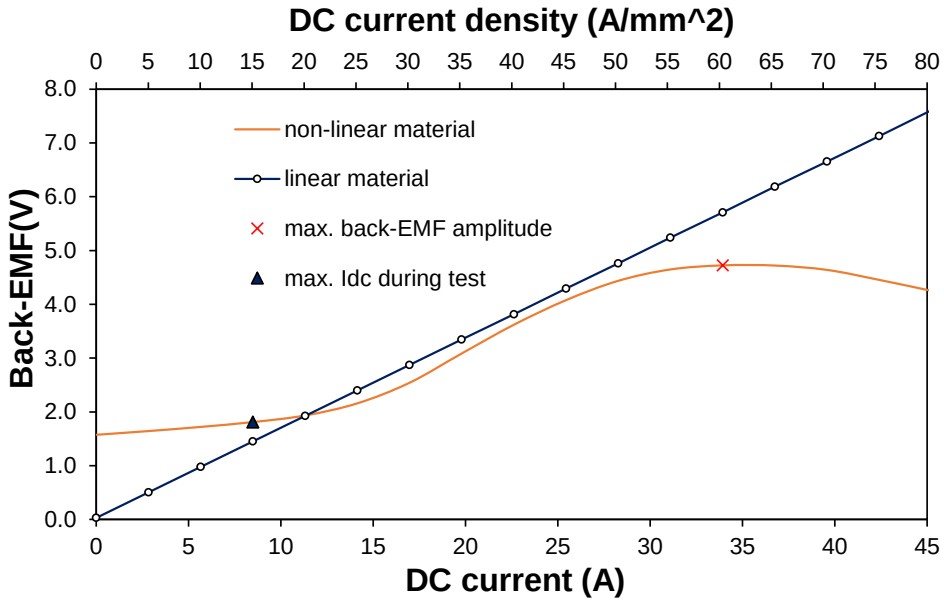

Fig. 5.19 Variation of phase back-EMF magnitudes of the F1A3 HSSPM machine with non-linear and linear materials for stator and rotor with the increasing DC current and DC current density.

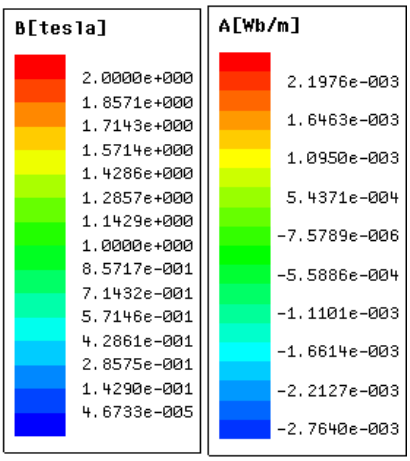

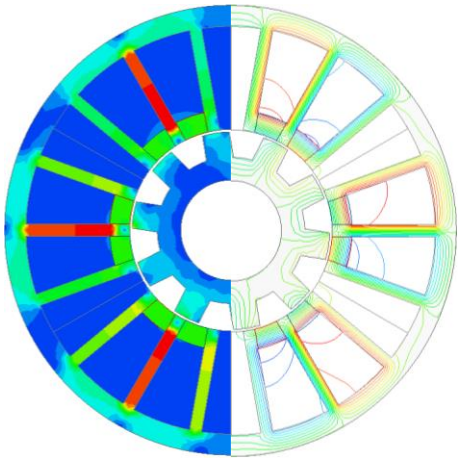

(a) J_{dc} = 0

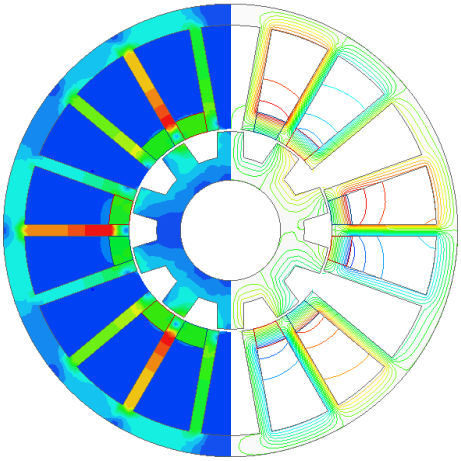

(b) J_{dc} = 15 A/mm^2

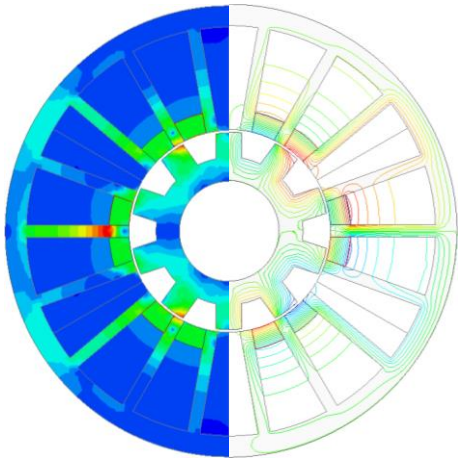

(c) J_{dc} = 40 A/mm^2

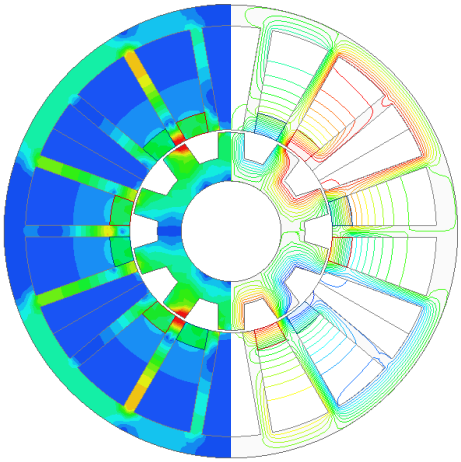

(d) J_{dc} = 60 A/mm^2

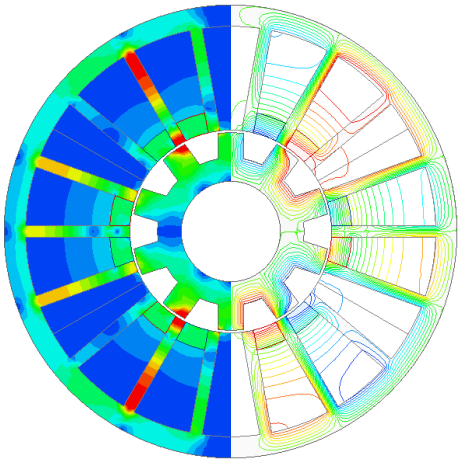

(e) J_{dc} = 80 A/mm^2

Fig. 5.20 Flux density distributions of F1A3 HSSPM machine under different DC current density at initial rotor position.

Based on the test results, the coil back-EMF waveforms for phase A are almost similar, whilst the coil back-EMF waveforms for coil B1 and C1 are almost twice larger than those of B2 and C2, respectively. Thus, the rotor of the prototype is suspected to be eccentric towards coils B1 and C1 due to the machine assembly tolerance. The prototype is simulated by 2D FEA with the static rotor eccentricity of 0%, 25%, 50% and 75% towards to the centre between coils B1 and C1. The phase back-EMF and coil back-EMF waveforms are shown in Fig. 5.21. From the Fig. 5.21, the test results are quite similar to the machine with rotor shaft eccentricity of 50% based on coils in phase 'B' and phase 'C'. The coil back-EMF waveforms in phase 'A' have same amplitude. However, since the amplitude of the measured back-EMF for Coil A1 is slightly larger than that for Coil A2, the rotor eccentricity is found to be further 6% towards coil A1 based on the rotor shaft eccentricity of 50% towards the centre between coils B1 and C1, which is selected according to the amplitude difference. Then, the comparison of measured and FEA predicted phase and coil back-EMF waveforms are presented in Fig. 5.22. From Fig. 5.22, the amplitudes of measured back-EMF waveforms are smaller than the amplitudes of FEA predicted back-EMF waveforms. The predicted and measured waveforms are of good agreement but not perfectly the same since the exact eccentric positon of the rotor is not sure since the 3D rotor eccentricity may exist and may be different from the 2D FEA predicted rotor eccentricity. The rotor shaft may also be slightly dynamically eccentric.

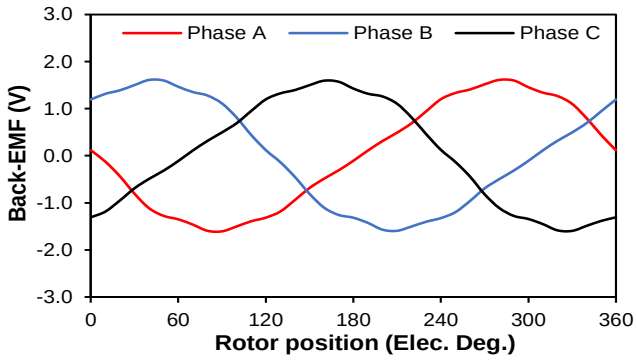

(a) 0% rotor shaft eccentricity

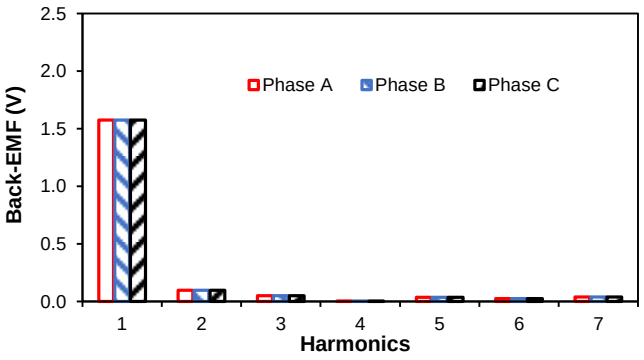

(b) Harmonics

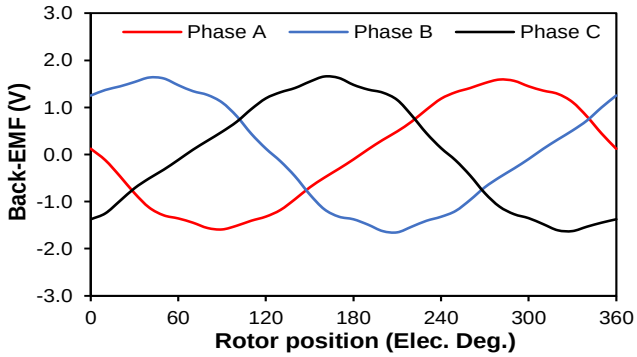

(c) 25% rotor shaft eccentricity

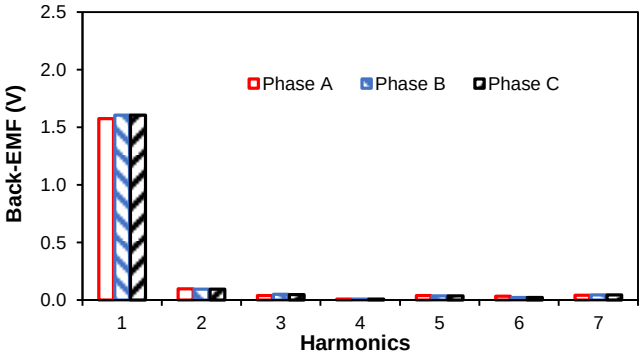

(d) Harmonics

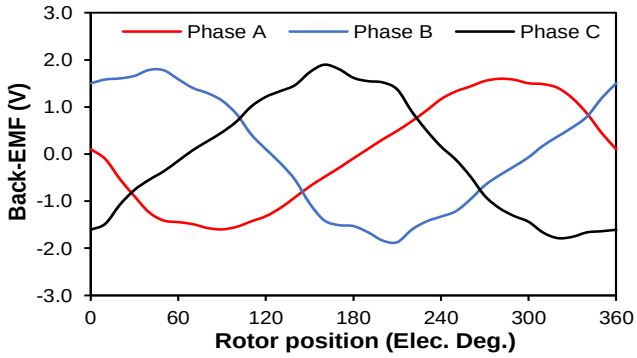

(e) 50% rotor shaft eccentricity

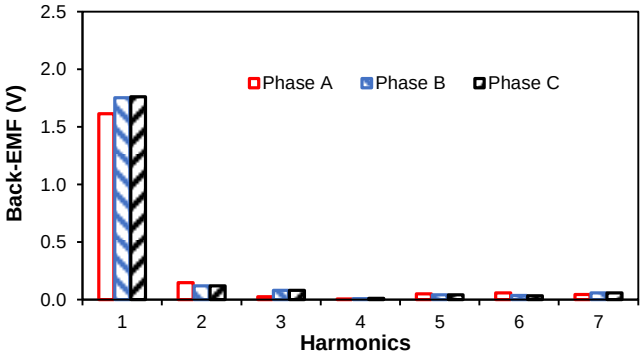

(f) Harmonics

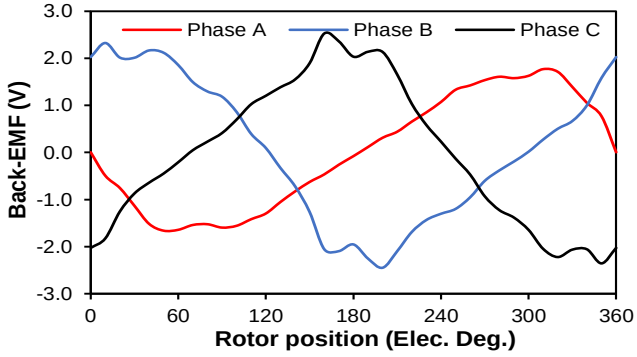

(g) 75% rotor shaft eccentricity

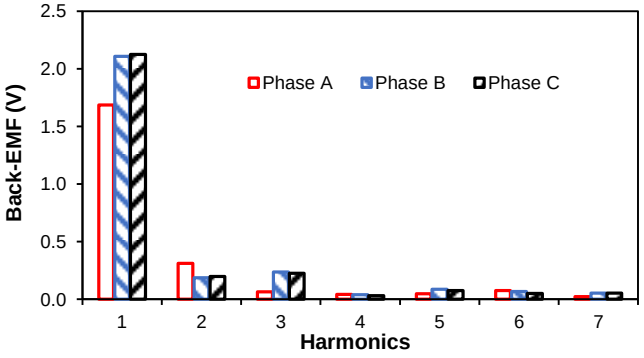

(h) Harmonics

(I) FEA predicted phase back-EMF waveforms (400 rpm)

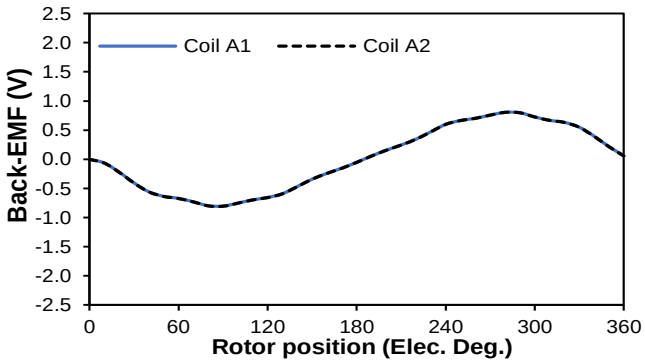

(a) 0% rotor shaft eccentricity

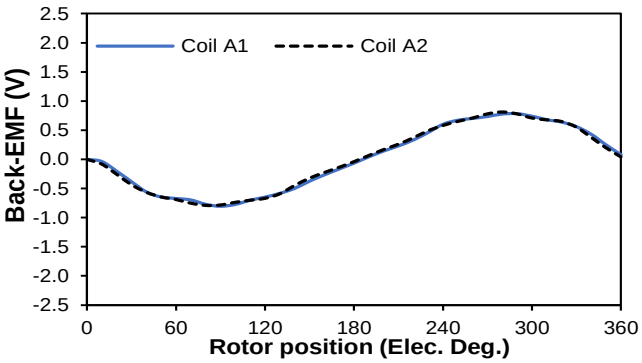

(b) 25% rotor shaft eccentricity

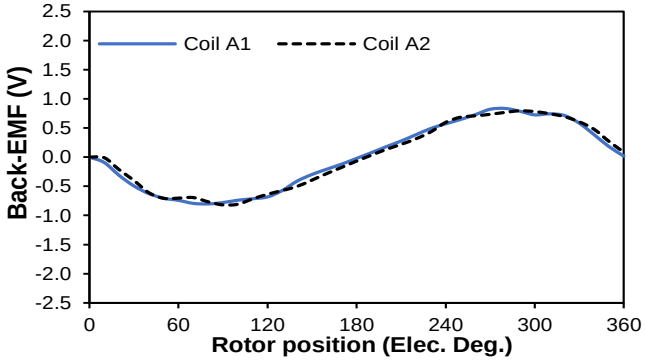

(c) 50% rotor shaft eccentricity

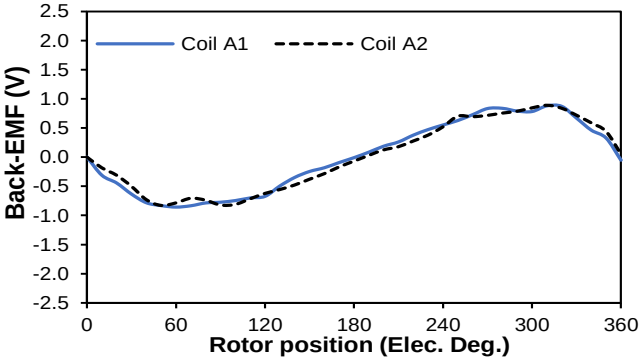

(d) 75% rotor shaft eccentricity

(II) FEA predicted Coils A1 and A2 back-EMF waveforms (400 rpm)

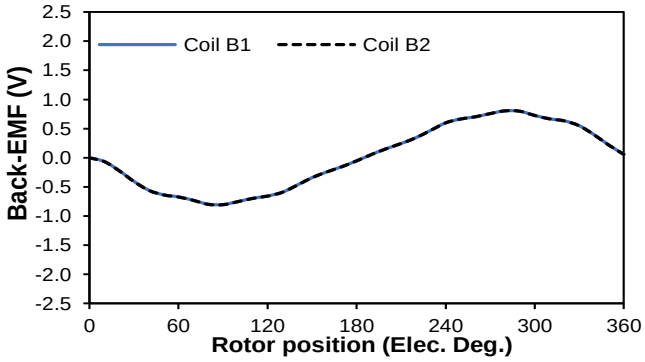

(a) 0% rotor shaft eccentricity

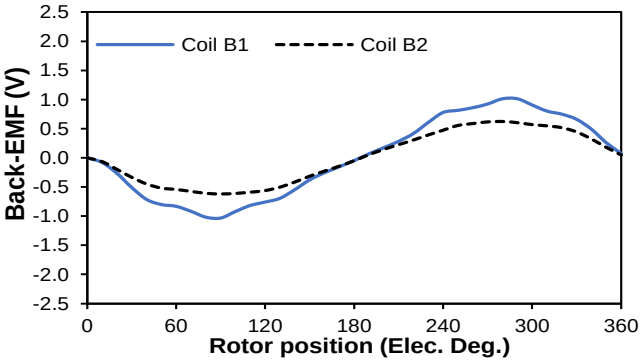

(b) 25% rotor shaft eccentricity

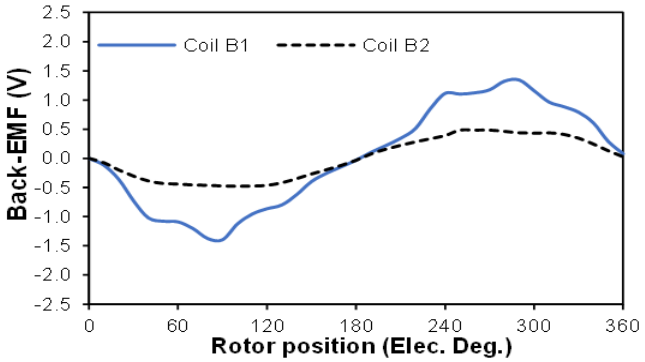

(c) 50% rotor shaft eccentricity

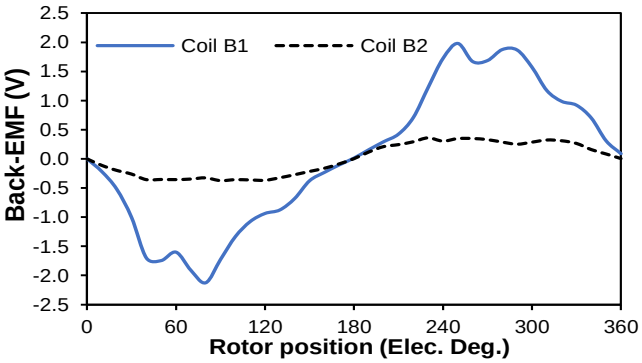

(d) 75% rotor shaft eccentricity

(III) FEA predicted Coils B1 and B2 back-EMF waveforms (400 rpm)

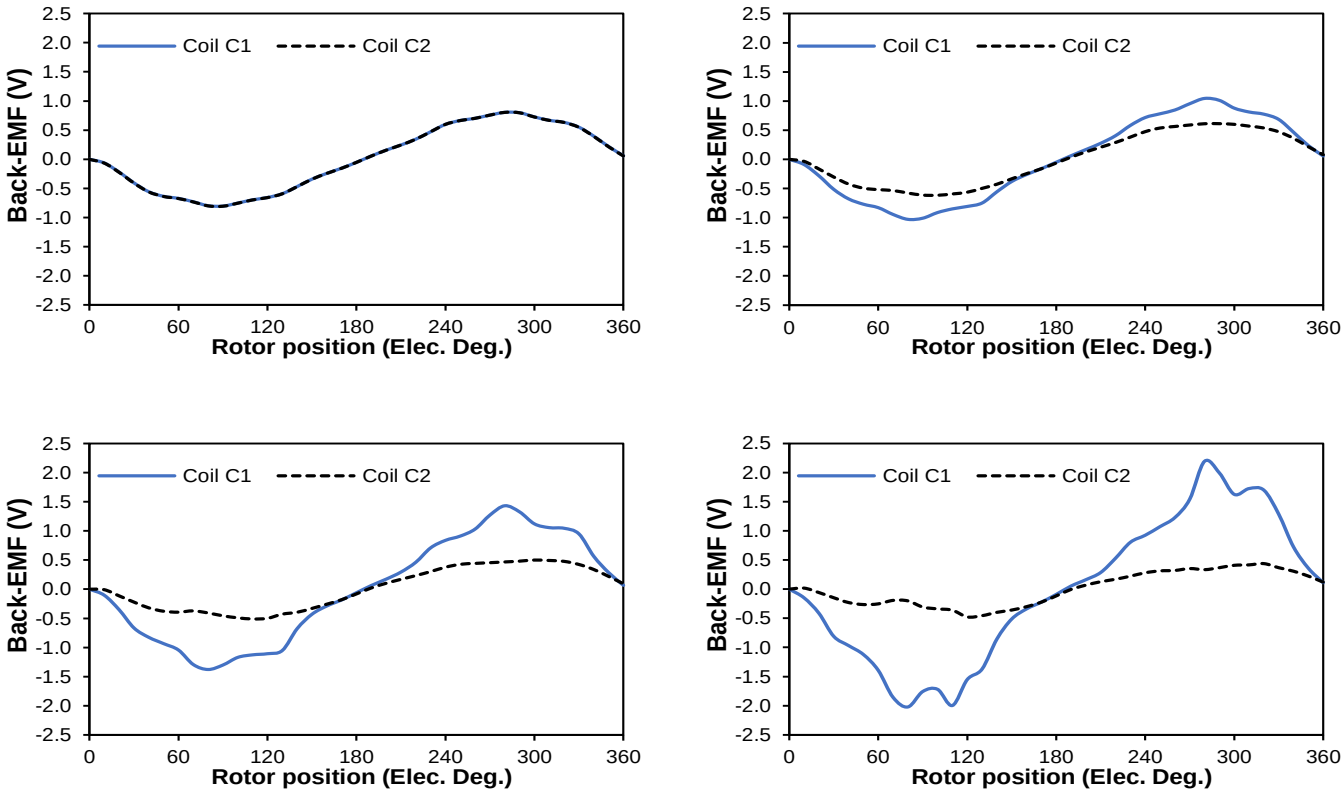

(IV) FEA predicted Coils C1 and C2 back-EMF waveforms (400 rpm)

Fig. 5.21 FEA predicted phase back-EMF and coil Back-EMF waveforms with the rotor shaft eccentricity of 0%, 25%, 50% and 75% towards to the centre between coils B1 and C1, 400rpm.

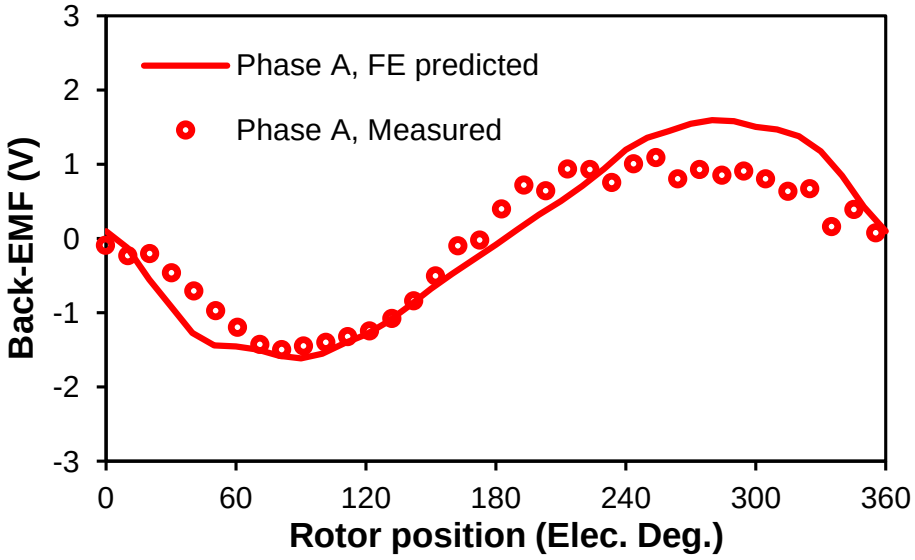

(a) Phase A

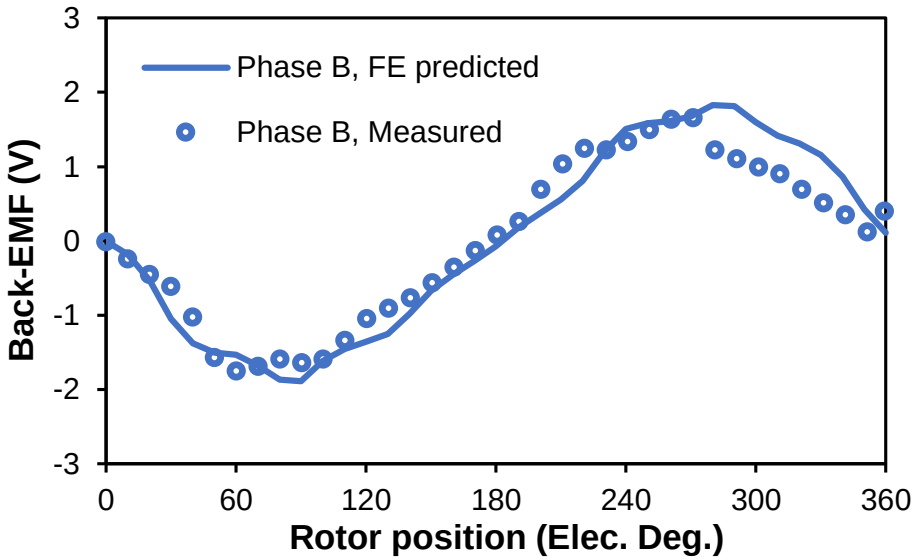

(b) Phase B

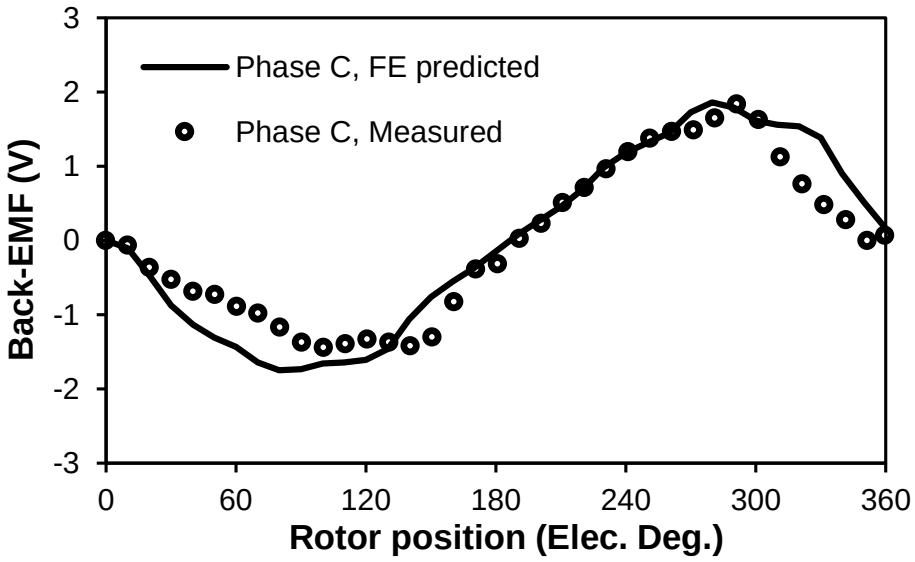

(c) Phase C

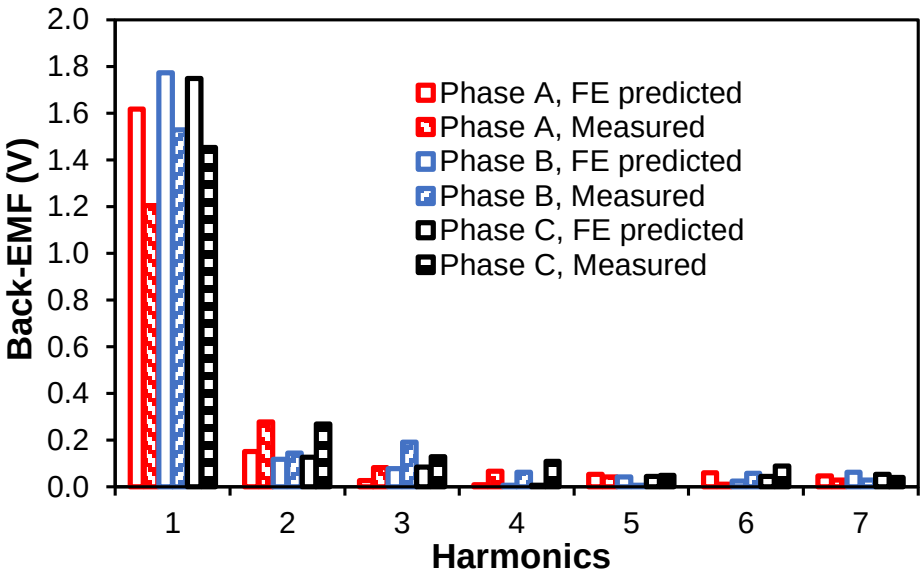

(d) Harmonics for FEA predicted and measured phase back-EMFs

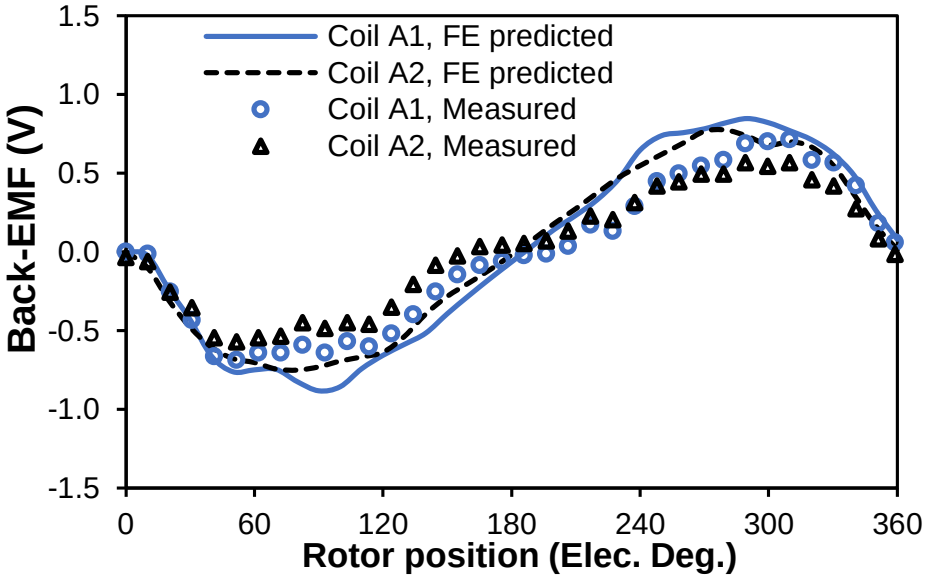

(e) Coil A1 and coil A2

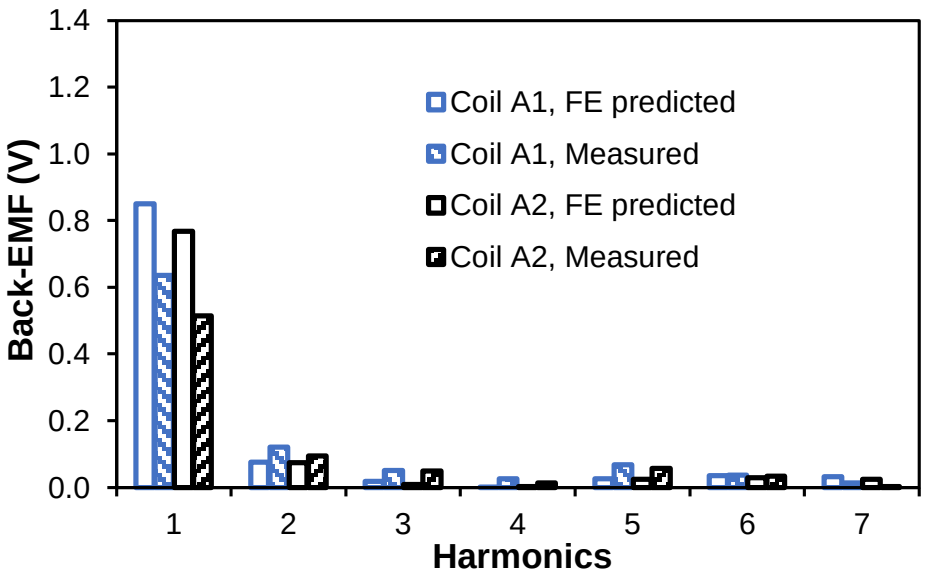

(f) Harmonics for FEA predicted and measured Coil A1 and A2 back-EMFs

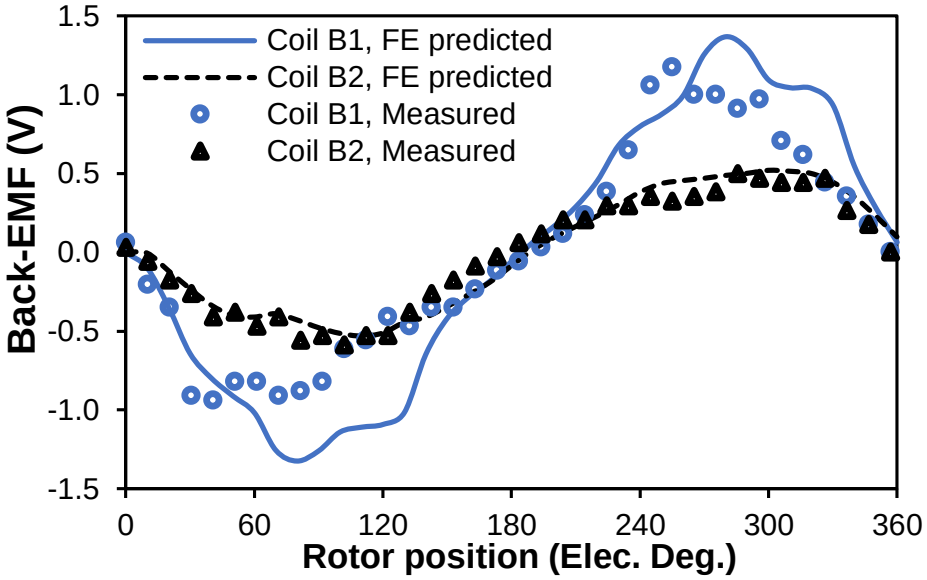

(g) Coil B1 and coil B2

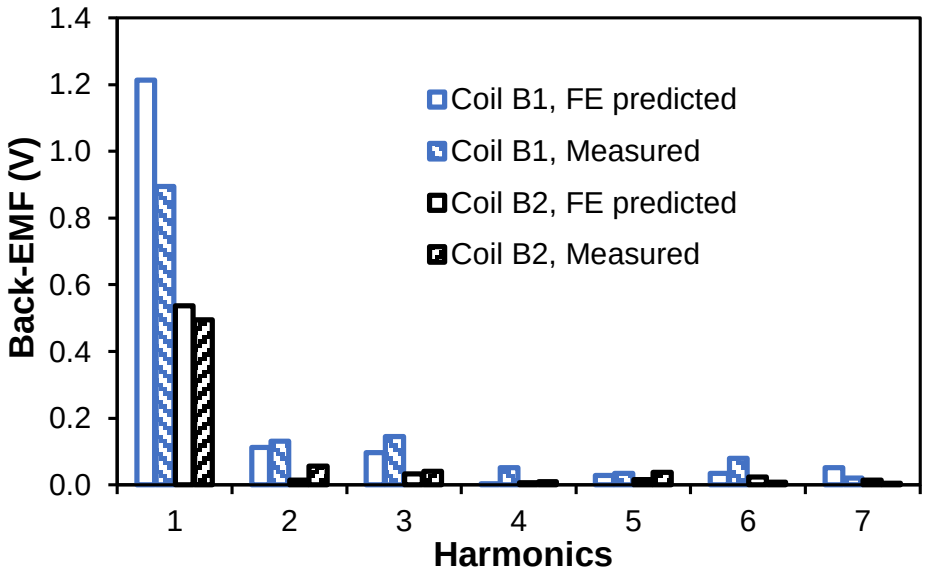

(h) Harmonics for FEA predicted and measured phase back-EMFs

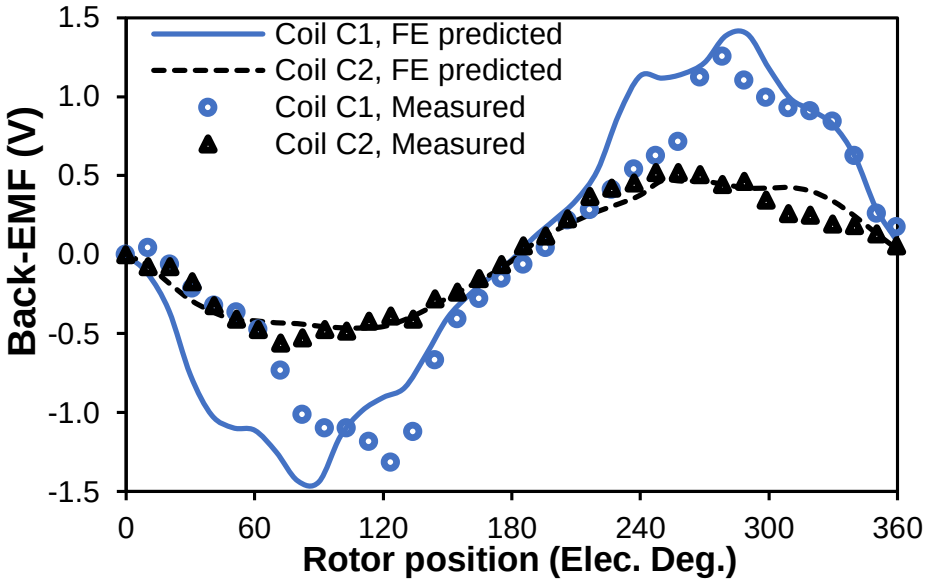

(i) Coil C1 and coil C2

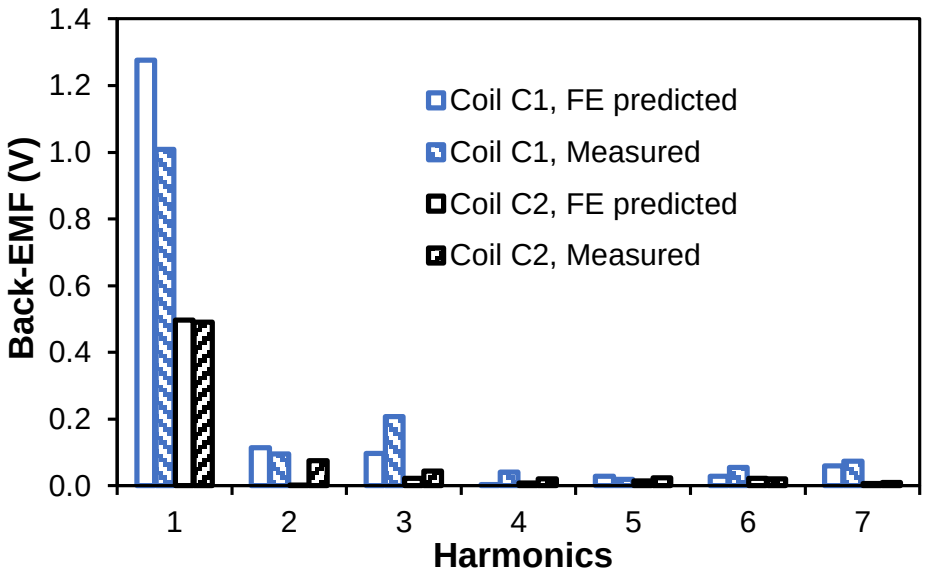

(j) Harmonics for FEA predicted and measured phase back-EMF

Fig. 5.22 Comparison of measured and FEA predicted back-EMF waveforms with the rotor shaft eccentricity of 50% towards to the centre between coils B1 and C1, and 6% towards the centre of coil A1, 400rpm.

5.4. Conclusions

In this chapter, the prototypes of the F1A3 and F3A2 HSSPM machines are described and the basic electromagnetic performance of the machines is experimentally validated. For the prototypes of F3A2 HSSPM machines with 7-, 8-, 10- and 11-rotor pole, both the open-circuit back-EMF and on-load static torque are measured. Excellent agreement is achieved between the measured and 2D FEA predicted results. For the F1A3 HSSPM machine, the magnetic saturation is very significant on open circuit which has prevented the test of static torque with practical field current, and the rotor shaft is also found to be eccentric due to manufacturing tolerance. The existence of rotor shaft eccentricity in the F1A3 HSSPM machine is confirmed by 2D FEA simulation and measurement of phase and coil EMF waveforms.

Chapter 6 General Conclusions

6.1. Summary

The novel stator hybrid excited synchronous machines, i.e. the stator DC-excited switched flux machines with PMs on the slot openings for the DC winding slots, have been designed and investigated in this thesis. The PMs are utilized to reduce the magnetic saturation caused by DC current excitation in the DC-excited switched flux machines, thereby the output performance is enhanced. Two types of novel hybrid-excited stator slots opening PM machines are developed with field coils span 1 stator slot pitch and armature coils span 3 stator slot pitches (F1A3), and field coils span 3 stator slot and armature coils span 2 stator slot pitches (F3A2). The machines are analysed by the 2D finite element method and the operation principle is experimentally validated. Besides, the modular stator machines are also investigated in this thesis and are developed from the conventional hybrid-excited stator slots opening PM machine (HSSPMMs) and stator slots opening PM machines (SSPMMs). The influence of stator and rotor pole combinations on the electromagnetic performance of the novel machines are investigated and compared in this thesis.

6.2. F1A3 hybrid-excited stator slot opening PM machines

Since the machine has PMs located in the stator slot opening area for field windings, the PM volume of the machine needs to be fixed. The novel machine has similar operation principle as the conventional HSSPMM. Thus, the conventional HSSPMM is also considered and provides the reference of the PM volume for the F1A3 HSSPMM. The electromagnetic performance and the losses of the F1A3 HSSPMM and the conventional HSSPMM are compared. Furthermore, the influences of different rotor poles on the electromagnetic performance of the F1A3 HSSPMMs are investigated as well and the F1A3 HSSPMM with 13-rotor pole is found to have the lowest open-circuit characteristics and electromagnetic torque. The findings in this thesis for the F1A3 HSSPMM can be summarized as:

- ***The influence of DC field current excitation***. The open-circuit characteristics without DC field excitation, i.e. flux-linkage, back-EMF and cogging torque, of the F1A3 HSSPMM are quite large due to the large flux-leakage caused by the magnetic saturation in the stator and the simulation for the machine with linear iron material has proved this. The saturation is caused by the flux produced by PMs since the stator tooth

between two adjacent PMs is too narrow to carry such a large amount of flux. Thus, the DC field excitation is firstly utilized to reduce the saturation and then enhance the performance, and in this case, the over-excited current for the F1A3 HSSPMM is higher than the conventional HSSPMM.

- ***Losses***. The iron losses of the F1A3 HSSPMM are slightly larger than the conventional HSSPMM due to the mass of iron for the F1A3 HSSPMM is slightly larger than that of the conventional HSSPMM. The F1A3 HSSPMM has larger eddy current loss than the conventional HSSPMM.
- ***Electromagnetic torque***. The F1A3 HSSPMM with 10-rotor poles have larger average torque than the conventional HSSPMM with 10-rotor poles, albeit with higher torque ripple. When compared the F1A3 HSSPMMs with different rotor pole numbers, it is found that the 8- and 10- rotor pole machines have quite similar torque waveforms and average torque values. The 8- and 10-rotor pole machines have the highest electromagnetic torque while the 13-rotor pole machine has the lowest. Moreover, the average electromagnetic torque of the 13-rotor pole machine remains low with the increasing copper loss.
- ***Cogging torque***. Due to the flux-leakage, the F1A3 HSSPMMs have non-zero cogging torque. The even number rotor pole machines exhibit large cogging torque and have dominant 3^{rd} harmonic, while the odd number rotor pole machines have relative low cogging torque with dominant 6^{th} harmonic. Due to the large flux-leakage, the cogging torque does not increase much as other open-circuit characteristics, i.e. flux-linkage and back-EMF, which is different from the conventional HSSPMM.
- ***Torque ripple***. Due to the cogging torque, the on-load torque ripple of the F1A3 HSSPMMMs with even rotor pole numbers have larger torque ripple which is around 28% with larger 3^{rd} harmonic. The torque ripple of the 7- and 11-rotor pole machines are less than 10%.

6.3. F3A2 hybrid-excited stator slot opening PM machines

Similar to the F1A3 HSSPMMs, the PM volume of the F3A2 HSSPMMs is fixed and similar as the conventional HSSPMM. The F3A2 HSSPM has 18 stator slots and 6 stator poles as the F1A3 HSSPMM, but with half numbers of PMs. According to the position of the PMs, the flux-leakage caused by PMs of the F3A2 HSSPMM is significantly reduced. The F3A2 HSSPMMs of different rotor pole numbers are investigated in terms of electromagnetic

performance and unbalanced magnetic force. The 14-rotor pole machine has the worst torque performance. The findings in this thesis can be summarized as:

- ***The influence of DC field current excitation***. Since the PM flux leakages of the F3A2 HSSPMMs with different rotor pole numbers are small, the open-circuit characteristics, i.e. the flux linkage, back-EMF and cogging torque, are small and will be significantly increased with the DC field current excitation. When the DC field excitation current is over 10A, the F3A2 HSSPMMs will be over-excited. The magnitude of back-EMF for even number rotor pole machines is reduced significantly when the machines are over-excited, and that of the 14-rotor pole machine remains low with the increasing DC field excitation.
- ***Electromagnetic torque***. The average electromagnetic torque is the highest in the 11-rotor pole machine and the lowest in the 14-rotor pole machine. Meanwhile, the average torque of 11-rotor pole machine remains high while that of 14-rotor pole machine remains low with the increasing copper loss.
- ***Cogging torque***. Due to the flux leakage, the variation of cogging torque of the machines is not negligible but remains small. The 8- and 10-rotor pole machines have relatively larger cogging torque.
- ***Torque ripple***. The machines with even number rotor poles have high torque ripple, especially for the 14-rotor pole machine which has torque ripple higher than 100%. The torque ripple of the 7- and 11-rotor pole machines are low and around 4%.
- ***Unbalanced magnetic force***. The unbalanced magnetic force is caused by magnetic asymmetry which occurs in odd number rotor pole machines. The 11-rotor pole machine has the largest UMF at rated currents. The UMF of 5- and 7-rotor pole machine is insensitive to the DC field excitation even the stator of the machine is magnetically saturated which is different from the 11- and 13- rotor pole machines.

6.4. Modular stator HSSPMMs and SSPMMs

The modular stator (MS) machines are modified from the conventional single layer HSSPMMs and single layer SSPMMs by removing half of the back-irons and PMs. Due to the reduction of stator iron, the stator iron loss of the MS-HSSPMM is lower than that of the conventional HSSPMMs. The MS-HSSPMM is optimized with equal/unequal stator back-iron thickness and stator tooth width, and the electromagnetic performance and losses of the optimized machines

are compared. Furthermore, the electromagnetic performances of MS-HSSPMMs and MS-SSPMMs with different stator and rotor pole combinations are investigated. The findings in this thesis are summarized as:

- ***Different optimization parameters***. When the MS-HSSPMM is optimized with equal stator back-iron thickness and stator tooth width, the PM volume is much lower than the machine optimized with unequal stator back-iron thickness and tooth width. Hence, the PM volume can be limited by stator back-iron and stator tooth. The stator segments of MS-HSSPMM with equal stator back-iron thickness and tooth width are not magnetically saturated at rated current when removing PMs, which is different from another machine with unequal stator back-iron thickness and tooth width, and have slightly lower average torque and 14% higher torque ripple. Due to the much lower volume of PMs and slightly lower average torque, the machine with equal stator back-iron and tooth width has approximately 50% higher average torque per unit PM.
- ***Open-circuit characteristics***. The MS-HSSPMMs have nearly negligible open-circuit characteristics, i.e. flux-linkage, back-EMF and cogging torque, without current excitation since the PM fluxes are mainly shunted in stator segments. The MS-SSPMMs have relatively larger amplitude for open-circuit characteristics due to the PM flux leakage in air-gap caused by severe magnetic saturation in stator segments. For the MS-HSSPMMs, the flux-linkage and back-EMF will be significantly enhanced with DC field current excitation and the 10- and 14-rotor pole machines have large 5^{th} and 7^{th} harmonics in back-EMF which can lead to high on-load torque ripple. The amplitudes of cogging torque waveforms for MS-HSSPMMs remain small, and the 14 rotor pole machine has relatively larger cogging torque.
- ***Electromagnetic torque and torque ripple***. The MS-SSPMMs have higher average torque and larger torque ripple than the MS-HSSPMMs for all stator and rotor pole combinations. The value of the average electromagnetic torque of the 13-rotor pole machine is the highest and that of the 10-rotor pole machine is the lowest, for both in MS-HSSPMMs and MS-SSPMMs. The odd number rotor pole machines have better torque performance than the even number rotor pole machines with the increasing copper loss. The larger torque ripple of even number rotor pole machines due to the machines have non-sinusoidal open-circuit back-EMF waveforms.

6.5. Experimental validation of F1A3 and F3A2 HSSPMMs

The operation principles of the F1A3 and F3A2 HSSPMMs are experimentally validated in this thesis. The test results of cogging torque, open-circuit phase back-EMF and static torque of F3A2 HSSPMMs with 7/8/10/11 rotor poles have excellent agreement with the predicted results obtained by the 2D element finite method (FEM). The test results of open-circuit back-EMF validate that the F1A3 HSSPMM has large PM flux-leakage. However, the back-EMF waveforms for phases and coils have verified that the F1A3 HSSPM exhibits rotor eccentricity due to the manufacture faults. The 2D FEM is used to identify the eccentric position of the rotor.

6.6. Future work

Potential further research activities are listed as follows:

- Investigate F1A3 and F3A2 HSSPMMs with unequal stator slots for DC field and armature windings.
- Compare the performance of F1A1, F1A3, F2A2 and F3A2 HSSPMMs.
- Rebuild the prototype for F1A3 HSSPMM and do the tests for open-circuit and on-load performances.
- Build up the prototypes for MS-HSSPMMs and MS-SSPMMs and do the tests for open-circuit and on-load performances.
- Further investigate the magnetic noise and vibration, short circuit fault, and thermal modelling.

References

[1] I. Boldea, L. N. Tutelea, L. Parsa, and D. Dorrell, "Automotive electric propulsion systems with reduced or no permanent magnet: an overview," *IEEE Trans. on Ind. Electron.*, vol. 61, no. 10, pp. 5696-5711, 2014.

[2] K.T. Chau, K. T., C. C. Chan, C. C. and C.H. Liu, C. H., "Overview of permanent-magnet brushless drives for electric and hybrid electric vehicles," *IEEE Trans. on Ind. Electron.*, vol. 55, no. 6, pp. 2246-2257, 2008.

[3] A. Binder, T. Schneider, and M. Klohr, "Fixation of buried and surface-mounted magnets in high-speed permanent-magnet synchronous machines," *IEEE Trans. on Ind. Appl.*, vol. 42, no. 4, pp. 1031-1037, July/August 2006.

[4] K. Kurihara, T. Kubota, T. Kosaka, and T. Nakamura, "A single-phase reluctance generator with permanent magnets between stator teeth," *Int. Conf. Elect. Machine (ICEM)*, pp. 1-6, 2010.

[5] K. Kurihara, T. Kubota, M. Shimazaki, and T. Nakamura, "EMF and efficiency measurements of a novel self-excited reluctance generator," *IEEE Int. Electric Machines & Drives Conf. (IEMDC)*, pp. 1195-1200, 2011.

[6] P. P. Acanley and J. F. Watson, "Review of position-sensorless operation of brushless permanent-magnet machines," *IEEE Tans. on Indus. Electronics*, vol. 53, no. 2, pp. 352-362, 2006.

[7] Z. Q. Zhu and D. Howe, "Electrical machines and drives for electric, hybrid and fuel cell vehicles," *in Proc. IEEE*, vol. 95, no. 4, pp. 746–765, Apr. 2007.

[8] A. G. Jack, B. C. Mecrow, and J. A. Haylock, "A comparative study of permanent magnet and switched reluctance motors for high-performance fault-tolerant applications," *IEEE Trans. on Ind. Appl.*, vol. 32, no. 4, pp. 889– 895, 1996.

[9] J. D. Ede, K. Attalah, and D. Howe, "Design variants of modular permanent magnet brushless motor," *J. Appl. Phys.*, vol. 91, no. 10, pp. 6973– 6975, 2002

[10] N. Bianch, S. Bolognani, “Design techniques for reducing the cogging torque in surface-mounted pm motors,” *IEEE Trans. on Ind. Appl.*, vol.38, no. 5, pp. 1259-1265, Sep/Oct 2002

[11] A. M. El-Refaie and T. M. Jahns, “ Optimal flux-weakening in surface PM machines using concentrated windings,” *IEEE Trans. on Ind. Appl.*, vol. 41, no. 3, pp. 790–800, May/Jun. 2005.

[12] A. M. El-Refaie, “Fractional slot concentrated windings synchronous permanent magnet machines: opportunities and challenges,” *IEEE Trans. on Ind. Electron.*, vol.57, no.1, pp.107-121, Jan. 2010.

[13] C. C. Chan, J. Z. Jiang, G. H. Chen, X. Y. Wang, and K. T. Chau, “A novel poly phase multipole square-wave permanent magnet motor drive for electric vehicles,” *IEEE Trans. on Ind. Appl.*, vol. 30, no. 5, pp. 1258-1266, 1994.

[14] J. Cros and P. Viarouge, “Synthesis of high performance PM machines with concentrated windings,” *IEEE Trans. on Energy Convers.*, vol. 17, no. 2, pp. 248–253, Jun. 2002.

[15] D. Ishak, Z. Q. Zhu, and D. Howe, “Permanent magnet brushless machines with unequal tooth widths and similar slot and pole numbers,” *IEEE Trans. on Ind. Appl.*, vol. 41, no. 2, pp. 584–590, Mar./Apr. 2005.

[16] D. Ishak, Z. Q. Zhu, and D. Howe, “Comparison of PM brushless motors, with either all or alternative wound teeth,” *IEEE Trans. on Energy Convers.*, vol. 21, no. 1, pp. 95–103, Mar. 2006.

[17] K. Halbach, “Design of permanent magnet multipole magnets with oriented rare-earth cobalt material,” *Nuclear Instruments and Methods*, vol. 169, pp. 1–10, 1980.

[18] J. Ofori-Tenkorang, and J. H. Lang, “A comparative analysis of torque production in Halbach and conventional surface-mounted permanent-magnet synchronous motors,” *Ind. App. Conf., 13th IAS Annual Meeting, IEEE*, Oct. 1995, pp. 657-663, 1995.

[19] Y. Shen, and Z. Q. Zhu, "General analytical model for calculating electromagnetic performance of permanent magnet brushless machines having segmented Halbach array," *Electrical Systems in Trans., IET,* vol. 3, no. 3, pp. 57-66, 2013.

[20] Z. Q. Zhu, and D. Howe, "Halbach permanent magnet machines and applications: a review," *IEE, Electric Power Appl.*, vol. 148, no. 4, pp. 299-308, 2001.

[21] T. Sebastian and G. R. Slemon, "Operating limits of inverter-driven permanent magnet motor drives," *IEEE Trans. on Ind. Appl.,* vol. 23, pp. 327–333, 1987.

[22] J. Gan, K. T. Chau, C. C. Chan, and J. Z. Jiang, "A new surface-inset, permanent-magnet, brushless DC motor drive for electric vehicles," *IEEE Trans. on Magn.*, vol. 36, no. 5, pp. 3810–3818, Sep. 2000.

[23] T. M. Jahns, "Flux-weakening regime operation of an interior permanent-magnet synchronous motor drive," *IEEE Trans. on Ind. Appl.*, vol. 23, no. 4, pp. 681–689, 1987.

[24] D. Evans, Z. Azar, L. J. Wu, and Z. Q. Zhu, "Comparison of optimal design and performance of PM machines having non-overlapping windings and different rotor topologies," *5th IET International Conf. on Power Electronics and Drives (PEMD)*, 2010, pp. 1-7.

[25] T. A. Lipo, "Synchronous reluctance machines - a viable alternative for AC drives?" *Elect. Mach. Power Syst.,* vol. 19, pp. 659–671, 1991.

[26] F. B. Chaaban, T. S. Birch, D. Howe, and P. H. Mellor, "Topologies for a permanent magnet generator/speed sensor for the ABS on railway freight vehicles," *in Proc. IEE Int'l Conf. Electrical Machines and Drives*, Sep. 11–13, 1991, pp. 31–35.

[27] N. Bianchi, and E. Fornasiero, "Impact of MMF space harmonic on rotor losses in fractional-slot permanent-magnet machines," *IEEE Trans. on Energy Convers.*, vol.24, no.2, pp.323-328, Jun. 2009.

[28] P. J. Lawrenson, J. M. Stephenson, P. T. Blenkinsop, J. Corda, and N. N. Fulton, "Variable-speed switched reluctance motors," *IEE Electric Power Appl.*, vol. 127, no. 4, pp. 253-265, 1980.

[29] C. M. Stephens, "Fault detection and management system for fault tolerant switched reluctance motor drives," *IEEE Ind. Appl.*, vol. 27, no. 6, pp. 1098-1991, 1991.

[30] J. Li, X. Song, and Y. Cho, "Comparison of 12/8 and 6/4 switched reluctance motor: noise and vibration aspects, " *IEEE Trans. on Magn.*, vol. 44, no. 11, pp. 4131-4134, 2008.

[31] Y. Liao, F. Liang, and T. A. Lipo, "A novel permanent magnet motor with doubly salient structure," *IEEE Trans. on Ind. Appl.*, vol. 31, pp. 1059–1078, 1995.

[32] W. Hua, Z. Q. Zhu, M. Cheng, Y. Pang, and D. Howe, "Comparison of flux-switching and doubly-salient permanent magnet brushless machines," *Int'l Conf. on Electrical Machines and Systems (ICEMS)*, 2005, vol. 1, pp. 165-170.

[33] J. T. Shi, Z. Q. Zhu, D. Wu and X. Liu, "Comparative study of novel biased flux permanent magnet machine with doubly salient permanent magnet machine," *Int'l Conf. on Electr. Mach. and Syst. (ICEMS)*, 2014.

[34] J. T. Shi, Z. Q. Zhu, D. Wu and X. Liu, "Influence of flux focusing on electromagnetic torque of novel biased flux PM machines," *Int'l Conf. on Electr. Mach. (ICEM)*, 2014, pp. 523-529.

[35] R. P. Deodhar, S. Andersson, I. Boldea, and T. J. E. Miller, "The flux-reversal machine: A new brushless doubly-salient permanent magnet machine," *IEEE Trans. on Ind. Appl.*, vol. 33, no. 4, pp. 925–934, Jul./Aug. 1997.

[36] S. E. Rauch and L. J. Johnson, "Design principles of flux-switching alternators," *AIEE Trans. Part III*, vol. 74, pp. 1261–1268, 1955.

[37] Cao, R., Mi, C., and Cheng, M., "Quantitative comparison of flux-switching permanent-magnet motors with interior permanent magnet motor for EV, HEV and

PHEV applications," *IEEE Trans. on Ind. Appl.*, vol. 48, no. 8, pp. 2374-2384, Aug. 2012.

[38] A. S. Thomas, Z. Q. Zhu, and G. W. Jewell, "Comparison of flux switching and surface mounted permanent magnet generators for high-speed applications, " *IET Electrical Systems in Trans.*, vol. 1, no. 3, pp. 111-116, 2011.

[39] J. T. Chen and Z. Q. Zhu, "Comparison of all- and alternate-poles-wound flux-switching PM machines having different stator and rotor pole numbers," *IEEE Trans. on Ind. Appl.*, vol. 46, no. 4, pp. 1406-1415, 2010.

[40] J. T. Chen, Z. Q. Zhu, A. S. Thomas, and D. Howe, "Optimal combination of stator and rotor pole numbers in flux-switching PM brushless AC machines," *Int'l Conf. on Electrical Machines and Systems (ICEMS)*, 2008, pp. 2905-2910.

[41] R. L. Owen, Z. Q. Zhu, A. S. Thomas, G. W. Jewell, and D. Howe, "Fault tolerant flux switching permanent magnet brushless AC machines," *IEEE Ind. App. Society Annual Meeting*, 2008. Pp. 1-8.

[42] T. Raminosoa and C. Gerada, "Novel fault tolerant design of flux switching machines," *5th IET Int'l Conf. on Power Electronics and Drives (PEMD)*, 2010, pp. 1-6.

[43] J. T. Chen, Z. Q. Zhu, S. Iwasaki, and R. P. Deodhar, "A novel E-core switched-flux PM brushless AC machine," *IEEE Tran. on Ind. Appl.*, vol. 47, no. 3, pp. 1273-1282, 2011.

[44] J. T. Chen, Z. Q. Zhu, S. Iwasaki, and R. P. Deodhar, "Influence of stator opening on optimal stator and rotor pole combination electromagnetic performance of switched-flux PM brushless AC machines," *IEEE Tran. on Ind. Appl.*, vol. 47, no. 4, pp. 1681-1691, 2011.

[45] Z. Q. Zhu, J. T. Chen, Y. Pang, D. Howe, S. Iwasaki, and R. Deodhar, "Analysis of a novel multi-tooth flux-switching PM brushless AC machine for high torque direct-drive applications," *IEEE Trans. on Magn.*, vol. 44, no. 11, pp. 4313-4316, 2008.

[46] J. T. Chen, Z. Q. Zhu, and D. Howe, "Stator and rotor pole combinations for multi-tooth flux-switching permanent-magnet brushless AC machines," *IEEE Trans. on Magn.*, vol. 44, no. 12, pp. 4659-4667, 2008.

[47] P. Taras, G. J. Li, and Z. Q. Zhu, "Comparative study of fault-tolerant switched-flux permanent-magnet machines," *IEEE Trans. on Ind. Appl.*, vol. 64, no. 3, 2017.

[48] B. S. Lee, N. Pothi, M. M. J. Al-Ani, and Z. Q. Zhu, "Experimental study of torque and flux weakening performance of alternative switched flux PM machines," *7th IET International Conf. on Power Electronics and Drives (PEMD)*, 2014, pp. 1-6.

[49] W. Z. Fei and J. X. Shen, "Novel permanent magnet switching flux motor," *in Proc. 41st Int. Univ. Power Eng. Conf.*, 2006, pp. 729–733.

[50] Y. J. Zhou and Z. Q. Zhu, "Torque density and magnet usage efficiency enhancement of sandwiched switched flux permanent magnet machines using V-shaped magnets," *IEEE Trans. on Magn.*, vol. 49, no. 7, pp. 3834-3837, 2013.

[51] A. S. Thomas, Z. Q. Zhu and L. J. Wu, "Novel modular-rotor switched flux permanent magnet machines," *IEEE Trans. on Ind. Appl.*, vol. 48, no. 6, pp. 2249-2258, 2012

[52] W. Z. Fei, P. C. K. Luk, J. X. Shen, Y. Wang, and M, J. Jin, "A novel permanent-magnet flux switching machine with an outer-rotor configuration for in-wheel light traction applications," *IEEE Trans. on Ind. Appl.*, vol. 48, no. 5, pp. 1496-1506, 2012.

[53] D. J. Evans and Z. Q. Zhu, "Novel partitioned stator switched flux permanent magnet machines," *IEEE Trans. on Magn.*, vol. 51, no. 1, 2015.

[54] D. J. Evans, Z. Q. Zhu, H. L. Zhan, Z. Z. Wu, and X. Ge, "Flux-weakening control performance of partitioned stator-switched flux PM machines," *IEEE Trans. on Ind. Appl.*, vol. 52, no. 3, 2016, pp. 2350-2358.

[55] C. C. Awah, Z. Q. Zhu, Z. Z. Wu, H. L. Zhan, J. T. Shi, D. Wu, and X. Ge, "Comparison of partitioned stator switched flux permanent magnet machines having single- or double-layer windings," *IEEE Trans. on Magn.*, vol. 52, no. 1, 2016.

[56] Z. Z. Wu and Z. Q. Zhu, "Analysis of magnetic gearing effect in partitioned stator switched flux PM machines," *IEEE Trans. on Energy Convert.*, vol. 31, no. 4, pp. 1239-1249, 2016.

[57] C. Rossi, D. Casadei, A. Pilati, and M. Marano, "Wound rotor salient pole synchronous machine drive for electric traction," *in Conf. Rec. IEEE IAS Annual Meeting*, 2006, pp. 1235–1241.

[58] D. G. Dorrell, "Are wound-rotor synchronous motors suitable for use in high efficiency torque-dense automotive drives?" *in Proc. 38th Annual Conf. on IEEE Ind. Electron. Society (IECON)*, 2012, pp. 4880–4885.

[59] W. Q. Chu, Z. Q. Zhu, J. Zhang, X. Ge, X. Liu, D. Stone, and M. Foster, "Comparison of electrically excited and interior permanent magnet machines for hybrid electric vehicle application," *Int'l Conf. on Electrical Machines and Systems (ICEMS)*, 2014, pp. 401-407.

[60] L. R. Huang, Z. Q. Zhu, and W. Q. Chu, "Optimization of electrically excited synchronous machines for electrical vehicle applications," *IET Int'l Conf. on Power Electronics and Drives (PEMD)*, 2016, pp. 1-6.

[61] M. Cheng, Y. Fan, and K. T. Chau, "Design and analysis of A Novel Stator-Doubly-Fed Doubly Salient Motor for Electric Vehicles," *J. Appl. Phys.*, 2005, vol. 97, no. 10, pp. 10Q508-1-3.

[62] Y. Fan, and K. T. Chau, "Design, modelling and analysis of a brushless doubly fed doubly salient machine for electric vehicles," *IEEE Trans. on Indus. Appl.*, vol. 44, no. 3, pp. 727–734, 2008.

[63] X. X. Kong and M. Cheng, "Static characteristics of a novel stator-doubly-fed doubly salient motor for electric vehicles," *Int'l Conf. on Elect. Mach. and Syst. (ICEMS)*, 2005, vol. 1, pp. 866-869,

[64] J. T. Chen, Z. Q. Zhu, S. Iwasaki, and R. Deodhar, "Low cost flux-switching brushless AC machines," *IEEE Vehicle Power and Propulsion Conf. (VPPC)*, pp. 1-6, 2010.

[65] Y. Tang, J. J. H. Paulides, T. E. Motoasca and E. A. Lomonova, "Flux switching machine with DC excitation," *IEEE Trans. on Magn.*, vol. 48, no. 11, pp. 3583-3586, 2012.

[66] Y. Tang, E. Ilhan, J. J. H. Paulides, and E. A. Lomonova, "Design considerations of flux-switching machines with permanent magnet or DC excitation," *15th European Conf. on Power Electron. and Appl. (EPE)*, 2013, pp. 1-10.

[67] E. Sulaiman, M. F. M. Teridi, Z. A. Husin, M. Z. Ahmad, and T. Kosaka, "Performance comparison of 24S-10P and 24S-14P Field excitation flux switching machine with single DC-coil polarity," *IEEE 7th Int'l Power Engineering and Optimization Conf. (PEOCO)*, 2013.

[68] F. Khan, E. Sulaiman, and M.Z. Ahmad, "Coil test analysis of wound- field three-phase flux switching machine with non-overlapping winding and salient rotor," *in Proc. IEEE Int'l Power Eng. Opt. Conf.*, Mar. 2014, pp. 243–247.

[69] Y. Kano, "Design optimization of brushless synchronous machines with wound-field excitation for hybrid electric vehicles," *IEEE Energy Conversion. Congress and Exposition (ECCE)*, 2015, pp. 2769-2775.

[70] A. Zulu; B. C. Mecrow; M. Armstrong, "Topologies of wound-field three-phase segmented-rotor flux-switching machines," *5th IET Int'l Conf. on Power Electronics and Drives (PEMD)*, 2010.

[71] A. Zulu; B. C. Mecrow; M. Armstrong, "A wound-field three-phase flux-switching synchronous motor with all excitation sources on the stator," *IEEE Trans. on Ind. Appl.*, Vol. 46, no. 6, pp. 2363-2371, 2010.

[72] Z. Q. Zhu, Y. J. Zhou, J. T. Chen, and James E. Green, "Investigation of non-overlapping stator wound-field synchronous machines," *IEEE Trans. on Energy Conversion*, vol. 30, no. 4, pp. 1420-1427, 2015.

[73] Z. Q. Zhu and Y. J. Zhou, "Recent development in stator wound field synchronous machines," *Journal of Electrical Engineering*, vol. 10, no. 4, pp.11-25, 2015.

[74] Y. J. Zhou, Z. Q. Zhu, and X. Ge, "Comparison of torque density in alternate wound-field switched flux machines," *17th Int'l Conf. on Electr. Mach. and Syst. (ICEMS)*, pp. 2151-2157, 2014.

[75] S. M. Yang, J. H. Zhang, and J. Y. Jiang, "A maximum torque control strategy for wound-field flux switching motor drives," *41st Annual Conf. on the Ind. Electron. Society (IECON)*, 2015.

[76] Y. J. Zhou and Z. Q. Zhu, "Comparison of wound-field switched-flux machines," *IEEE Trans. on Ind. Appl.*, vol. 50, no. 5, pp. 3314-3324, 2014.

[77] L. R. Huang, Z. Q. Zhu, J. H. Feng, S. Y. Guo, J. X. Shi, and W. Q. Chu, "Analysis of stator/rotor pole combination in variable flux reluctance machines using magnetic gearing effect," *IEEE Energy Convers. Congress and Exposition (ECCE)*, 2017, pp. 3187-3194.

[78] T. Fukami, Y. Matsuura, K. Shima, M. Momiyama, M. Kawamura, "Development of a low-speed multi-pole synchronous machine with a field winding on the stator side," *Int'l Conf. On Electrical Machines (ICEM)*, 2010, pp. 1-6.

[79] T. Fukami, Y. Matsura, K. Shima, M. Momiyama, and M. Kawamura, "A multipole synchronous machine with non-overlapping concentrated armature and field windings on the stator," *IEEE Trans. on Ind. Electron.*, vol. 59, no. 6, pp. 2583-2591, 2012.

[80] X. Liu and Z. Q. Zhu, "Electromagnetic performance of novel variable flux reluctance machines with DC-field coil in stator," *IEEE Trans. on Magn.*, vol. 49, no. 6, pp. 3020-3028, 2013.

[81] X. Liu and Z. Q. Zhu, "Stator/rotor pole combinations and winding configurations of variable flux reluctance machines," *IEEE Trans. on Ind. Appl.*, vol. 50, no. 6, pp. 3675-3684, 2014

[82] Z. Q. Zhu, Z. Z. Wu, and X. Liu, "A partitioned stator variable reluctance machine," *IEEE Trans. on Energy Conversion*, vol. 31, no. 1, pp. 78-92, 2016.

[83] X. Liu and Z. Q. Zhu, "Comparative study of novel variable flux reluctance machines with doubly fed doubly salient machines," *IEEE Trans. on Magn.*, vol. 49, no. 7, pp. 3838-3841, 2013.

[84] X. Liu and Z. Q. Zhu, "Design and investigation of flux weakening capability in variable flux reluctance machine," *IEEE Vehicle Power and Propulsion Conf. (VPPC)*, 2016, pp. 1-6.

[85] K. Nakamura, K. Murota, and O. Ichinokura, "Characteristics of a novel switched reluctance motor having permanent magnets between the stator pole-tips," *Power Electron. and Appl. Conf*., European, 2-5 Sept. 2007.

[86] P. Andrada, B. Blanqué, E. Martínez, M. Torrent, "New hybrid reluctance motor drive," *Int'l Conf. On Electrical Machines (ICEM)*, 2012.

[87] W. Ding, S. Yang, Y. F. Hu, S. Li, T. Wang and Z. G. Yin, "Design consideration and evaluation of a 12/8 high-torque modular-stator hybrid excitation switched reluctance machine for EV applications," *IEEE Trans. on Ind. Appl.*, vol. 64, no. 12, pp. 9221-9232, 2017.

[88] I. A. A. Afinowi, Z. Q. Zhu, Y. Guan, J. Mipo, and P. Farah, "A novel brushless ac doubly salient stator slot permanent magnet machine," *IEEE Trans. on Energy Conversion*, vol. 31, no. 1, pp. 283-292, 2016.

[89] I. A. A. Afinowi, Z. Q. Zhu, Y. Guan, J. Mipo, and P. Farah, "Electromagnetic performance of stator slot permanent magnet machines with/without stator tooth-tips and having single/double layer windings," *IEEE Trans. on Magn.*, vol. 52, no. 6, 2016.

[90] S. Ullah, S. P. McDonald, R. Martin, G. J. Atkinson, "A permanent magnet assisted switched switched-reluctance machine for more electric aircraft," *Int'l Conf. On Electr. Mach. (ICEM)*, 2016, pp. 79-85.

[91] K. F. Xue, D. W. Li, R. H. Qu, Y. T. Gao, and Y. Pan, "A novel flux reversal PM machines with Halbach array magnets in stator slot opening," *Int'l Conf. on Electr Mach and Syst (ICEMS)*, 2017, pp. 1-6.

[92] I. A. A. Afinowi, Z. Q. Zhu, Y. Guan, J. C. Mipo, and P. Farah, "Hybrid-excited doubly salient synchronous machine with permanent magnets between adjacent salient stator poles," *IEEE Trans. on Magn.*, vol. 51, no. 10, 2015.

[93] Z. Q. Zhu, I. A. A. Afinowi, Y. Guan, J. C. Mipo, and P. Farah, "Hybrid-excited stator slot permanent magnet machines—influence of stator and rotor pole combinations," *IEEE Trans. on Magn.*, vol. 52, no. 2, 2016.

[94] H. Yang, Z. Q. Zhu, Y. Liu, H. Y. Li, and J. C. Mipo, "Comparative study of double salient machines with/without stator slot permanent magnets," *IEEE Int'l Electric Machines and Drives Conf. (IEMDC)*, 2017, pp. 1-6.

[95] B. Gaussens, E. Hoang, M. Lecrivain, P. Manfe, and M. Gabsi, "A hybrid excited flux-switching machine for high-speed DC-alternator applications," *IEEE Trans. on Ind. Electron.*, vol. 61, no.6, pp. 2976-2989, 2014.

[96] W. Hua, M. Cheng, and G. Zhang, "A novel hybrid excitation flux-switching motor for hybrid vehicles," *IEEE Trans. on Magn.*, vol. 45, no.10, pp. 4728-4731, Oct. 2009.

[97] G. Zhang, M. Cheng, W. Hua, and J. Dong, "Analysis of the oversaturated effect in hybrid excited flux-switching machines," *IEEE Trans. on Magn.*, vol. 47, no.10, pp. 2827-2830, Oct. 2011.

[98] R. L. Owen, Z. Q. Zhu, and G. W. Jewell, "Hybrid excited flux-switching permanent magnet machines," *13th Eur. Conf. Power Electron. Appl.*, Sep. 8–10, 2009, pp. 1–10.

[99] R. L. Owen, Z. Q. Zhu, and G. W. Jewell, "Hybrid-excited flux-switching permanent-magnet machines with iron flux bridges" *IEEE Trans. on Magn.*, vol. 46, no. 6, pp.1726-1729, 2010.

[100] E. Hoang, M. Lecrivain, and M. Gabsi, "A new structure of a switching flux synchronous polyphased machine with hybrid excitation," *European Conf. on Power Electron. and Appl.*, 2007, pp.1-8.

[101] E. Hoang, M. Lecrivain, S. Hlioui, and M. Gabsi, "Hybrid excitation synchronous permanent magnets synchronous machines optimally designed for hybrid and full electrical vehicle," *8th Int'l Conf. on Power Electron.-ECCE Asia*, 2011, pp. 153-160.

[102] E. Sulaiman, T. Kosaka, Y. Tsujimori, and N. Matsui, "Design of 12-slot 10-pole permanent magnet flux-switching machine with hybrid excitation for hybrid electric vehicle," *5th IET Int'l Conf. on Power Electronics and Drives (PEMD)*, 2010, pp. 1-5.

[103] E. Sulaiman, T. Kosaka, N. Matsui, and M. Z. Ahmad, "Design study on high torque and high power density hybrid excitation flux switching synchronous motor for HEV applications," *IEEE Int'l Power Engineering and Optimization Conf.*, Melaka, Malaysia, 2012, pp. 333-338.

[104] M. Cheng, W. Hua, J. Z. Zhang, and W. X. Zhao, "Overview of stator-permanent magnet brushless machines," *IEEE Trans. on Ind. Electron.*, vol. 58, no.11, pp.5087-5101, Nov. 2011.

[105] E. Hoang, A. H. Ben-Ahmed and J. Lucidarme, "Switching flux permanent magnet polyphased synchronous machines," *7th European Conf. on Power Electron. and Appl.*, pp.903-908, 1997.

[106] Z. Q. Zhu and J. T. Chen, "Advanced flux-switching permanent magnet brushless machines,", *IEEE Trans. on Magn.*, vol.46, no.6, pp.1447- 1453, 2010.

[107] Y. Tang, J. J. H. Paulides, and E. A. Lomonova, "Energy conversion in DC excited flux-switching machines," *IEEE Trans. on Magn.*, vol. 50, no. 11, pp. 1-4, November 2014.

[108] A. Zulu, B. C. Mecrow, and M. Armstrong, "Prediction of performance of a wound-field segmented rotor flux-switching synchronous motor using a dq-equivalent model," *Int. Conf. on Electrical Machines (ICEM)*, pp. 1-6, 2010.

[109] X. Liu and Z. Q. Zhu, "Winding configurations and performance investigations of 12-stator pole variable flux reluctance machines," *IEEE Energy Convers. Congress & Exposition (ECCE)*, 2013, pp. 1834-1841.

[110] H. Nakane, T. Kosaka, and N. Matsui, "Design studies on hybrid excitation flux switching motor with high power and torque densities for HEV applications," *IEEE Int'l Electric Machines & Drives Conf. (IEMDC)*, 10-13 May 2015.

[111] J. F. Gieras, "PM synchronous generators with hybrid excitation systems and voltage control capabilities: a review," *in Proc. Int. Conf. Electr. Mach. (ICEM)*, Marseille, France, Sept. 2-5, pp. 2573-2579, 2012.

[112] Y. Amara, L. Vido, M. Gabsi, E. Hoang, A. H. B. Ahmed, and M. Lécrivain, "Hybrid excitation synchronous machines: energy-efficient solution for vehicles propulsion," *IEEE Trans. on Vehicular Tech.*, vol. 58, no. 5, pp. 2137-2149, June 2009.

[113] B. N. Naoe, and T. Fukami "Trial production of a hybrid excitation type synchronous machine," *Int'l Electr. Mach. and Drives Conf. IEMDC'01*, Boston, MA, 2001, pp. 545 – 547.

[114] Y. Wang , and Z. Q. Deng , "Hybrid excitation topologies and control strategies of stator permanent magnet machines for DC power system" *IEEE Trans. on Ind. Electron.*, vol. 59, no. 12, pp. 4601-4614, December 2012.

[115] X. Luo and T. A. Lipo, "A synchronous/permanent magnet hybrid AC machine," *IEEE Trans. on Energy Convers.*, vol. 15, no. 2, pp. 203–210, Jun. 2000.

[116] J. A. Tapia, F. Leonardi, and T. A. Lipo, "Consequent-pole permanentmagnet machine with extended field-weakening capability," *IEEE Trans. on Ind. Appl.*, vol. 39, no. 6, pp. 1704–1709, Nov./Dec. 2003.

[117] B. Bickel, J. Franke, and T. Albrecht, "Manufacturing cell for winding and assembling a segmented stator of PM-synchronous machines for hybrid vehicles," *in Proc. 20th Int'l Conf. on Electrical Machines (ICEM)*, 2012, pp. 1–5.

[118] Z. Q. Zhu, "Fractional slot permanent magnet brushless machines and drives for electric and hybrid propulsion systems," *COMPEL - The Int'l Journal for Computation and Mathematics in Electrical and Electronic Engineering*, vol. 30, no. 1, pp. 9–31, 2011.

[119] G. Dajaku and D. Gerling, "A novel 12-teeth/10-poles PM machine with flux barriers in stator yoke," *in Proc. 20th Int'l Conf. on Electrical Machines (ICEM)*, 2012, pp. 36–40.

[120] G. Heins, D. M. Ionel, M. Thiele, "Winding factors and magnetic fields in permaent-magnet brushless machines with concentrated windings and modular stator cores," *IEEE Trans. on Ind. Appl.*, vol. 51, no. 4, pp, 2924-2932, 2015.

[121] Z.Q. Zhu, D. Ishak, and D. Howe, "Modular permanent magnet brushless machines having a fractional number of slots per pole – Influence of stator teeth and back-irons," *in Proc. 2006 Int'l Conf. on Electr. Mach. and Syst. (ICEMS)*, Nagasaki, Japan, 2006.

[122] Z. Q. Zhu, Z. Azar, and G. Ombach, "Influence of additional air gaps between stator segments on cogging torque of permanent-magnet machines having modular stators," *IEEE Trans. on Magn.*, vol. 48, no. 6, pp. 2049–2055, 2012.

[123] G. J. Li, Z. Q. Zhu, M. Foster, and D. Stone, "Comparative studies of modular and unequal tooth PM machines either with or without tooth tips," *IEEE Trans. on Magn.*, vol. 50, no. 7, pp. 1–10, Jul. 2014.

[124] G. Li, Z. Q. Zhu, W. Chu, M. Foster, and D. Stone, "Influence of flux gaps on electromagnetic performance of novel modular PM machines," *IEEE Trans. on Energy Convers.*, vol. 29, no. 3, pp. 716–726, Sep. 2014.

[125] P. Taras, G. J. Li, and Z. Q. Zhu, "Comparative study of alternative modular switched-flux permanent-magnet machines," *in Proc. Int. Conf. Ind. Technol.*, Seville, Spain, Mar. 2015, pp. 658–663.

[126] G. Heins, D. M. Ionel, and M. Thiele, "Winding factors and magnetic fields in permanent-magnet brushless machines with concentrated windings and modular stator cores," *IEEE Trans. on Ind. Appl.*, vol. 51, no. 4, pp. 2924-2932, 2015.

[127] Z. Q. Zhu, Y. J. Zhou, and J. T. Chen, "Electromagnetic performance of non-overlapping stator wound field synchronous machine with salient pole rotor," *IEEE Trans. on Magn.*, vol. 51, no. 11, 2015.

[128] Z. Q. Zhu, "Permanent magnet machines for traction applications," *Encyclopaedia of Automotive Engineering*, pp. 1–20. 2014.

[129] J. T. Chen and Z. Q. Zhu, "Winding configurations and optimal stator and rotor pole combination of flux-switching PM brushless AC machines," *IEEE Trans. on Energy Conver.*, vol. 25, no. 2, pp. 293 – 302, 2010.

[130] J. T. Chen, Z. Q. Zhu, S. Iwasaki, and R. P. Deodhar, "A novel hybrid-excited switched-flux brushless AC machine for EV/HEV applications" *IEEE Trans. on Vehicular Tech.*, vol. 60, no. 4, pp.1365-1373, May 2011.

[131] Z. Q. Zhu, "A simple method for measuring cogging torque in permanent magnet machine," *in Proc. IEEE Power & Energy Society General Meeting*, 2009, pp. 1-4.